

REPORT DOCUMENTATION PAGE		READ INSTRUCTIONS BEFORE COMPLETING FORM
1. REPORT NUMBER NAVENVPREDRSCHFAC Contractor Report CR 83-05	2. GOVT ACCESSION NO.	3. RECIPIENT'S CATALOG NUMBER
4. TITLE (and Subtitle) FURTHER DEVELOPMENTS OF THE A.R.A.P. MODEL FOR THE ATMOSPHERIC MARINE ENVIRONMENT		5. TYPE OF REPORT & PERIOD COVERED Final 13 Aug. 1981-12 Feb. 1983
7. AUTHOR(s) W.S. Lewellen, R.I. Sykes, and D.A. Oliver		6. PERFORMING ORG REPORT NUMBER ARAP # 488
9. PERFORMING ORGANIZATION NAME AND ADDRESS Aeronautical Research Associates of Princeton, Inc. 50 Washington Road, P.O. Box 2229 Princeton, New Jersey 08540		8. CONTRACT OR GRANT NUMBER(s) N00228-81-C-H459
11. CONTROLLING OFFICE NAME AND ADDRESS Naval Air Systems Command Department of the Navy Washington, DC 20361		10. PROGRAM ELEMENT, PROJECT, TASK AREA & WORK UNIT NUMBERS PE 62759N PN WF59-551 NEPRF WU 6.2-4
14. MONITORING AGENCY NAME & ADDRESS (if different from Controlling Office) Naval Environmental Prediction Research Facility Monterey, California 93940		12. REPORT DATE May 1983
		13. NUMBER OF PAGES 172
		15. SECURITY CLASS. (of this report) UNCLASSIFIED
		15a. DECLASSIFICATION DOWNGRADING SCHEDULE
16. DISTRIBUTION STATEMENT (of this Report) Approved for public release; distribution unlimited.		
17. DISTRIBUTION STATEMENT (of the abstract entered in Block 20, if different from Report)		
18. SUPPLEMENTARY NOTES		
19. KEY WORDS (Continue on reverse side if necessary and identify by block number) Turbulent Transport Modeling Fog Model Simulations Turbulent Cloud Microphysics Cumulus Parameterization Kelvin-Helmholtz Wave Breaking		
20. ABSTRACT (Continue on reverse side if necessary and identify by block number) This report presents further developments of A.R.A.P.'s model for computing the detailed low-level atmospheric distribution of velocity, temperature, moisture, refractive index, and the turbulent variations of these quantities. A number of simulations of possible fog scenarios have been run and compared with Calspan data. The detailed evolution of wave turbulent interactions in the inversion which caps the mixed layer has been analyzed with a view towards simpler parameterization of this phenomenon. (continued on reverse)		

Block 20, Abstract, continued.

The model has been extended in two quite separate areas: (1) to exhibit the role of turbulent agglomeration in cloud microphysics; and (2) to examine the conditions under which the turbulent macroscale becomes highly anisotropic and to provide a relatively simple means for incorporating this effect into our turbulent transport model whenever necessary. Preliminary analysis is given to argue that the A.R.A.P. model can be used as the basis of parameterization of the influence of sub-grid turbulent fluxes in mesoscale meteorological models.

AN (1) AD-A129 862
FG (2) 040200
FG (2) 120100
CI (3) (U)
CA (5) AERONAUTICAL RESEARCH ASSOCIATES OF PRINCETON INC NJ
TI (6) Further Developments of the A. R. A. P. Model for the
Atmospheric Marine Environment.
TC (8) (U)
DN (9) Final rept. 13 Aug 81-12 Feb 83.
AU (10) Lewellen, W. S.
AU (10) Sykes, R. I.
AU (10) Oliver, D. A.
RD (11) May 1983
PG (12) 173p
RS (14) ARAP-488
CT (15) N00228-81-C-H459
PJ (16) F59551
TN (17) WF59551
RN (18) NEPRF-CR-83-05
RC (20) Unclassified report
DE (23) *Marine atmospheres, *fog, *Mathematical models,
Atmosphere models, Ocean environments, Boundary layer
transition, Air water interactions, Navier Stokes
equations, Cartesian coordinates, Troposphere, Low
altitude, Turbulence
DC (24) (U)
ID (25) PE62759N, WU624
IC (26) (U)
AB (27) This report presents further developments of A.R.A.P.'s
model for computing the detailed low-level atmospheric
distribution of velocity, temperature, moisture,
refractive index, and the turbulent variations of these
quantities. A number of simulations of possible fog
scenarios have been run and compared with Calspan data.
The detailed evolution of wave turbulent interactions
in the inversion which caps the mixed layer has been
analyzed with a view towards simpler parameterization
of this phenomenon. The model has been extended in two
quite separate areas: (1) to exhibit the role of
turbulent agglomeration in cloud microphysics; and (2)
to examine the conditions under which the turbulent
macroscale becomes highly anisotropic and to provide a
relatively simple means for incorporating this effect
into our turbulent transport model whenever necessary.
Preliminary analysis is given to argue that the A.R.A.
P. model can be used as the basis of parameterization
of the influence of sub-grid turbulent fluxes in
mesoscale meteorological models. (Author)
AC (28) (U)
DL (33) 01
SE (34) F
CC (35) 008400

ROUTINE REPLY, ENDORSEMENT, TRANSMITTAL OR INFORMATION SHEET
 OPNAV 5216/158 (Rev. 7-78) A WINDOW ENVELOPE MAY BE USED
 SN 0107 LF 052 1091 Formerly AFEXOS 1789

CLASSIFICATION (UNCLASSIFIED when detached from enclosures, unless otherwise indicated)
UNCLASSIFIED

FROM (Show telephone number in addition to address)
 Commanding Officer, Naval Environmental Prediction Research
 Facility, Monterey, CA 93940 AVN 878-2928

DATE
 21 June 1983

SERIAL OR FILE NO.
 5600 NEPRF/SBB:sb
 SER 252

SUBJECT
 NAVENVPREDRSCHFAC technical publication; forwarding of

REFERENCE

TO:

Distribution
 [see Encl (1), pp 167-170]

ENCLOSURE

(1) NAVENVPREDRSCHFAC
 Contractor Report CR 83-05:
 Further Developments of the
 A.R.A.P. Model for the
 Atmospheric Marine
 Environment

VIA: _____ ENDORSEMENT ON _____

FORWARDED RETURNED FOLLOW-UP, OR TRACER REQUEST SUBMIT CERTIFY MAIL FILE

GENERAL ADMINISTRATION	CONTRACT ADMINISTRATION	PERSONNEL
FOR APPROPRIATE ACTION UNDER YOUR COGNIZANCE	NAME & LOCATION OF SUPPLIER OF SUBJECT ITEMS	REPORTED TO THIS COMMAND:
<input checked="" type="checkbox"/> INFORMATION & retention	SUBCONTRACT NO. OF SUBJECT ITEM	
APPROVAL RECOMMENDED <input type="checkbox"/> YES <input type="checkbox"/> NO	APPROPRIATION SYMBOL, SUBHEAD, AND CHARGEABLE ACTIVITY	DETACHED FROM THIS COMMAND
<input type="checkbox"/> APPROVED <input type="checkbox"/> DISAPPROVED	SHIPPING AT GOVERNMENT EXPENSE <input type="checkbox"/> YES <input type="checkbox"/> NO	OTHER
COMMENT AND/OR CONCURRENCE	A CERTIFICATE, VICE BILL OF LADING	
CONCUR	COPIES OF CHANGE ORDERS, AMENDMENT OR MODIFICATION	
LOANED, RETURN BY:	CHANGE NOTICE TO SUPPLIER	
SIGN RECEIPT & RETURN	STATUS OF MATERIAL ON PURCHASE DOCUMENT	
REPLY TO THE ABOVE BY:		

REFERENCE NOT RECEIVED

SUBJECT DOCUMENT FORWARDED TO:

SUBJECT DOCUMENT RETURNED FOR:

SUBJECT DOCUMENT HAS BEEN REQUESTED, AND WILL BE FORWARDED WHEN RECEIVED

COPY OF THIS CORRESPONDENCE WITH YOUR REPLY

ENCLOSURE NOT RECEIVED

ENCLOSURE FORWARDED AS REQUESTED

ENCLOSURE RETURNED FOR CORRECTION AS INDICATED

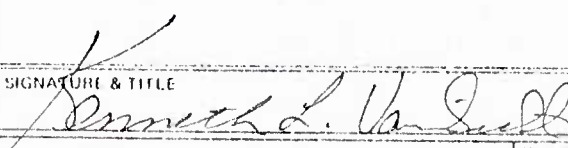
CORRECTED ENCLOSURE AS REQUESTED

REMOVE FROM DISTRIBUTION LIST

REDUCE DISTRIBUTION AMOUNT TO:

REMARKS (Continue on reverse)

Enclosure (1) describes new capabilities that have been developed for the A.R.A.P. planetary boundary layer model. Significant advances discussed include parameterization of wave-turbulence interaction, the role of turbulence in cloud microphysics, and the use of an anisotropic length scale in second-order closure modeling.

SIGNATURE & TITLE
 Commanding Officer

COPY TO:

CLASSIFICATION (UNCLASSIFIED when detached from enclosures, unless otherwise indicated)
UNCLASSIFIED



NAVENVPREDRSCHFAC
CONTRACTOR REPORT
CR 83-05

LIBRARY
RESEARCH REPORTS DIVISION
NAVAL POSTGRADUATE SCHOOL
MONTEREY, CALIFORNIA 93940

NAVENVPREDRSCHFAC CR 83-05

FURTHER DEVELOPMENTS OF THE A. R. A. P. MODEL FOR THE ATMOSPHERIC MARINE ENVIRONMENT

Prepared By:

W. S. Lewellen, R. I. Sykes, D. A. Oliver

at Aeronautical Research Associates of Princeton, Inc., *at* Princeton, NJ 08540

Report
ARAP 488

Contract No. N00228-81-C-H459

MAY 1983

APPROVED FOR PUBLIC RELEASE
DISTRIBUTION UNLIMITED



Prepared For:
NAVAL ENVIRONMENTAL PREDICTION RESEARCH FACILITY,
MONTEREY, CALIFORNIA 93940

CONTENTS

	<u>Page</u>
1. INTRODUCTION	1
2. PARTICIPATION IN THE CALSPAN FOG MODEL EVALUATION STUDY.	2
Introduction.	2
Brief Review of the A.R.A.P. Model Operation for this Fog Study.	2
Modifications Arising after the NEPRF Meeting	3
Model Results - Cases 1 through 6	17
Summary and Conclusions	34
3. ON THE ONE-DIMENSIONAL PARAMETERIZATION OF WAVE-TURBULENT INTERACTIONS	36
Introduction.	36
Summary of Numerical Results.	37
Previous Results.	38
Variations in Initial Profile Shape	39
Larger Initial Richardson Numbers	51
One-Dimensional Calculations of the Kelvin-Helmholtz Instability.	63
Development of Parameterizations.	72
4. COMMENTS ON THE EXTENSION OF OUR INTEGRAL BOUNDARY LAYER MODEL FROM ONE-DIMENSIONAL TO THREE-DIMENSIONAL.	77
5. PRELIMINARY CONSIDERATIONS OF CUMULUS PARAMETERIZATION BASED ON SECOND-ORDER CLOSURE	81
Introduction.	81
Second-Order Closure Turbulence Equations with Cloud Correlations.	82
Turbulence Closure Theory on an Intermittent Turbulence Field	89
Data Comparisons.	96
6. CONCLUDING REMARKS	100
7. REFERENCES	103
APPENDIX A. MODELING THE ROLE OF TURBULENCE IN CLOUD MICROPHYSICS	107
APPENDIX B. THE INCORPORATION OF AN ANISOTROPIC SCALE INTO THE SECOND-ORDER CLOSURE MODEL	145

1. INTRODUCTION

For several years, A.R.A.P., Inc. has been developing a computer model for determining the detailed low-level atmospheric distributions of velocity, temperature, moisture, refractive index, and the turbulent variations of these quantities for marine environments. The three physical processes most critical for determining the atmospheric marine boundary layer are turbulent transport, thermal radiation, and change of phase of atmospheric water. Reference 1 provides a review of our understanding of these processes and a review of some of the sample calculations which successfully illustrate features expected in the atmospheric marine boundary layer. The most recent status report on this model is given in Reference 2. Details of the foundation of the model, yearly developments and a number of exemplary simulations are given in References 3-19.

Our efforts over the past 18 months have again been divided between simulations using the existing model and model developments. A major part of our model simulations have been associated with the particular scenarios chosen by Calspan for use in their fog model study. These simulations, along with the model modifications made as a result of these calculations, are discussed in Chapter 2. Another important segment of model simulations has been devoted to further understanding the process of wave breaking in stably stratified regions of the atmosphere. The goal of these simulations discussed in Chapter 3 is to provide an adequate representation of this wave-turbulent interaction for one-dimensional models of the atmospheric boundary layer.

The two principal model developments during this time period are improved modeling of the cloud microphysics, and the incorporation of the possibility of an anisotropic scale into our second-order closure model. These two developments are presented in Appendix A and B, which are written for submission as separate journal articles. Preliminary explorations of two major model developments are presented in Chapters 4 and 5. These are the development of a three-dimensional model, and cumulus parameterization.

2. PARTICIPATION IN THE CALSPAN FOG MODEL EVALUATION STUDY

Introduction

As part of an assessment of the Naval Air System Command's Marine Fog Investigation program, Calspan organized an evaluation study of fog models based on comparison of model simulations for six observational cases chosen by Calspan. A.R.A.P. participated in this evaluation study by first responding with the "blind" model simulations requested by Calspan, and second by a rerun of each of these cases after the preliminary results were made public at the workshop at NEPRF in May 1982.

The initial model results were rather disappointing for us, with only three of the cases showing reasonable correspondence with data. Our prime purpose here is to report on subsequent model developments and the information gained from model reruns of these fog scenarios.

Brief Review of the A.R.A.P. Model Operation for this Fog Study

We used the one-dimensional version of our Reynolds-stress transport closure model, in which differential equations are solved for all first and second-order moments of the dynamic and thermodynamic variables. The equations are described in detail by Lewellen¹, and by Oliver et al.,¹². The differential equations are solved numerically using finite-difference techniques and a self-adjusting grid system, i.e., the numerical mesh changes as the solution changes to maintain good resolution of sharp features such as the capping inversion.

The six Calspan fog cases were simulated by marching forward with time as the independent variable, and converting the spatial surface temperature variation into a temporal variation using the mean velocity in the boundary layer. We recognize that this does not yield a completely consistent simulation of the data which represents vertical distributions of temperature and humidity at different horizontal positions at different times. However, it probably represents as consistent a simulation as is possible using data which are insufficient to specify the effects of horizontal advection. Our simulation thus necessarily neglects contributions from horizontal advection, which are very likely to be a significant source of error.

The atmospheric radiation scheme treats terrestrial long wave and solar shortwave radiation separately. The long wave component is calculated using the usual convolution integrals over the emission and transmissivity profiles. The transmissivities are parameterized as sums of exponential functions of the liquid water, water vapor, and carbon dioxide path integrals. The emission functions are taken to be the black body emission at the local absolute temperature of the air.

Shortwave radiation is calculated using the "two-stream" model for upward and downward flux components. The scheme includes a direct absorption coefficient, and also a scattering effect when liquid water is present. Details of the radiation schemes can be found in Lewellen et al.,¹⁴.

Modifications Arising After the NEPRF Meeting

As a result of the comparison between initial model results and observations shown in Figures 1 to 12 and presented at the meeting at NEPRF in May 1982, we made an extensive review of our model. The program was modified to correct several possible problems, and all six cases rerun with the improved model. In addition to correcting some input conditions, the following program changes were made:

- (i) The full temperature profiles through the troposphere and higher have been incorporated into the downward long wave radiative flux calculation. This eliminates the need to estimate downward fluxes at the top of the boundary layer from the profile; the flux is now explicitly calculated using the same radiative transfer model as the boundary layer program.
- (ii) The reflection of long wave radiative flux at the ground has been set to zero. In our original runs, there was a reflection at the surface of 10% of the downward radiation. This produced unreasonable heating close to the ground in the stable cases 2 and 5, and seems to be due to the inconsistency between assuming black body emission properties and non-zero reflectivity.

- (iii) A numerical finite-differencing problem at the top of the cloud layer was pointed out by Steve Burk where the radiative fluxes are virtually discontinuous. Our use of a central difference resulted in part of the large cooling being applied to the dry layer immediately above the cloud. This produces a spurious entrainment of the dry air into the boundary layer. This problem was corrected by using one-sided differences, and care was taken to ensure that the total flux budget was preserved.
- (iv) The approximate formula for the radiative convolution integral as described in Lewellen et. al,¹⁴ was replaced by the full integral expression; this is more expensive to compute but should be more accurate.

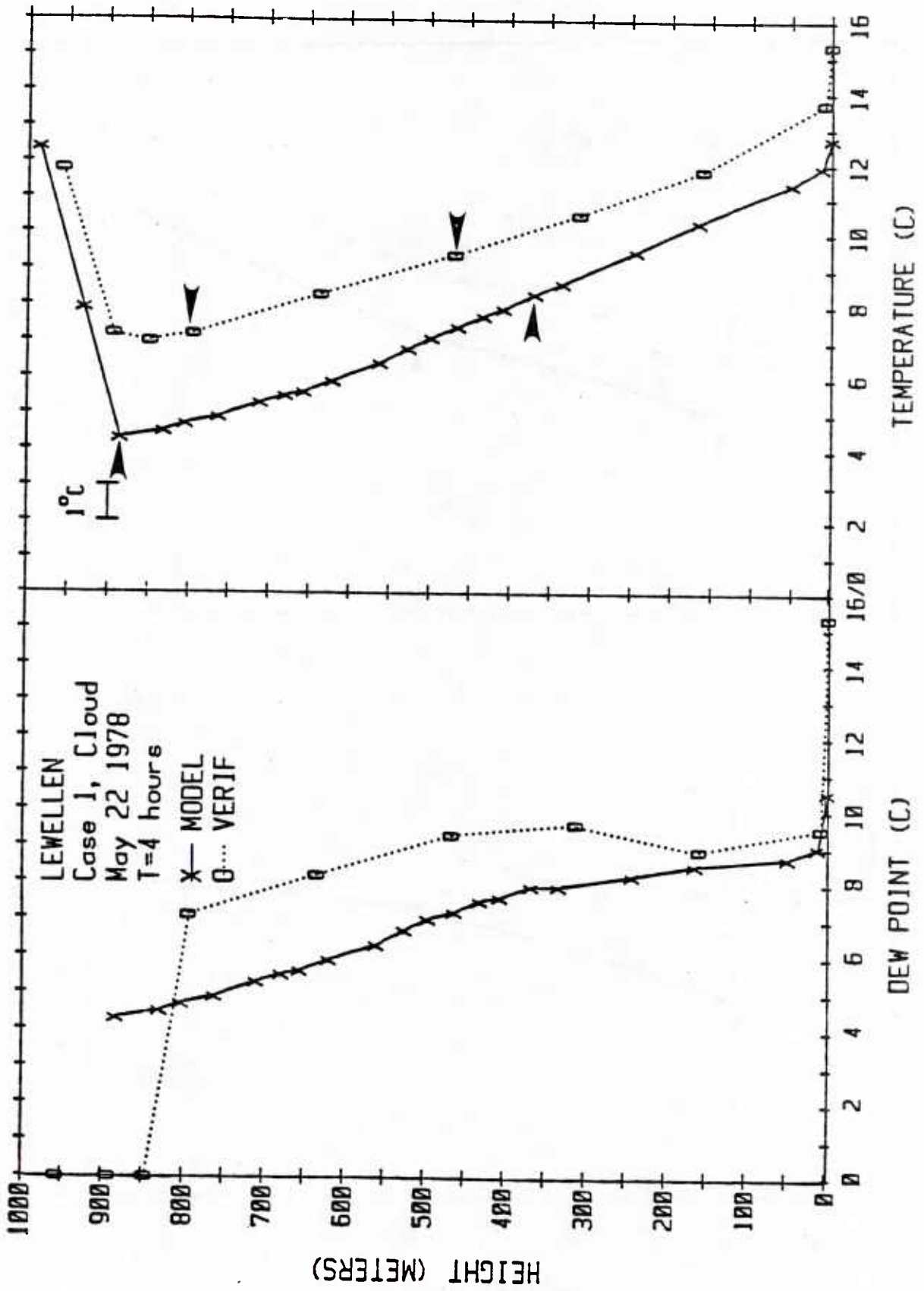


Figure 2.1

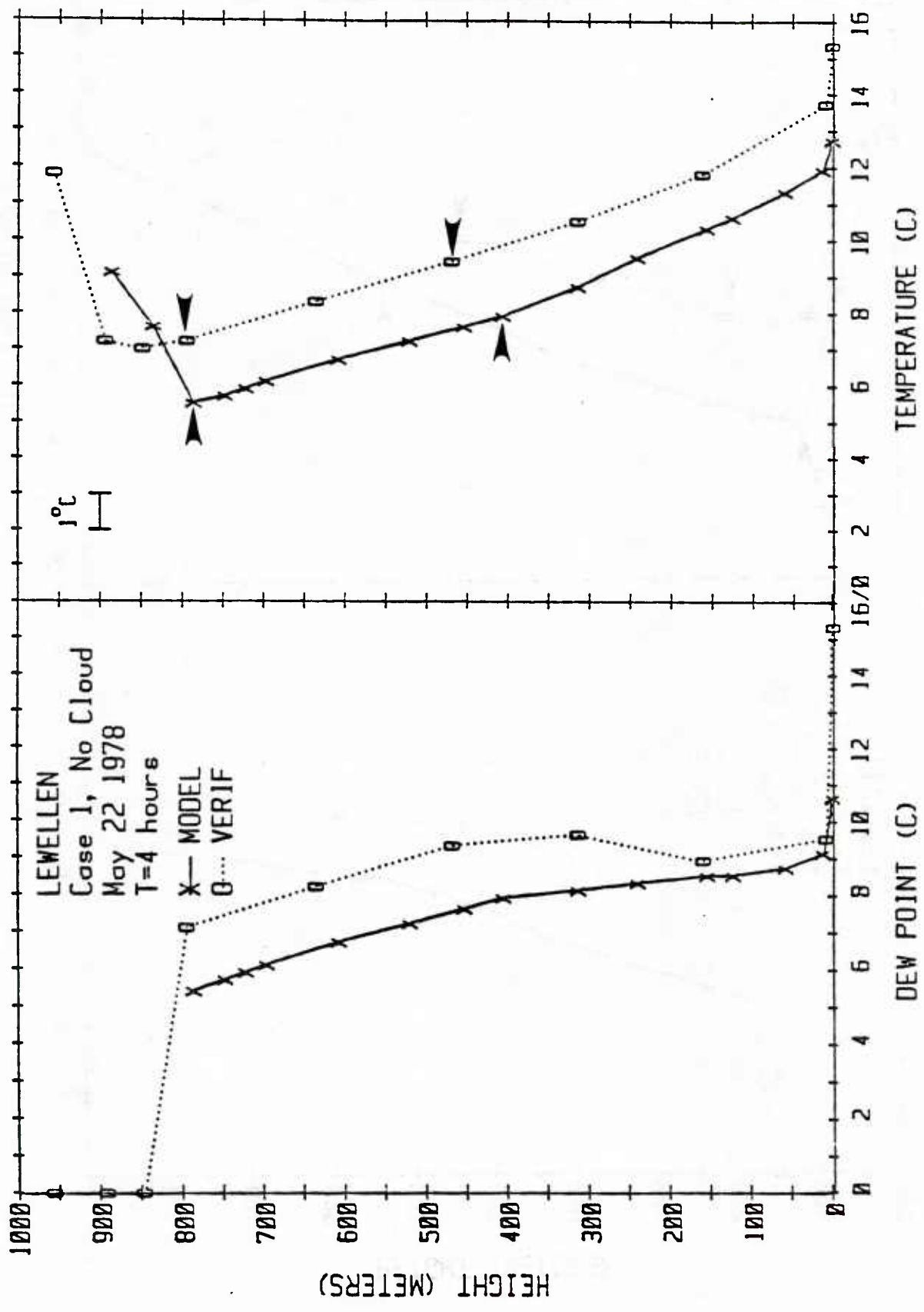


Figure 2.2

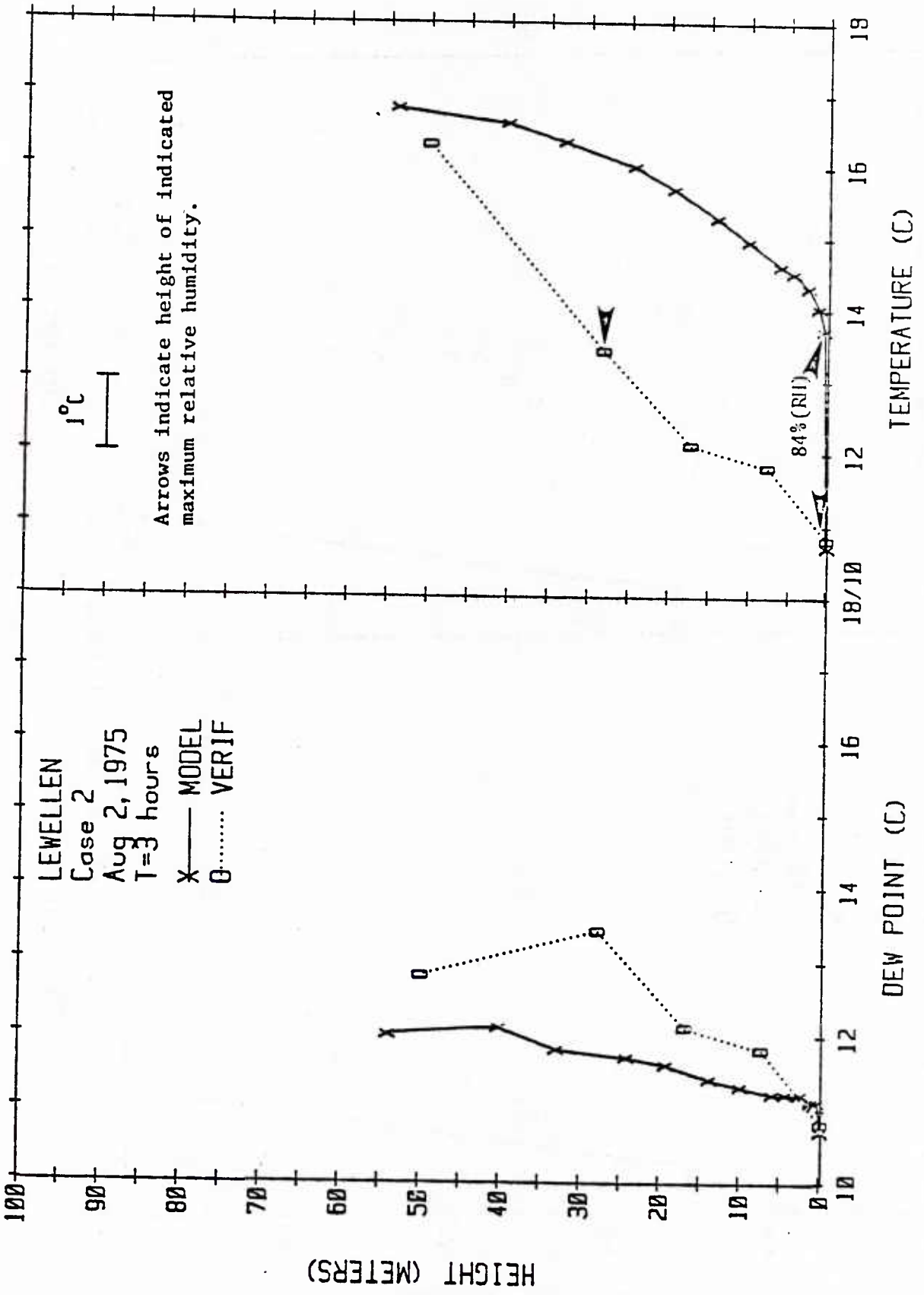


Figure 2.3

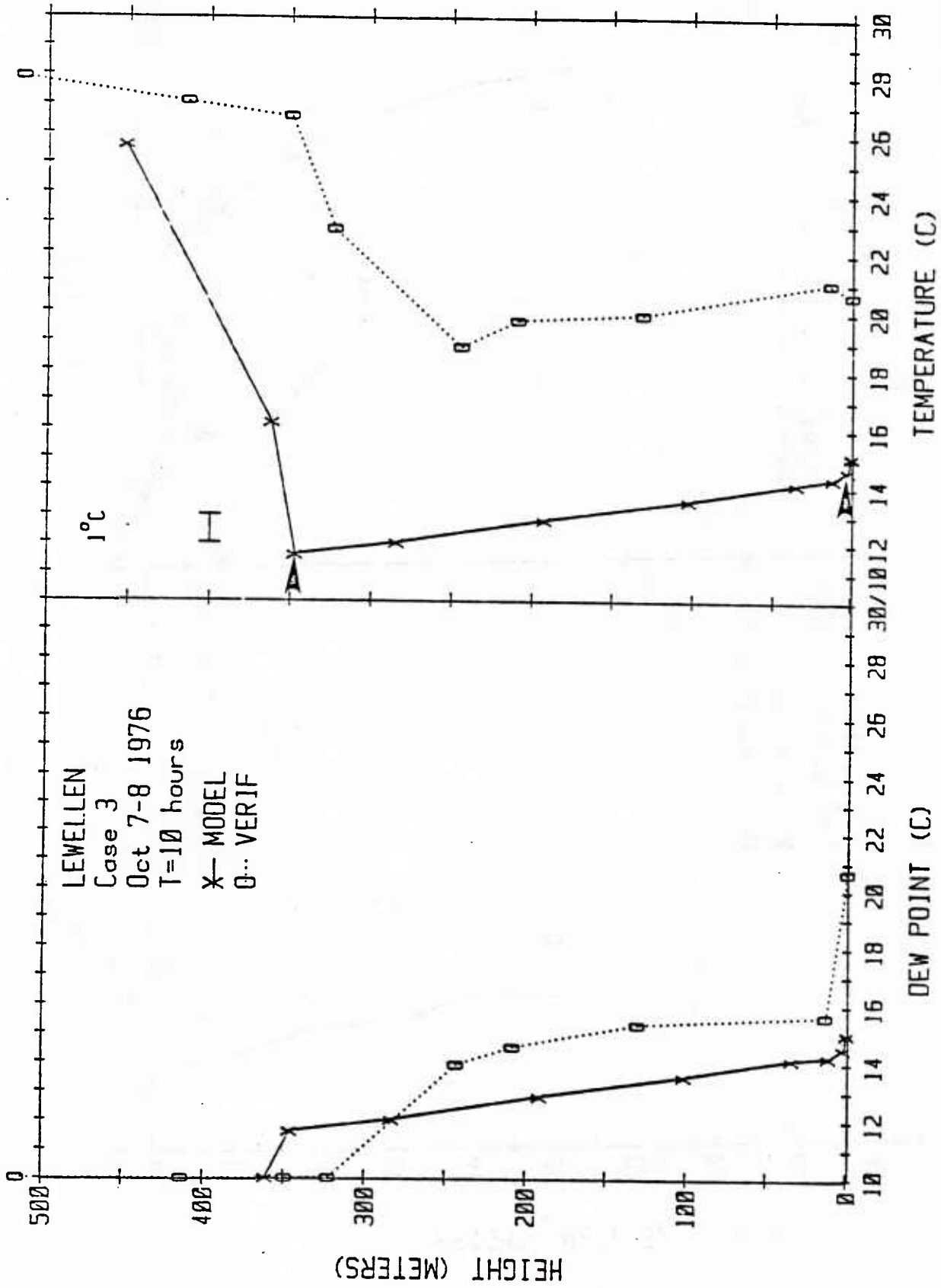


Figure 2.4

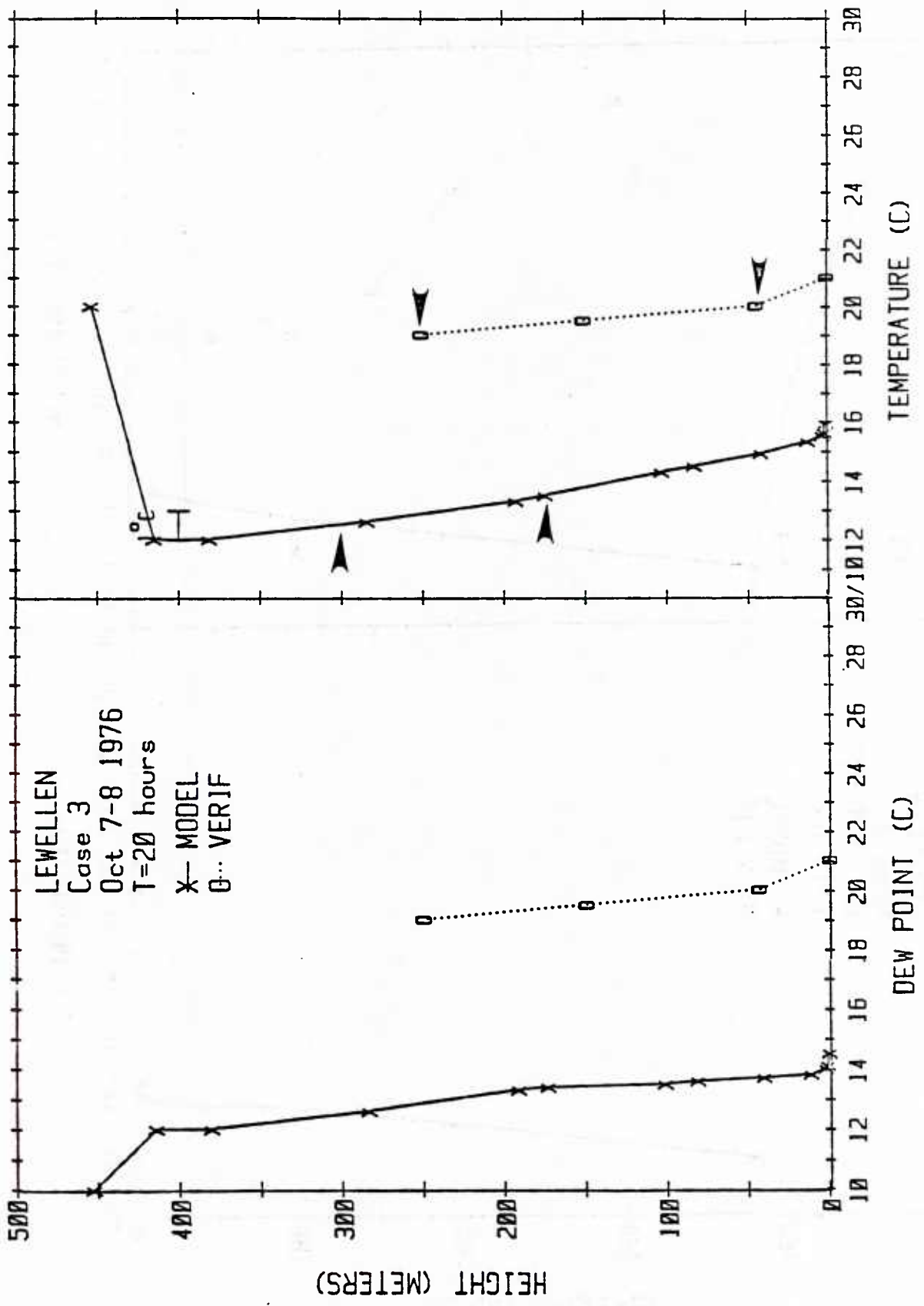


Figure 2.5

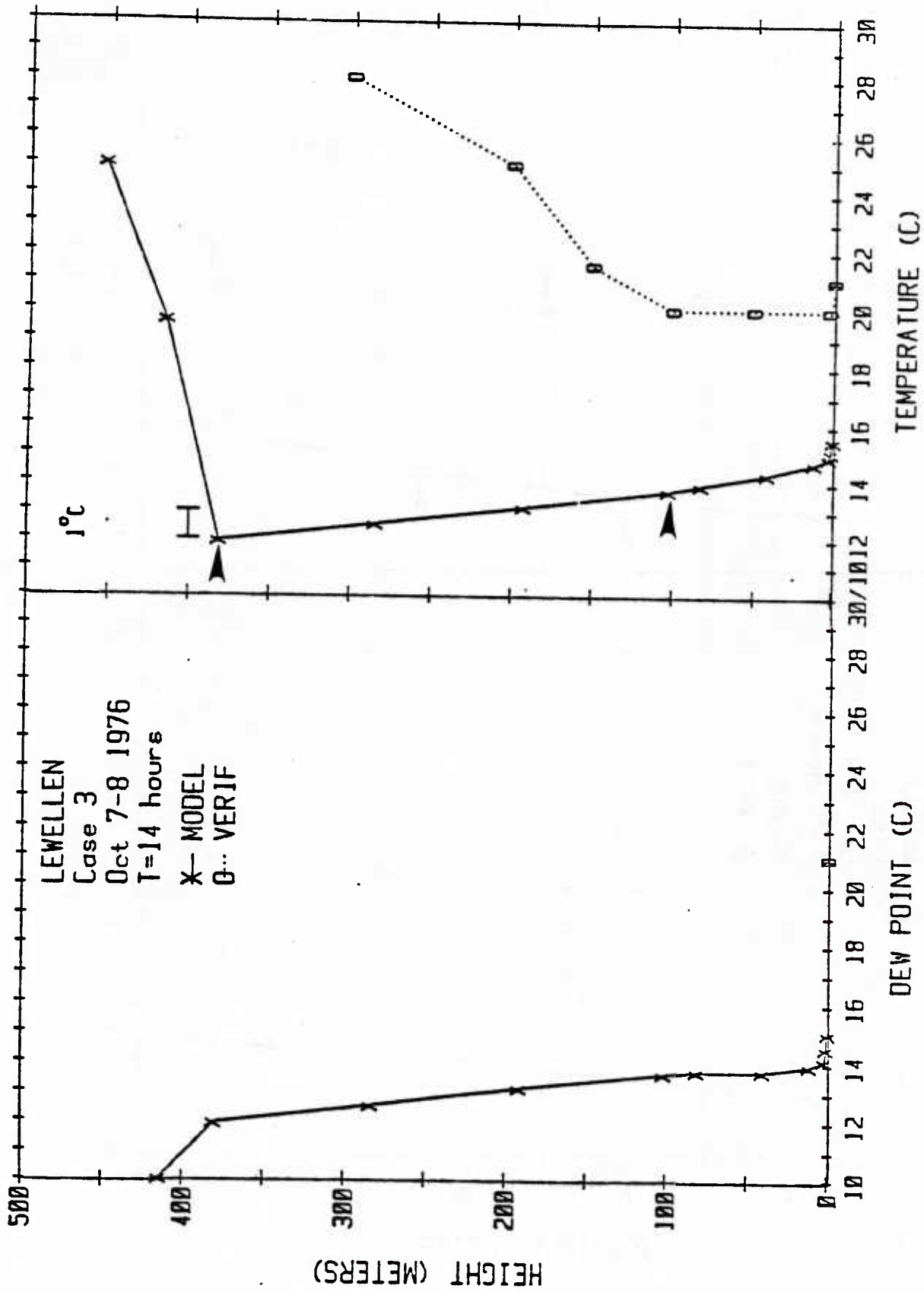


Figure 2.5

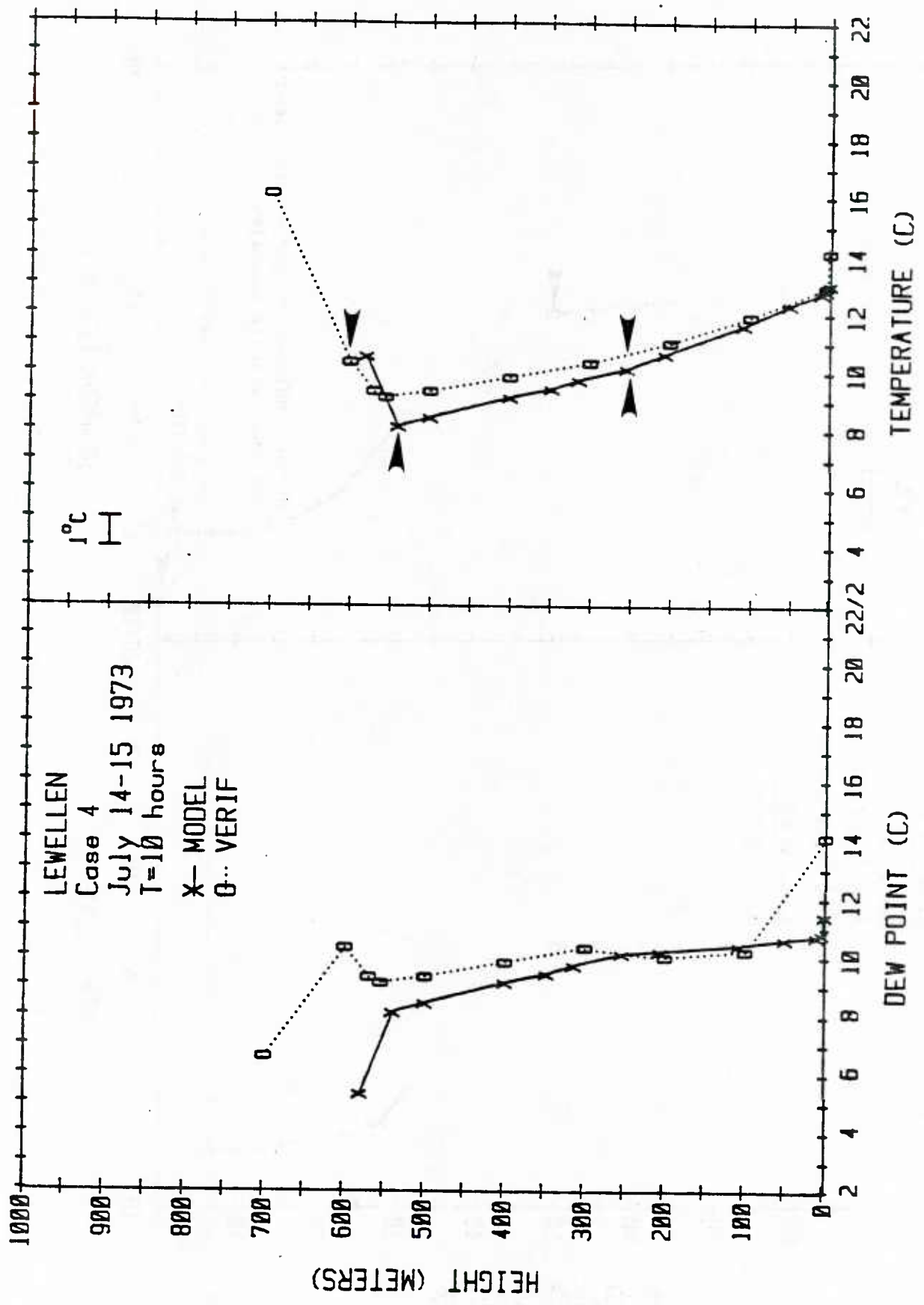


Figure 2.7

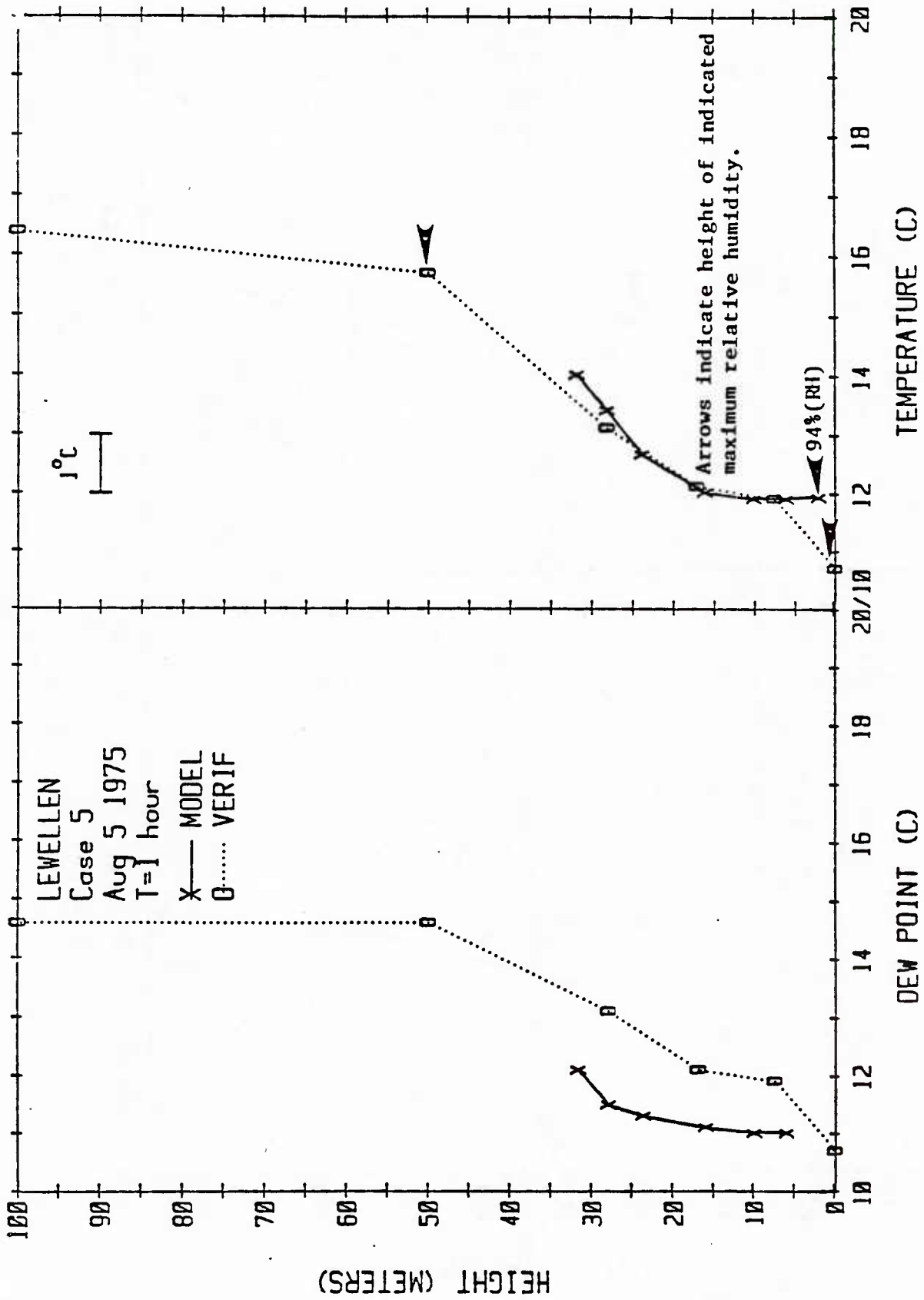


Figure 2.8

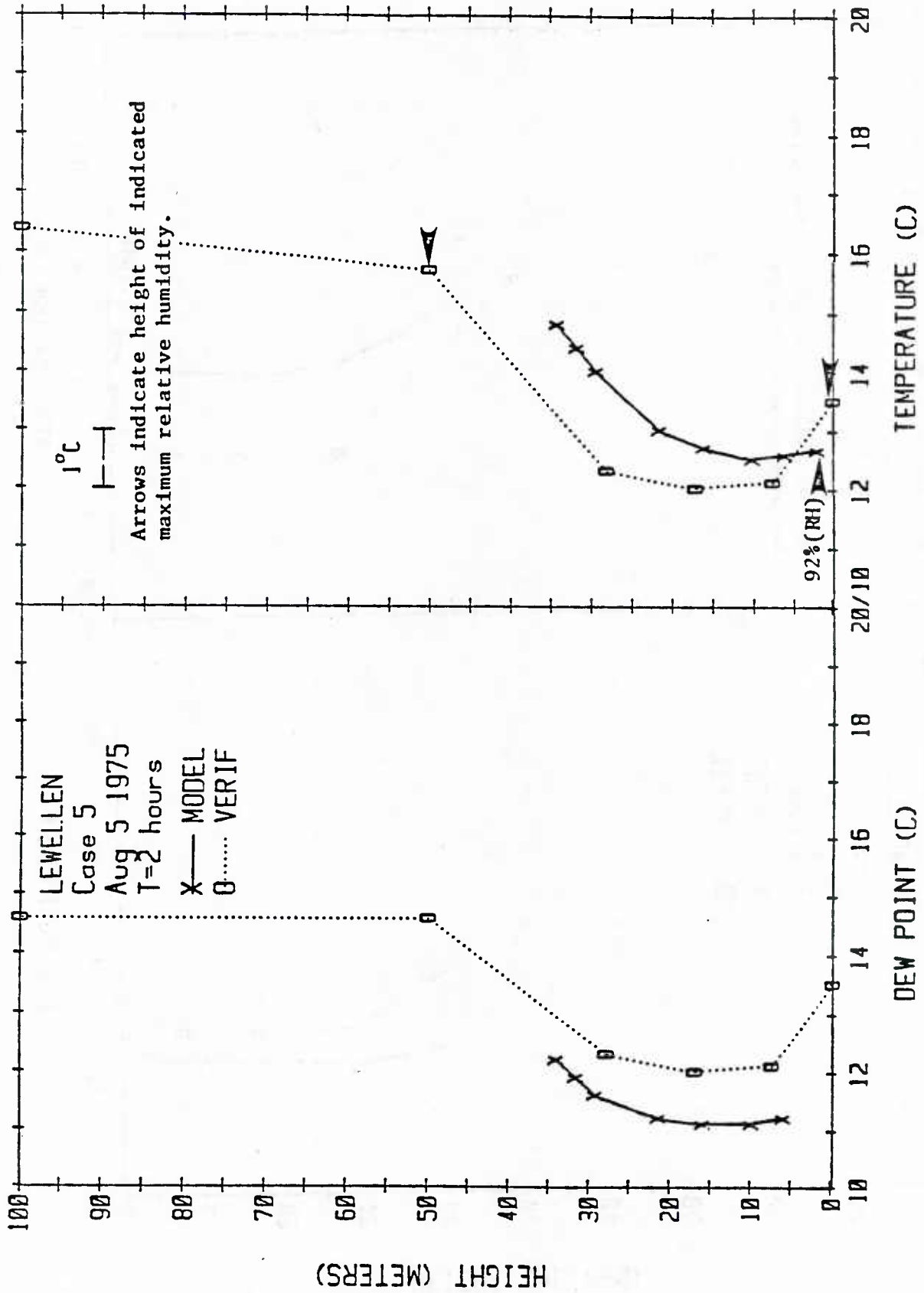


Figure 2.9

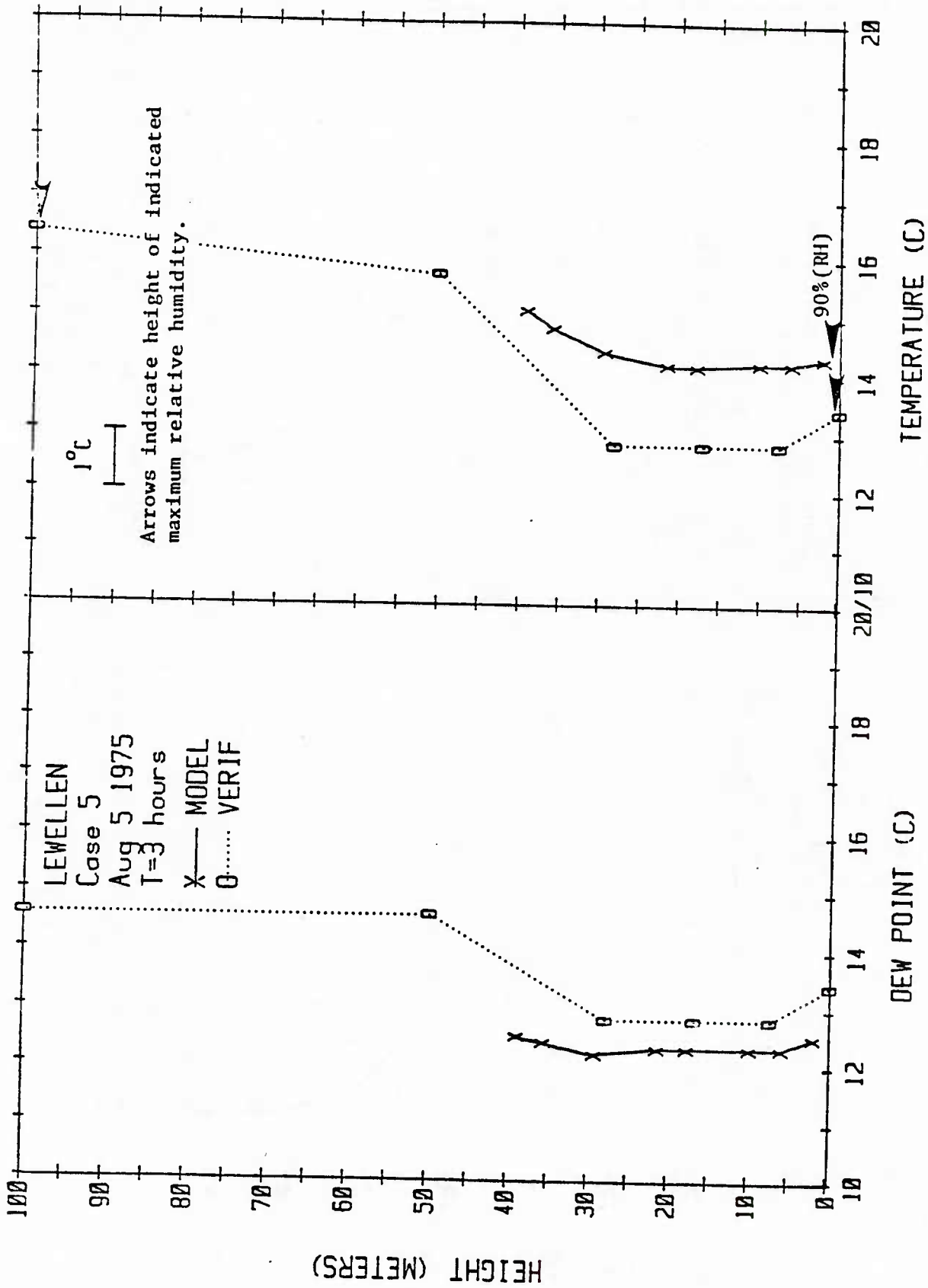


Figure 2.10

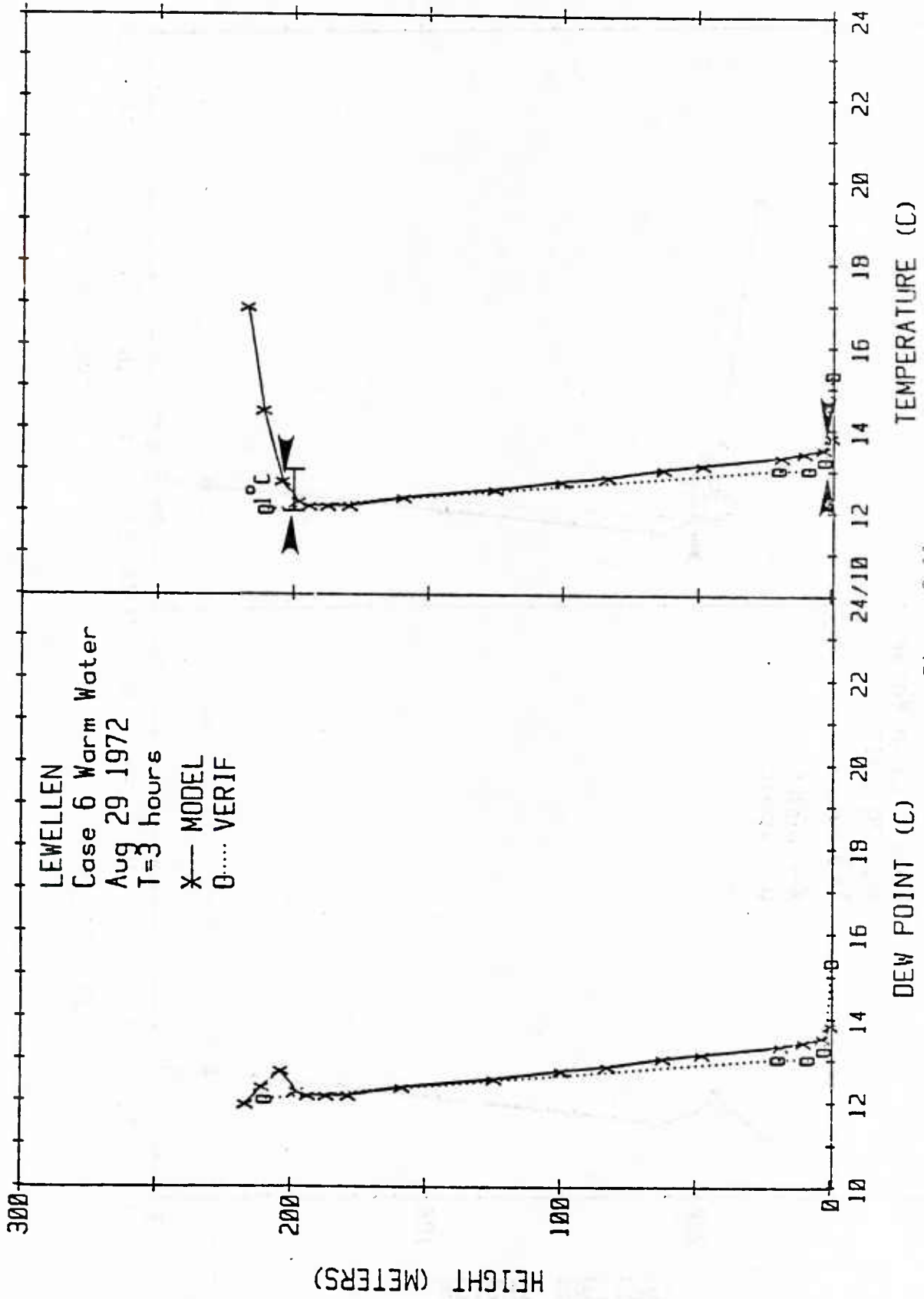


Figure 2.11

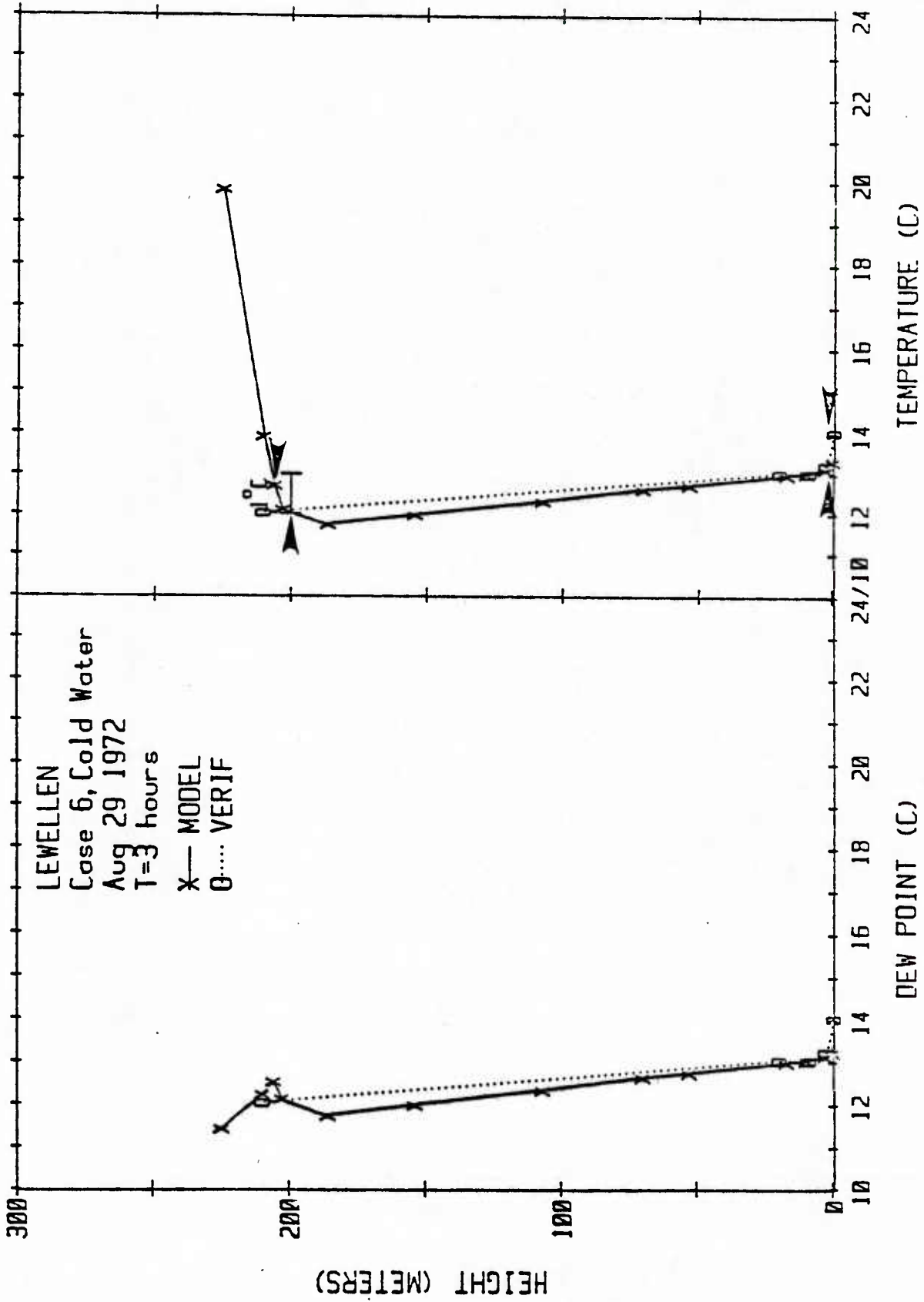


Figure 2.12

Model Results

Case 1

This case corresponds to observations during a cruise Northwest of San Nicolas Island on 22 May 1978. The simulation covers 4 hours from 0500 PDT to 0900 PDT. Air temperature was colder than the sea surface temperature. This case was run with two different initial conditions, first with a thin cloud layer, then with no initial cloud. In both cases the cloud base lowers and the cloud becomes thicker. After four hours, the results are not very dependent on the initial conditions. No fog was observed or predicted. The new model results for temperature, Figures 13 and 14, are slightly closer than the old results, but both runs were in reasonable agreement with the observations. The major difference in our most recent run and the initial run was a correction to the input solar radiation which was erroneously set at only 4% of its correct value.

Case 2

This case calls for the simulation of the shallow advection fog formed over the cold sea surface during a 3 hour evening period (1700 to 2000 EDT) off the coast of Nova Scotia on 2 August 1975. The new run for this case, Figure 15, is much closer to the observations than our original result. The ground reflection of long wave radiation was the cause of the low-level heating in our earlier integration and gave temperatures roughly 3°C too warm. Without the reflection, our predicted temperatures are very close to the observations below 30 m where the measurements were made. We still do not predict fog, but our maximum relative humidity is now about 96% in the lowest few meters. We believe the relatively large horizontal gradients in sea surface temperature observed at this time (Figure 16) play a key role in this type fog. As mentioned previously, the simulation of this as an unsteady, horizontally homogeneous flow should not be expected to accurately simulate the role of horizontal advection of temperature and humidity. This could only be the case if vertical gradients in wind velocity were unimportant.

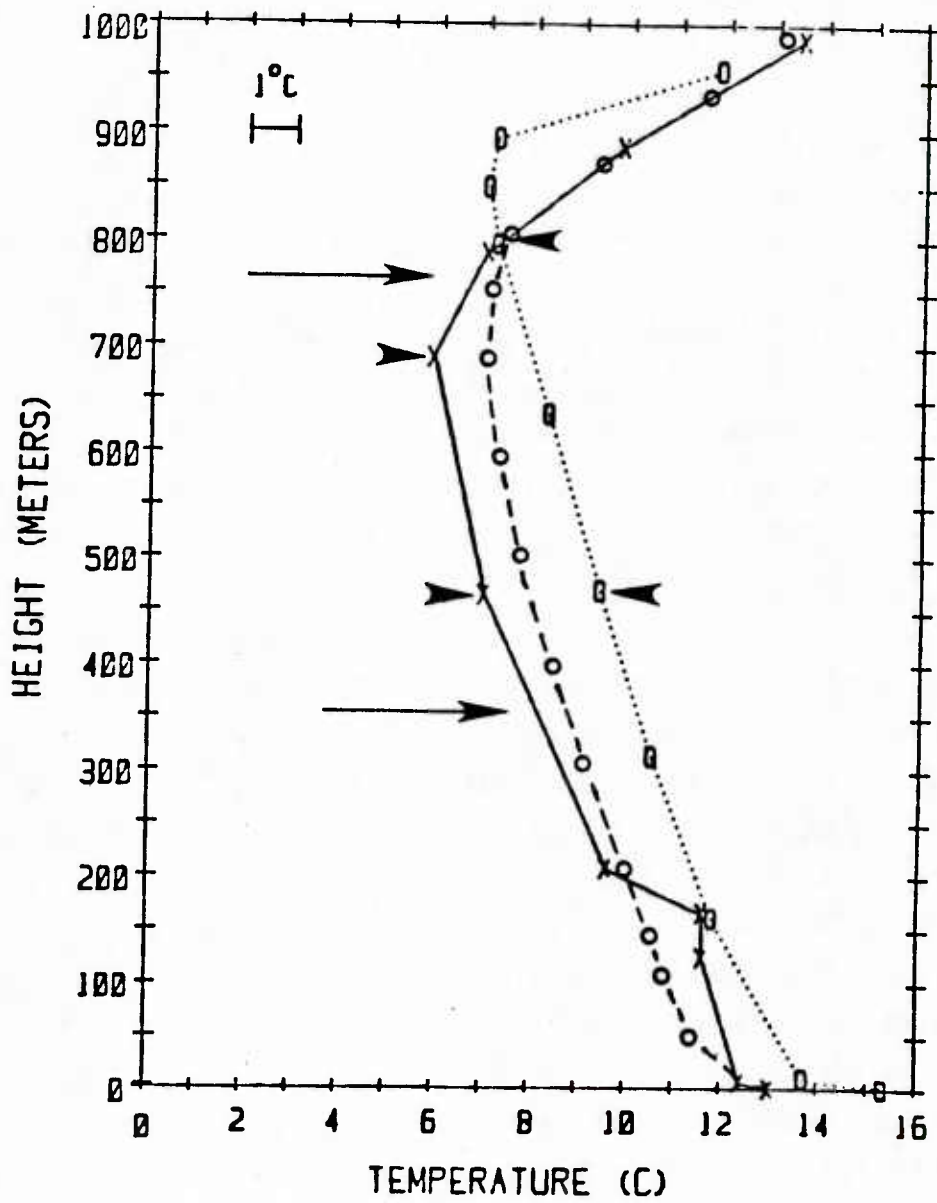


Figure 2.13 Case 1, Cloud, T = 4 hours

x ——— INITIAL
 o ······· VERIF
 o - - - - - MODEL

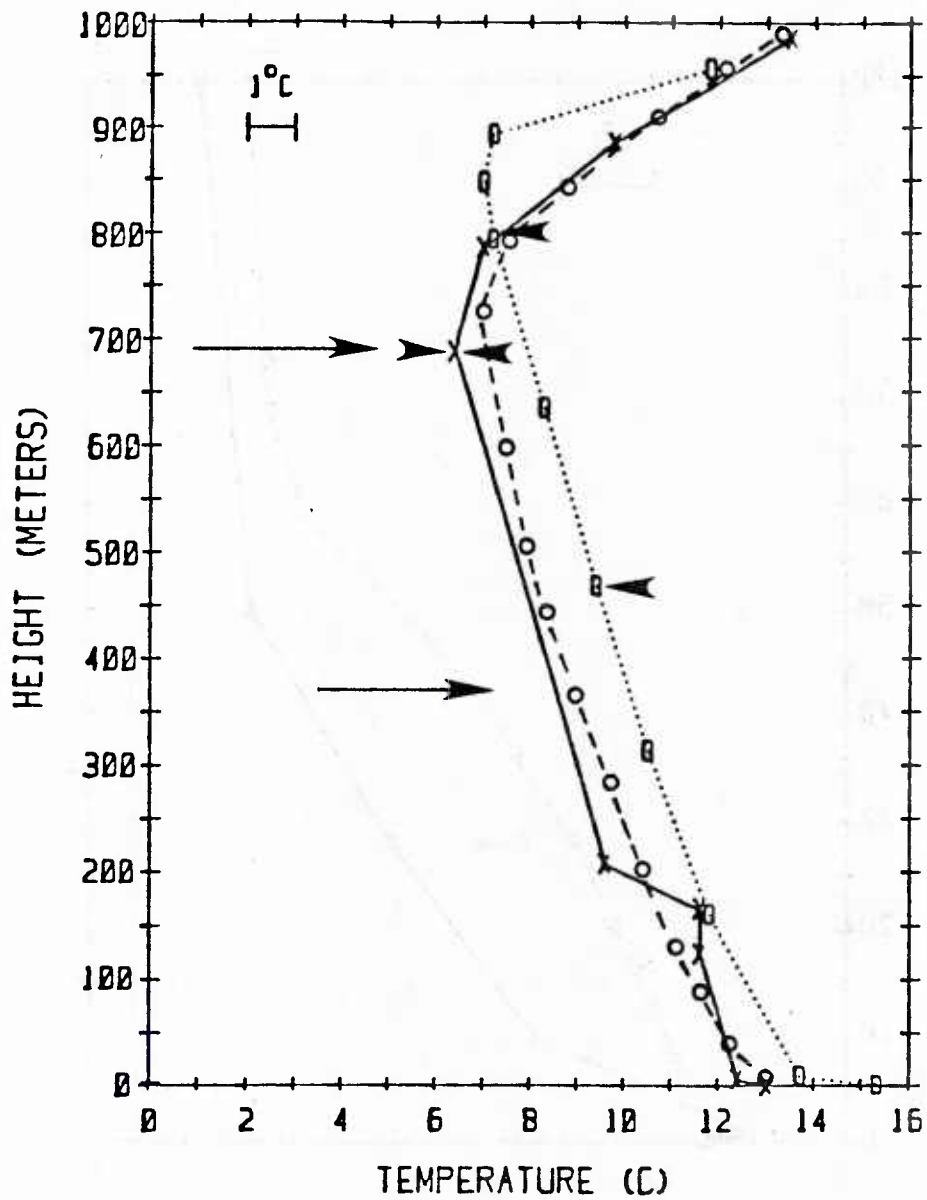


Figure 2.14 Case 1, Cloud, T = 4 hours

x _____ INITIAL
 o VERIF
 o - - - - - MODEL

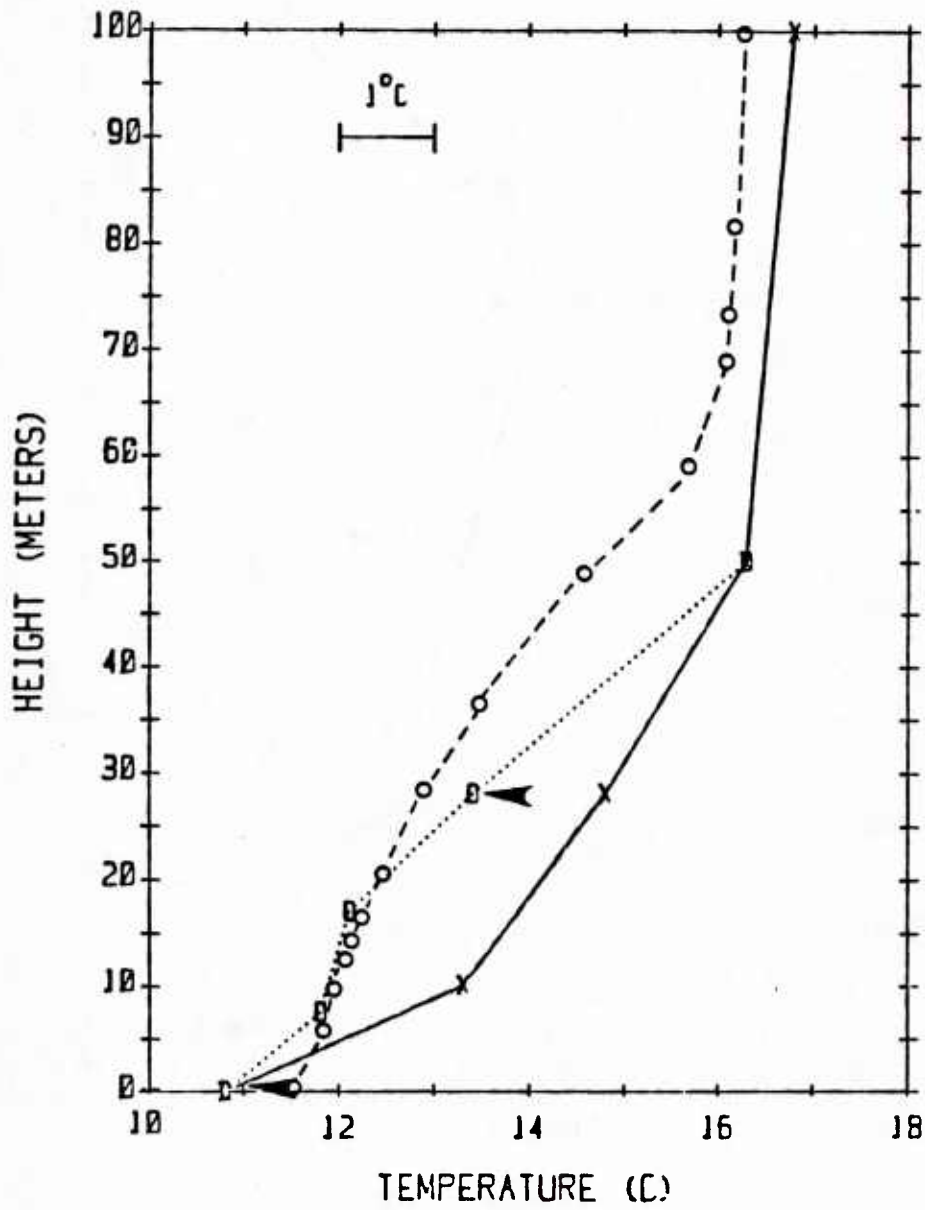


Figure 2.15 Case 2, T = 3 hours

x _____ INITIAL
 o VERIF
 o - - - - - MODEL

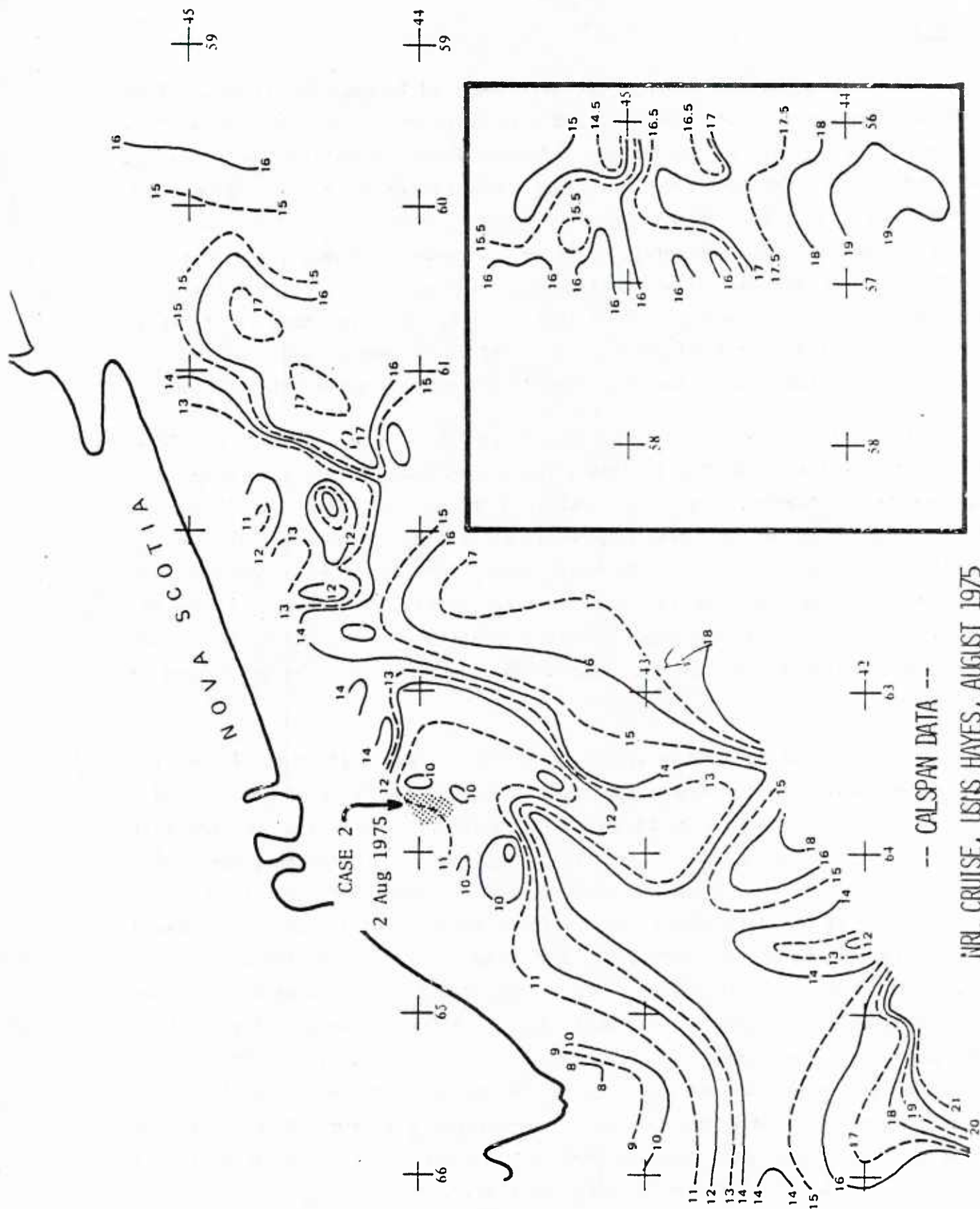


Figure 2.16 Isopleths of sea surface temperature ($^{\circ}\text{C}$) and regions of fog demonstrating the spatial inhomogeneities present during the case 2 simulation.

Case 3

This case is a simulation of 20 hours observed between San Nicolas Island and San Diego on 7 October 1976. A 100 m thick stratus cloud, beneath a 250 m inversion, dissipates during the day and redevelops during the early evening to produce fog under conditions of strong subsidence above the inversion. Our original run for this case was grossly in error because the shortwave solar radiation was set, inadvertently, at 4% of its correct value. Since this case runs throughout the day, solar heating is quite important, and the differences in the new run are mainly due to this change. For the three verification times, we see that the model predicts a shrinking boundary layer in response to the applied subsidence, and also significant heating during the daytime.

The run is initialized with a cloud about 100 m thick and base at 175 m. This cloud actually lowers to form a fog around dawn, but is then evaporated by the solar heating over the next 2-3 hours, so that at the first verification time of 10 hours, Figure 17, we have no cloud. At this time our prediction is somewhat cold in the mixed layer, and the mixed layer depth is too shallow. However, at the next verification time of 14 hours, Figure 18, the prediction is in almost exact agreement with the observations. It seems that the subsidence rate was not uniform over the first 14 hours as assumed in the model run.

The prediction is also in error at the final time of 20 hours, Figure 19, where the observations show a fog layer up to 250 m. Our prediction gives a 70 m boundary layer with a 97.5% relative humidity. There are two possible causes of the discrepancy. Firstly, the assumption of constant subsidence rate may be incorrect; it may well be reduced in the later part of the run since there is no data above the inversion to indicate a continued downward trend. Indeed, to entrain over 150 m over 6 hours, i.e., from 100 m to 250 m between 14 hours and 20 hours in the face of a 0.3 cm s^{-1} subsidence at that height, seems a formidable entrainment rate. The second possibility is that the predicted entrainment rates are too small; this is quite possible also since we are aware of deficiencies in the model entrainment in the free convection regimes. The discrepancy is most probably a combination of the two effects, but without an observational measurement of one of them it is impossible to determine their relative importance.

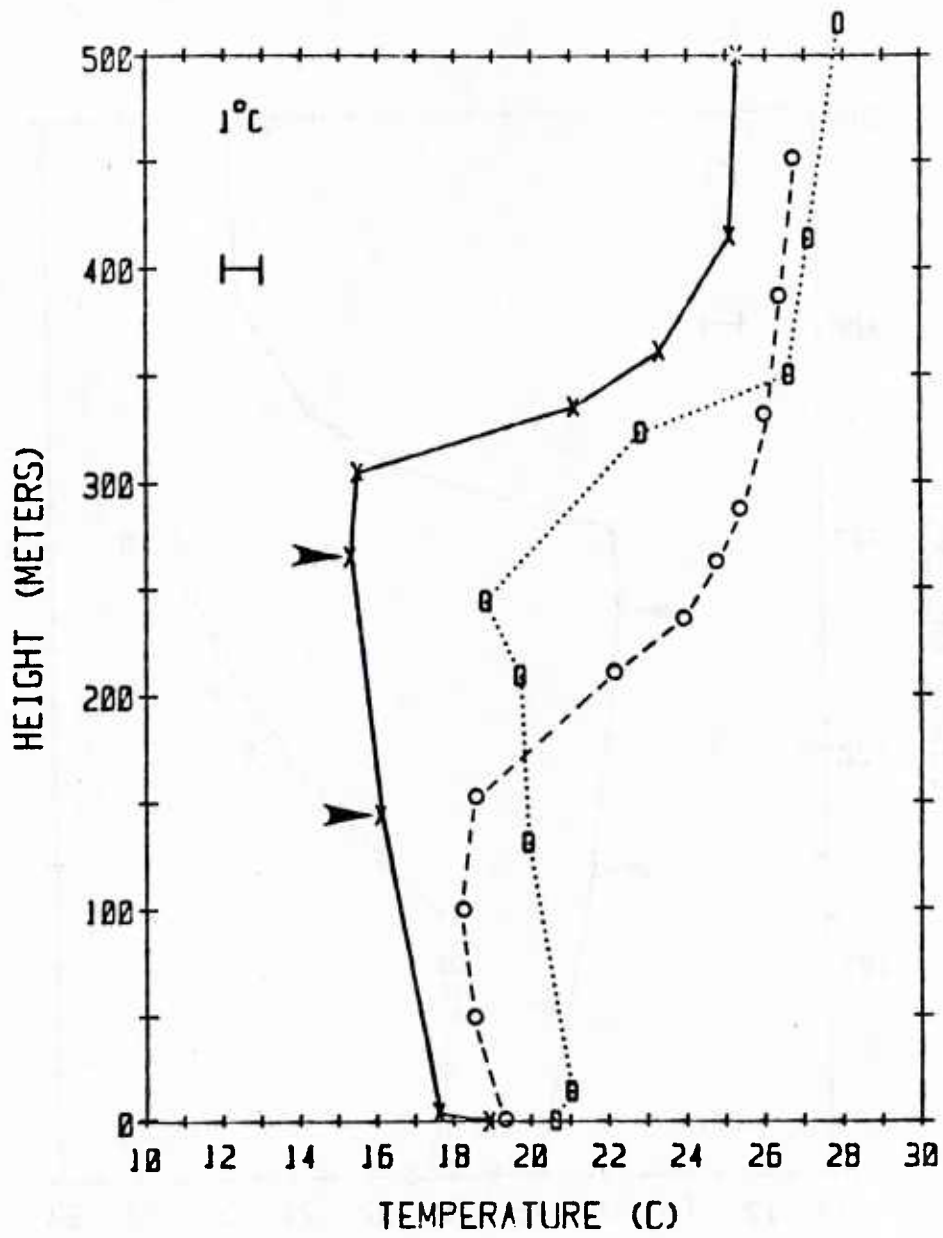


Figure 2.17 Case 3, T = 10 hours

x _____ INITIAL
 o VERIF
 o - - - - - MODEL

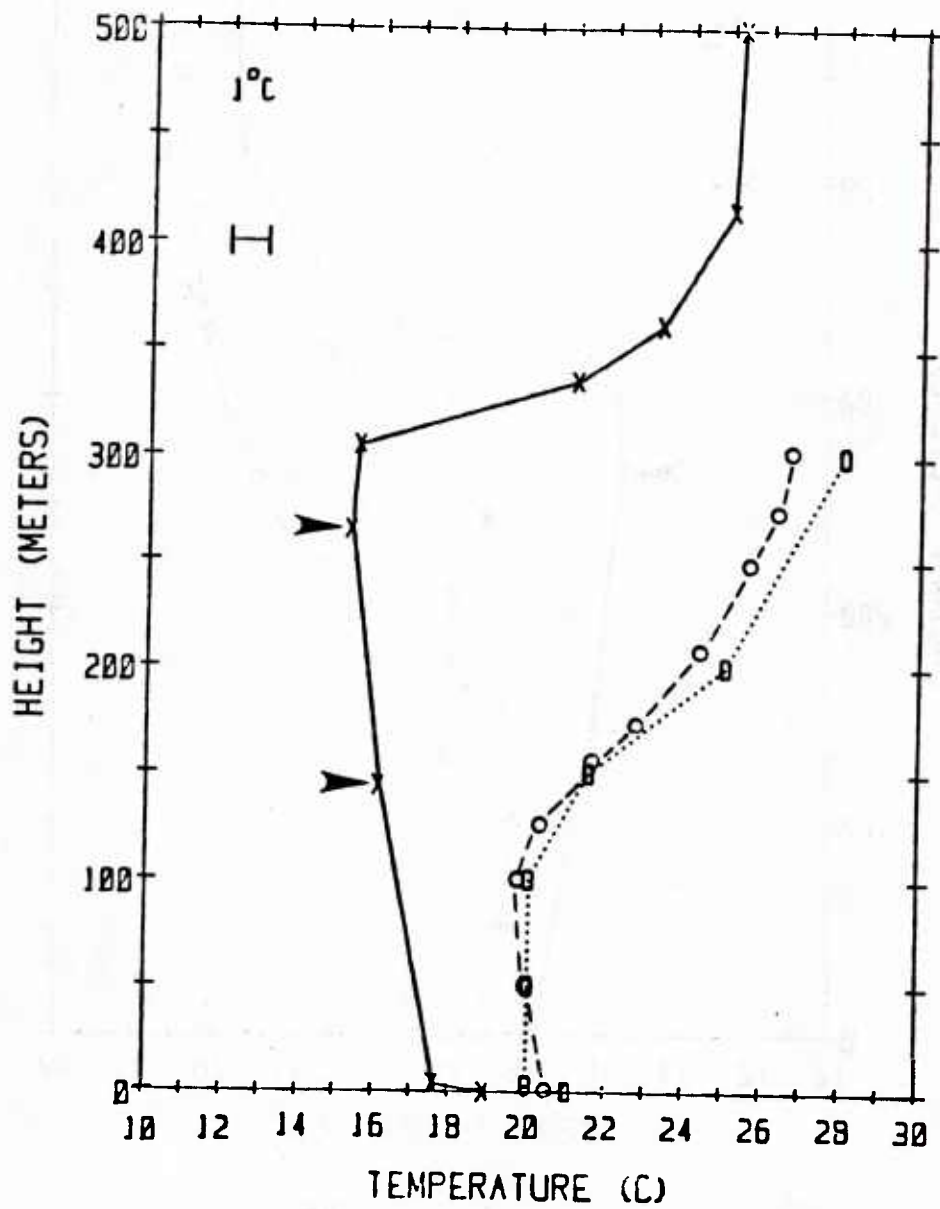


Figure 2.18 Case 3, T = 14 hours

x ——— INITIAL

o ······· VERIF

o - - - - - MODEL

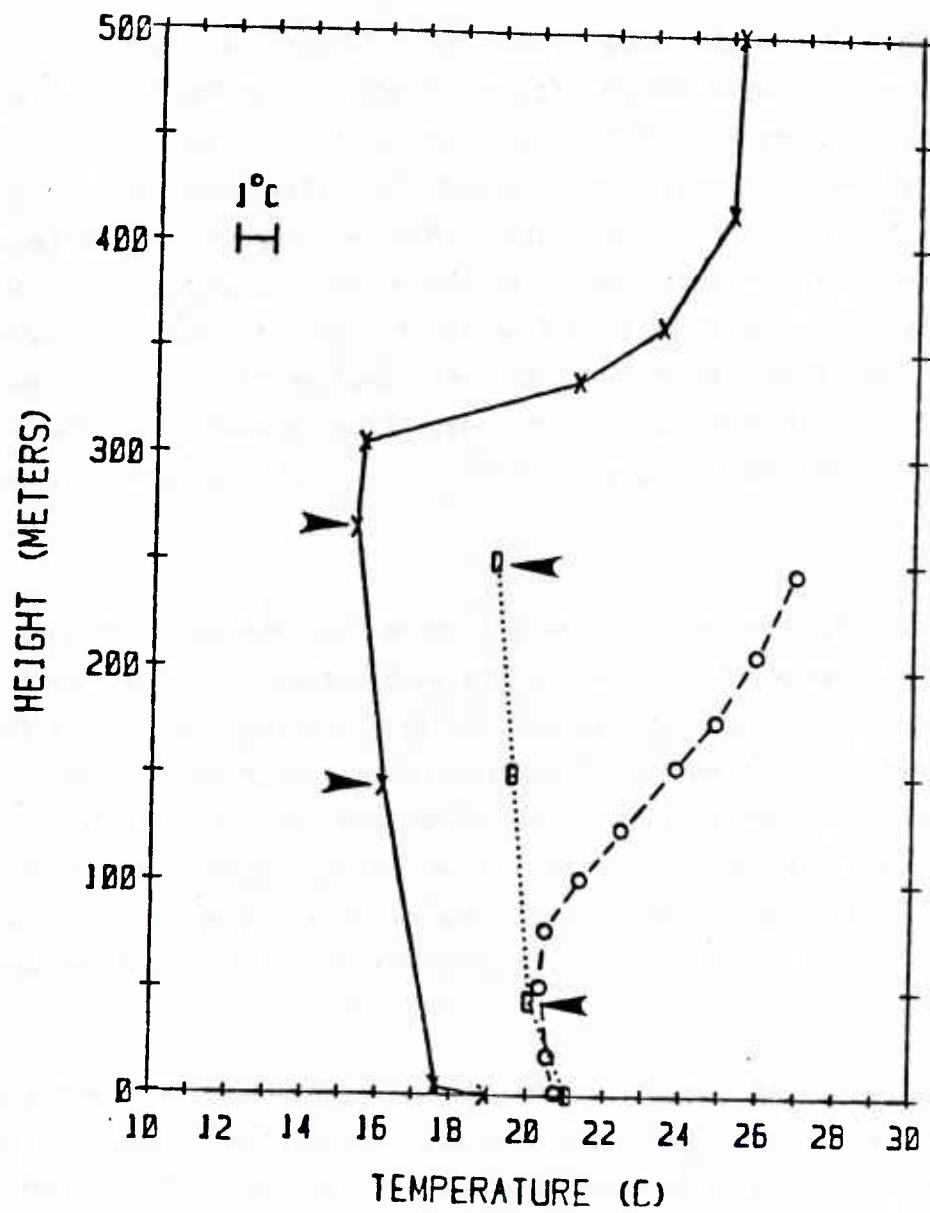


Figure 2.19 Case 3, T = 20 hours

- x ——— INITIAL
- o ······· VERIF
- o - - - - - MODEL

Case 4

This overnight case, 2000 PDT, 14 July to 0530 PDT, 15 July, 1973, simulates a cruise 80 km offshore Northwest of Pt. Conception. The coastal stratus thickens from 2100 m to ~ 350 m depth under an inversion at 500 m. Although our original integration for this case was quite close to the observations, it must be noted that we needed to apply a significant subsidence to prevent the mixed layer from growing. This was a result of spurious entrainment arising from the finite difference approximation for the radiative flux divergence as mentioned earlier. The new run has no subsidence, and does not give boundary layer growth. The new run, Figure 20, is even closer to the observations; in fact the agreement is almost exact.

Case 5

This is another shallow advection fog formed over cold water ~ 80 km offshore Southeast of Nova Scotia on 5 August 1975. A 3 hour time period is simulated starting 1 hour after sunrise. The fog shows a dramatic increase in depth when it flows over substantially warmer water. As in Case 2, our original run for this case was dominated by the reflection of long wave radiation at the ground. With the reflection removed, our predictions are now much closer to the observations. The predictions are still somewhat too warm, Figures 20-22, with the result that our relative humidities are too low, and no fog is formed.

We note that the fog in this case is formed during the first hour, before the surface temperature has changed. Inspection of the profiles at $t=1$ hour suggests that the water vapor has been brought down from aloft where it was initially higher than the surface by some 20%. The model fails to predict this transport. We initialize the run with super-equilibrium turbulence in a stable layer, which implies very little mixing away from the surface; however, the problem is not solved by specifying higher initial turbulence levels. The profiles at $t=1$ hour show the curious phenomenon of humidity being mixed down from aloft but not temperature. When the model turbulence levels are increased, both quantities are transported downward with very little change in relative humidity, and no fog formation. In view of the lack of fog in this run, it is not surprising that our predicted temperatures are

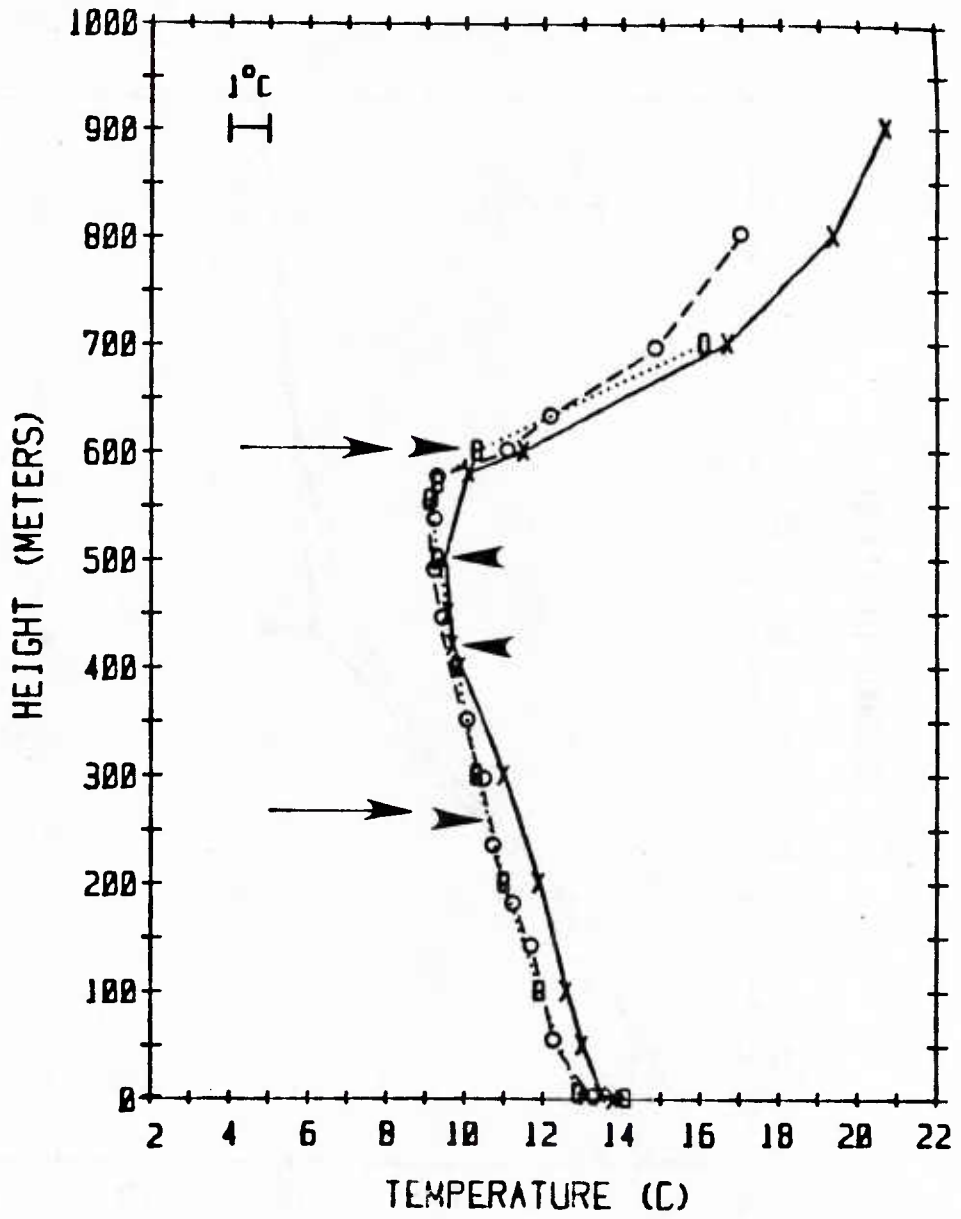


Figure 2.20 Case 4, T = 10 hours

x ——— INITIAL
 o ······· VERIF
 o - - - - - MODEL

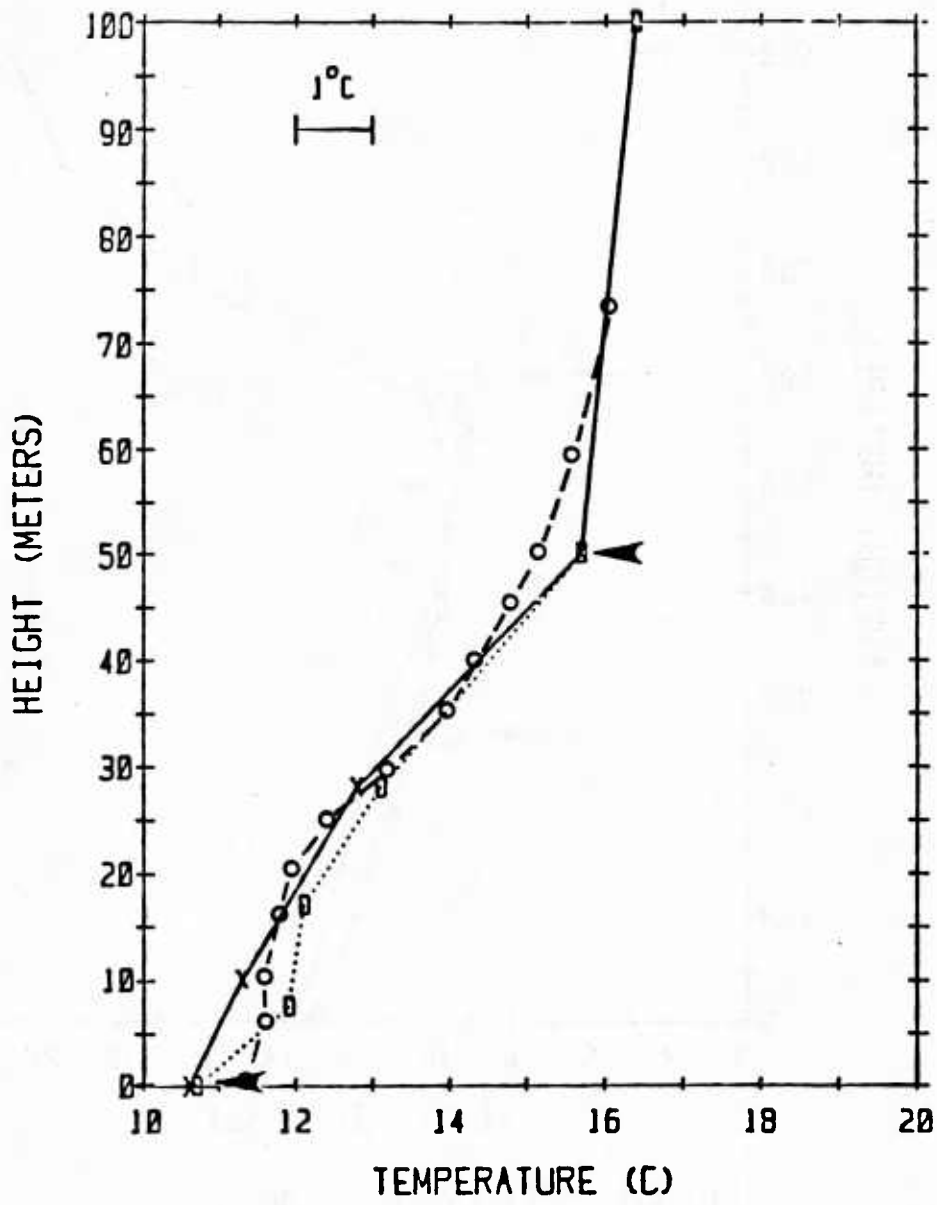


Figure 2.21 Case 5, T = 1 hour

x _____ INITIAL

θ VERIF

o - - - - - MODEL

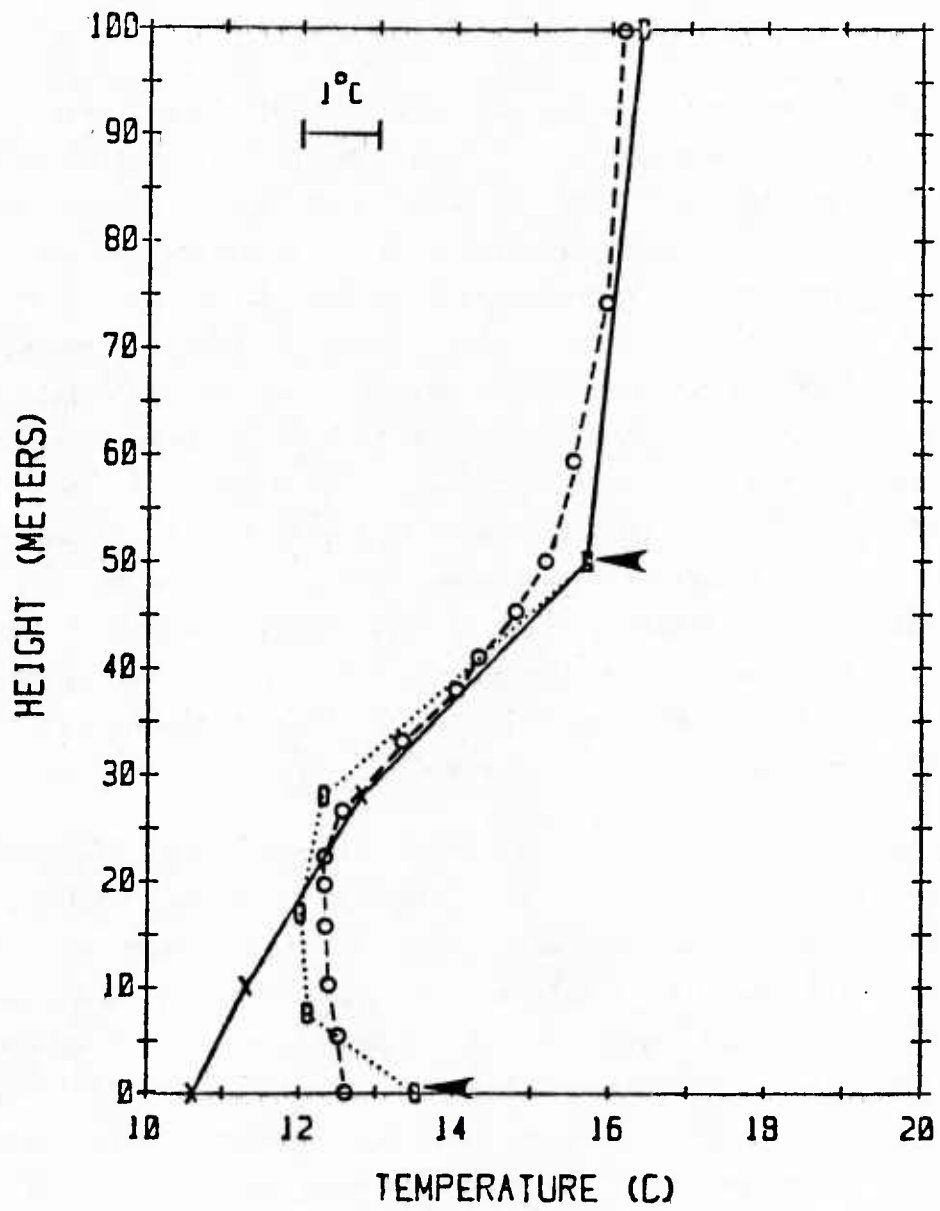


Figure 2.22 Case 5, T = 2 hours

x _____ INITIAL

o VERIF

o - - - - - MODEL

too high, since we do not have the fog-top long wave radiation cooling which must have been present in the observations.

Case 6

This case simulates 3 hours just before sunset during which stratus was observed to thicken and produce fog in a marine layer capped at a height of 200 m in the Farallon Islands on 29 August 1972. Although our earlier runs for this case were in good agreement with the observations, the new runs are significantly different. The main cause of the difference is the corrected value for the solar constant. The sunset is at $t=2.5$ hours, while the verification time is $t=3$ hours. It appears that our formulation for the shortwave scattering produces too much heating in this case, because the heating exceeds the long wave cooling in the early stages and quickly evaporates the cloud. A possible cause is the failure to account for the low solar angle, which reduces the shortwave absorption as the sun approaches the horizon, according to Stephens (Ref. 42, Figure 3). The effect depends on the state of the atmosphere above the cloud, and has not been examined in any detail, but the remedy would clearly involve making the absorption coefficients dependent on the solar angle.

The temperature profiles at $t=3$ hours, Figures 23 and 24, show that the prediction is too warm; this is as expected since the cloud has evaporated and the cooling mechanism has been lost. A run has been made without the shortwave radiation, and this shows the cloud descending but does not reach the ground in 3 hours. Examination of the details of the integration reveals some sensitivity to the initial development in this case. At $t=0$, we have a region of high humidity in the cloud, and lower humidity below. As the cloud top cools (without the sun), the entire boundary layer mixes, and reduces the humidity in the cloud. The timing of this mixing event is important, in that if it is delayed then there is more cooling of the layer prior to the cloud humidity reduction. In our model runs, the turbulence builds up and mixes the layer in 30 minutes or less, even if we begin with very low turbulence levels. At this stage, the cloud thickness is drastically reduced, and the cloud becomes optically thin since it has not cooled sufficiently to maintain its opacity. The cooling rate is therefore reduced, the development is set back considerably, and the cloud does not manage to reach the ground in 3 hours.

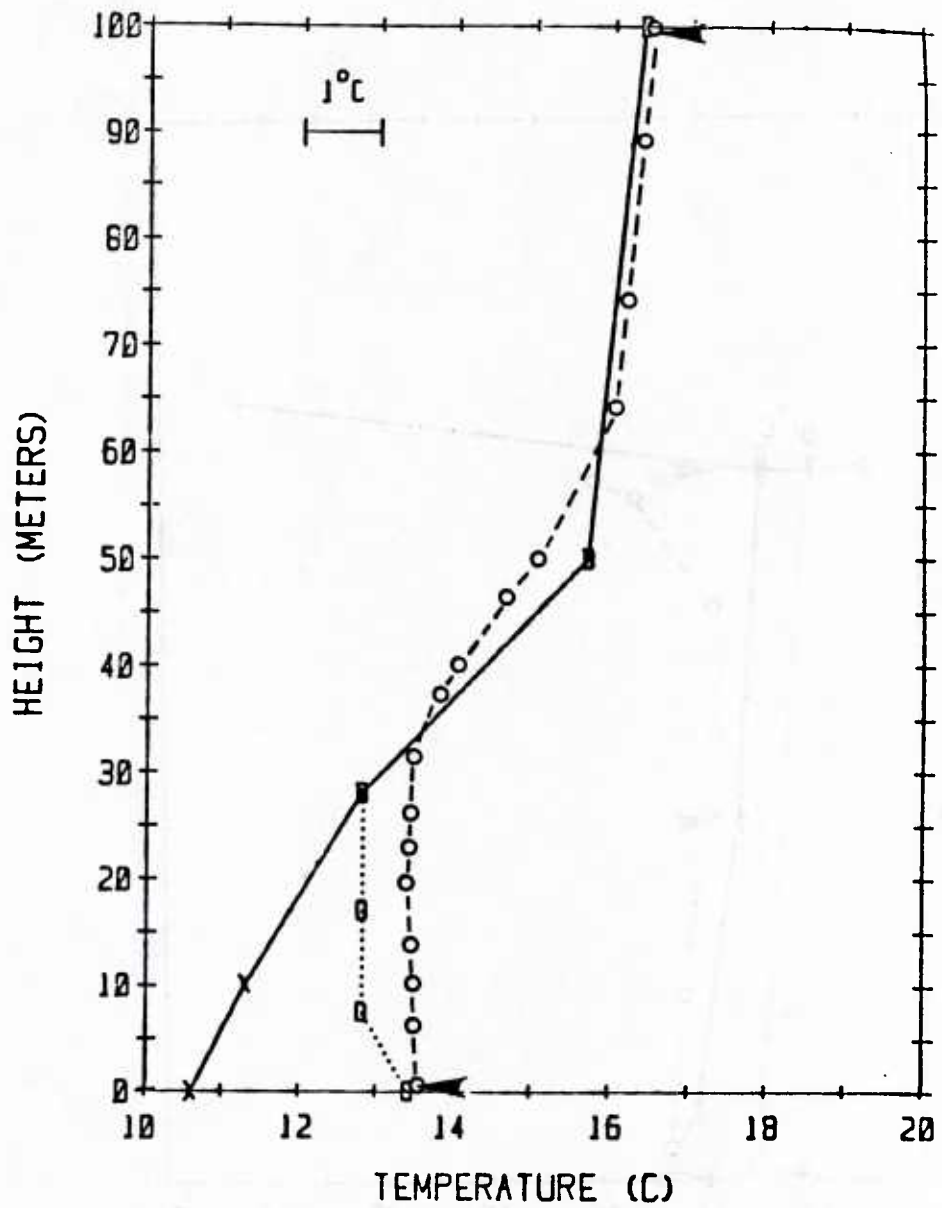


Figure 2.23 Case 5, T = 3 hours

- x _____ INITIAL
- o VERIF
- o - - - - - MODEL

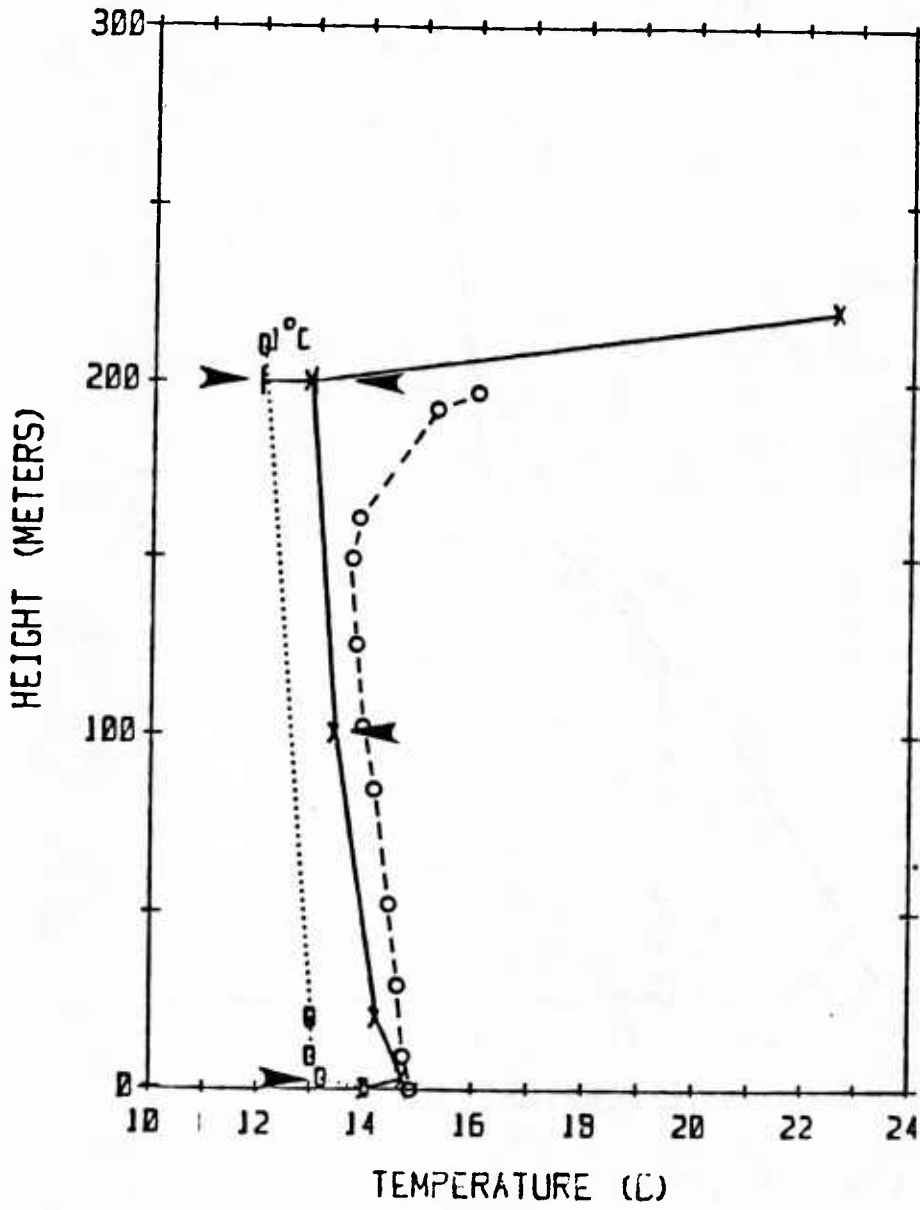


Figure 2.24 Case 6 Warm Water, T = 3 hours

x ——— INITIAL
 o ······· VERIF
 o - - - - - MODEL

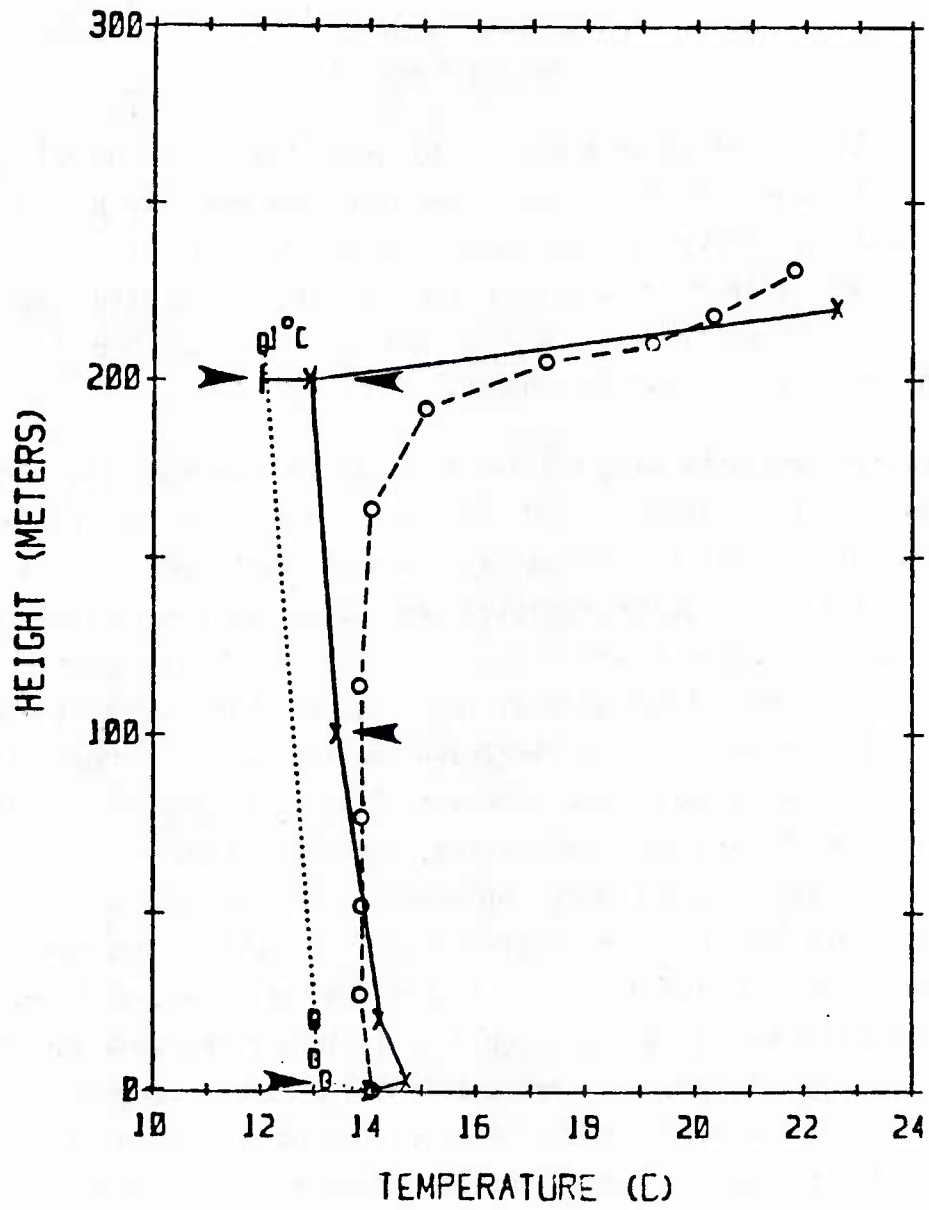


Figure 2.25 Case 6, Cold Water, T = 3 hours

x ——— INITIAL

θ ······· VERIF

o - - - - - MODEL

Thus, case 6 is not a simple status lowering event dependent only on cloud-top cooling rate, but is also strongly affected by the mixing of the initial profile.

Summary and Conclusions

The conclusions which we are able to draw from these model comparisons are limited because we only have temperature and humidity profiles at a few isolated stations. Discrepancies between model predictions and verification data may be due either to modeling deficiencies or to the neglect of all horizontal advective effects. We believe it is possible to make some conclusions about the radiation schemes.

In general, the long wave cooling seems to be reasonably well represented by our convolution integral and in most cases even by the approximate convolution. Case 4 is the most straightforward nocturnal cooling case, and this is the most accurately predicted case using the new finite-differencing scheme for the radiative fluxes. Cases 1, 3, and 6 all involve shortwave solar radiation for at least part of the time, so that interpretation is more difficult. It appeared that the shortwave heating was too strong in Case 6, where the solar angle was low. However, Case 1 is similar in this respect, and also produces large shortwave heating, but still remains colder than the observations. Case 3 shows good agreement with the temperature rise during the day, but this may be inconclusive since the cloud continues to absorb strongly until it evaporates; thus, if the absorption was smaller, the cloud would presumably remain longer but could still absorb the same amount of heat. The heating rates in clear air are unaffected by the scattering formulation, therefore it is possible that the predictions could be relatively insensitive to the details of the radiation scheme. Comparisons with data cases which include direct measurement of radiative fluxes are necessary if we are to determine the reliability of the radiation schemes.

We cannot really conclude much about the turbulence modeling on the basis of these runs. Although it appeared that Case 6 was inaccurately predicted partly due to rapid mixing of the initial profile, we do not know whether this was a model problem or whether neglected factors such as horizontal advection were important. This remark also applies to Case 5, where the transport of

humidity was not predicted during the first hour, yet the transport of humidity and temperature are so dissimilar in this case that the presence of horizontal advection seems very likely.

Regarding the modifications made to the model, we can say something about their relative importance. The inclusion of the full atmospheric temperature profiles did not make a profound difference to the results. Our original estimates of the long wave flux from aloft were within $20\text{-}30\text{ Wm}^{-2}$ in most of the cases, so that this change resulted in a 1°C temperature change at most.

The removal of long wave reflection at the surface had a large effect on the stable cases, 2 and 5. Although we still do not predict fog formation, the spurious heating is absent, and the temperatures are much closer to the observations.

The change in the finite-difference scheme only affected Case 4, where the entrainment was reduced to almost zero. It is strange that none of the other cases were affected by this numerical problem, but we have no explanation for their insensitivity.

Finally, the full convolution integral only affected Case 6 significantly, where it contributed to the reduced cooling. This is apparently because the approximation for the convolution gives a reasonable representation of an optically thick cloud, which most cases are, but gives excessive cooling for thin clouds.

3. ON THE ONE-DIMENSIONAL PARAMETERIZATION OF WAVE-TURBULENT INTERACTIONS

Introduction

One of the principal mechanisms controlling the development of the planetary boundary layer under well-mixed conditions is the rate of entrainment of heat and momentum from the free atmosphere above the turbulent mixing region. This is due to the fact that the boundary layer eddies do produce a well-mixed region, and therefore it is possible to describe many of the gross features such as boundary-layer depth, mean temperature, and mean velocity by use of a 'slab' model which only requires knowledge of fluxes at the top and bottom of the slab. The 'slab' model does not predict details of the turbulence variations across the layer, of course; but the gross dynamics of the actual physical system, and therefore any sophisticated mathematical model of it, are also controlled by these surface and entrainment fluxes.

There are several mechanisms which are responsible for fluxes at the top of the boundary layer. The relative importance of the various mechanisms will be determined both by the details of the profiles in the atmosphere above the boundary layer, and by the boundary-layer turbulence itself which is the driving force for the entrainment. The atmosphere above the boundary layer is generally stably-stratified and thus inhibits vertical mixing, since the turbulence has to expend its kinetic energy in order to provide the increase in potential energy required to transport the overlying warm air down into the mixed region.

Since the air from just above the boundary layer is rapidly cooled to the average mixed-layer temperature, there is usually a significant temperature change across a relatively short distance at the top of the layer; this is the so-called "capping inversion". The first type of entrainment mechanism is due to rapidly-rising thermals which, under convective conditions, have sufficient vertical momentum upon reaching the inversion to continue rising for some distance. The thermal then spreads out in the horizontal and falls back into the boundary layer, entraining some of the free atmosphere as it does so. This mechanism is largely controlled by the vertical velocities in the thermals, which in turn depend strongly on the surface heat flux. A simple parameterization, e.g., Carson²⁰, Stull²¹, sets the entrained heat flux

proportional to the surface heat flux under conditions of strong convection.

A second entrainment mechanism which will be more important under more neutral conditions, i.e., higher wind speeds or smaller surface heat fluxes, is stratified shear instability of the inversion itself. Since the inversion is continually perturbed by turbulent eddies from below and possibly by wave disturbances from above, we have a situation where the inversion can break down locally into relatively small scale turbulent patches which entrain the free atmospheric air.

We are interested here in this latter mechanism, which seems more difficult to parameterize, in view of the fact that it can be affected by both local conditions at the inversion and the perturbations produced by the turbulence in the boundary layer. In attempting to gain some insight into the physical processes, we have first studied idealized stratified shear instabilities and their development through turbulent mixing to a final mixed state. The response of the idealized inversion layers to imposed disturbances has provided a basis for understanding the more general atmospheric problem. In the next section, we present a summary of the numerical experiments performed with the two-dimensional, second-order closure model on simple stratified shear profiles. Finally, in Sections 3.3 and 3.4, we indicate the application of these studies in the development of a simpler model of the entrainment process as it occurs at the capping inversion of the atmospheric boundary layer.

Summary of Numerical Results

In a previous report (Lewellen, et al.²) the application of the two-dimensional, A.R.A.P. second-order closure model to the problem of Kelvin-Helmholtz billow growth and breakdown into turbulence was described in detail. It was demonstrated that the closure model has considerable merit as a means of investigating the detailed dynamics of the turbulent breakdown process. The results have been extended to investigate the sensitivity of the mixing process and final state to changes in the initial profiles and in the imposed initial disturbance. We may say here that it appears there is one very simple result - namely, that the final state after turbulent mixing is the same for a wide range of initial conditions. This mixed layer has a nearly constant

Richardson number roughly between 0.35 and 0.40. We now proceed to discuss these numerical results in more detail.

Previous Results

The results of Lewellen, et al.² indicated that the final Richardson number in the mixed layer varied from about 0.3 to 0.4 as the initial Richardson number varied from 0.1 to 0.2. Sensitivity tests showed that the most sensitive initial parameter was the turbulence length scale, which needed to be set at some large fraction of the initial shear layer thickness. The initial profile for these studies was taken to be

$$u = \Delta u \tanh z/\delta, \quad T = \Delta T \tanh z/\delta \quad (3.1)$$

where u is the horizontal velocity, and T is the temperature perturbation (which is proportional to density perturbation in the Boussinesq equations which are used in the model). The numerical results proved relatively insensitive to variations in initial vorticity perturbation amplitude or initial turbulence energy level.

The main gross dynamical quantities presented were the total large-scale roll energy

$$EK = \frac{1}{\Delta u^2 \delta^2} \int (u^2 + w^2) dx dz. \quad (3.2)$$

and the small scale turbulence energy

$$EQ = \frac{1}{\Delta u^2 \delta^2} \int q^2 dx dz \quad (3.3)$$

where

$$q^2 = \overline{u'^2} + \overline{v'^2} + \overline{w'^2} . \quad (3.4)$$

The development of these dimensionless energies for the cases with $Ri = 0.1$ and 0.2 are shown in Figure 3.1. Here $Ri = (g/T_0)\Delta T\delta/\Delta u^2$, where g is the gravitational acceleration, and T_0 is the mean temperature of the layer, i.e. Ri is the minimum Richardson number in the initial profile. The dimensionless time τ is defined as $\tau = t (g\Delta T/T_0\Delta u)$. Figure 3.1 shows the initial growth of the large-scale roll instability and its subsequent breakdown and generation of small scale turbulence energy. At the end of the integration, the large-scale perturbation has completely decayed so that we have a horizontally homogeneous flow again, and the turbulence is also decaying.

The initial and final Richardson numbers for those two runs are shown in Figure 3.2. This figure shows the mixing effect of the instability. In both cases, the Richardson number of the mixed layer is almost constant, although the actual value is somewhat higher for the higher initial Ri . For $Ri = 0.2$, the final value is close to 0.4.

Variations in Initial Profile Shape

In a real billow turbulence event, the initial profiles will not be precisely identical hyperbolic tangents, and we therefore need some information about the dependence of the phenomenon on the initial profile shapes. One special feature of the previously used profiles was that the temperature and velocity both had the same vertical length scale. Hazel²² performed linear, inviscid stability analyses of a wide range of profile shapes, and his results seem to show that the most profound changes in stability characteristics are caused by making the temperature profile change across a thinner layer than the velocity, i.e., $u = \Delta u \tanh z/\delta$

$$T = \Delta T \tanh \frac{Rz}{\delta} \quad (3.5)$$

with $R > 1$. As R increases, the initial Richardson number profile changes

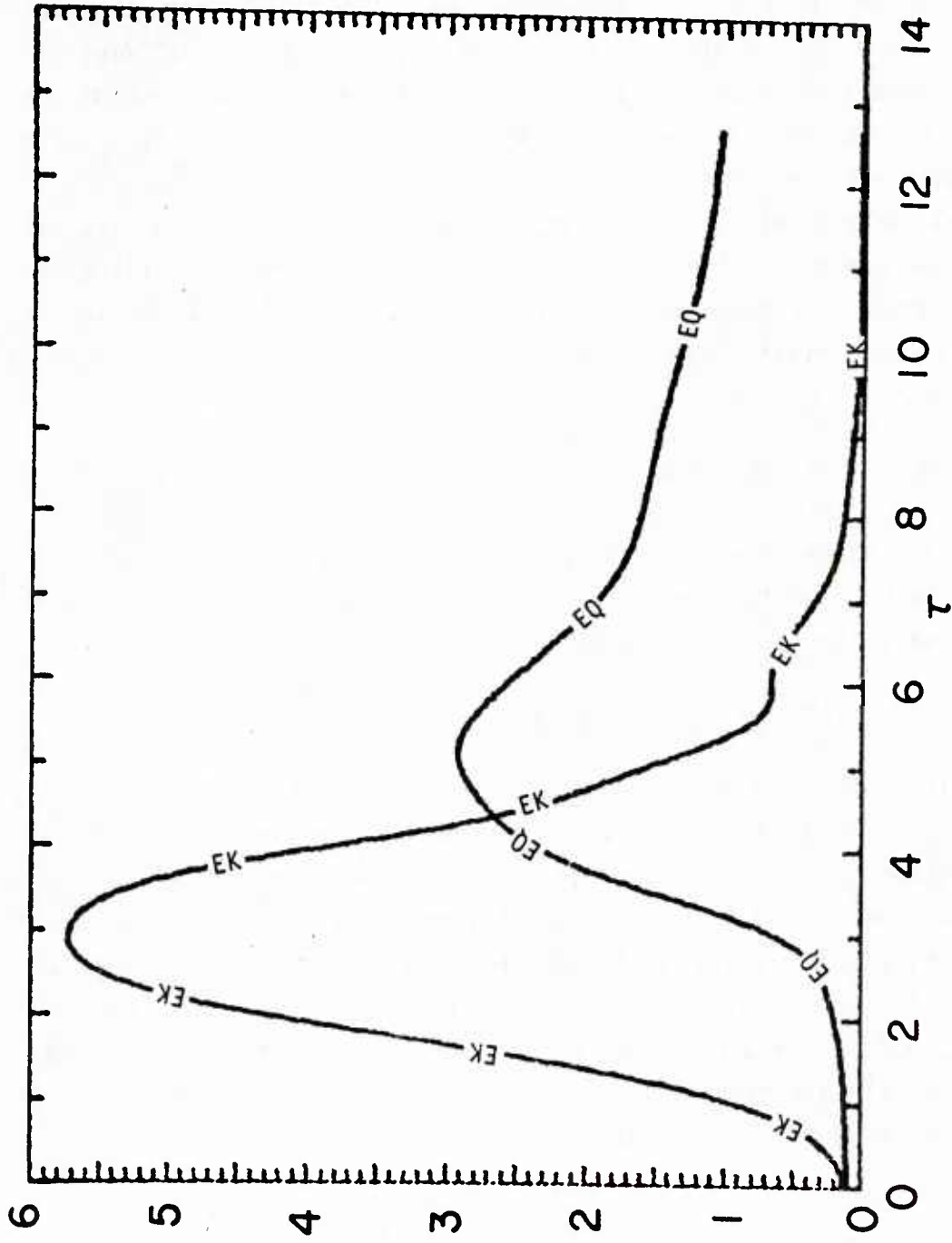


Figure 3.1: Evolution of large scale (EK) and small scale (EQ) eddy kinetic energies.
 (a) $Ri = 0.1$

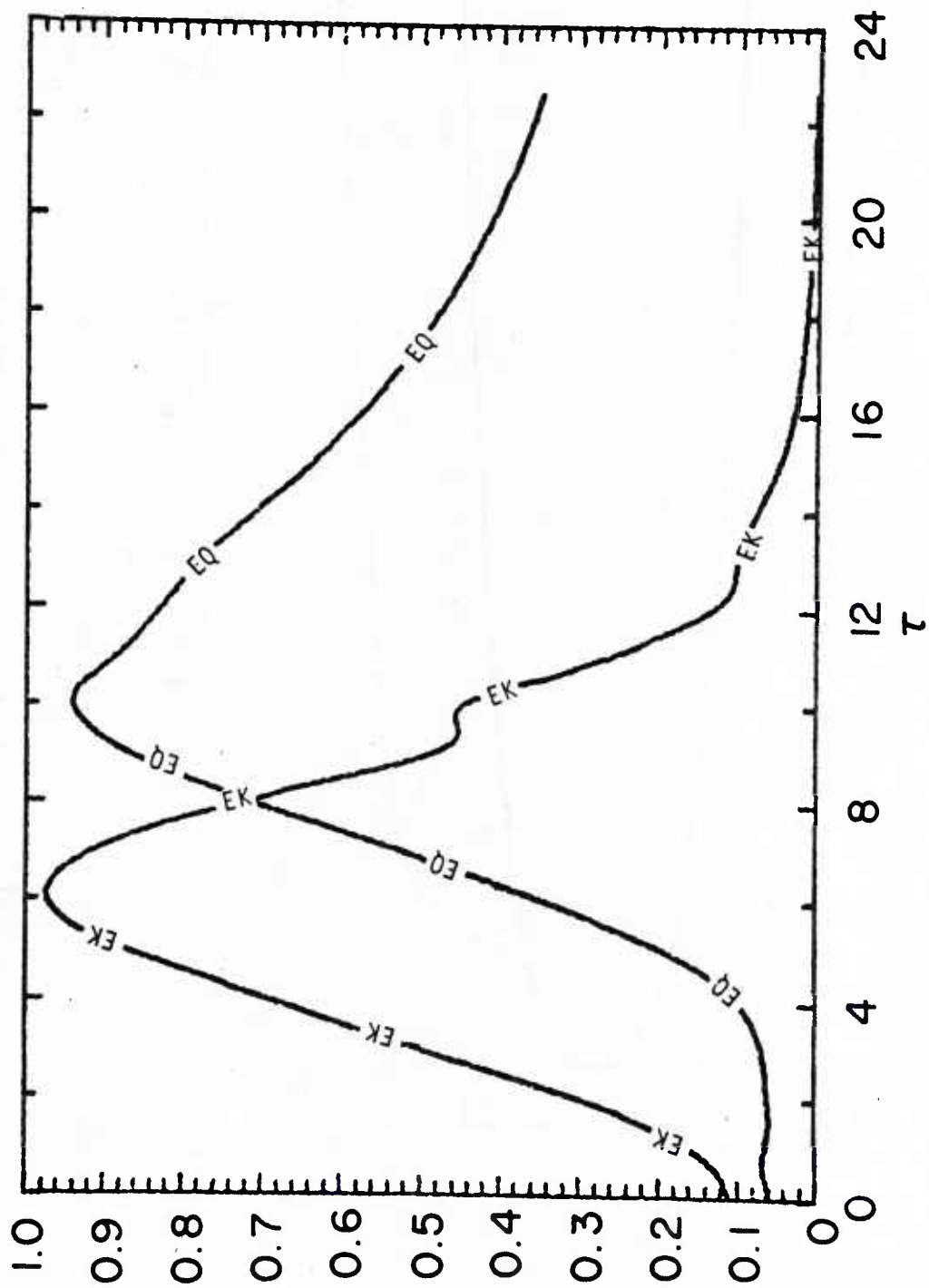


Figure 3.1(b): $Ri = 0.2$

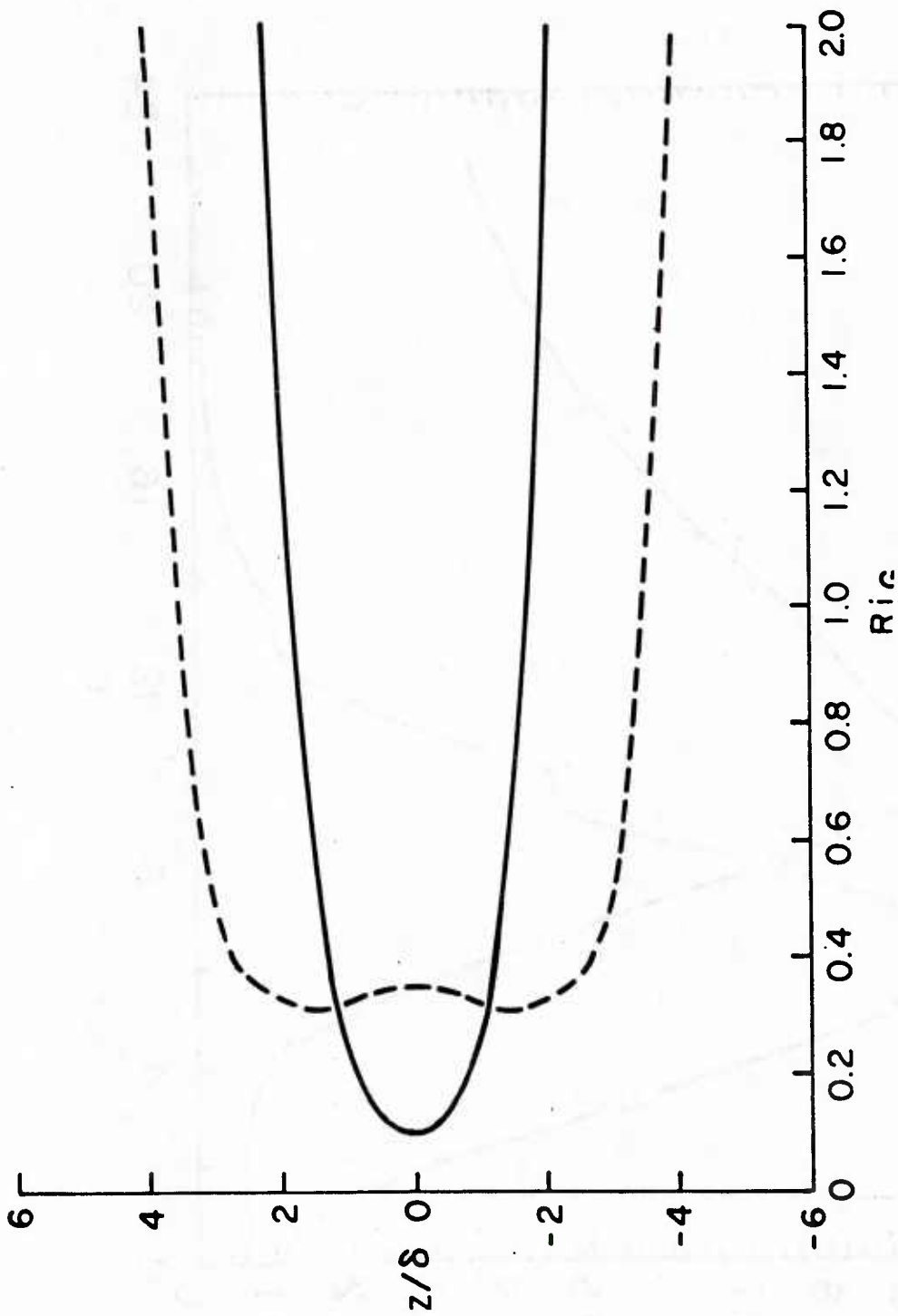


Figure 3.2: Initial and final Richardson number profiles.
 The initial profile is denoted by a solid line.
 (a) $Ri = 0.1$

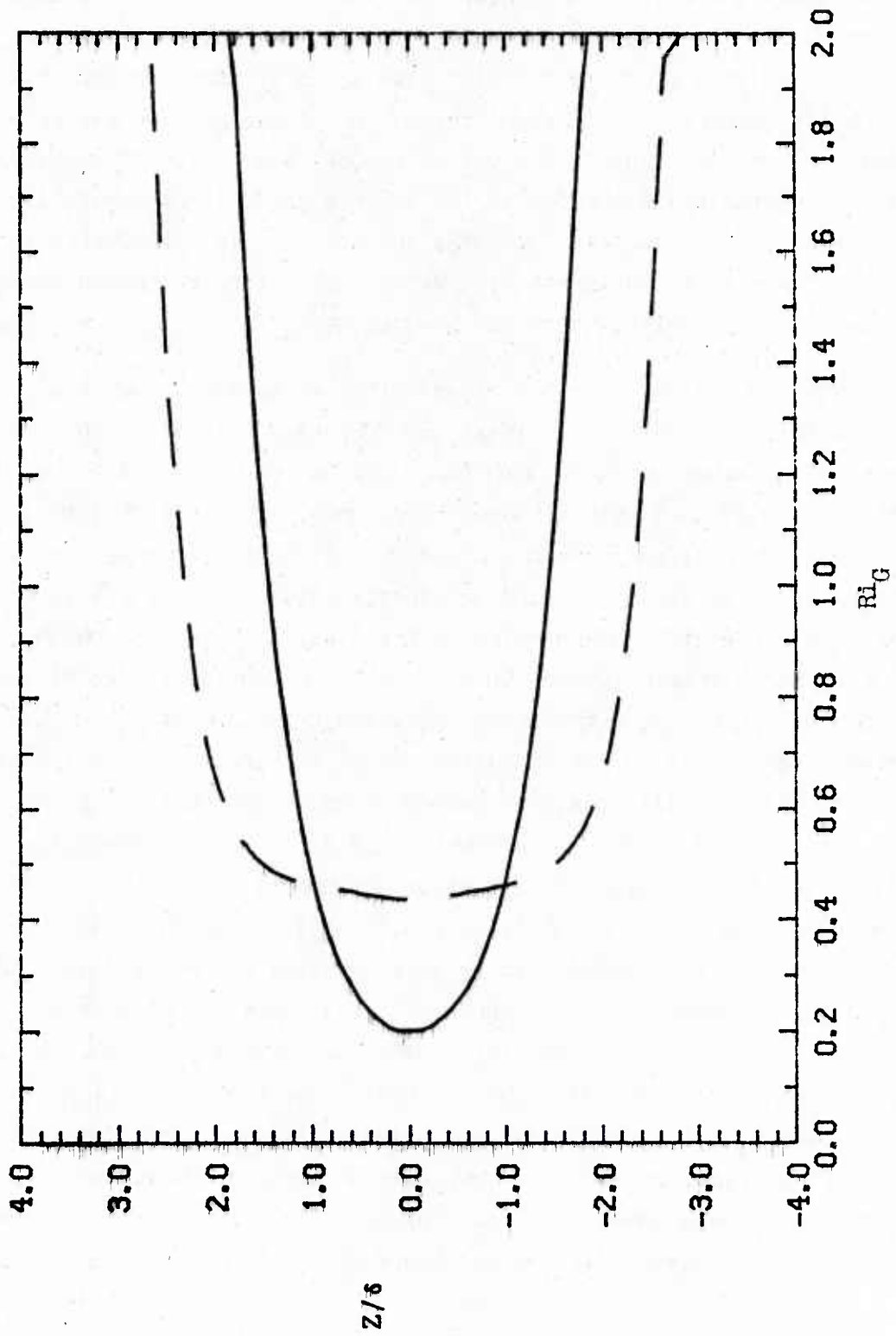


Figure 3.2(b): $Ri = 0.2$

from a single minimum at $z = 0$ to a local maximum at $z = 0$ when $R > \sqrt{2}$ with minima above and below the centerline. When $R > 2$, $z = 0$ becomes a global maximum and the Richardson number tends monotonically to zero as $z \rightarrow \infty$. Detailed analyses of the particular case $R = 5$ by Hazel shows that when $Ri \cdot R$ (J in his notation) is larger than 0.25, there are two unstable stationary modes, and when $Ri > 0.37$, the unstable modes are no longer stationary. Hazel also found that small changes in the profile shape (from hyperbolic tangent to error function) or small asymmetries about $z = 0$ did not materially alter the linear stability characteristics. We have therefore concentrated on variation in the thickness ratio, R , in our studies here.

Figure 3.3 shows the initial and final Richardson number profiles for a case with $R = 1.7$. The initial profile has a local maximum at $z = 0$ as mentioned previously, with secondary minima at $z = \pm 1.4$. The maximum at $z = 0$ is 0.22 and the minimum is roughly 0.15. At a time $\tau = 24$, the turbulence has largely decayed, and the Richardson number profile shows a minimum value of about 0.37 and an average value of about 0.4 across the mixed layer. The evolution of the kinetic energies is shown in Figure 3.4. There is a primary breaking event at $\tau \approx 3$ which generates most of the turbulent energy, but this is followed by a secondary break at $\tau \approx 6$ which gives a further increase in EQ. Examination of the temperature contour patterns shows that the primary billow is the symmetric mode centered on $z = 0$, as can be seen in Figure 3.5 at $\tau = 2.8$ and $\tau = 4.3$. This is presumably because the inflection point at $z = 0$ is the major source of instability, and since the Richardson number at $z = 0$ is only 0.22 initially, the fastest growing mode is centered there. However, after this initial system roll-up and turbulent breaking, a secondary mode appears. This mode is evident at $\tau = 5.8$ and $\tau = 7.3$, and seems to be associated with the secondary minima in the initial Richardson number profile. The secondary mode also rolls up the remaining vortex sheet above and below the primary billow, and generates its own small scale turbulence. Thus the billow event is more complicated than the previously studied cases, but the final result of the mixing process is to produce a layer with a Richardson number of about 0.4.

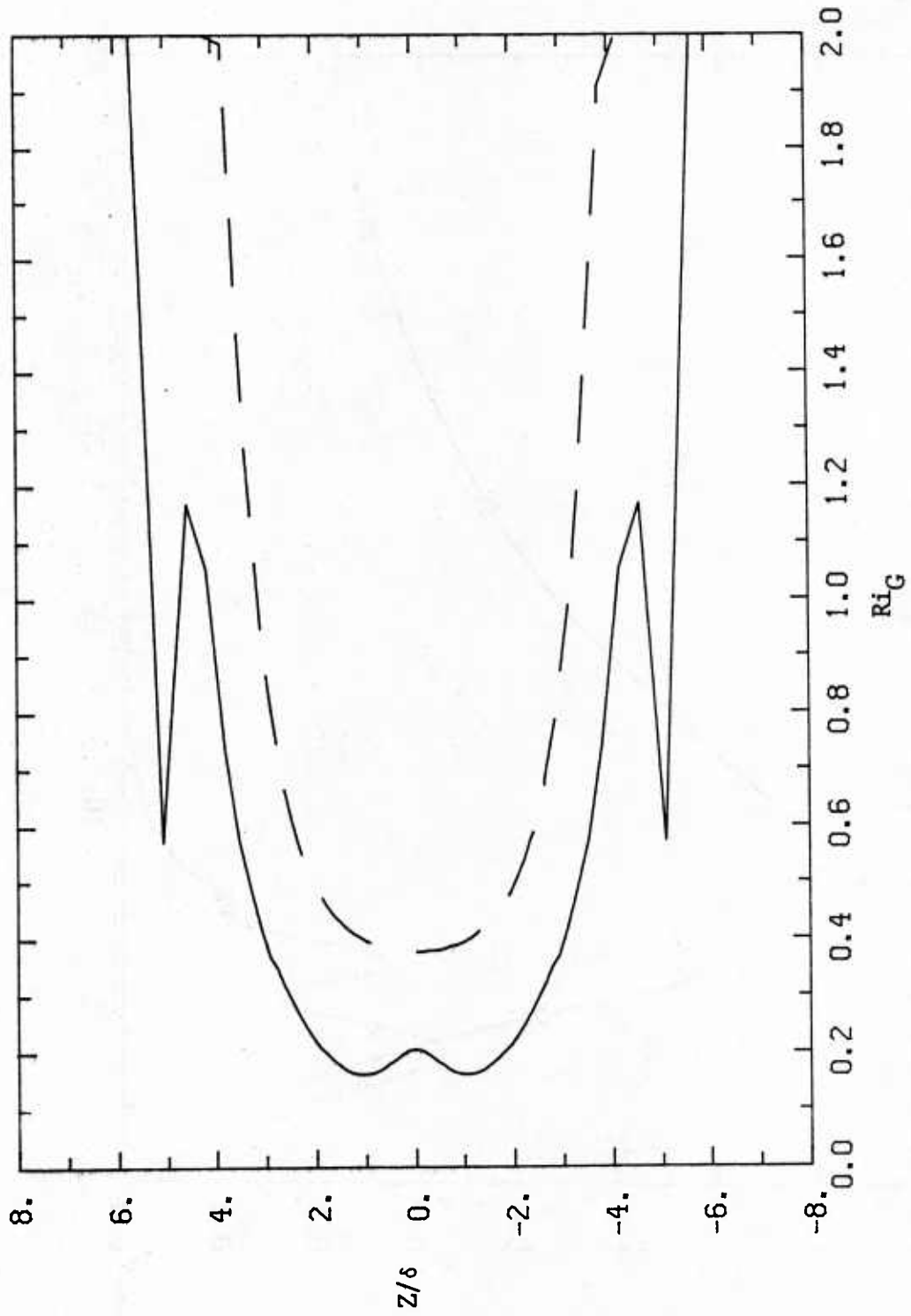


Figure 3.3: Initial and final Richardson number profiles for $R = 1.7$.

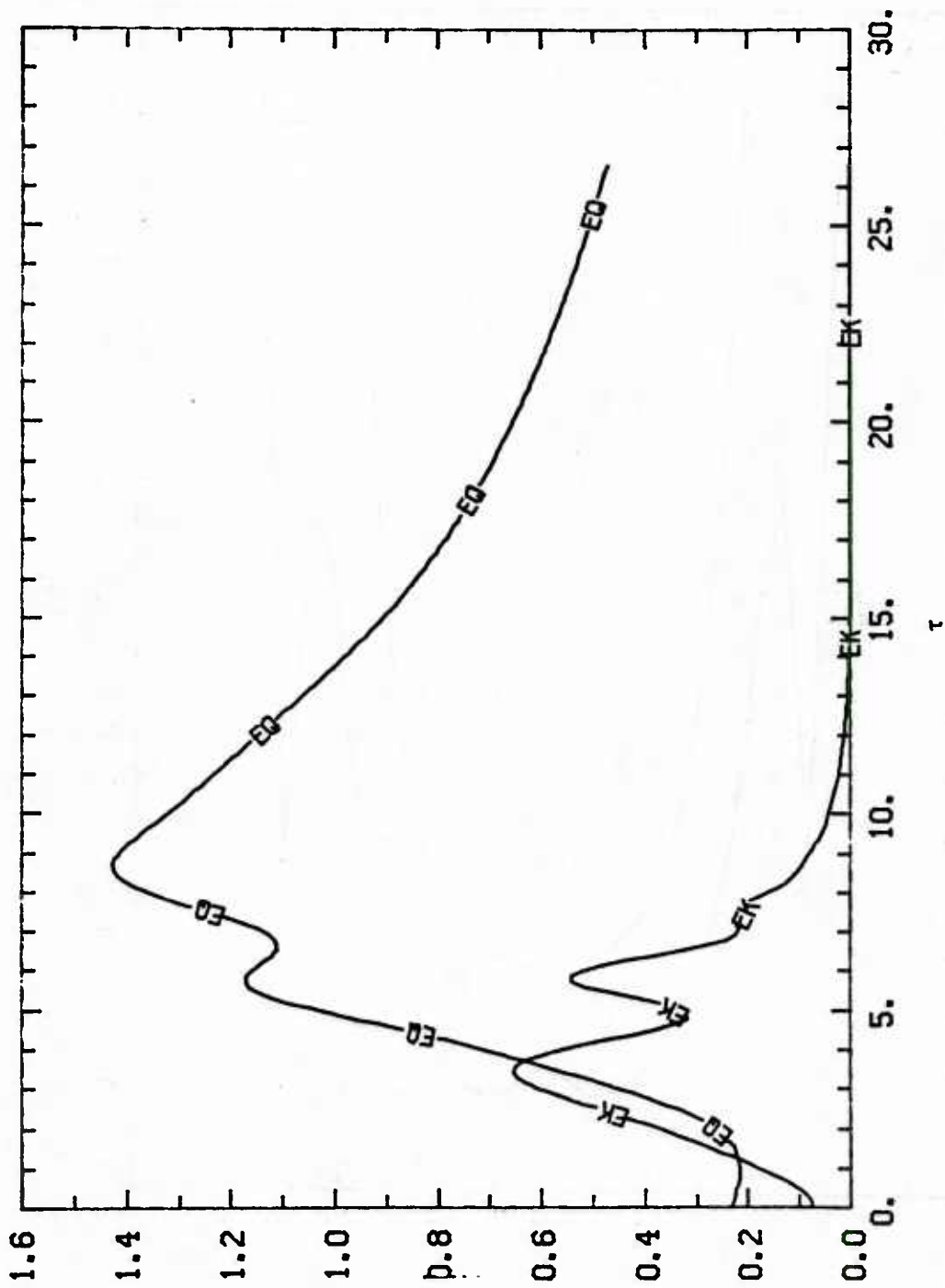


Figure 3.4: Evolution of kinetic energies for the case with $R = 1.7$.

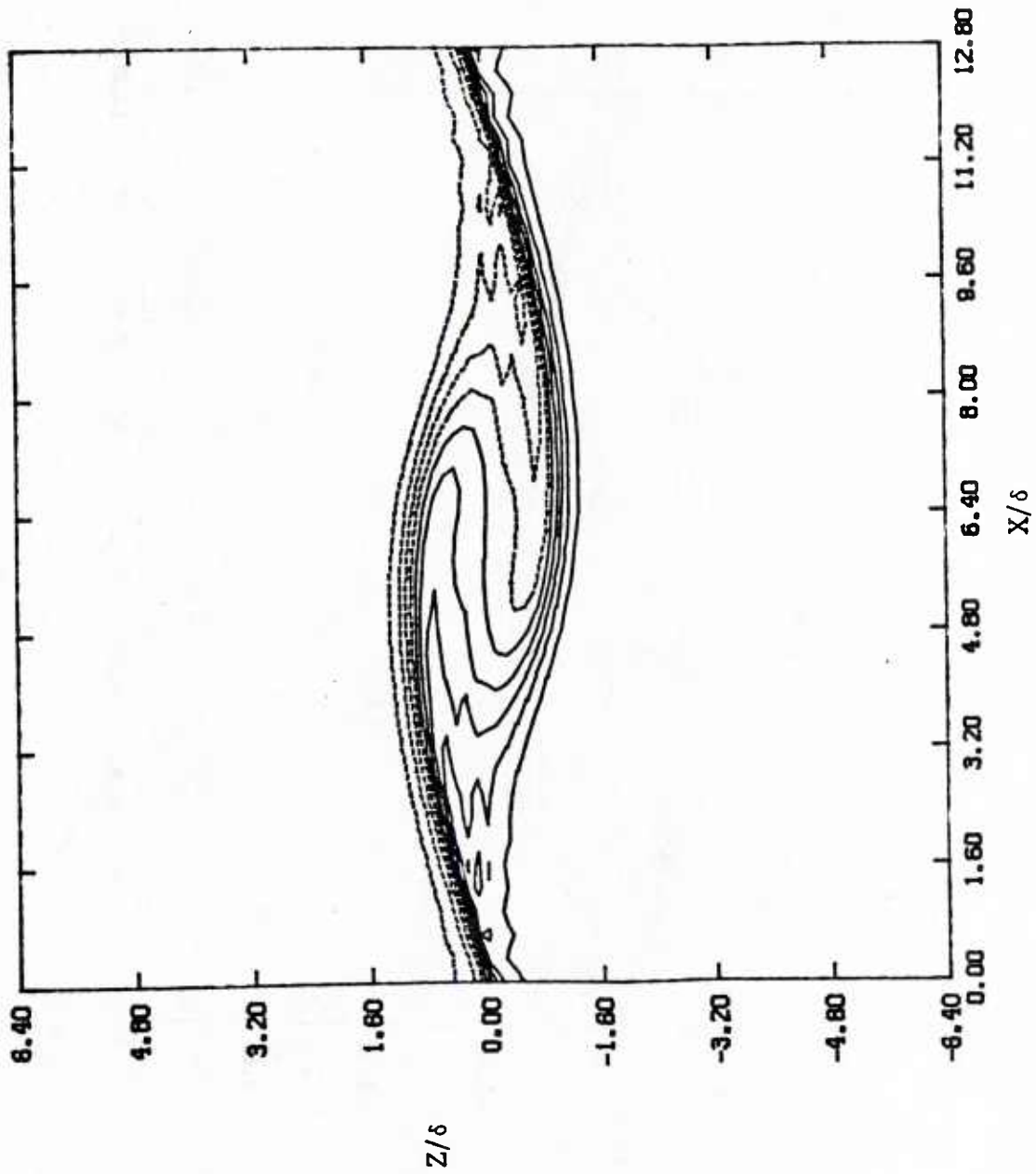


Figure 3.5: Isopleths of dimensionless temperature, $(T-T_0)/\Delta T$, for the case with $R = 1.7$ at (a) $\tau = 2.8$

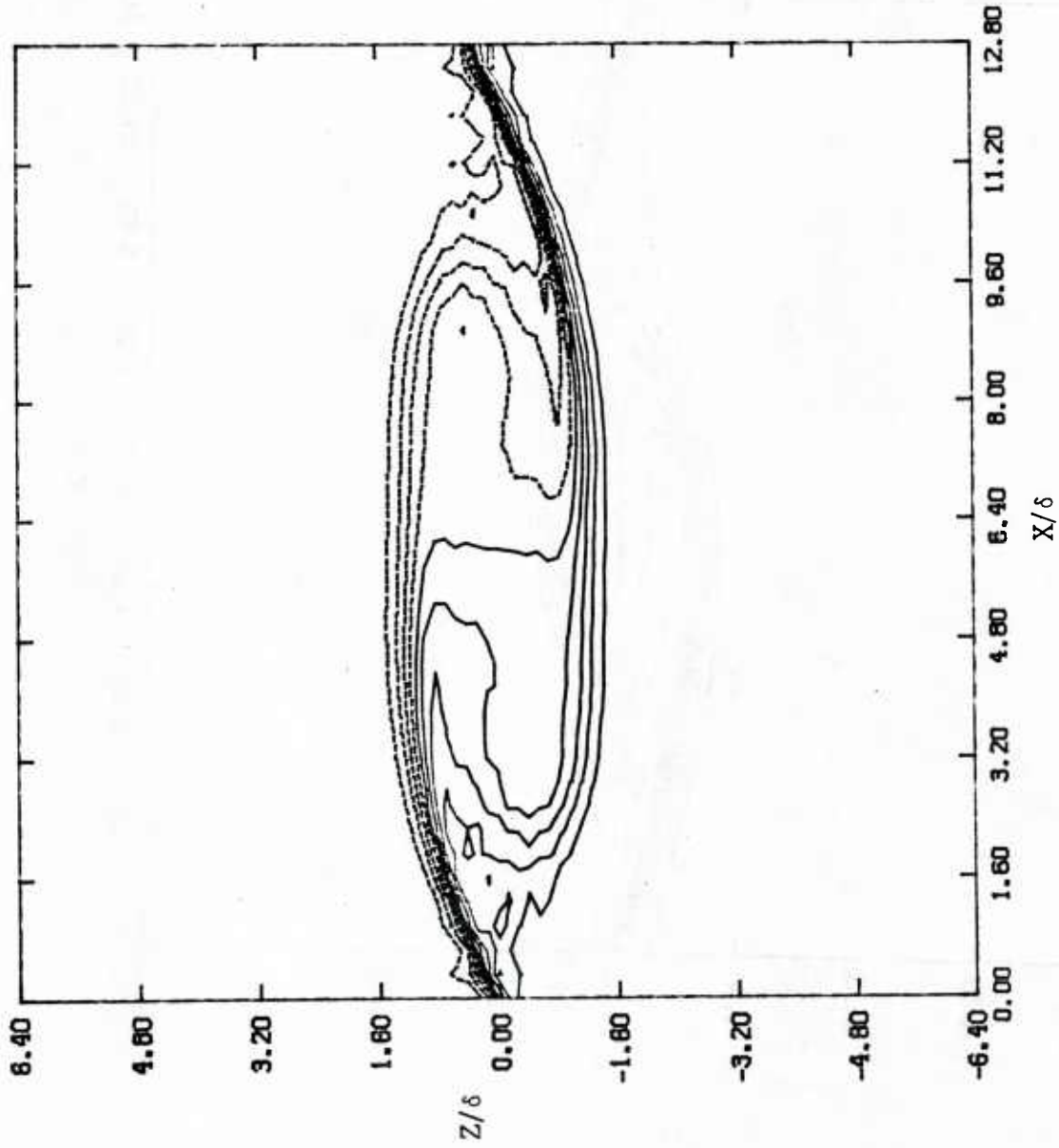


Figure 3.5(b): $\tau = 4.3$

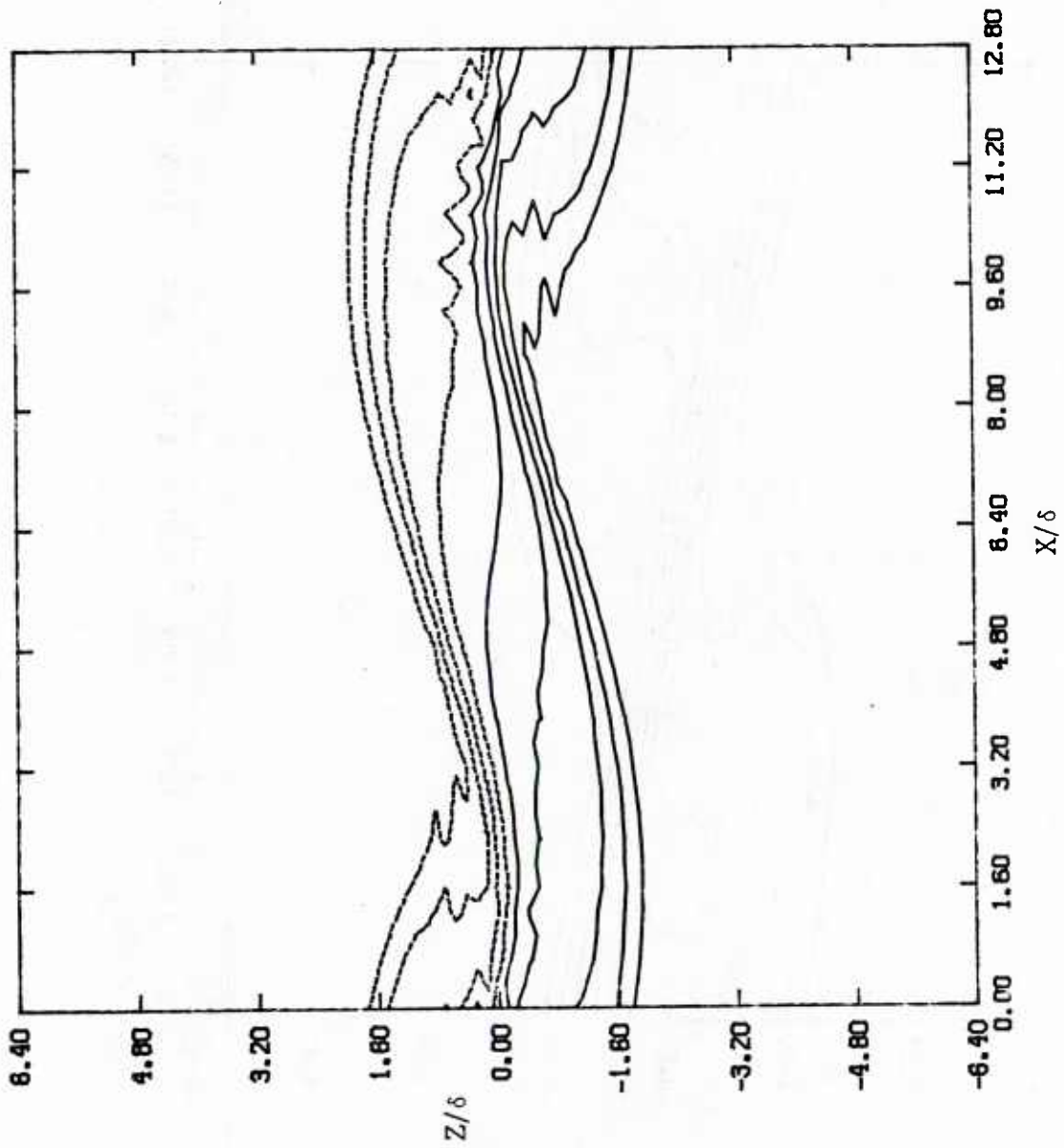


Figure 3.5(c): $\tau = 5.8$

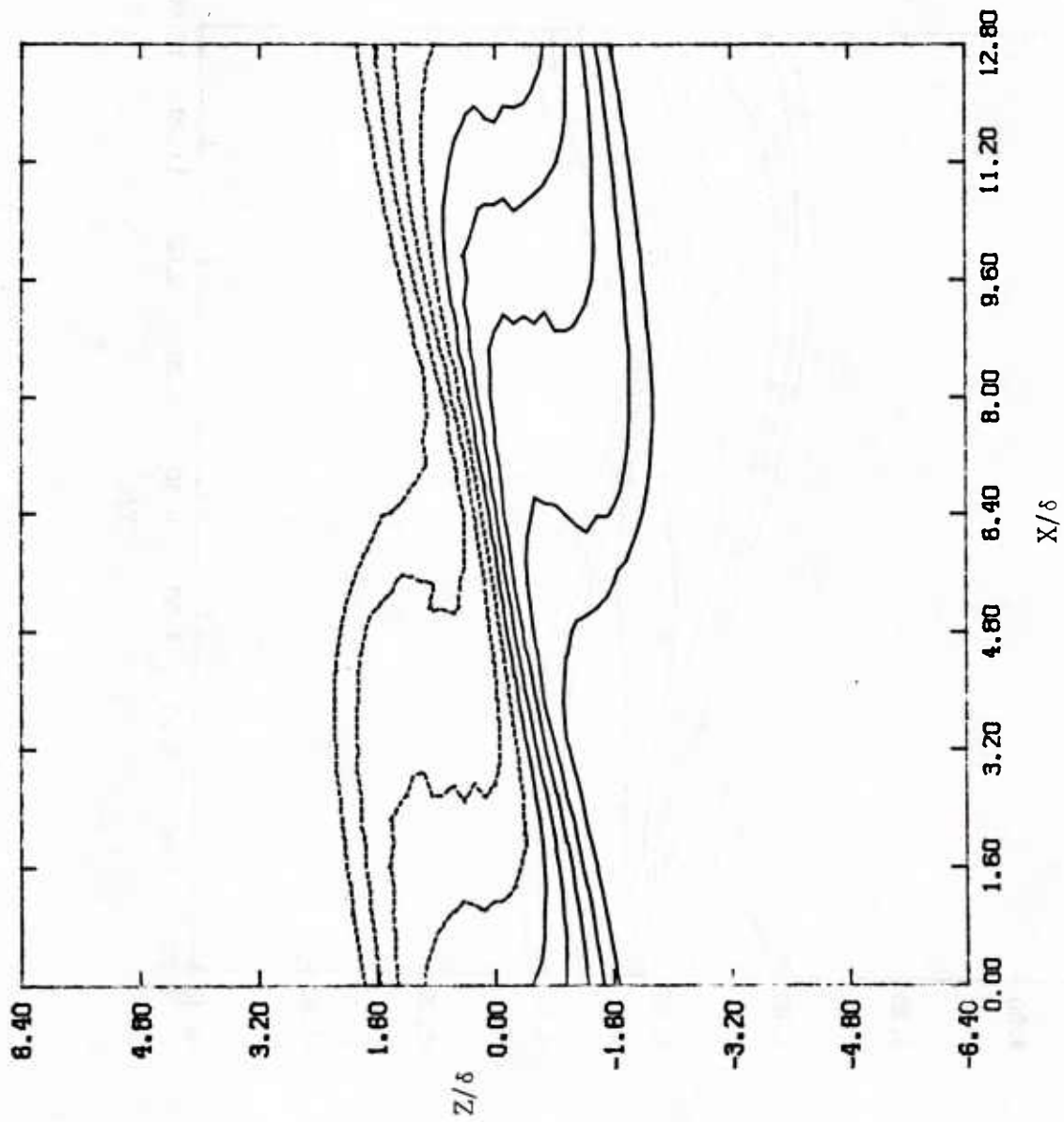


Figure 3.5(d): $\tau = 7.3$

When $R = 2.5$, the Richardson number profile has a maximum at $z = 0$ as can be seen in the initial profile in Figure 3.6. Also shown in this figure are the late time profiles from two numerical integrations using the given initial profile. In the first run, a short domain of length 12δ was used with an initial perturbation of vorticity amplitude. In the second, a domain of length 24δ and an initial perturbation of the isotherms was applied. The evolution of the energies from the runs is shown in Figure 3.7. It is obvious that very different modes are excited in the two integrations. Temperature contours at two times from each run are shown in Figures 3.8 and 3.9. In the short domain, only a very weak symmetric disturbance is excited, but there is enough turbulent growth in the low Richardson number regions to produce the required mixing and stabilize the profile. In the long domain, the initial wave does not immediately decay in amplitude, but feeds energy into a large-scale mode which does produce a large disturbance and convective instabilities in the rolled-up vortex cores. Turbulence levels are much higher, although the time scales are also much longer. However, the final result is, in both cases, a mixed-layer with a Richardson number of roughly 0.4. We do not wish to dwell on the details of these integrations, since neither are ideal examples; for example, the long domain case is probably significantly affected by the upper and lower boundary conditions. However, these factors do not seem to affect the overall mixing effect of the instability.

Larger Initial Richardson Numbers

Finally, and briefly, we show the results from initial Richardson numbers closer to the critical value of 0.25. This has relevance to the problem of a slowly decreasing Richardson number, as might be produced in the atmosphere by some large-scale flow feature. In this case, the shear layers would presumably begin to roll up before the Richardson number had time to fall much below 0.25.

Using the simple hyperbolic tangent profiles, and $Ri = 0.23$, an integration was made with a domain of length 11δ . The energy evolution is shown in Figure 3.10, and the Richardson number at $\tau = 8$ is shown in Figure 3.11. Although the mixing is not completed, it is clear that there has been the usual breaking event, and the final Richardson number will be close

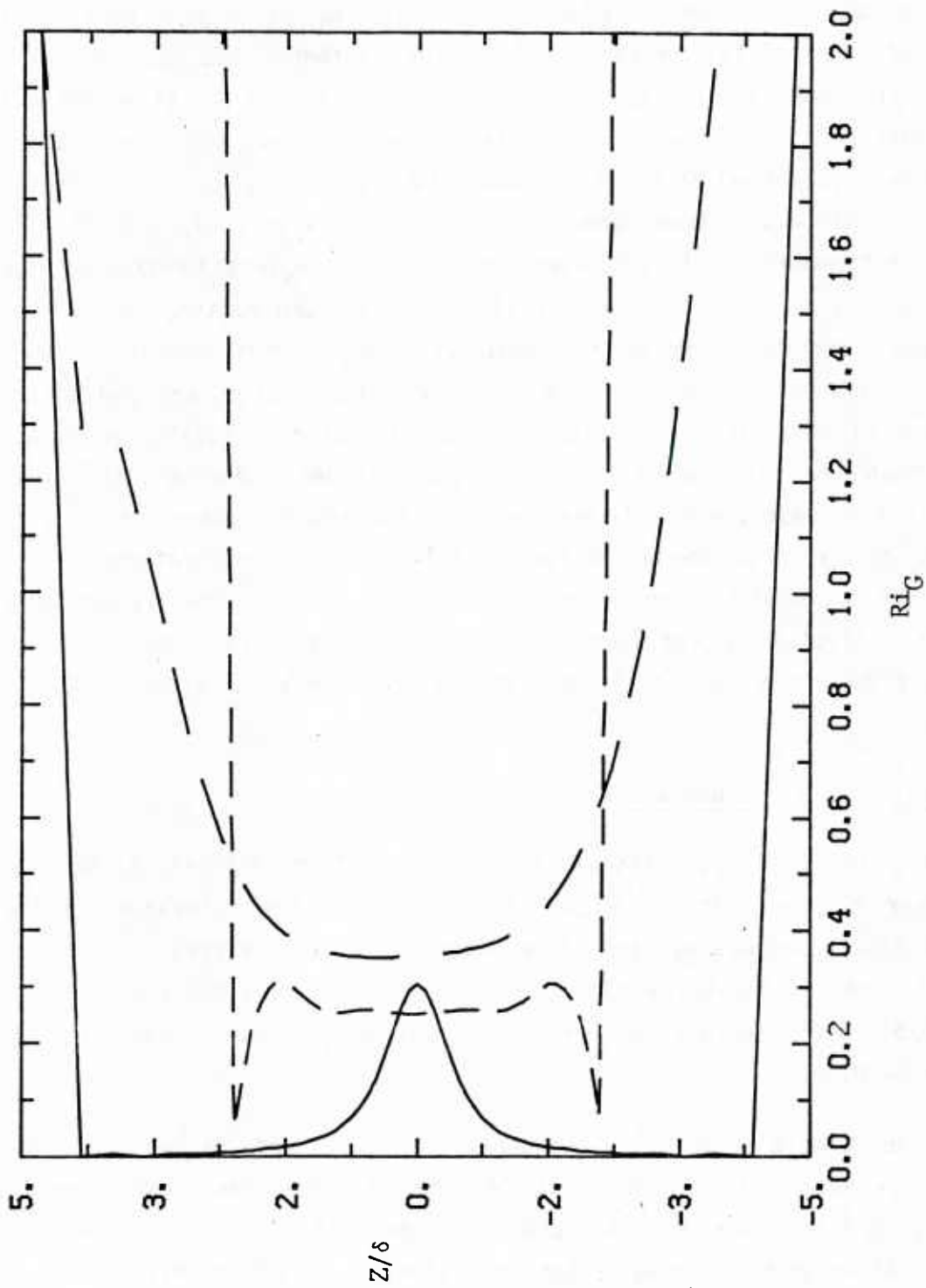


Figure 3.6: Initial and final Richardson number profiles for the case with $R = 2.5$.

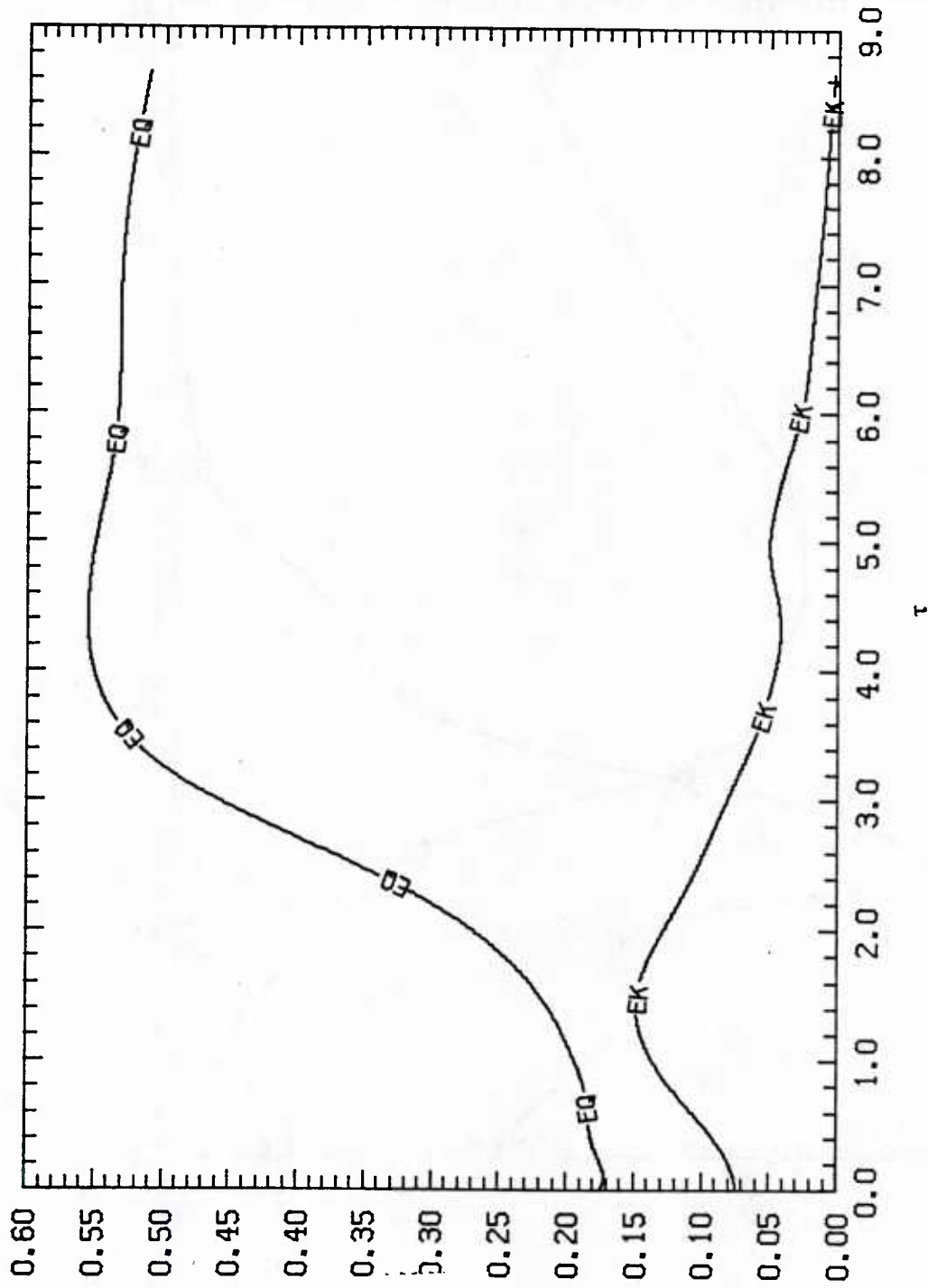


Figure 3.7: Evolution of kinetic energies for the case with $R = 2.5$.
 (a) Short domain

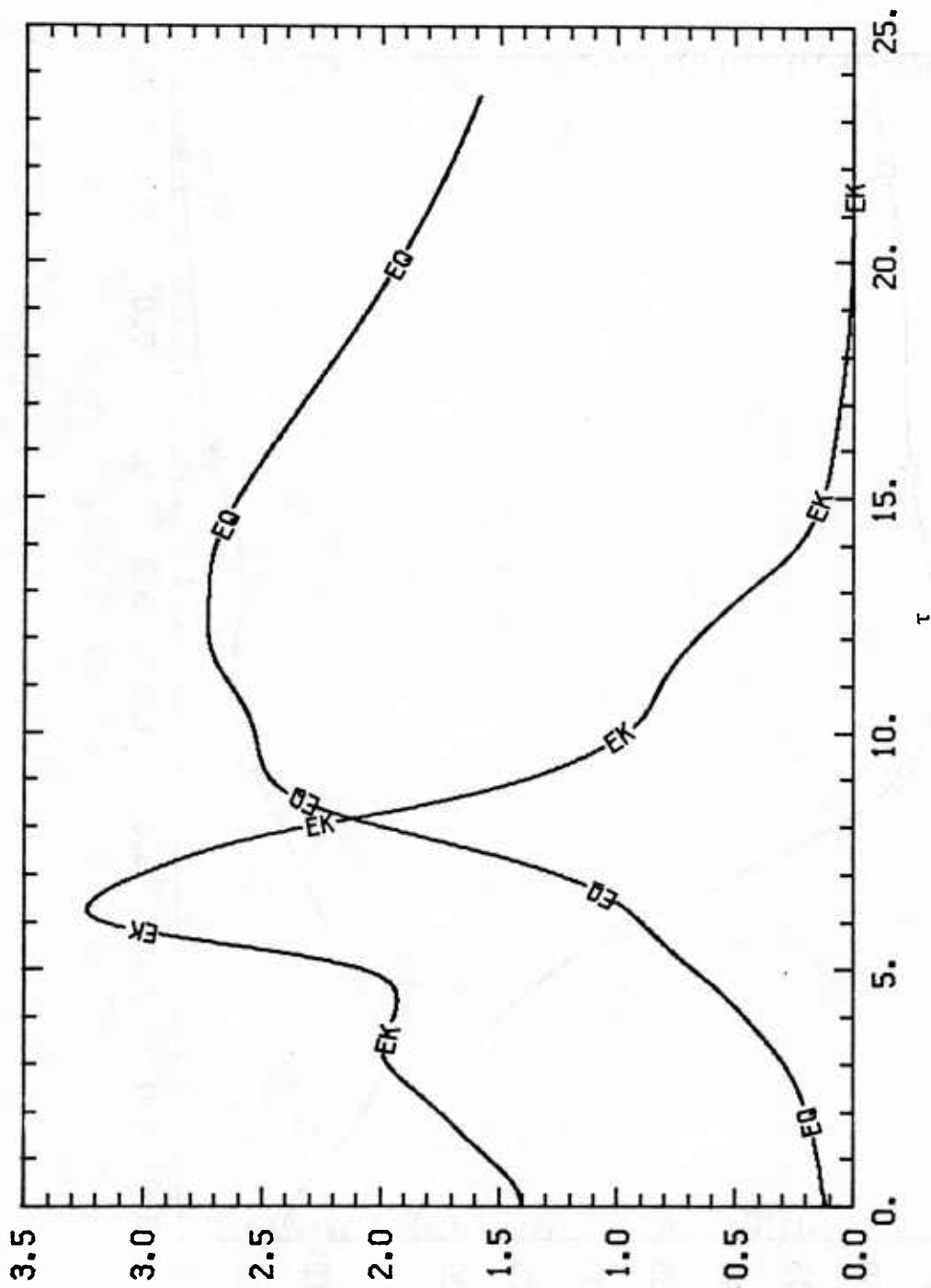


Figure 3.7(b): Long domain

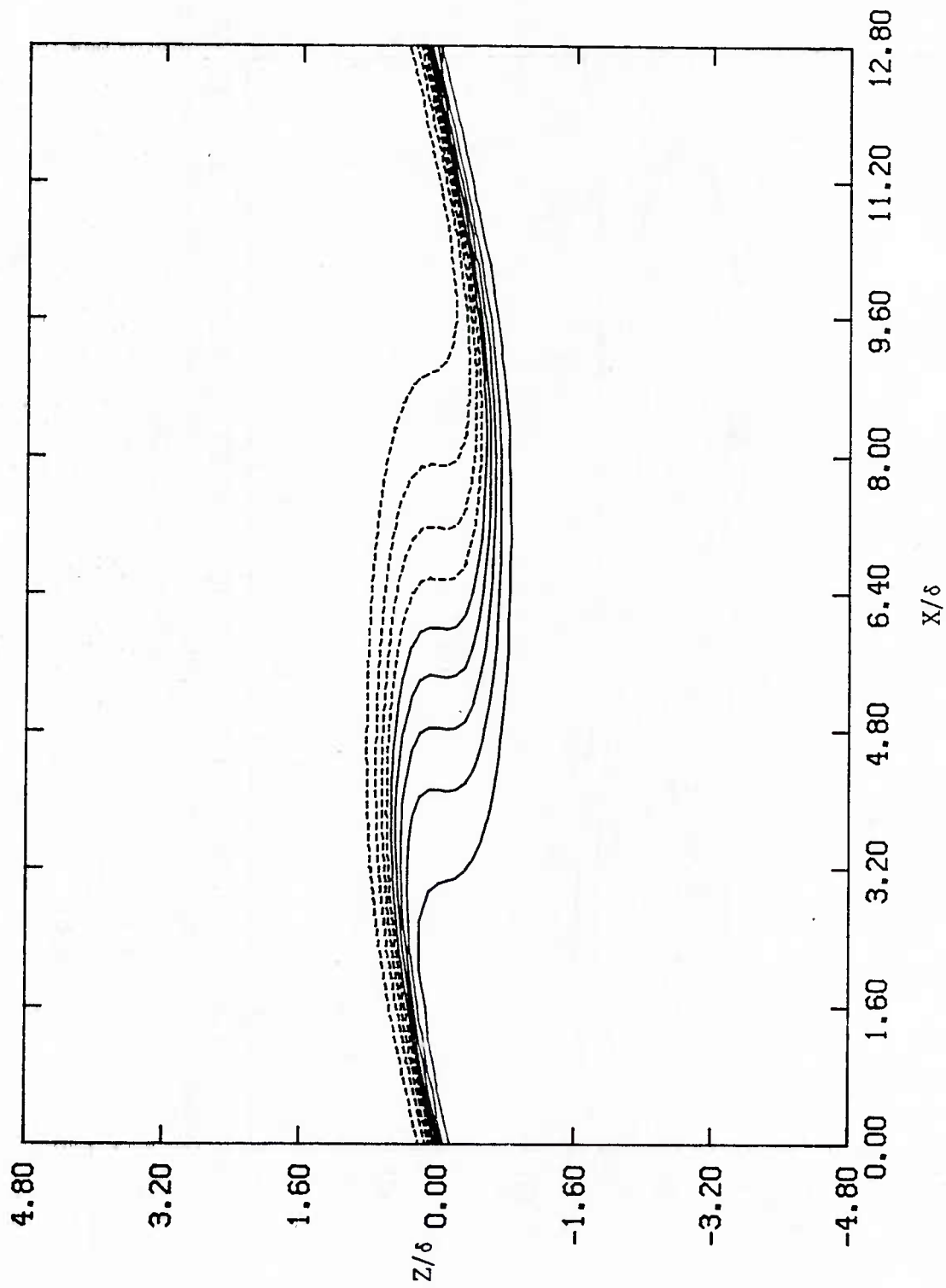


Figure 3.8: Isopleths of dimensionless temperature for $R = 2.5$ and short domain.
 (a) $\tau = 1.5$ Contour interval is 0.2.

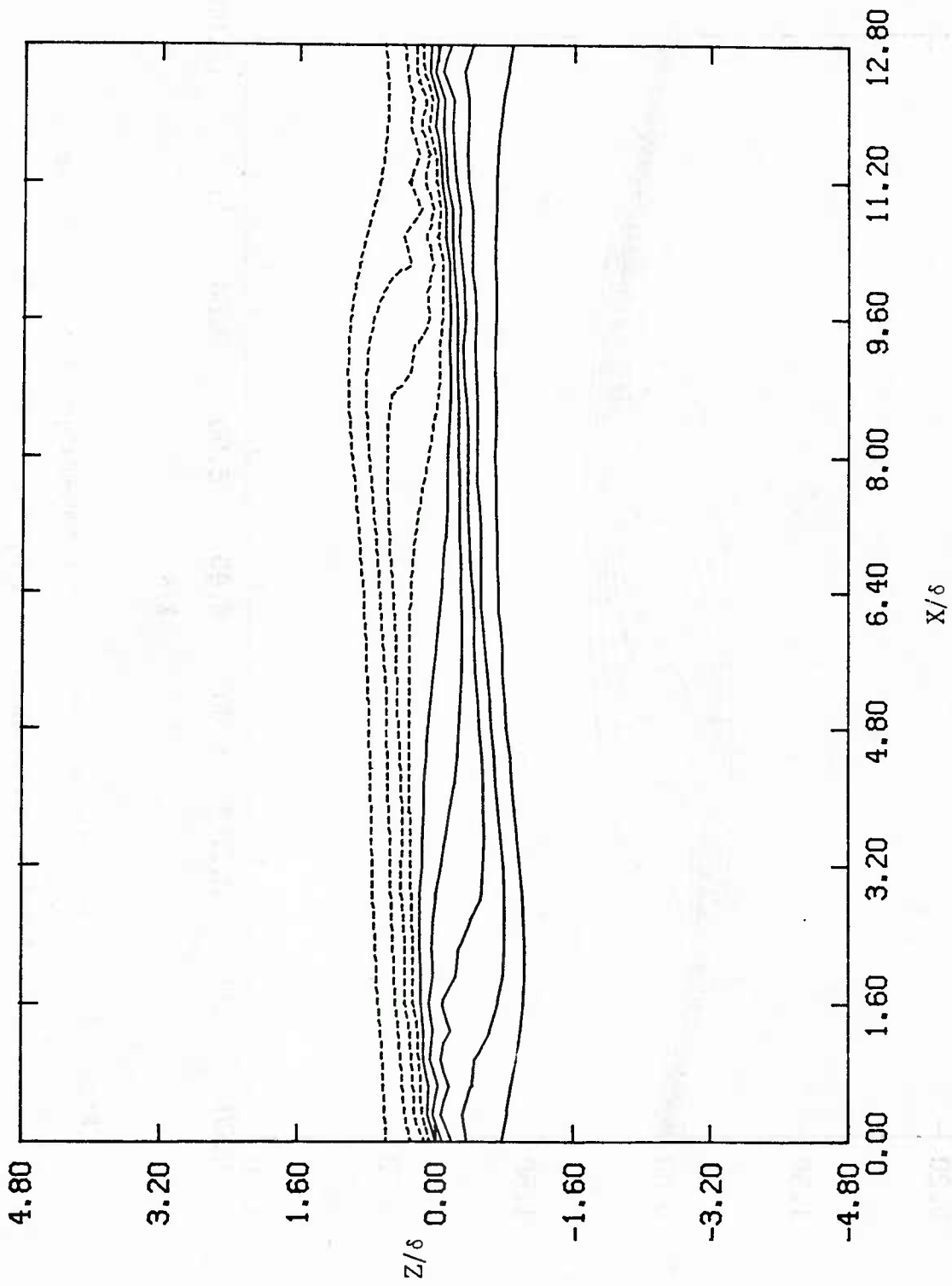


Figure 3.8(b): $\tau = 1.5$

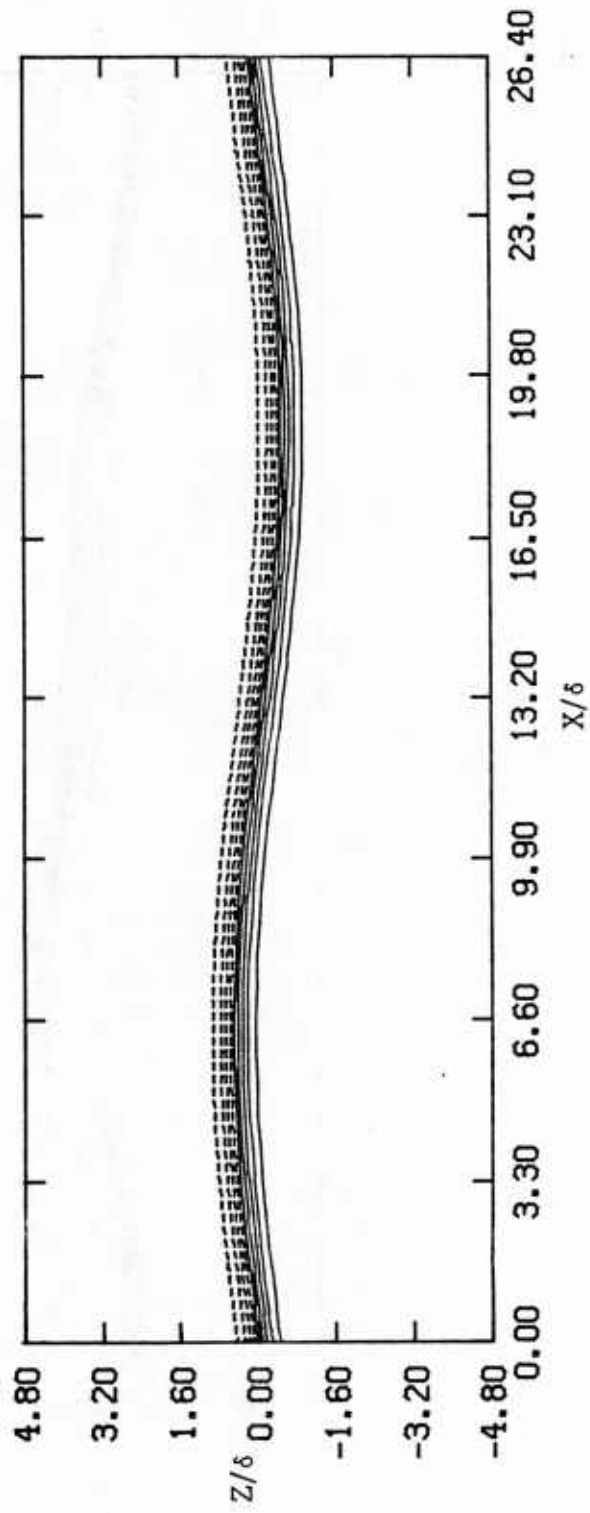


Figure 3.9: As Figure 3.8 but with the long domain.
 (a) $\tau = 4.5$

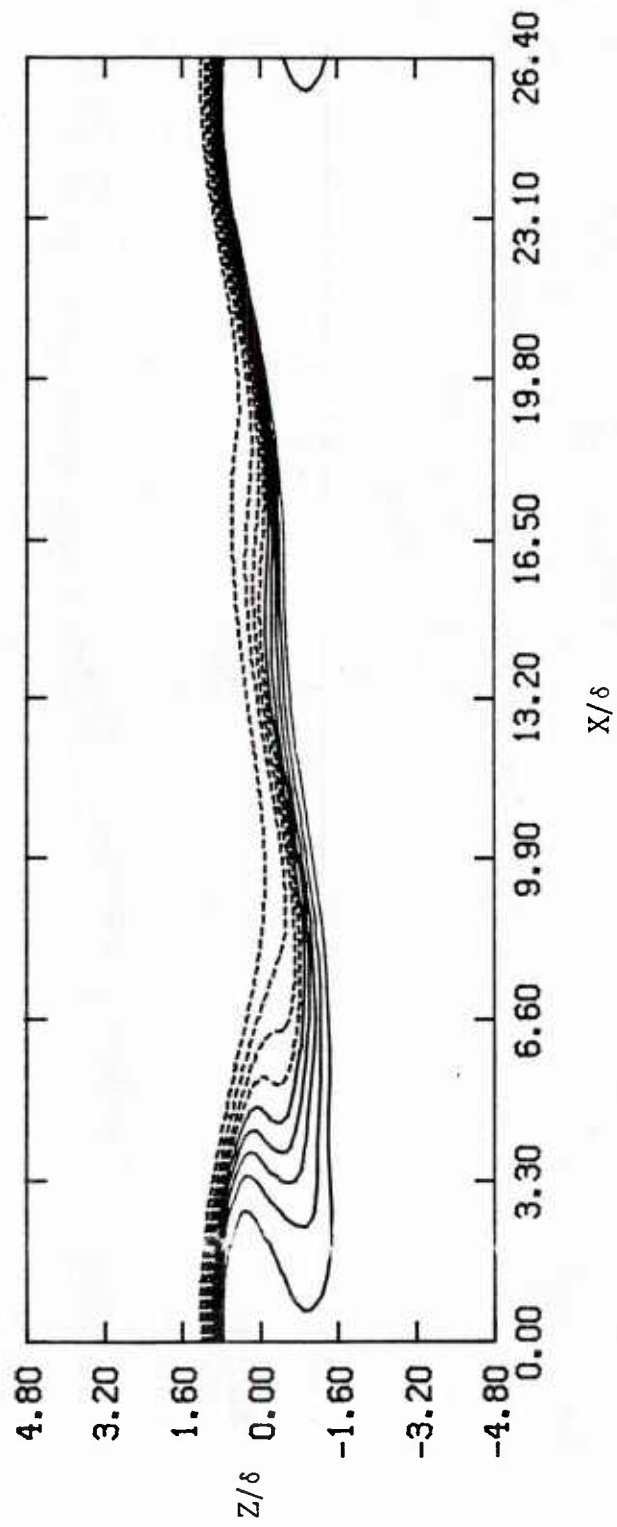


Figure 3.9(b): $\tau = 4$

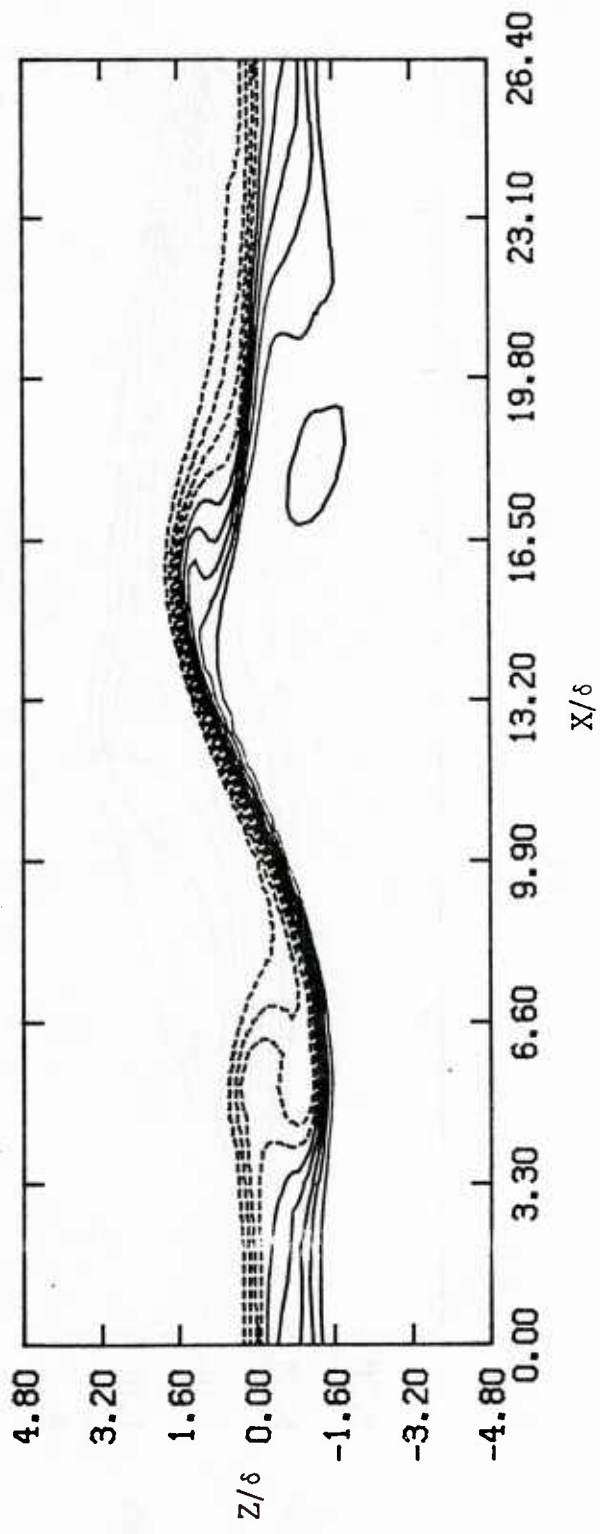


Figure 3.9(c): $\tau = 5.8$

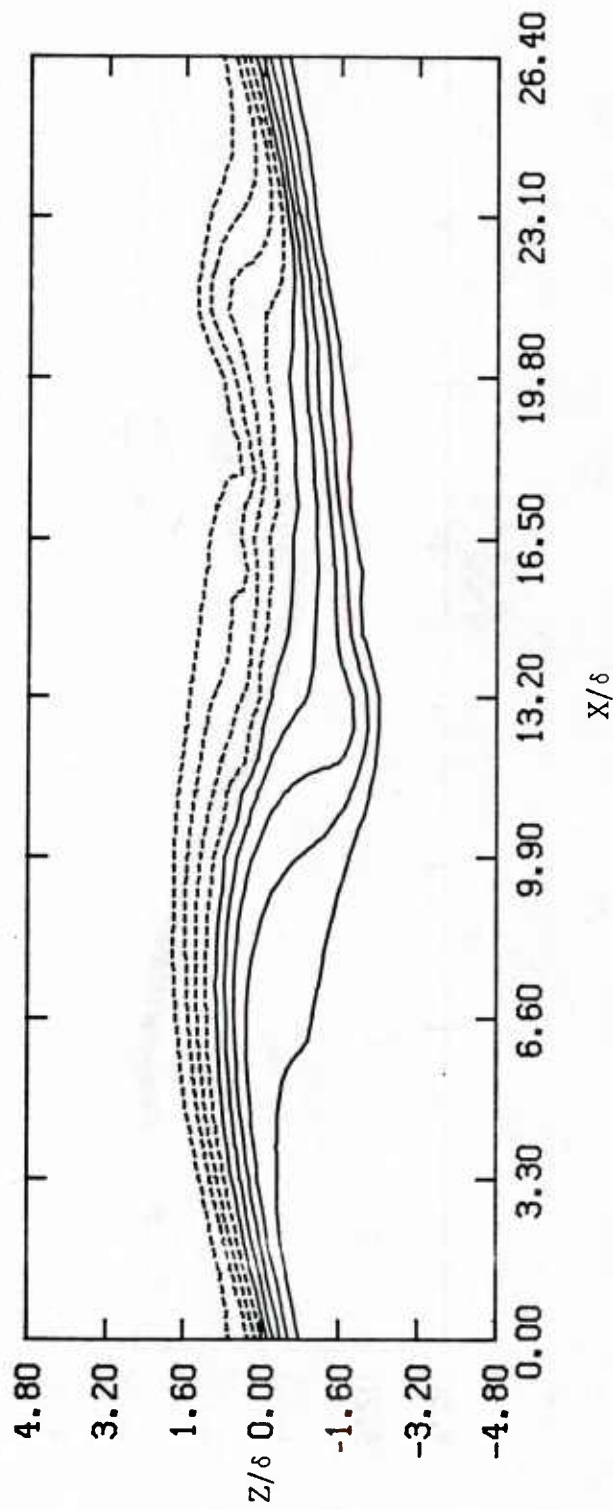


Figure 3.9(d): $\tau = 9.5$

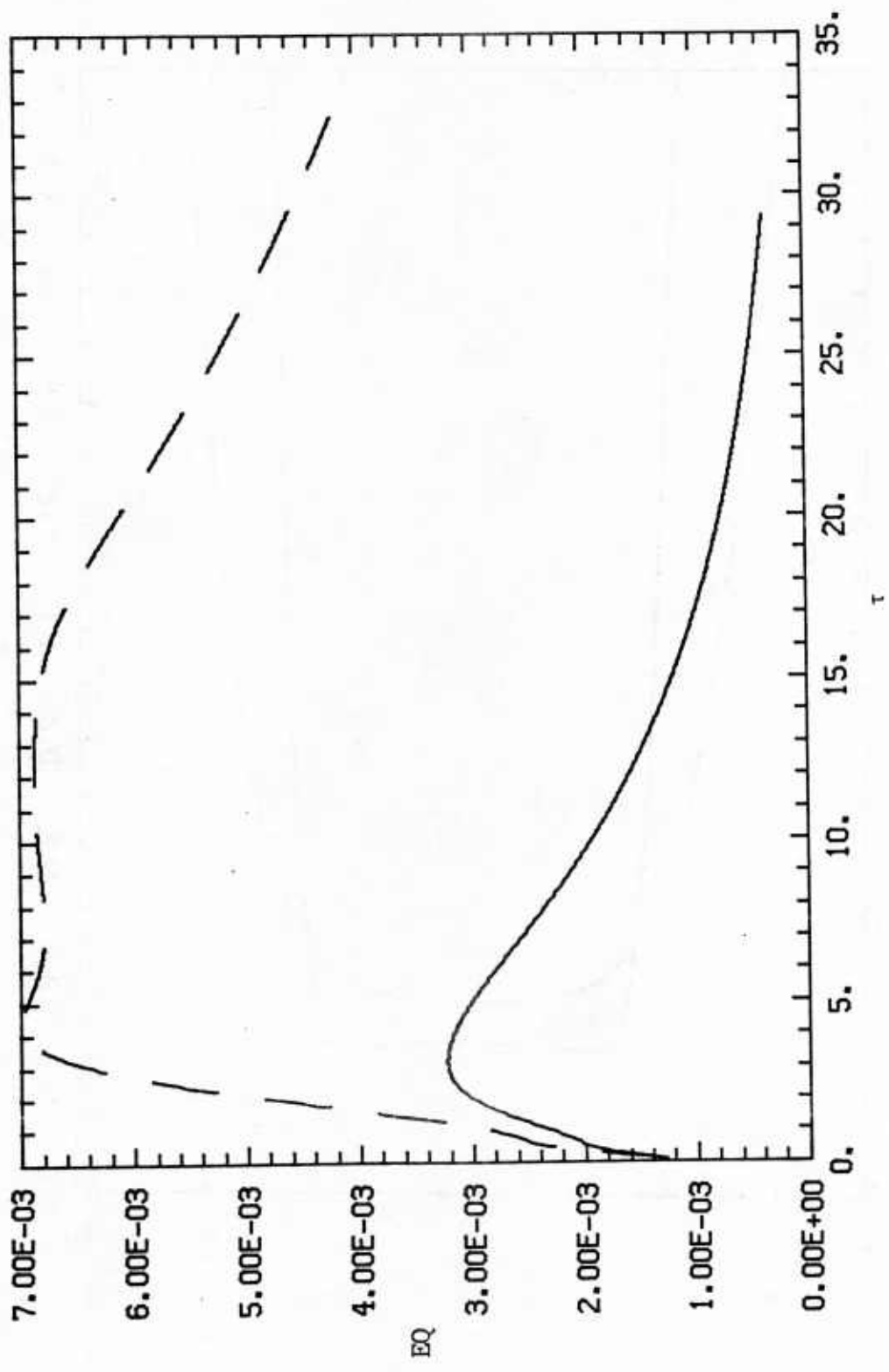


Figure 3.10: Evolution of kinetic energies for the case with $Ri = 0.23$.

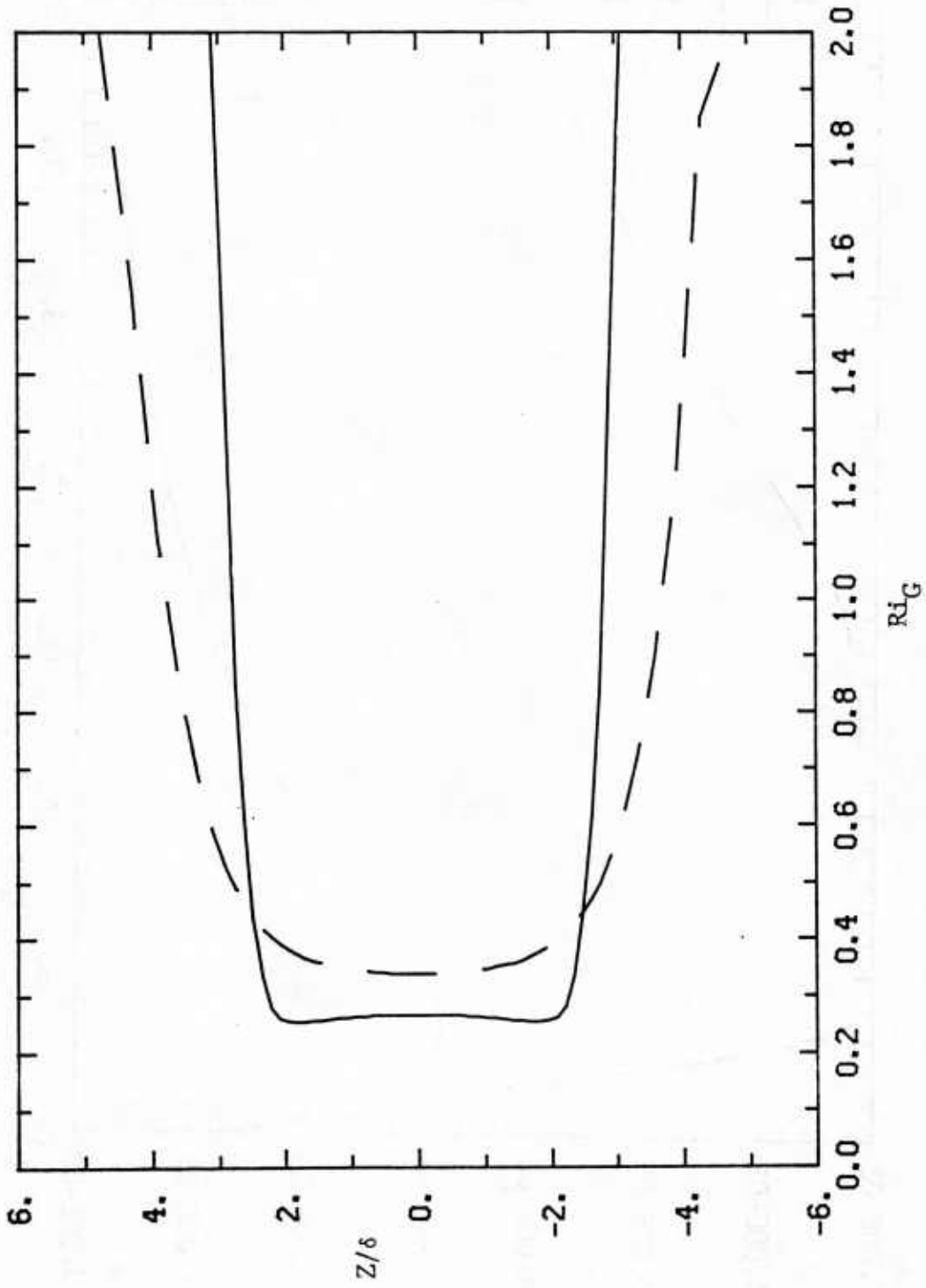


Figure 3.11: Richardson number of $\tau = 18$ for the case with $Ri = 0.23$.

to 0.4. In fact, the temperature contour plots show a breaking billow very similar to the $Ri = 0.2$ case.

This result raises the question of whether the instability is quenched when $Ri > 0.25$. Thus, a case with $Ri = 0.27$ was run with all other parameters identical to the previous run. The energy evolution and final Richardson number profiles are shown in Figures 3.12 and 3.13. Once again, there is a vortex roll-up and collapse giving a final Richardson number of about 0.4. Clearly, there is a finite amplitude instability of the shear layer profile for $Ri = 0.27$ (linear theory predicts stability), and our initial perturbation of amplitude 10% of the background vorticity is sufficiently large to trigger it.

We have not performed extensive studies of the dependence of the flow on initial perturbations or length of integration domain, and so we can only say that the triggering of atmospheric billow events is likely to occur at $Ri \approx 0.25$ and will depend on a finite amplitude perturbation, unless the Richardson number is reduced very quickly into the linear instability regime.

One-Dimensional Calculations of the Kelvin-Helmholtz Instability

Our two-dimensional model of the stratified shear instability has demonstrated the mechanism for billow breakdown into small scale turbulence, and also the ability of the second-order closure scheme to model this process. In these detailed integrations, attention was focussed on the individual billow event, and the initial coherent vortex roll-up stage was calculated explicitly. In a larger scale problem where individual billows are no longer resolved, the closure model has to describe the vortex roll-up stage as well as the vortex breakdown. In this section, we discuss the problems involved in such a calculation.

The first point to emphasize is that the initial stage of the instability is linear, giving exponential growth of a coherent wave. We immediately encountered problems with the A.R.A.P. model because it does not predict any linear exponential growth for Richardson number greater than or equal to zero. Exponential growth is only achieved when the nonlinear terms, i.e., the return-to-isotropy term, is significant, and the growth rate in this regime is

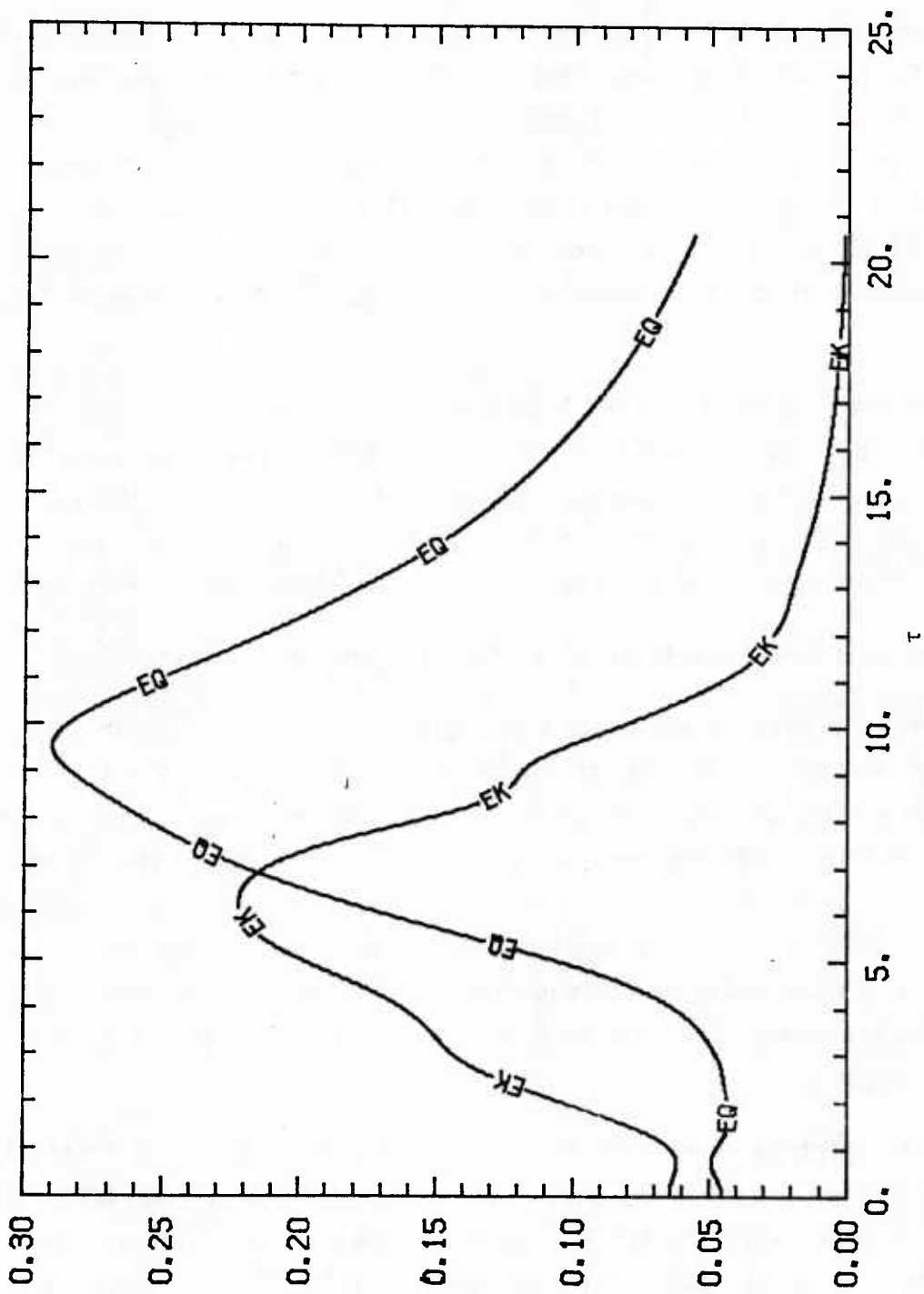


Figure 3.12: Evolution of kinetic energies for the case with $Ri = 0.27$.

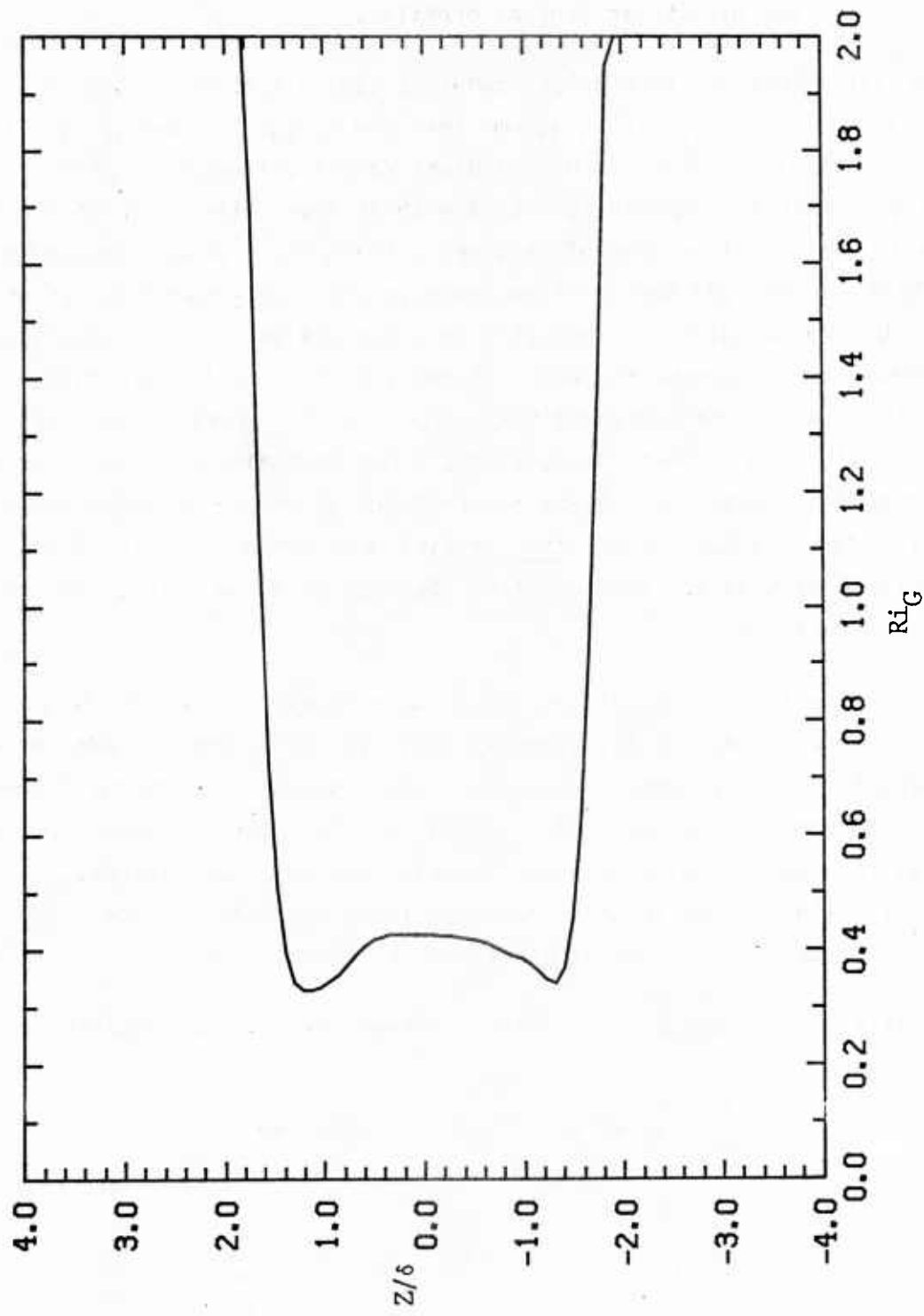


Figure 3.13: Final Richardson number profile for the case with $Ri = 0.27$.

almost an order of magnitude slower than the linear stability analysis prediction for the hyperbolic tangent profiles.

The deficiency of the A.R.A.P. model is easily traced to the absence of "rapid" pressure terms. If we assume that the turbulence energy, q^2 , is very small, so that $q/\Lambda \ll dU/dz$ or N , the Brunt Vaisaila frequency, then only the production terms are important. For the shear layer, the turbulence needs to develop a considerable degree of anistropy through shear production before the Rotta term can provide the positive feedback which we require for exponential growth. We should point out here that this discussion does not invalidate the two-dimensional integrations, where we required the small scale turbulence in the billow to grow exponentially from small levels to model the three-dimensional secondary instability. The mechanism for the latter was shown to be the convective instability produced by overturning the temperature gradient; the A.R.A.P. model does predict exponential growth of this mode, because there is a direct feedback from the heat flux, $\overline{w\theta}$, into the vertical energy component, $\overline{w^2}$.

The remedy in the case of the shear layer appears to be the inclusion of "rapid" pressure terms, as advocated by Hanjalic and Launder²³, and Lumley and Khajeh-Nouri²⁴. These terms redistribute the production of energy between the tensor components instantaneously, and arise from the pressure fluctuations driven by the mean velocity gradient and the buoyancy fluctuations. There is, however, still a problem in that the model terms suggested by e.g., Gibson and Launder²⁵ do not give a critical Richardson number of 0.25.

Briefly, Gibson and Launder write the Reynolds-averaged equation as

$$\frac{D}{Dt} \overline{u_i u_j} = P_{ij} + G_{ij} + \phi_{ij} + D_{ij} - \epsilon_{ij}$$

$$\frac{D}{Dt} \overline{u_i \theta} = P_i + G_i + \phi_i + D_i - \overline{u_i u_j} \frac{\partial \theta}{\partial x_j} \quad (3.6)$$

where

$$P_{ij} = - \overline{u_i u_k} \frac{\partial U_j}{\partial x_k} - \overline{u_j u_k} \frac{\partial U_i}{\partial x_k}, \quad P_i = - \overline{u_j \theta} \frac{\partial U_i}{\partial x_j}$$

$$G_{ij} = g_i \overline{u_j \theta} + g_j \overline{u_i \theta}, \quad G_i = g_i \overline{\theta^2} \quad (3.7)$$

where ϕ , D , and ϵ represent pressure correlations, triple correlations and dissipation, respectively. The A.R.A.P. model sets

$$\phi_{ij} = \phi_{ij}^{(1)} = - \frac{q}{\Lambda} \left(\overline{u_i u_j} - \frac{q^2}{3} \delta_{ij} \right); \quad \phi_i = \phi_i^{(1)} = - \Lambda \frac{q}{\Lambda} \overline{u_i \theta} \quad (3.8)$$

where $q^2 = \overline{u_i u_i}$, and Λ is the turbulence length-scale. $\phi_{ij}^{(1)}$ is the Rotta term.

Gibson and Launder²⁵ recommend the inclusion of extra pressure terms:

$$\phi_{ij}^{(2)} = - c_2 \left(P_{ij} - \frac{P_{kk}}{3} \delta_{ij} \right)$$

$$\phi_{ij}^{(3)} = - c_3 \left(G_{ij} - \frac{G_{kk}}{3} \delta_{ij} \right) \quad (3.9)$$

and

$$\phi_i^{(2)} = - c_{2\theta} P_i$$

$$\phi_i^{(3)} = - c_{3\theta} G_i \quad (3.10)$$

where $c_2=0.6$, $c_3=0.5$, $c_{2\theta}=c_{3\theta}=0.33$. These coefficients also involve a change in the coefficient on the Rotta term, $\phi_{ij}^{(1)}$, from unity to 0.45. Note that the production term $\overline{u_i u_j} \partial \theta / \partial x_j$ does not give rise to any rapid pressure term, because this term does not come from multiplying the momentum equations, as discussed by Launder²⁶.

We have used the above model for the rapid terms (but used 0.375 for the Rotta coefficient in line with Launder, Reece, and Rodi²⁷, since this gave better agreement in the neutral surface layer) in the atmospheric surface layer, and obtained results comparable with the A.R.A.P. model. (Note that these results were obtained without the complicated wall functions of Gibson and Launder.) Thus, the rapid terms do not degrade the model performance in this regime; although it must be admitted that the inclusion of four extra empirical constants does not significantly improve the results, either. However, we do have rapid terms which can promote exponential growth in the shear layer.

Unfortunately, the critical Richardson number for this model in the linear regime is 0.15, which is significantly smaller than the actual value of 1/4. Adjusting the constants to move the critical value to 1/4 degraded the surface layer performance of the model quite seriously. The remedy we found was to include a rapid term proportional to the scalar flux production term, $-\overline{u_i u_j} \partial \theta / \partial x_j$. If we apply a coefficient of 1/3 to this term, i.e., the entire production of $\overline{u_i \theta}$ is reduced by 1/3, and set $c_3 = c_2 = 0.6$, then this simple model has a critical Richardson number of 0.25, and produces very similar results to the A.R.A.P. model in the surface layer. The linear growth rates predicted by the model are actually very close to the hyperbolic tangent profile growth rates calculated by Hazel²², as can be seen from Figure 3.14.

A calculation for the tanh profile shows reasonable agreement with the two-dimensional calculations, provided we fix the length at a reasonable fraction of the shear layer thickness. Figure 3.15 shows the evolution of the integrated turbulence energy for a case with $Ri = 0.1$ initially. The time scales and maximum values are close to the two-dimensional values, as is the final Richardson number as shown in Figure 3.16.

The problem cannot be claimed to be entirely solved, however, because in the case of a passive scalar, we would not want to include any rapid term corresponding to $\overline{u_i u_j} \partial \theta / \partial x_j$ in the scalar flux equation. Analytical solutions for the initial rate of diffusion from a point source show that there is no such rapid term. We are therefore unable to present a truly invariant model which adequately describes both the initial growth of turbulence in a shear layer and the initial rate of diffusion from a scalar

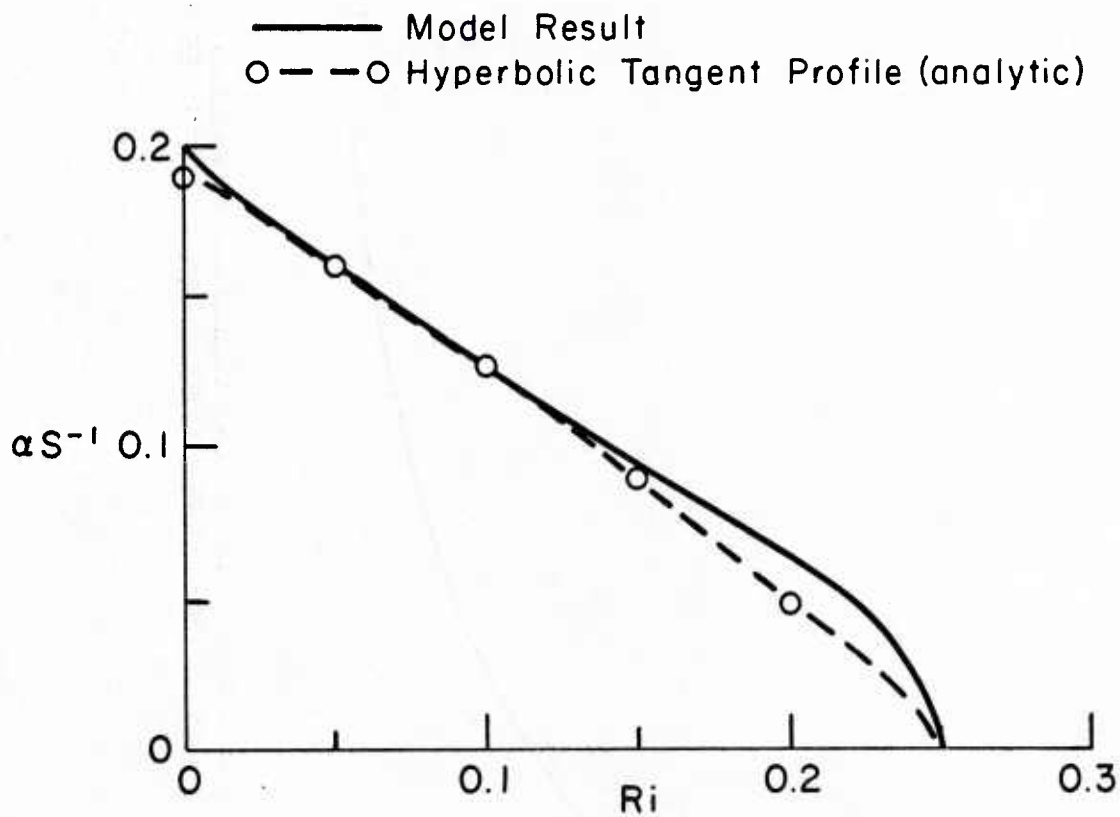
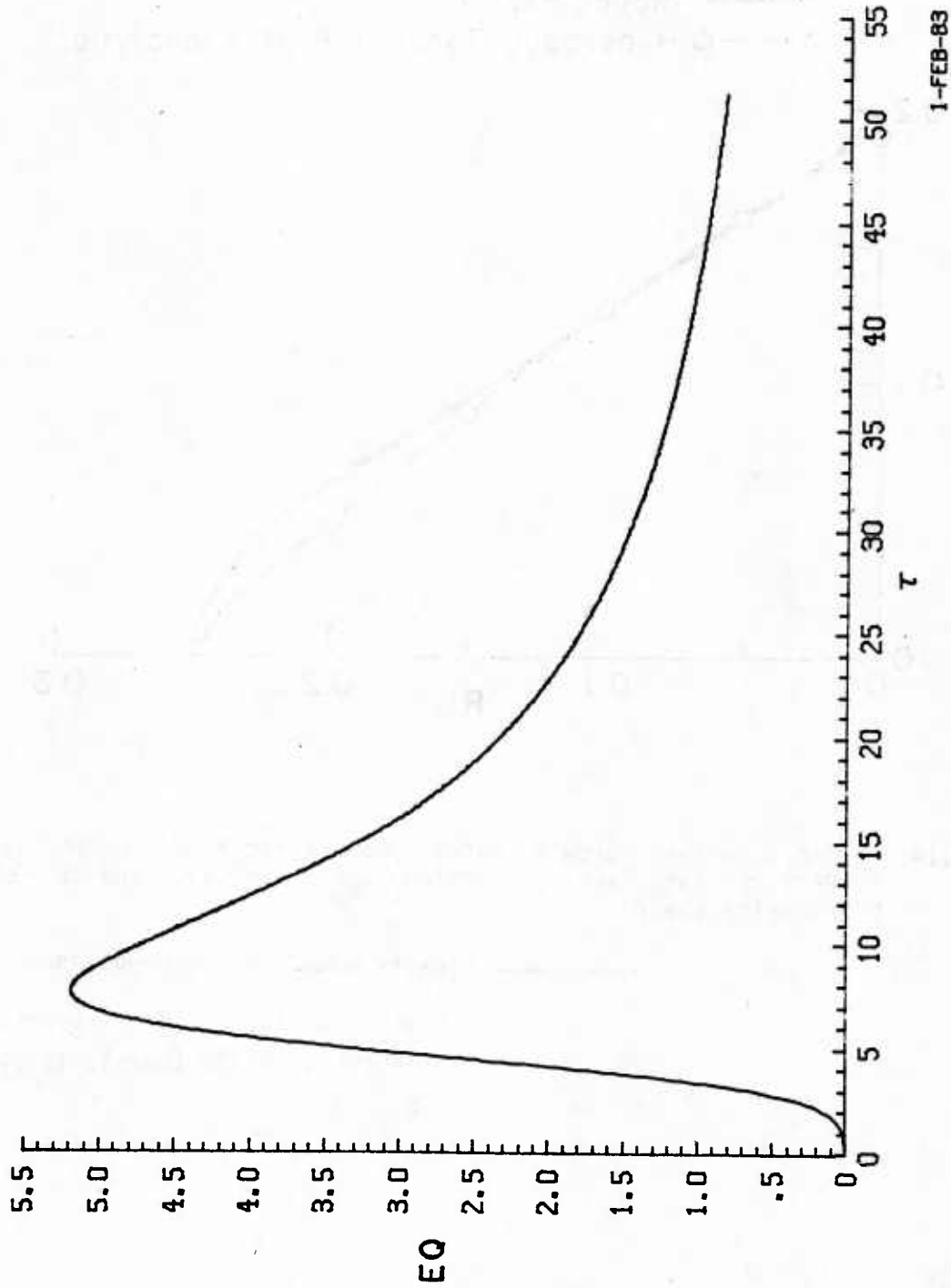


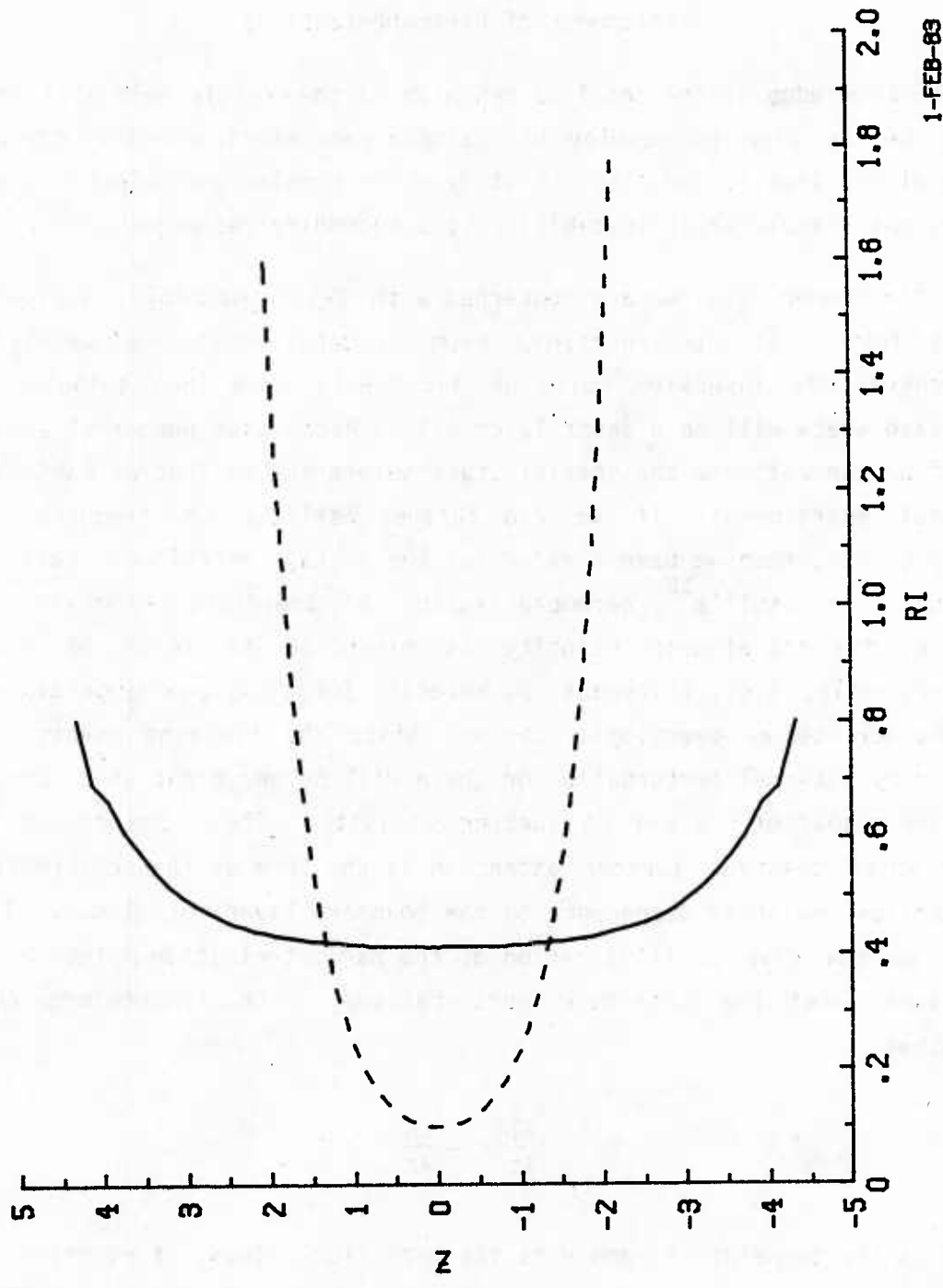
Figure 3.14: Dimensionless growth rates for stratified shear layer. Perturbations are proportional to $\exp(\alpha t)$, and S is the velocity shear.

——— closure model, homogeneous shear
 - - - - - linear analysis for hyperbolic tangent profile (Hazel, 1972)



1-FEB-83

Figure 3.15: Evolution of total energy, EQ, for one-dimensional closure model integration. Horizontal length of the domain was taken to be 165 for direct comparison with two-dimensional cases.



1-FEB-89

Figure 3.16: Profile of Richardson number at the end of the one-dimensional closure model integration.

point source.

Development of Parameterizations

The knowledge of the detailed dynamics of the Kelvin-Helmholtz breaking process can be used to develop both simple parameterizations of the billow-induced mixing itself, and also to study more complex entrainment processes when the small scale shear instability is a secondary mechanism.

In the former case, we are concerned with Kelvin-Helmholtz billows as a dominant feature of the inversion. From our detailed studies, we may assert that whenever the inversion rolls up and breaks down into turbulence, the final mixed state will be a shear layer with a Richardson number of about 0.4. Thus, if we can estimate the initial state before the roll-up we can calculate the total entrainment; if we can further estimate the frequency of the breaking events, then we have a value for the average entrainment rate at the interface. In Stull's²⁸ parameterization of shear-induced mixing at the inversion, the entrainment velocity is expressed in terms of inversion parameters only, i.e., thickness, δ , velocity jump, ΔU , and temperature jump, ΔT . This may be an oversimplification, since the breaking events must be triggered by external perturbation or there will be one event which produces a Richardson number of 0.4 and no further activity. Thus, one aspect of the problem which deserves further attention is the form of the perturbations at the interface and their dependence on the boundary layer turbulence. For the moment, we can give an illustration of the parameterization method by making assumptions about the interface perturbations. The temperature equation states that

$$\frac{\partial T}{\partial t} = - \frac{\partial H}{\partial z} \quad (3.11)$$

where T is the temperature, and H is the heat flux. Thus, if we define

$$F = \int H(z,t) dt \quad (3.12)$$

where the integral is carried out over the entire billow event, then

$$\frac{\partial F}{\partial z} = T_0(z) - T_f(z), \quad (3.13)$$

where T_0 and T_f are the initial and final temperature profiles.

For the sake of simplicity, let us assume piecewise linear profiles so that

$$T_{0,f} = \begin{cases} \Delta T/2 & , \quad z > \ell_{0,f}/2 \\ \Delta Tz/\ell_{0,f} & , \quad z < \ell_{0,f}/2 \\ -\Delta T/2 & , \quad z < -\ell_{0,f}/2 \end{cases} \quad (3.14)$$

where ℓ_0, ℓ_f are the initial and final shear layer thickness. If we assume that the velocity profile has the same shape, then the initial Richardson number, $Ri_0 = (g/T_0)\Delta T\ell_0/\Delta u^2$, and the final value,

$$Ri_f = \frac{g}{T_0} \frac{\Delta T\ell_f}{\Delta u^2} . \quad (3.15)$$

Now we know $Ri_f = 0.4$. Thus

$$\ell_f = \frac{0.4}{Ri_0} \ell_0 . \quad (3.16)$$

For definiteness, let us assume that $Ri_0 = 0.133$, so that $\ell_f = 3\ell_0$; we can now calculate the integrated heat flux. To obtain the maximum value, $F(0)$, we have

$$F(0) = - \int_0^{\infty} (T_0(z) - T_f(z)) dz$$

$$\begin{aligned}
&= \Delta T \int_0^{3\ell_0/2} \frac{z}{3\ell_0} dz - \Delta T \int_0^{\ell_0/2} \frac{z}{\ell_0} dz \\
&= \Delta T \left[\frac{3\ell_0}{8} - \frac{\ell_0}{8} \right] \\
&= \frac{\ell_0 \Delta T}{4} \tag{3.17}
\end{aligned}$$

To obtain the average heat flux, \bar{H} , at the inversion, we now need to estimate the frequency of those breaking events; then

$$\bar{H} = \frac{F(0)}{\tau} = \frac{\ell_0 \Delta T}{4\tau} \tag{3.18}$$

where τ is the period between events.

As we have already stated, τ will depend on the boundary layer turbulence, but a lower limit on τ is given by the time scale of the breaking event. This is because the layer must recover from the turbulent breakdown, otherwise we do not have distinct events. From our detailed calculations, the time scale is on the order of $10\alpha/\Delta u$, where α is the wavelength of the disturbance, which is roughly $10\ell_0$. Thus a minimum value for τ is $100\ell_0/\Delta u$. Therefore

$$\bar{H} < \frac{\ell_0 \Delta T \Delta u}{400 \cdot \ell_0} = 2.5 \times 10^{-3} \Delta u \Delta T \tag{3.19}$$

To obtain our entrainment velocity, W_e , we divide \bar{H} by ΔT giving $W_e < 2.5 \times 10^{-3} \Delta u$.

Stull²⁸ parameterizes the entrainment velocity as

$$W_e = \frac{A_3}{Ri_B} \Delta U \tag{3.20}$$

where Ri_B is the bulk Richardson number of the inversion, and A_3 is an empirical constant which is derived from experimental results to be 10^{-3} . If we take $Ri_B = 0.4$ as a typical value of the inversion, we obtain precisely the same estimate as our crude upper bound. The exact agreement is obviously fortuitous, since we only made rough estimates of the effects of the boundary layer turbulence - but is nevertheless encouraging. The experiments used in deriving the value for A_3 were explicitly concerned with the shear-induced instability, so we would expect the value to be near our upper bound. More work is required to determine the dependence of A_3 on the boundary layer turbulence.

The second application of the detailed study is in the parameterization of shear instability as a secondary mechanism; for example, in the case of entrainment by penetrative convection. These processes may be studied using a numerical model of the large scale features in conjunction with a simple model of the small scale processes. In this regard, the one-dimensional integrations test the ability of the second-order closure model to describe the overall mixing event without resolving the detailed billows themselves. Our integrations show that this can be achieved with reasonable success provided that the length scales can be adequately described. This may require more effort in the specification of the length scale, for example, resetting the length scale to some specified fraction of the shear layer thickness whenever the Richardson number falls below some critical value and the turbulence energy is small. It does seem likely that these small scale processes can be described as sub-grid mixing using the second-order closure model, which will permit the further study of larger scale inversion dynamics.

As noted earlier, in considering the problem of entrainment at the top of the atmospheric boundary layer, the small scale shear instabilities are generally a secondary mechanism. Having achieved some understanding of these small scale processes, the next problem is to investigate how they are triggered by the turbulent boundary layer eddies. This requires consideration of the whole mixing layer, and there are two feasible numerical approaches. One can choose to model the boundary layer eddies in either two or three dimensions. Three dimensions is clearly more realistic but is much more expensive and demands a very simple sub-grid closure. The simple closures

have proven very effective in neutral and convectively unstable flows, but have not been tested sufficiently in stratified cases. On the other hand, two-dimensional calculations have reproduced many of the observed features of boundary-layer eddies, and also have some observational justification insofar as longitudinal rolls are quite common under certain circumstances. The two-dimensional calculations would also permit a more sophisticated sub-grid closure, which would give more confidence in the stratified shear layer at the inversion.

4. COMMENTS ON THE EXTENSION OF OUR INTEGRAL BOUNDARY LAYER MODEL FROM ONE-DIMENSIONAL TO THREE-DIMENSIONAL

As detailed in past reports (References 2 and 17) we have spent some time attempting to reduce the grid resolution required to adequately represent the atmospheric boundary layer by imposing integral constraints on the finite difference algorithms. The goal has been to develop a hybrid integral-differential method which can be used with any number of vertical layers from 1 to 10. The single layer representation is purely integral but should provide (at best) a rough approximation to the boundary-layer dynamics. The extent to which we have been able to do this for the homogeneous boundary layer in some different dynamical situations is illustrated in Figures 3.2 to 3.5 of Reference 2. Some effort has been expended on continuing this approach during the current contract period. These efforts have convinced us that the most promising way to proceed with this approach is to combine it with the general problem of sub-grid flux parameterization. This may be elucidated by discussing the problems and promises of using this integral approach for a fully three-dimensional boundary layer model.

If the boundary layer can be adequately represented by only a few vertical layers, then the three-dimensional, boundary-layer problem in x, y, z , and t can be reduced to a quasi-two-dimensional problem in x, y , and t . This very attractive possibility has supplied most of the impetus for our integral modeling efforts. Single layer representations of the planetary boundary layer (PBL) for such a reduced three-dimensional problem have met with mixed success in the literature. The simple mixed layer models of Lavoie²⁹ and by Keyser and Anthes³⁰ appear to provide considerable realism for the relatively small computing requirements they have in comparison to multi-level, fully three-dimensional models such as Warner et al.³¹. However, Anthes et al.^{32, 33} have shown that, at least, their version of a mixed layer PBL is not able to adequately represent the flow within the PBL when horizontal inhomogeneities associated with differential heating over complex terrain or across land-water boundaries is a dominant mechanism.

Anthes, et al., attribute this deficiency of the mixed layer model to difficulties in representing the horizontal pressure gradient at the top of their mixed layer. However, in more general terms, it appears to be a

reflection of the difficulty of providing a simple parameterization which can represent a wide variety of profiles of the mean variables within the PBL. The sea breeze example, which they consider, represents a case where the boundary layer dynamics impose a circulatory flow pattern in the vicinity of the shoreline. They identified the on-shore flow as occurring within their mixed layer PBL and forced the return flow to occur above it. Their analysis then shows that the parameterization of the return flow layer is as important as the parameterization of the mixed layer itself. It is perhaps more appropriate to think of the return flow as the outer part of the total PBL. When viewed in this way, the sea breeze involves flow with a reversal in direction of the velocity within the PBL. The representation of reversed flow profiles necessarily complicates any parameterization of a single layer model. The history of integral boundary layer models in aeronautics (Schlichting³⁴) have shown them to have quite limited success under separated flow conditions which yield a flow reversal in the boundary layer. This leads us to be rather pessimistic about the prospective adequacy of any single layer representation of the PBL for general three-dimensional meteorological problems. This still leaves the possibility that a model with a few layers can be quite successful.

The extension of our hybrid integral model to fully three-dimensional situations requires extending the complete second-order closure model to three-dimensions first. Problems associated with programming algorithms for computing the mean flow variables in existing three-dimensional, primitive Equation models such as Pielke's³⁵ must be tackled along with those required for computing the second-order fluxes. A task that should be simpler, and thus of more immediate utility, is to use our turbulent transport model to construct algorithms to parameterize the role of sub-grid turbulent fluxes in existing mesoscale meteorological models. Integral constraints generated by integrating the second-order flux equations over the resolved grid lengths can be very useful in this sub-grid parameterization role without the need to construct a completely new three-dimensional model.

As a simple example to illustrate the latter idea, consider the sub-grid flux parameterization of the lowest layer of the flow where the vertical grid spacing is such as to completely contain the boundary layer within the lowest level. The flux term in the u momentum equation we wish to parameterize is

$$-\frac{\partial \overline{u'w'}}{\partial z} \quad (4.1)$$

The level 1 Equation for u then involves some representation of

$$-(\overline{u'w'_2} - \overline{u'w'_0})/2\Delta z \quad (4.2)$$

If the eddy parameterization is used, then

$$\overline{u'w'} = -\epsilon \partial U / \partial z \quad (4.3)$$

and a very poor representation of the surface shear stress is obtained, unless a compensating slip velocity is permitted at the surface. A simple useful form for $\overline{u'w'}$ can be obtained for the superequilibrium balance of the turbulent correlation equations

$$\overline{u'w'} = -\frac{\sqrt{2}}{4} \Lambda^2 \left| \frac{\partial U}{\partial z} \right| \left| \frac{\partial U}{\partial z} \right| \quad (4.4)$$

This mixing length form of the parameterization is quite appropriate in the surface layer with $\Lambda \propto z$, but some integral form of it must be used to relate the surface shear stress to the velocity at the first grid point. If the first grid point is placed within the surface layer then

$$\overline{u'w'}_0 = -\frac{k^2 U_1 U_1}{(\ln z_1/z_0)^2} \quad (4.5)$$

where $k=0.4$ and z_0 is the effective aerodynamic roughness of the surface. A combination of Equations 4.4 and 4.5 is quite effective in Equation 4.2, when the boundary layer is fairly well-resolved and there is no influence of stratification or pressure gradient on the turbulence. However, even in this simple case it is clear that Equation 4.5 needs some adjustment if the resolution is reduced so that the first grid point lies outside the constant flux surface layer.

In summary, we believe it is appropriate to change the present emphasis of our integral modeling effort from that aimed at developing a fully three-dimensional version of our second-order closure model, to that of providing support for our future work of parameterizing the role of sub-grid turbulent fluxes for mesoscale meteorological models. This simple example above is meant to illustrate how we expect our past work on hybrid integral models of the PBL to be quite helpful in this new task.

5. PRELIMINARY CONSIDERATIONS OF CUMULUS PARAMETERIZATION BASED ON SECOND-ORDER CLOSURE

Introduction

Some of the most important turbulent transport processes in the lower troposphere involve cumulus clouds. In global models this calls for the introduction of a cumulus parameterizations scheme to represent the turbulent transport of humidity, heat, and momentum by these cumulus clouds. Such schemes (Arakawa & Schubert³⁶, Lord³⁷, Kuo³⁸) require a phenomenological description of the most important effects of clouds.

In what follows we take up a preliminary consideration of the application of higher-order closure turbulence methodology to such flows. We note that such a higher-order closure description should be capable of describing a range of atmospheric flows from boundary layers to mesoscale motions in which cloudiness and conditional instability are of importance. In addition, with appropriate modifications for the large density changes over the turbulent macroscale, such a higher-order closure turbulence theory should naturally describe the effects of deep cumulus convection and hence provide an alternative approach to the problem of cumulus parameterization.

The presence of both saturated and unsaturated regions within a buoyant flow has at least two important influences on the turbulent description of such flows. The first is the appearance of new correlations in the turbulence equations, which result from the turbulent fluctuations of the clouds. Principal among these cloud correlations are the mean cloudiness \bar{r} , the cloud flux $w'r'$, and the cloud turbulence energy $1/2 w'w'r'$, where r is a conditional variable, with the values $r=1$ in cloud and $r=0$ in clear air. Second, flows that contain both saturated and unsaturated regions are very likely to be conditionally unstable. Thus, most of the large scale field may be virtually devoid of turbulence while local isolated regions consisting of cloudy and non-cloudy updrafts and downdrafts may be in strong convection. This latter effect requires the introduction of the concept of an intermittent turbulence field for the large scale flow.

In Part 2 we review the partly cloudy correlations which must appear in the turbulence equations. In Part 3 we consider second-order closure turbulence modeling of an intermittent flow. In Part 4 we consider the application of this model and we make some data comparisons and checks with the theory of Parts 2 and 3.

Second-Order Closure Turbulence Equations with Cloud Correlations

We begin with the instantaneous energy Equation written in terms of the virtual potential temperature θ_v . (Oliver, Lewellen, and Williamson¹²):

$$D\theta_v/Dt = \kappa_s S + \kappa_g \Gamma w \quad (5.1)$$

where w is the vertical velocity, Γ the adiabatic lapse, and S the radiant and precipitation source term. We may express κ_s and κ_g as

$$\kappa_s = 1 + (\beta_s - 1)r \quad (5.2a)$$

$$\kappa_g = \beta_g r \quad (5.2b)$$

with

$$\beta_s = \mu/\tilde{\mu} \quad \beta_g = \alpha - \mu^2/\tilde{\mu}$$

and μ , $\tilde{\mu}$, and α are the functions of the saturation mixing as given by Oliver et al.¹².

The variable r is the instantaneous cloudiness defined as

$$r = H(q_\lambda) \quad (5.3)$$

where H is the Heaviside function and q_λ is the difference mixing ratio

$$q_\lambda \equiv q - q_s \quad (5.4)$$

with q_s the saturation mixing ratio. The instantaneous liquid water mixing

ratio q_ℓ is given by

$$q_\ell = q_\lambda r \quad (5.5)$$

We note that because of the sensitive dependence of radiative transport on the presence of liquid water drops, the radiant flux divergence S will depend upon the cloudiness present (as well as the water vapor in both clear and cloudy air). We do not take up the procedure of treating the ensemble averaging of S here. We merely indicate its presence through the source term Σ defined as

$$\Sigma = \kappa_s S = [1 + (\beta_s - 1)r]S \quad (5.6)$$

We may express Equation (5.1) as

$$D\theta_v/Dt = \beta r \Gamma w + \Sigma \quad (5.7)$$

where for brevity in what follows we let $\beta = \beta_g$.

The ensemble average equations in the second-order closure system involving θ_v through Equation (5.7) are those governing $\overline{\theta_v}$, $\overline{u_i \theta_v'}$, $\overline{\theta_v'^2}$, and $\overline{q' \theta_v'}$. These moments derived from Equation (5.7) and the corresponding conservation laws for the other variables are

$$D\overline{\theta_v}/Dt = - \partial(\overline{u_i \theta_v'})/\partial x_i + \beta \Gamma (\overline{r' w'} + \overline{r} \overline{w}) + \overline{\Sigma} \quad (5.8)$$

$$\begin{aligned} D(\overline{u_i \theta_v'})/Dt &= - \overline{u_i' u_j'} (\partial \overline{\theta_v}/\partial x_j - \beta \Gamma_j \overline{r}) - \overline{u_i' \theta_v'} \partial \overline{u_i}/\partial x_j \\ &+ (g_i/T_r) \overline{\theta_v'^2} - 2\epsilon_{ijk} \Omega_j \overline{u_k' \theta_v'} + 0.75(\hat{q}/\Lambda) \overline{u_i' \theta_v'} \\ &+ 0.3 \partial(\hat{q} \Lambda \overline{u_i' \theta_v'} / \partial x_j) / \partial x_j + \beta \Gamma_j \overline{u_i' u_j' r'} \end{aligned}$$

$$+ \beta \Gamma_j \overline{u_j} \overline{u_j' r'} + \overline{\Sigma' u_j'} \quad (5.9)$$

$$\begin{aligned} D(\overline{\theta_V'^2})/Dt &= -2\overline{u_j' \theta_V'} (\partial \overline{\theta_V} / \partial x_j - \beta \Gamma_j \overline{r}) - 0.45(\hat{q}/\Lambda) \overline{\theta_V'^2} \\ &+ 0.3 \partial (\hat{q} \Lambda \overline{\theta_V'^2} / \partial x_j) / \partial x_j \\ &+ \beta \Gamma_j \overline{u_j' \theta_V' r'} + \beta \Gamma_j \overline{u_j} \overline{\theta_V' r'} + \overline{\Sigma' \theta_V'} \end{aligned} \quad (5.10)$$

$$\begin{aligned} D(\overline{q' \theta_V'})/Dt &= -\overline{u_j' q'} (\partial \overline{\theta_V} / \partial x_j - \beta \Gamma_j \overline{r}) - \overline{u_j' \theta_V'} \partial \overline{q} / \partial x_j \\ &- 0.45(\hat{q}/\Lambda) \overline{q' \theta_V'} + \beta \Gamma_j \overline{u_j' q' r'} \\ &+ 0.3 \partial (\hat{q} \Lambda \overline{q' \theta_V'} / \partial x_j) / \partial x_j + \beta \Gamma_j \overline{u_j} \overline{q' r'} + \overline{\Sigma' q'} \end{aligned} \quad (5.11)$$

In the above equations $\Gamma_j \equiv \Gamma g_j / g$, and \hat{q} and Λ are characteristic velocity and length scales for the turbulence.

We observe that the effective buoyancy driving the production terms is the generalized buoyancy θ_w defined as

$$\theta_w = \theta_V - \beta \Gamma R \quad (5.12)$$

where R is defined as the cloud depth

$$R(z) = \int_{z_0}^z r(\hat{z}) d\hat{z} \quad (5.13)$$

and z is the coordinate direction aligned with the gravitational body force. From Eqs. (5.12) and (5.13) we then have

$$\partial\theta_w/\partial x_j = \partial\theta_v/\partial x_j - \beta\Gamma_j r \quad (5.14)$$

$$D\theta_w/Dt = D\theta_v/Dt - \beta\Gamma r w \quad (5.15)$$

Equation (5.7) expressed in terms of the generalized buoyancy thus becomes conservative (except for the radiation and precipitation source term Σ):

$$D\theta_w/Dt = \Sigma \quad (5.16)$$

The generalized buoyancy θ_w is an appropriate conserved variable for partly cloudy situations. Although θ_w is conserved, it is important to note that θ_v (not θ_w) remains as the determinant buoyancy for the momentum equation.

It will be observed that new second and third order correlations involving r are introduced into the system. After the mean cloudiness \bar{r} , the most important second order correlation is the cloud flux $\overline{w'r'}$. The cloud flux appears directly as a heating source term in the mean virtual potential temperature Equation and carries the essence of cumulus heating in partly cloudy situations. A third order correlation, particularly important in conditionally unstable flows, is the cloud vertical turbulence energy $1/2 \overline{w'w'r'}$ which represents the vertical turbulence energy which is correlated with the cloud fluctuations. Similarly important are the cloud heat and moisture fluxes $\overline{w'\theta_v'r'}$, $\overline{w'q'r'}$ which represent the fluxes of heat and moisture which are embedded in the fluctuating clouds. (Note that all these correlations vanish in uniformly saturated stratus for which $\bar{r} \equiv 1$, $r' \equiv 0$.)

The ensemble mean liquid water \bar{q}_ℓ and variance σ_{q_ℓ} (which do not appear directly in Eqs. (5.8)-(5.11) but control the radiative transport and precipitation microphysics) are, assuming liquid-vapor equilibrium,

$$\bar{q}_\ell = \bar{q}_\lambda \bar{r} + \overline{q'_\lambda r'} \quad (5.17a)$$

$$\begin{aligned}
\sigma_{q_\ell}^2 &= \overline{q_\ell' q_\ell'} = \overline{q_\lambda^2 r'^2} + 2 \overline{q_\lambda r q_\lambda' r'} + \overline{r^2 q_\lambda'^2} \\
&+ 2 (\overline{q_\lambda q_\lambda' r'^2} + \overline{r q_\lambda'^2 r'}) \\
&+ \overline{q_\lambda'^2 r'^2} - \overline{q_\lambda' r'}^2
\end{aligned} \tag{5.17b}$$

It can be seen that the liquid water variance (a second-order correlation) involves third and fourth order correlations of the basic variable $q_\lambda = q - q_s$.

Since r itself can be directly expressed in terms of q_λ , it is not a new dependent variable of the flow; rather it is a function of the basic set (u_i, θ_v, q). Thus, the above moments can be expressed in terms of moments involving only the basic set. If the distribution function of the variables over the ensemble were known, this would then be a simple matter of formal calculation. We shall show how the partly cloudy correlations can be reduced to expressions involving only the fundamental set and certain coefficients which relate cross-correlations and variances of the partial cloudiness r with the fundamental variables. To proceed further to explicit forms for these coefficients, further information about the distribution functions must be specified. We have carried through the complete explicit evaluations of the coefficients and all correlations for the case of Gaussian distributions; we shall quote the results of the evaluations below.

We now consider the reduction of the new correlations involving r appearing in Eqs. (5.8)-(5.11) to expressions in terms of the fundamental set of variables (u_i, θ_v, q). For equilibrium systems, the quantity $q_\lambda \equiv q - q_s$ is central to these partly cloudy correlations. From Oliver, Lewellen, and Williamson¹², the fluctuation q_λ' may be expressed in terms of the fundamental set as

$$q_\lambda' = a q' - b \theta_v' \tag{5.18}$$

where

$$a \equiv 1 - \bar{\gamma}_q \beta_T \bar{q}_s \quad (5.19a)$$

$$b \equiv \bar{\gamma}_\theta \beta_T \bar{q}_s / T_r \quad (5.19b)$$

and

$$\bar{\gamma}_q = -0.61 + (\tilde{\mu}^{-1} + 0.61) \bar{r} \quad (5.20a)$$

$$\bar{\gamma}_\theta = 1 + (\tilde{\mu}^{-1} - 1) \bar{r} \quad (5.20b)$$

The correlations σ_{q_λ} and $\overline{\phi' q'_\lambda}$ can now be expressed in terms of the fundamental variables as

$$\sigma_{q_\lambda}^2 = \overline{q'_\lambda q'_\lambda} = a^2 \overline{q'^2} - 2ab \overline{q' \theta'_V} + b^2 \overline{\theta_V'^2} \quad (5.21)$$

$$\overline{\phi' q'_\lambda} = a \overline{q' \phi'} - b \overline{\theta_V' \phi'} \quad (5.22)$$

Let us define the coefficients $C(\phi)$ by the statement

$$\overline{\phi' r'} = C(\phi) (\sigma_r / \sigma_{q_\lambda}) \overline{\phi' q'_\lambda} \quad (5.23)$$

where $\sigma_r = (\overline{r' r'})^{1/2}$ is the cloudiness variance. Equation (5.23) is, in effect, the defining Equation for the coefficient $C(\phi)$. For variables ϕ , q_λ which are Gaussian, the coefficients $C(\phi)$ are unity.

We may then express the partly cloudy second-order correlations in terms of the fundamental variables (using Eqs. (5.22)-(5.23)) as

$$\overline{u_i' r'} = C(u_i) (\sigma_r / \sigma_{q_\lambda}) (a \overline{u_i' q'} - b \overline{u_i' \theta_V'}) \quad (5.24a)$$

$$\overline{\theta_V' r'} = C(\theta) (\sigma_r / \sigma_{q_\lambda}) (a \overline{q' \theta_V'} - b \overline{\theta_V'^2}) \quad (5.24b)$$

$$\overline{q'r'} = C(q) (\sigma_r/\sigma_{q_\lambda}) (a \overline{q'^2} - b \overline{q'\theta'_V}) \quad (5.24c)$$

The correlation σ_{q_λ} is given by Equation (5.21) in terms of the fundamental set. The representation of σ_r and the coefficients $C(\phi)$ require further information about the distribution function. We summarize the results for Gaussian variables here. The cloudiness state Q is defined as

$$Q = \overline{q_\lambda}/\sigma_{q_\lambda} \quad (5.25)$$

and represents the ratio of the mean saturation difference to the rms saturation difference. For $Q \rightarrow \infty$ the state must approach one of full cloudiness ($\overline{r} \rightarrow 1$) and vanishing fluctuations ($\sigma_r \rightarrow 0$). For $Q \rightarrow -\infty$ the state must be fully clear air ($\overline{r} \rightarrow 0$) with similarly vanishing fluctuations ($\sigma_r \rightarrow 0$). When $Q=0$ the mean flow is just at the saturation point and the fluctuations should be at a maximum ($\sigma_r \rightarrow \sigma_{rmax}$). For Gaussian distributions of any variable ϕ and the difference mixing ratio q_λ , it can be shown that

$$\overline{r} = \frac{1}{2} [1 + \text{Erf} (Q/\sqrt{2})] \quad (5.26)$$

$$\sigma_r = \frac{1}{\sqrt{2}} \exp (-Q^2/2) \quad (5.27)$$

$$C(\phi) \equiv 1 \quad (5.28)$$

Hence the cloud state Q is determined by the fundamental mean and second-order variables; and this single parameter in turn determines σ_r , \overline{r} , and $C(\phi)$. The cloudiness variables are thus closed in terms of the fundamental variables.

From Equation (5.24a) the cloud flux is represented in terms of the total moisture flux and heat flux as

$$\overline{w'r'} = C(w) (\sigma_r/\sigma_{q_\lambda}) (a \overline{w'q'} - b \overline{w'\theta'_V}) \quad (5.29)$$

The cloud flux represents the net flux resulting from partly cloudy updrafts and down drafts. When $\overline{w'q'}$ and $\overline{w'\theta'_v}$ have the same sense the cloud flux is diminished by the presence of heat flux due to warming which is positively correlated with moistening. When $\overline{w'\theta'_v}$ is opposite sense to $\overline{w'q'}$ the cloud flux is enhanced by the positive correlation of cooling with moistening.

Third-order correlations appearing in Eqs. (5.9)-(5.11) present more tasks in modeling. Following Donaldson (1973), we may possibly model these terms as gradient-driven diffusion of second-order correlations:

$$\overline{u'_i w' r'} = - v_r (\hat{q}\Lambda) \partial \overline{u'_i r'} / \partial z \quad (5.30a)$$

$$\overline{\theta'_v w' r'} = - v_r (\hat{q}\Lambda) \partial \overline{\theta' r'} / \partial z \quad (5.30b)$$

$$\overline{q' w' r'} = - v_r (\hat{q}\Lambda) \partial \overline{q' r'} / \partial z \quad (5.30c)$$

The diffusion coefficient v_r may be taken as equal to v_c the general diffusion coefficient in the second-order closure system. However, we also recognize that this simple approach may not be adequate for intermittent turbulent flows.

Turbulence Closure Theory on an Intermittent Turbulence Field

The modeling procedure and modeling coefficients developed for second-order closure theory rest on the assumption that the smallest resolvable regions of the flow field under consideration are fully turbulent (or fully laminar). In large scale meteorological models, a conditionally unstable atmospheric flow is often in a quite different state. It may be composed mostly of stable regions of vanishingly small turbulence which co-exist with a small fraction of highly turbulent zones. We believe that second-order modeling can quite accurately describe the kinds of turbulent features present in these turbulent zones such as plumes and jets, penetrating downdrafts, and gust fronts if the detailed structure of these features is resolved. On the other hand, if we choose to resolve only the large scale flow which consists at any instant of a small fraction of turbulent zones

embedded in fluid which is otherwise weakly turbulent, we must describe such a field by introducing an intermittency function ω^2 . There are a variety of ways of defining the intermittency; however, we shall use a simple partition definition. Let Ω denote a volume of flow which is small compared to the large scale gradients of interest yet contains a number of disturbed zones within it. Let Ω_d denote the fraction of Ω which contains the disturbed regions, while $(\Omega - \Omega_d)$ denotes the undisturbed portion. The intermittency ω^2 is then defined as

$$\omega^2 = \Omega_d / \Omega \quad (5.31)$$

In this preliminary investigation we shall temporarily set aside the mean velocity field effects and illustrate what amounts to the free convection limit. The mean velocity and corresponding shearing production effects can later be incorporated with the same methodology.

The governing equations of the large scale variables are the equations for the virtual potential temperature and water mixing ratio with the partly cloudy correlations presented in Part 5.

$$D\bar{\theta}_v/Dt = - \overline{\partial w' \theta'_v / \partial z} + \beta \Gamma (\overline{r w' + r' w'}) + \bar{\Sigma} \quad (5.32)$$

$$D\bar{q}/Dt = - \overline{\partial w' q' / \partial z} - \bar{C} \quad (5.33)$$

In the above \bar{C} is the mean precipitation rate and $\bar{\Sigma}$ contains the effects of radiative transport as well as precipitation.

Because of intermittency, the second-order closure system described in Part 2 must be modified to describe the large scale correlations $\overline{w' \theta'_v}$, $\overline{w' r'}$, $\overline{w' q'}$. We assume, however, that in the disturbed regions of fraction ω^2 , turbulent correlations may be defined which are governed by the usual second-order closure equations. Let $(\quad)_d$ denote an average for the disturbed regions. The usual second-order equations, assumed descriptive of these disturbed regions, are then of the typical form

$$\begin{aligned}
D(\overline{w'\theta'_v})_d/Dt = & - (\overline{w'w'})_d (\partial\overline{\theta_w}/\partial z)_d + g/T_r(\overline{\theta'^2})_d - \underline{0.75(\hat{q}_d/\Lambda)(\overline{w'\theta'})_d} \\
& + \underline{0.3 \hat{q}_d \Lambda \partial(\overline{w'\theta'})_d/\partial z} + \beta\Gamma(\overline{w'w'r'} + \underline{w'w'r'})_d + (\overline{\Sigma'w'})_d \quad (5.34)
\end{aligned}$$

Since we assume the turbulence is negligible in the fraction $(1-\omega^2)$ of the flow field, the large scale higher-order correlations ($\overline{\quad}$) may be related to the disturbed region correlations ($\overline{\quad}$)_d as

$$(\overline{\quad}) = \omega^2(\overline{\quad})_d \quad (5.35)$$

and for the rms quantities,

$$\hat{q} = \omega\hat{q}_d \quad (5.36a)$$

$$\sigma_r = \omega(\sigma_r)_d \quad (5.36b)$$

$$\sigma_{q_\lambda} = \omega(\sigma_{q_\lambda})_d \quad (5.36c)$$

The large scale mean cloudiness is given by

$$\overline{r} = \omega^2(\overline{r})_d + (1-\omega^2)(\overline{r})_e \quad (5.37)$$

where $(\overline{r})_e$ is the environmental region cloudiness of fraction $(1-\omega^2)$.

Let us now summarize the developments required to apply the second-order closure system to partly cloudy and possibly intermittent flows. The first development concerns the dissipation and conventional triple correlation (diffusion) terms which are indicated by a single underline in Equation (5.34). We expect that the characteristic velocity \hat{q} in these modeled terms should be based on the average turbulent velocity in the turbulent region rather than on the average over the larger scale region. Consistent with Equation (5.36a), it therefore appears that one of the principal modifications required in the system of equations to make them

applicable to an intermittent flow is to divide the single underlined terms by ω so that these modeled terms are now based on the appropriate characteristic velocity. Thus, the large scale second-order correlation equations in intermittent flow may be expected to be modeled as

$$D\hat{q}^2/Dt = g/\bar{T}r_r \overline{w'\theta'_v} - \omega^{-1}(\hat{q}/4\Lambda)\hat{q}^2 + \omega^{-1}0.3\hat{q}\Lambda\partial\hat{q}^2/\partial z)/\partial z \quad (5.38)$$

$$\begin{aligned} D(\overline{\theta_v'^2})/Dt = & - \overline{w'\theta'_v} (\partial\bar{\theta}_v/\partial z - \beta\bar{\Gamma}r) + 0.3\omega^{-1} \partial\hat{q}\Lambda\overline{\theta_v'^2}/\partial z \\ & - \omega^{-1}0.45\hat{q}/\Lambda(\overline{\theta_v'^2}) + \beta\bar{\Gamma}(\overline{w'\theta'_vr'} + \underline{\underline{\overline{w'\theta'_vr'}}}) + (\underline{\underline{\overline{\Sigma'\theta'_v}}}) \end{aligned} \quad (5.39)$$

$$\begin{aligned} D\overline{w'q'}/Dt = & - \overline{w'w'}\partial\bar{q}/\partial z + (g/\bar{T}r_r) \overline{q'\theta'_v} + 0.3\omega^{-1} \partial\hat{q}\Lambda\overline{w'q'}/\partial z \\ & - 0.75\omega^{-1}(\hat{q}/\Lambda)\overline{w'q'} \end{aligned} \quad (5.40)$$

$$\begin{aligned} D\overline{w'\theta'_v}/Dt = & - \overline{w'w'} \partial\bar{\theta}_w/\partial z + (g/\bar{T}r_r)\overline{\theta_v'^2} - 0.75 \omega^{-1}(\hat{q}/\Lambda)\overline{w'\theta'_v} \\ & + 0.3 \omega^{-1} \partial(\hat{q}\Lambda\overline{w'\theta'_v})/\partial z + \beta\bar{\Gamma}(\underline{\underline{\overline{w'w'r'}}} + \overline{w'w'r'}) + \underline{\underline{\overline{\Sigma'w'}}} \end{aligned} \quad (5.41)$$

$$\begin{aligned} D(\overline{q'\theta'_v})/Dt = & - (\overline{w'q'})((\partial\bar{\theta}_v/\partial z) - \beta\bar{\Gamma}r) - (\overline{w'\theta'_v})(\partial\bar{q}/\partial z) \\ & + 0.3\omega^{-1}\partial\hat{q}\Lambda\overline{q'\theta'_v}/\partial z)/\partial z \\ & - 0.45\omega^{-1}(\hat{q}/\Lambda)\overline{q'\theta'_v} + \beta\bar{\Gamma}w \overline{q'r'} + \underline{\underline{\overline{w'q'r'}}} + \underline{\underline{\overline{\Sigma'q'}}} \end{aligned} \quad (5.42)$$

$$D(\overline{q'^2})/Dt = -(\overline{w'w'})_d(\partial\bar{q}/\partial z)_d - 0.45\omega^{-1}(\hat{q}/\Lambda)\overline{q'^2}$$

$$+ 0.3\omega^{-1}\partial(\hat{q}\Lambda\overline{q'^2}/\partial z)/\partial z \quad (5.43)$$

New modeling may be required for the doubly underlined terms which are triple correlations involving cloud fluctuations. In strongly intermittent flow, the gradient-driven modeling previously given may well be inadequate for these terms. It is possible that in such flows a model of the form

$$\overline{w'\phi'r'} = a_r\omega^{-1}\sigma_r \overline{w'\phi'} \quad (5.44)$$

(where a_r is an order unity modeling constant) may be appropriate. Such a form has the correct limiting behavior in that it vanishes in clear air or stratus situations when $\sigma_r \rightarrow 0$ and in strongly intermittent flow it has the property

$$\overline{w'\phi'r'} \sim \overline{w'\phi'}$$

since $(\sigma_r)_d \sim 1$ and thus $\omega^{-1}\sigma_r \sim 1$ in strongly intermittent flow, as indicated by Equation (5.36b). Another possibility is that some more global integral type model may be more appropriate for these terms.

The third development required is a theory of closure for the intermittency ω^2 itself. In our discussion up to this point we have utilized the intermittency ω^2 simply to distinguish the disturbed regions from the undisturbed regions. We now present the conditions which determine ω^2 . For absolutely unstable flows in which

$$\overline{\partial\theta_w/\partial z} < 0 \quad (5.45)$$

the flow is non-intermittent and we set $\omega \equiv 1$ for such flows.

For flows which are conditionally stable, we have

$$0 < \overline{\partial\theta_w/\partial z} < (1-\overline{r})\beta\Gamma \quad (5.46a)$$

$$\overline{r} < 1 \quad (5.46b)$$

For conditionally unstable flow we offer the following tentative closure for the intermittency. Convection is induced by the condensation of moisture. Thus, the convectively active zones are necessarily the cloudy zones. As the mean cloudiness declines, a point is reached in which the partly cloudy updrafts and downdrafts cannot fill the whole space and a bifurcation into disturbed and undisturbed regions occurs.

In the conditionally unstable regime, the flow will be unstable to vanishingly small disturbances for all $\bar{q}_\lambda > 0$. At $\bar{q}_\lambda = 0$, the stability is neutral. We postulate that this neutral stability point is also the point of bifurcation into disturbed and undisturbed regions. For $\bar{q}_\lambda < 0$ and $\partial\bar{\theta}_w/\partial z$ satisfying Equation (5.46a) the flow is intermittent with $(\bar{q}_\lambda)_e < 0$ in the undisturbed regions. We postulate that in this intermittent regime $(\bar{q}_\lambda)_d$ remains at the level of the flow at the bifurcation point; thus

$$(\bar{q}_\lambda)_d = 0, \text{ when } \bar{q}_\lambda < 0 \quad (5.47)$$

That is, the disturbed or cloudy region should be characterized by a mean moisture level which is approximately equal to the local saturation level. From Equation 5.26 it then follows that

$$\bar{r}_d = \frac{1}{2}, \quad \sigma_{r_d} = \frac{1}{\sqrt{2}} \quad (5.48)$$

consistent with identifying the cloudy regions with the disturbed regions we must take the undisturbed zones as cloud free. Then from Eqs. (5.36), (5.37) and (5.48)

$$\bar{r} = \omega^2/2, \quad \sigma_r = \frac{\omega}{\sqrt{2}} \quad (5.49)$$

Closure may now be completed by recognizing that some fraction of the humidity fluctuations in the disturbed region must be of sufficient magnitude to exceed the amount by which the environmental humidity departs from the saturated area. Thus

$$(\sigma_{q_\lambda})_d = -c_0 (q_\lambda)_e \quad (5.50)$$

where c_0 now becomes a modeling coefficient determined by what fraction of the fluctuations are assumed to exceed $-(q_\lambda)_e$. If this is set at the 5% level then our assumption of a Gaussian distribution in the disturbed region would give $c_0 = 0.6$. As long as c_0 is assumed, Eqs. (5.36c) and (5.50) then determine the intermittency

$$\omega = \sigma_{q_\lambda} / (\sigma_{q_\lambda})_d = -(\sigma_{q_\lambda} / c_0 \bar{q}_\lambda) (1-\omega^2) \quad (5.51)$$

where we have used $(\bar{q}_\lambda)_e = \bar{q}_\lambda / (1-\omega^2)$.

The system of equations is now complete with the mean variables determined by Eqs. (5.32) and (5.33). The second-order correlations of the mean variables are determined by Eqs. 5.38 to 5.43; the cloud flux term $\overline{w'r'}$ by Equation 5.29; \bar{r} and σ_r by Equation 5.49; σ_{q_λ} by Equation 5.21 and finally ω by Equation 5.51.

For application to the problem of sub-grid cumulus description (cumulus parameterization), we would expect to develop simplified approximate solutions to this set. Some of the simplifications which may be possible include the approximations of quasi-equilibrium, super-equilibrium, or self-similarity. The most appropriate approximations for cumulus parameterization remain to be determined. It is important to note that the only inputs to the turbulence equations are the large scale mean fields and the input fluxes at the cloud base (or the full boundary layer may be solved concurrently). From these inputs the cloud flux $\overline{w'r'}$ should emerge naturally yielding the heating rate distribution.

Data Comparisons

To examine the consistency of this modeling procedure, we make some order of magnitude analyses with an actual data set. The data set chosen is that for the Gate B Scale Array (Thompson et al.³⁹). Selected observations from this data set are tabulated in Table 1.

TABLE 1. SELECTED DATA FROM THE GATE B SCALE ARRAY
(Thompson et al.³⁹)

$(\overline{w'q'})_0$	(from precipitation)	1.4×10^{-4} m/s
h	region of conditional stability (950 mb to 185 mb)	10^4 m
$\overline{\partial q / \partial z}$	(characteristic moisture gradient in mid portion of layer ($\sim h/2$))	-1.8×10^{-6} m ⁻¹
$\overline{\partial \theta_v / \partial z}$	(characteristic buoyancy gradient in mid portion of layer ($\sim h/2$))	+ 0.0035 °C/m
τ_c^{-1}	Low Level Convergence and Evaporation Rate	7.5×10^{-6} s ⁻¹
$\beta \Gamma$	(in mid portion of layer $\sim h/2$)	0.0040 °C/m
$\overline{q_\lambda}$		-0.002
Average observed heating rate by cumulus convection		5°C/day

Although the cloudiness \overline{r} is not measured, it is observed to be small. From Table 1 it can therefore be seen that the system is conditionally stable, since $\beta \Gamma > \overline{\partial \theta_v / \partial z} > 0$. Since the latent heat release is important in conditionally stable systems, the buoyancy flux is determined principally by moisture flux. Let $(\overline{w'q'})_0$ be the characteristic moisture flux. The characteristic buoyancy is then $(\overline{w'\theta'_v})_0 \sim (L/C_p)(\overline{w'q'})_0$. From the turbulence

kinetic energy Equation (5.38), we have in super-equilibrium

$$\omega^{-1} \hat{q}^3 / \Lambda \sim (g/T_r) \overline{w'\theta'_v}; \quad (5.52)$$

hence we may construct a characteristic velocity scale w_+ as

$$w_+^3 = (g/T_r)(L/C_p) \overline{(w'q')}_0 \omega h \quad (5.53)$$

where h is the thickness of the conditionally stable region.

The characteristic scale of the moisture fluctuation, q_+ , is defined as

$$q_+ = \overline{(w'q')}_0 / w_+ \quad (5.54)$$

Then from Equation 5.51

$$\omega = - \frac{\overline{\sigma q}_\lambda}{0.6 \overline{q}_\lambda} = - \frac{q_+}{0.6 \overline{q}_\lambda} \quad (5.55)$$

$$\omega^{4/3} = - \frac{\overline{(w'q')}_0^{2/3}}{0.6 \overline{q}_\lambda \left(\frac{g}{T_r} \frac{Lh}{c_p} \right)^{1/3}} \quad (5.56)$$

For the data values given in Table 1, we find

$$\omega^{-1/3} w_+ = 4.9 \text{ m/s}$$

$$\omega^{1/3} q_+ = 0.29 \times 10^{-4} \text{ m/s}$$

$$\omega = 0.06$$

$$w_+ = 1.9 \text{ m/s}$$

$$q_+ = 0.7 \times 10^{-4}$$

$$\bar{r} = 1.9 \times 10^{-3}$$

$$\sigma_r = 0.024$$

The value of mean cloudiness for this data set seems a bit low; however, the cloudiness variance is of the order of 2%.

If the cumulus flux is approximated from the leading term of Equation (5.29) as

$$\overline{w'r'} \sim a(\sigma_r/\sigma_{q_\lambda}) \frac{(\overline{w'q'})_0}{2}$$

With $a \sim 1$ and the above values, we obtain $\overline{w'r'} \approx 0.02$ and the cumulus heating rate is then

$$\beta \Gamma \overline{w'r'} = 8^\circ\text{C/day}$$

which is as close to the observed heating rate as we should expect for the current rough approximations.

As an independent check of the intermittency, we may calculate the moisture-flux in mid layer from super equilibrium using the observed moisture gradient and compare it with the precipitation derived value $(\overline{w'q'})_0$. In super-equilibrium

$$\overline{w'q'} \sim -\hat{q}\Lambda \frac{\partial \bar{q}}{\partial z}$$

with $\Lambda = 10^3 \text{m}$, $\hat{q} \sim w_+ \sim 1.9$, and $\partial \bar{q} / \partial z \sim 2 \times 10^{-6} \text{ m}^{-1}$ we find

$$\overline{w'q'} \sim 1.8 \times 10^{-4} \text{ m/s}$$

which corresponds with the observed 1.4×10^{-4} m/s surface value.

Although we have not yet used this set in a predictive model, this exercise does indicate, at least, an order of magnitude consistency for this new set of equations.

We believe that this is a promising approach to the problem of cumulus parameterization. This is particularly true for mesoscale models, for which the Arakawa and Schubert scheme, most favored for global models, would have difficulty in regions where the intermittency is not much less than one.

6. CONCLUDING REMARKS

We believe that the results of the Calspan fog simulations are as accurate as should be expected for a one-dimensional simulation of what may generally be expected to be a three-dimensional phenomenon. Further, substantial improvements in modeling the atmospheric boundary layer in the marine environment appear to require addressing directly the problem of three dimensionality. This is particularly true of the coastal regions which are vital to the Navy's interests. We have the choice of either developing a complete unsteady, three-dimensional version of our second-order closure model, or using the existing one- and two-dimensional versions of our model to develop appropriate turbulent flux parameterization schemes which may be used to adequately specify the sub-grid processes in three-dimensional, regional meteorological models developed by others. As discussed in Chapter IV, we believe the latter approach is preferable at the present time, because it should permit our model developments to have an earlier impact on operational models.

The grid resolution in any mesoscale meteorological model will never be adequate to completely resolve the turbulent transport processes of importance in the troposphere. Thus, accuracy of the physical mechanisms which are controlled by turbulence will depend on how faithfully the sub-grid parameterization can simulate these processes. Our second-order closure model of turbulent transport in the atmosphere provides two ways of developing this parameterization. First, there are the dynamic equations for the second-order flux quantities of interest, which may be approximated in some fashion. Second, our existing one- and two-dimensional models of the atmospheric boundary layer may be run with relatively fine resolution to test the accuracy of any tentative parameterization schemes.

In order to investigate how well a candidate parameterization scheme may be integrated into a mesoscale model, we expect to use the three-dimensional Navier-Stokes model which Dr. Sykes has currently running on A.R.A.P.'s computer. This model currently exists in two forms: as a model of the full Navier-Stokes equations in cartesian coordinates as used by Mason and Sykes⁴⁰ and as a hydrostatic model in a terrain-following coordinate system as proposed by Clark⁴¹. This model should serve as a test vehicle to determine

the relative merits of increasingly complex parameterization schemes.

Some of the most important turbulent transport processes in the lower troposphere involve clouds. Therefore, in order for any sub-grid flux parameterization scheme to be very successful on the mesoscale level, it must incorporate some of the essential elements of cloud dynamics. As discussed in Chapter V, we have reviewed the cumulus parameterization schemes proposed by Arakawa and Schubert³⁶ and Kuo³⁸. It appears that the Arakawa and Schubert model which has found some success in global models would require extensive modifications to be used at the mesoscale level. On the other hand, we believe our second-order closure approach can provide a more realistic representation than the Kuo model which is much simpler than that of Arakawa and Schubert.

7. REFERENCES

1. Lewellen, W.S. (1981): "Modeling the Lowest 1 Km of the Atmosphere," AGARDograph No. 267, North Atlantic Treaty Organization.
2. Lewellen, W.S., D.A. Oliver, and R.I. Sykes (1982): "Final report on A.R.A.P.'s Model for the Atmospheric Marine Environment," NEPRF Contractor Report CR 82-02.
3. Donaldson, Coleman duP.: "Construction of a Dynamic Model of the Production of Atmospheric Turbulence and the Dispersal of Atmospheric Pollutants," in Workshop on Micrometeorology, pp. 313-392.
4. Lewellen, W.S. (1977): "Use of Invariant Modeling," in Handbook of Turbulence, edited by W. Frost, Plenum Press, pp. 237-290.
5. Lewellen, W.S. and M.E. Teske (1973): "Predictions of the Monin-Obukhov Similarity Functions," J. Atmos. Sciences, 30, pp. 1340-1345.
6. Lewellen, W.S., M.E. Teske, and Coleman duP. Donaldson (1974): "Turbulence Model of Diurnal Variations in the Planetary Boundary Layer," Proc. 1974 Heat Transfer and Fluid Mechanics Institute (L.R. Davis & R.E. Wilson, Eds.), Stanford University Press, pp. 301-319.
7. Lewellen, W.S., M.E. Teske, and Coleman duP. Donaldson (1976): "Examples of Variable Density Flows Computed by a Second-Order Closure Description of Turbulence," AIAA J., 14, 3, pp. 382-387.
8. Lewellen, W.S. and M.E. Teske (1976): "Second-Order Closure Modeling of Diffusion in the Atmospheric Boundary Layer," Boundary Layer Meteor. J., 10, pp. 69-90.
9. Lewellen, W.S. and M.E. Teske (1975): "Development of a Low-Level Atmospheric Turbulence Model for Marine Environments," A.R.A.P. Report No. 255.
10. Lewellen, W.S., D.A. Oliver, M.E. Teske, and G.G. Williamson (1976): "Status Report on a Low-Level Atmospheric Turbulence Model for Marine Environment," A.R.A.P. Report No. 289.
11. Lewellen, W.S. and M.E. Teske (1976): "A Second-Order Closure Model of Turbulent Transport in the Coastal Planetary Boundary Layer," Presented at Conference on Coastal Meteorology, Virginia Beach, Virginia.
12. Oliver, D.A., W.S. Lewellen and G.G. Williamson (1978): "The Interaction Between Turbulent and Radiative Transport in the Development of Fog and Low-Level Stratus," J. Atmos. Sci., 35, pp. 301-316.
13. Lewellen, W.S., D.A. Oliver, M.E. Teske, H. Segur, and O. Cote (1977): "1977 Status Report on Low-Level, Atmospheric Turbulence Model for Marine Environments," A.R.A.P. Report No. 320.

14. Lewellen, W.S., M.E. Teske, D.A. Oliver, Y.P. Sheng, and H. Segur (1979): "1979 Status Report on Low-Level, Atmospheric Turbulence Model for Marine Environments," A.R.A.P. Report No. 385.
15. Teske, M.E. and W.S. Lewellen (1979): "Horizontal Roll Vortices in the Planetary Boundary Layer," Presented at the AMS Fourth Symposium on Turbulence, Diffusion, and Air Pollution, Reno, Nevada.
16. Lewellen, W.S., M.E. Teske, and Y.P. Sheng (1980): "Micrometeorological Applications of a Second-Order Closure Model of Turbulent Transport," Turbulent Shear Flows 2 (Selected papers from the Second International Symposium on Turbulent Shear Flows, Imperial College, London, July 2-4, 1979), Springer-Verlag, pp. 366-378.
17. Lewellen, W.S., D.A. Oliver, R.D. Sullivan and G. Sandri (1980): "1980 Status Report on Low-Level, Atmospheric Turbulence Model for Marine Environments," A.R.A.P. Report No. 420.
18. Lewellen, W.S. (1979): "Transport of Water Vapor through the Atmospheric Boundary Layer," Atmospheric Water Vapor, (Selected papers from the Proceedings of the International Workshop on Atmospheric Water Vapor, Vail, Colorado, September 11-13, 1979), Academic Press, pp. 527-550.
19. Sykes, R.I. and W.S. Lewellen (1982): "A Numerical Study of Breaking Kelvin-Helmholtz Billows Using a Reynolds-Stress Turbulence Closure Model," J. Atmos. Sci., 39, 7, pp. 1506-1520.
20. Carson, D.J. (1973) "The Development of a Dry, Inversion-Capped, Convectively Unstable Boundary Layer," Quart. J. Roy. Met. Soc., 99, pp. 450-467.
21. Stull, R.B. (1973) "Inversion Rise Model Based on Penetration Convection," J. Atmos. Sci., 30, pp. 1092-1099.
22. Hazel, P. (1972) "Numerical Studies of the Stability of Universal Stratified Shear Flow," J. Fluid Mech., 51, pp. 39-61.
23. Hanjalic, K. and B.E. Launder (1972): "A Reynolds Stress Model of Turbulence and Its Application to Thin Shear Flows," J. Fluid Mech., 52, 609-638.
24. Lumley, J.L. and B. Khajeh-Nouri (1974): "Computational Modeling of Turbulent Transport," Advances in Geophysics, Vol. 18A, Academic Press, New York, 169-192.
25. Gibson, M. and B.E. Launder (1978): "Ground Effects on Pressure Fluctuations in the Atmospheric Boundary Layer," J. Fluid Mech., 86, 491-511.
26. Launder, B.E. (1975): "On the effects of a gravitational field on the turbulent transport of heat and momentum," J. Fluid Mech., 67, 569-581.

27. Launder, B.E., G.J. Reece, and W. Rodi (1975): "Progress in the Development of a Reynolds-Stress Turbulence Closure," *J. Fluid Mech.*, 68, 537-566.
28. Stull, R.B. (1976) "The Energetics of Entrainment Across a Density Interface," *J. Atmos. Sci.*, pp. 1260-1267.
29. Lavoie, R.L. (1972): "A mesoscale numerical model of the lake-effect storms," *J. Atmos. Sciences*, 29, 1025-1040.
30. Keyser, D., and R.A. Anthes (1977): "The applicability of a mixed-layer model of the planetary boundary layer to real-data forecasting," *Monthly Weather Review*, 105, 1321-1351.
31. Warner, T.T., R.A. Anthes and A.L. McNab (1978): "Numerical simulations with a three-dimensional mesoscale model," *Monthly Weather Review*, 106, 1079-1099.
32. Anthes, R.A., N.L. Seaman and T.T. Warner (1980): "Comparisons of numerical simulation of the planetary boundary layer by a mixed-layer and a multi-level model," *Monthly Weather Review*, 108, 365-376.
33. Anthes, R.A., D. Keyser and J.W. Deardorff (1982): "Further considerations on Modeling the Sea Breeze with a Mixed-Layer Model," *Monthly Weather Review*, 110, 757-765.
34. Schlichting, H. (1968): Boundary Layer Theory, McGraw-Hill Book Company.
35. Pielke, R.A. (1974): "A comparison of three-dimensional and two-dimensional numerical predictions of sea breezes," *J. Atmos. Sciences*, 31, 1577-1585.
36. Arakawa, A. and Schubert, W.H. (1974), "Interaction of a Cumulus Cloud Ensemble with the Large-Scale Environment, Part I," *J. Atmos. Sci.*, 31, 674-701.
37. Lord, S.J. (1982), "Interaction of a Cumulus Cloud Ensemble with the Large-Scale Environment. Part III: Semi-Prognostic Test of the Arakawa-Schubert Cumulus Parameterization," *J. Atmos. Sci.*, 39, 88-103.
38. Kuo, H.L. (1974), "Further Studies of the Parameterization of the Influence of Cumulus Convection on Large-Scale Flow," *J. Atmos. Sci.*, 31, 1232-1240.
39. Thompson, R.M. Jr., Payne, S.W., Recker, E.E., and Reed, R.J. (1979), "Structure and Properties of Synoptic-Scale Wave Disturbances in the Intertropical Convergence Zone of the Eastern Atlantic," *J. Atmos. Sci.*, 36, 53-75.
40. Mason, P.J. and R.I. Sykes (1979): "Three-dimensional numerical integrations of the Navier-Stokes equations for flow over surface-mounted obstacles," *J. Fluid Mech.*, 91, pp. 433-450.

41. Clark, T.L. (1977): "A Small-Scale Dynamic Model Using a Terrain-Following Coordinate Transformation," *Journal of Computational Physics*, 24, pp. 186-215.
42. Stephens, G.L. (1978): "Radiation profiles in extended water clouds. I: Theory," *J. Atmos. Sci.*, 35, pp. 2111-2122.

APPENDIX A
MODELING THE ROLE OF TURBULENCE IN CLOUD MICROPHYSICS

INTRODUCTION

In this work we present a model of cloud and warm precipitation which is naturally coupled to the turbulence of the atmosphere in which clouds reside. Models of precipitation previously developed have been constructed for specific cloud and storm systems (Kessler, 1969; Wilhelmson and Klemp, 1981; Orville and Chen, 1982) and take no mechanistic account of the effects of turbulence. In the present work we explicitly describe certain of the actions of turbulence upon the growth processes of cloud droplets. These include the effects of turbulence-induced shear and acceleration fields on the droplet coagulation.

In Part 2 we review the stages of condensation, cloud droplet spectrum evolution, and precipitation; and we point out the role of turbulence in the various microphysical processes. In Part 3 we present a microphysical closure model which reduces the integro-differential kinetic equation describing the droplet population to a tractable form which explicitly incorporates the effects of turbulence described in Part 2. In Part 4 we develop the turbulent ensemble average forms of the cloud and precipitation equations and the second-order correlation variables according to the methodology of higher order closure theory. A particular development of the ensemble average is required for description of the turbulent motion of the cloud and precipitation drops in the turbulent cascade and the corresponding ensemble average of droplet functions. In Part 5 we illustrate some of the properties of the model for homogeneous clouds.

CLOUD FORMATION, EVOLUTION, AND PRECIPITATION

To set the stage for the microphysical closure we shall develop, we first review the various processes which take place from the onset of a water mixing ratio in excess of the saturation value to the final stage (if it occurs in the time scale of a particular macro-event) in which drops precipitate to the surface. We are particularly interested in the role of turbulence in these various stages of development. The stages of drop evolution may be defined in the scheme of Table A1.

Once the water mixing ratio exceeds the local saturation value, nuclei must be activated before water may condense in realistic time scales. Following nuclei activation, drops grow by the direct condensation of vapor and are collisionally coupled only through Brownian motion. In most atmospheric situations the liquid water formed by the overall amount of excess mixing ratio over the saturation value and the number of nuclei available and activated results in a cloud with drop number densities ranging from 10^7 - 10^9 m^{-3} and radii ranging from 1 to 10 μm .

A particular feature of the growth of cloud droplets and the evolution of the spectrum is the creation of a small number of drops much larger than the average. This tail effect in the distribution function is intensified by the large collision cross-section of large drops. The mechanism by which droplets grow significantly beyond the range of radii $< 10\mu m$ up to precipitation sizes in excess of 100 μm is still an outstanding unresolved problem. One class of mechanism is collisional. Since Brownian collisional rates are much too small for significant collisions over characteristic macro time scales for this size range of droplet, gravitational sedimentation has long been identified as a collisional coalescence mechanism of atmospheric clouds, (Berry, 1967; Warshaw, 1967; Twomey, 1966). There seems little doubt that the collisional coalescence of droplets of different size by gravitational sedimentation is an important droplet growth mechanism at some stage of cloud evolution.

TABLE A1. STAGES OF CLOUD DROPLET SPECTRUM FORMATION AND EVOLUTION

(1)	The Nuclei Activation Stage	
	drop (nucleus) size	$10^{-2} \mu\text{m} - 1 \mu\text{m}$
	response time scale	1-10 sec
(2)	The Condensation Growth Stage	
	drop size	$1 \mu\text{m} - 20 \mu\text{m}$
	response time scale	10 sec
(3)	The Collisional Growth Stage	
	drop size	$10 \mu\text{m} - 10^{-3} \mu\text{m}$
	time scale	$10^2 - 10^4 \text{ sec}$
(4)	The Sedimentation Stage	
	drop size	$50 \mu\text{m} - 10^{-3} \mu\text{m}$
	time scale	0.1 - 1 hr

On the other hand, in the early stages of growth (radii from 5-30 μm) this mechanism possesses certain limitations. Two of these limitations are the inherent requirement of differential size for a non-zero collision rate and the sharply diminished collision efficiencies which result for the low Reynolds numbers of droplet sedimentation in the range of sizes from 5 to 30 μm (Mason, 1971). These two limitations when viewed in the light of a further result from classical condensation theory - namely the narrowing of the droplet spectrum during condensation growth (Sedunov, 1974; Levin and Sedunov, 1966) - suggest that growth mechanisms other than gravitational sedimentation may play an important role in the growth of cloud droplets into precipitation size drops.

It would appear that atmospheric turbulence can play an important and direct role in the evolution of the cloud droplet spectrum through both collisional and non-collisional processes. The collisional processes include

the coagulation induced by turbulent shearing and acceleration fields (Saffman and Turner, 1955). The non-collisional processes involve modification of the droplet spectrum by either fluctuations or turbulent mixing of the humidity and temperature during condensation and evaporation. This latter effect has been studied in a statistical manner (Levin and Sedunov, 1966; Sedunov, 1974; Jeou Jong, 1966) and in simplified homogeneous cloud models (Bartlett and Jonas, 1971; Mason and Jonas, 1974; Baker, et al., 1980; Jonas and Mason, 1982). These studies, which are not without contradiction of one another, indicate that turbulent fluctuations of supersaturation in absence of mixing do not necessarily broaden the cloud droplet spectrum. On the other hand, turbulent entrainment of environmental air into cloud coupled with large scale growth and decay fluctuations on the scale of the lifetime of individual clouds do appear to appreciably broaden the droplet spectrum. Such non-collisional "turbulent" broadening of the spectrum would clearly augment the collisional processes which ultimately complete the evolution of cloud into precipitation size drops.

The final stages of drop evolution occur when drops have grown large enough to develop a significant sedimentation velocity. These precipitable drops then leave the cloud and progress to the surface where they leave the atmosphere. Turbulence may often play a significant role at this stage. We shall show that under most atmospheric conditions, drops as large as 1000 μm are still strongly correlated with the largest turbulent eddies. Turbulent contributions to the sedimentation flux of precipitation must therefore be included in the construction of the total flux of water drops which reach the surface. In general, the turbulent flux can either oppose or augment the sedimentation flux and lead to a diminishment or enhancement of the net flux.

On the basis of the time scales presented in Table A1, we may regard the small size spectrum dynamics (nuclei activation and condensation - evaporation rates in the elementary spectrum) as occurring instantaneously on the time scale of turbulence. Correspondingly, the collisional growth and precipitation evaporation time constants are often much greater than the turbulence time scale. We shall use this difference in time scales in the construction of an approximate description of the microphysical processes and in simplifying the turbulent ensemble equations.

DESCRIPTION OF CLOUD AND PRECIPITATION

Cloud and Precipitation Moment Equations

Instead of considering the detail of the entire droplet spectrum, we divide the spectrum into two groups: cloud, consisting of small droplets which do not precipitate, and precipitation, consisting of large droplets which possess a sedimentation flux.

The choice of the spectrum dividing volume v_{p0} which separates cloud drops from precipitation must be made on the basis of two principal constraints. The first is that v_{p0} lie in the tail region of the elementary spectrum (i.e., the spectrum before collisional processes become active) thus we require $v_{p0} > \sigma_c v_0$, where v_0 is the average elementary volume and σ_c is the dispersion of the cloud elementary spectrum. Second, since the small droplets have negligible sedimentation velocities (over macro time scales) we do not specify the precipitation flux as an average over the entire liquid water distribution. Rather, it is more appropriate to define the precipitation group as those droplets with sedimentation velocities greater than a certain minimum value. This minimum value is determined by the overall macro-dynamics. This sedimentation velocity is selected so that a drop will fall over a characteristic macro-length in some characteristic macro-time. For example, for cloud with a length scale of the order of 1 km or less and precipitation on a time scale of the order of 1 hour or less, the minimum precipitation velocity, v_{p0} should be of the order of 10-100 m/hr which corresponds to the sedimentation velocity of a droplet of approximately 20-30 μm radius.

Since the elementary drop size lies in the range of 4-10 μm for most clouds, it appears that the rule of thumb $v_{p0}/v_0 \approx 10-20$ may be adequate for most situations yielding a spectrum dividing volume outside the bulk of the elementary cloud distribution, yet not being so great that a significant portion of the smallest precipitation drops are inadequately represented nor that the bulk of the cloud spectrum becomes included in the precipitation portion of the spectrum.

The number, mass, and size relationships within the cloud and precipitation are then as follows. Let v_0 be the smallest droplet volume of interest. Let $m=(v/v_0)$ be a size specification parameter based upon droplet volume and hence proportional to liquid mass. The spectrum dividing size parameter is $m_{p0}=(v_{p0}/v_0)$. We denote the number density of cloud drops of size m as $\hat{n}_c(m)$ and of precipitation drops as $\hat{n}_p(m)$. The cloud and precipitation distribution functions $f_c(m)$, $f_p(m)$ are then defined as

$$f_c(m) = \hat{n}_c(m)/n_c \quad 1 \leq m \leq m_{p0} \quad (\text{A.1})$$

$$f_p(m) = \hat{n}_p(m)/n_c \quad m_{p0} \leq m \quad (\text{A.2})$$

where n_c and n_p are the total number densities of cloud and precipitation, respectively (Figure A1). The distribution functions thus satisfy the normalization conditions

$$\sum_{m=1}^{m_{p0}-1} f_c(m) = 1 \quad (\text{A.3a})$$

$$\sum_{m=m_{p0}}^{\infty} f_p(m) = 1 \quad (\text{A.3b})$$

The mixing ratio of cloud q_c and precipitation q_p are given by

$$q_c = (\rho_0/\rho_\infty)v_0 n_c m_c \quad (\text{A.4a})$$

$$q_p = (\rho_0/\rho_\infty)v_0 n_p m_p \quad (\text{A.4b})$$

where the liquid water density is ρ_0 , the density of the air-cloud mixture is ρ_∞ and m_c , m_p are the average sizes of cloud and precipitation:

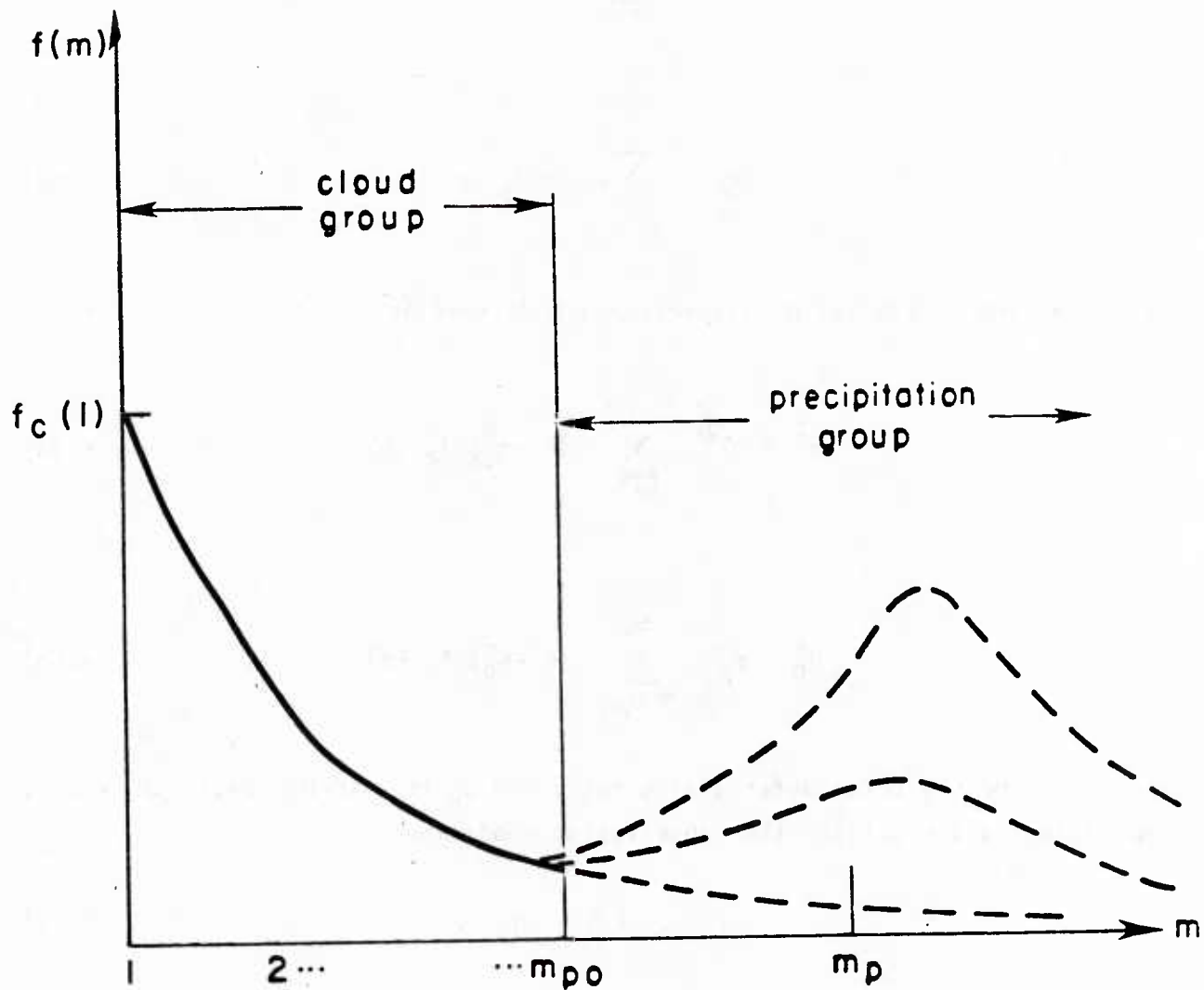


Figure A.1 Schematic of liquid drop distribution and cloud and precipitation groups. Source droplets exist at size $m=1$. The cloud group spans the range $1 < m < m_{p0}$. Bi-modality, when it occurs, occurs with the second mode in the precipitation group.

$$m_c = \sum_{m=1}^{m_{p0}-1} m f_c(m) \quad (\text{A.5a})$$

$$m_p = \sum_{m=m_{p0}}^{\infty} m f_p(m) \quad (\text{A.5b})$$

The cloud and precipitation dispersion are defined as

$$\sigma_c^2 = m_c^{-2} \sum_{m=1}^{m_{p0}-1} (m^2 - m_c^2) f_c(m) \quad (\text{A.6a})$$

$$\sigma_p^2 = m_p^{-2} \sum_{m=m_{p0}}^{\infty} (m^2 - m_p^2) f_p(m) \quad (\text{A.6b})$$

Let q be the total water mixing ratio and q_v the mixing ratio of vapor. The mixing ratios satisfy the conservation condition

$$q = q_v + q_c + q_p \quad (\text{A.7})$$

Utilizing the fact that the nuclei activation and condensation growth rates of droplets of sizes less than $50 \mu\text{m}$ are so rapid and that cloud will generally fall well within this range, we assume that cloud is in liquid-vapor equilibrium over the macro-time scale. Since precipitation may involve large drops with slow evaporation time scales in cloud-free air, we shall not require the precipitation to be in equilibrium. The presence of cloud will thus turn on the level of the saturation mixing ratio q_s relative to the total mixing ratio q . We introduce the cloudiness $r(q_\lambda)$ which is a conditional variable indicating the presence or absence of cloud. It is defined as the Heaviside function of the difference mixing ratio $q_\lambda = q - q_s$ as

$$r = H(q_\lambda) \quad . \quad (A.8)$$

The equilibrium liquid water mixing ratio q_ℓ is then given by

$$q_\ell = rq_\lambda \quad . \quad (A.9)$$

The cloud and vapor mixing ratios q_c , q_v are given in terms of q , q_p , q_s as

$$q_c = r (q_\lambda - q_p) \quad , \quad (A.10)$$

$$q_v = q - rq_\lambda - (1-r)q_p \quad . \quad (A.11)$$

We shall take as the dynamical equations governing cloud and precipitation the first two moments of the droplet kinetic equation for each group: the number density and mixing ratio moments. (We use the dynamical equation for q rather than q_c since either serves as an appropriate dependent variable). The results are

$$Dq/Dt + \partial(q_p V_{pi})/\partial x_i = 0 \quad , \quad (A.12)$$

$$Dn_c/Dt = -N_{cc} - N_{pc} - N_{cp} + N_{cv} \quad , \quad (A.13)$$

$$Dq_p/Dt + \partial(q_p V_{pi})/\partial x_i = M_{cp} + M_{pc} - M_{pv} \quad , \quad (A.14)$$

$$Dn_p/Dt + \partial(n_p V_{pi})/\partial x_i = N_{cp} - N_{pp} \quad . \quad (A.15)$$

In the above $N_{cc} + N_{cp}$ represents the loss of cloud droplets due to self-collisions among cloud droplets; N_{cp} and M_{cp} are the production of precipitation number and mixing ratio by self-collisions within cloud (auto-conversion of cloud). N_{pc} and M_{pc} are the rate of loss of cloud number and the rate of production of precipitation mixing ratio by collisions of precipitation drops with cloud drops (cloud collection). N_{pp} is the rate of

loss of precipitation number density by self collision of precipitation. For heavy precipitation with drops in excess of 2 mm, collisional de-coalescence and droplet instability break-up terms must be included in Equations A.13 through A.15. N_{CV} and M_{pV} are droplet-vapor interaction terms. N_{CV} represents the net production of cloud number due to condensation and evaporation. M_{pV} represents the evaporative rate of precipitation in cloud-free air.

The variables q , n_c , q_p , n_p and Eqs. A.12 through A.15 represent the basic dynamical variables and conservation laws for cloud and precipitation in our simplified description. The cloud and vapor mixing ratios are determined from Equations A.10 and A.11 and the sizes m_c and m_p from Equation A.4. The precipitation speed then follows from the sedimentation velocity function $V_i(m)$ as

$$V_{pi} = V_i(m_p) , \quad (A.16)$$

and the precipitation flux as $q_p V_{pi}$.

The closure of Equations A.12 through A.15 requires specification of the various collisional rates N , M and the liquid-vapor rates N_{CV} , M_{pV} . The exact representation of the collisional rates N_{CC} , N_{CP} , and M_{CP} are

$$N_{CC} = n_c^2 \sum_{m=1}^{m_{po}-2} \sum_{k=1}^{m_{po}-1-m} K(m,k) f_c(m) f_c(k) , \quad (A.17a)$$

$$N_{CP} = n_c^2 \sum_{m=1}^{m_{po}-2} \sum_{k=m_{po}-m}^{m_{po}-1} K(m,k) f_c(m) f_c(k) , \quad (A.17b)$$

$$M_{CP} = (m_{po}/m_c) (q_c/n_c) N_{CP} \quad (A.17c)$$

where $K(m,k)$ is the collision kernel between a droplet of size m and a droplet

of size k . We may express these results in terms of a non-dimensional collisional effectiveness $S_{\alpha\beta}$:

$$N_{CC} = n_c^2 K_{CC} S_{CC} \quad (\text{A.18a})$$

$$N_{CP} = n_c^2 K_{CP} S_{CP} \quad (\text{A.18b})$$

where K_{CC} and K_{CP} are appropriately defined average collision kernels. The collisional effectiveness is a measure of the effectiveness of all sizes within cloud in evolving the spectrum to precipitation size drops:

$$S_{CC} = K_{CC}^{-1} \sum_{m=1}^{m_{p0}-2} \sum_{k=1}^{m_{p0}-1-m} K(m,k) f_c(m) f_c(k) \quad , \quad (\text{A.19a})$$

$$S_{CP} = K_{CP}^{-1} \sum_{m=1}^{m_{p0}-2} \sum_{k=m_{p0}-m}^{m_{p0}-1} K(m,k) f_c(m) f_c(k) \quad . \quad (\text{A.19b})$$

We may similarly express the rates N_{pc} , M_{pc} , and N_{pp} as

$$N_{pc} = n_p n_c K_{pc} S_{pc} \quad , \quad (\text{A.20a})$$

$$M_{pc} = q_c n_p K_{pc} S_{pc} \quad , \quad (\text{A.20b})$$

$$N_{pp} = n_p^2 K_{pp} S_{pp} \quad , \quad (\text{A.20c})$$

where S_{pc} and S_{pp} are appropriate collisional effectiveness for the collection of cloud by precipitation and for precipitation self-collisions.

The collision kernel $K(m,k)$ appearing in the collision rate expressions is composed of shearing and differential sedimentation parts. Since we do not describe the detailed microphysics of the small size spectrum formation but only the collisional growth stage for droplets greater than $1 \mu\text{m}$ radii, we neglect Brownian collisions. The collision kernel is thus expressed as

$$K(m,k) = K^{(s)}(m,k) + K^{(ds)}(m,k) , \quad (\text{A.21})$$

where $K^{(s)}(m,k)$ is the kernel for droplets in a shear field and $K^{(ds)}$ is the kernel for differential sedimentation in a force or acceleration field. These kernels have the form

$$K^{(s)}(m,k) = v_0/\pi(m^{1/3}+k^{1/3})^3 G e^{(s)}(m,k) , \quad (\text{A.22})$$

$$K^{(ds)}(m,k) = \pi(3v_0/4\pi)^{2/3} (m^{1/3}+k^{1/3})^2 (1-\rho_\infty/\rho_0) V_i(m)-V_i(k) e^{(ds)}(m,k) , \quad (\text{A.23})$$

where G is the magnitude of the fluid shear, V_i is the droplet drift velocity, and $e^{(s)}(m,k)$ and $e^{(ds)}(m,k)$ are the collisional efficiencies.

The efficiencies for differential sedimentation $e^{(ds)}$ are given by Mason, 1971. The collisional efficiencies in shear flow are less well established. For particles of nearly identical size $e^{(s)} \approx 1$. Swift and Friedlander, 1964, suggest a value $e^{(s)} \approx 0.4$.

The sedimentation velocity function $V_i(m)$ may be expressed in terms of $\tau_r(m)$ as

$$V_i(m) = (1-\rho_\infty/\rho_0) \tau_r(m) \left(\frac{Du_i}{Dt} + g_i \right) , \quad (\text{A.24})$$

where Du_i/Dt is the fluid acceleration, g_i the acceleration of gravity, and $\tau_r(m)$ is the droplet relaxation time.

For the purposes of the present theory, the droplet relaxation time in air at the earth's surface may be adequately approximated as

$$\tau_r(m) = aR_m^\alpha \quad (\text{A.25})$$

where R_m is the radius of a drop in size class m and a , α are constants given in Table A2 which is constructed from the data of Gunn and Kinzer (1949):

TABLE A2

Droplet Radius R_m μm	a	α
$1 < R_m < 40$	$1.6 \times 10^7 \text{ s/m}^2$	2
$40 < R_m < 600$	$6.4 \times 10^2 \text{ s/m}$	1
$600 < R_m < 1500$	$20 \text{ s/m}^{1/2}$	1/2

Selected values of τ_r are given in Table A3.

TABLE A3

R (μm)	τ_r (ms)
10	1.6
50	32
100	64
500	320
1000	632

Microphysical Closure

The elementary volume v_0 as well as the collisional and liquid-vapor rates in Equations A.12 through A.15 involve the full distribution functions $f_c(m)$, $f_p(m)$ consistent with the fact that a reduced description of the full spectrum to two groups consisting of cloud and precipitation cannot be a

closed representation without additional closure approximation. Three overall properties of the full spectrum are critical for the macroscopic cloud and precipitation dynamics. These are the elementary volume v_0 , the dispersion of the cloud spectrum σ_c , and the structure of the cloud distribution tail in the vicinity $m \approx m_{p0}$. The elementary volume v_0 establishes the average size of the cloud drop. The cloud dispersion g as well as the average size v_0 are the determining microphysical properties for the collisional evolution of the bulk of the cloud spectrum and hence are critical to the rate N_{cc} . The structure of the tail of the cloud distribution function determines the population of tail droplets and hence is critical to the rates N_{cp} , M_{cp} or correspondingly the effectiveness S_{cp} .

Rigorous closure of the elementary volume requires a dynamical description of both the condensation nuclei and the supersaturation. In lieu of such a detailed description, we fix the elementary volume by specifying a parameter: the elementary number density n_0 , which may be thought of as the effective population of cloud droplets in the absence of collisions. The elementary volume is then determined by n_0 as

$$v_0 = \frac{q_\ell}{\left(\frac{\rho_0}{\rho_\infty}\right) n_0}, \quad (\text{A.26})$$

which from Equation A.4a then determines the cloud size m_c as

$$m_c = n_0/n_c. \quad (\text{A.27})$$

The elementary number density may be thought of as primarily an environmental and cloud type parameter. Typical values are given in Table A4.

TABLE A4

<u>Cloud/Environment</u>	<u>Elementary Number Density n_0 (cm^{-3})</u>
Continental Cumulus	200-800
Maritime Cumulus	100-200
Maritime Stratus	50-100

The presence of collisions which we shall discuss in what follows acts as a broadening mechanism for the spectrum and leads to an increasing dispersion σ_c . The manner in which non-collisional processes increase (or decrease) σ_c is not presently clearly understood. We shall therefore restrict attention to the case where the cloud spectrum in absence of collisions consists of droplets concentrated at a single size $m_c=1$ and a negligible dispersion $\sigma_c \approx 0$. Once collisions come into play, we have $m_c > 1$ and $\sigma_c > 0$.

Since the condensation and evaporation rates of the elementary spectrum are rapid compared to macroscopic time scales, we assume that the elementary drop number appears instantly when the saturation line is crossed. Correspondingly, the rate N_{cv} may be represented as

$$N_{cv} = \delta(q_\lambda) r \frac{Dq_\lambda}{Dt} \quad (\text{A.28})$$

where $\delta(q_\lambda)$ is the Dirac delta function. In cloud free air the rate M_{pv} is given by

$$M_{pv} = q_p / \tau_{pv} \quad (\text{A.29})$$

with the rate τ_{pv}^{-1} given by

$$\tau_{pv}^{-1} = \frac{3\eta}{R_p^2 \left(\frac{\rho_0}{\rho_\infty} \right) S_c} [1 + CR_e^{1/2} S_c^{1/3}] (q_s - q_v) \quad (\text{A.30})$$

where η is the kinematic viscosity of air, and R_e , S_c are Reynolds number and Schmidt number based upon droplet diameter $2R_p$ and sedimentation velocity V_p .

$C \approx 0.28$ is a correlation constant. Since $q_v = q_s$ when $r=1$ it can be seen that $M_{pv}=0$ except in clear air.

We now consider the collisionally generated tail of the distribution function which will allow us explicit closure for S_{CC} , and S_{CP} . The collisional processes will also determine σ_c . It can be shown that even for a constant collision kernel, the effectiveness S_{CP} is a sensitive function of the tail of the distribution. This can be demonstrated for the special case of a Smoluckowski cloud (droplet population initially $n_c(0)$ of a single size $m=1$ ($\sigma_c=0$) at time $t=0$ under the action of a constant collision kernel K (Smoluckowski, 1917).

For such a cloud, the distribution function is given by

$$f_c(m, T) = f_c(1, T) T^{m-1} \quad (\text{A.31})$$

where

$$f_c(1, T) = (1-T)/(1-T^{m_{p0}-1}) \quad (\text{A.32})$$

and the function T for the Smoluchowski's problem is given by

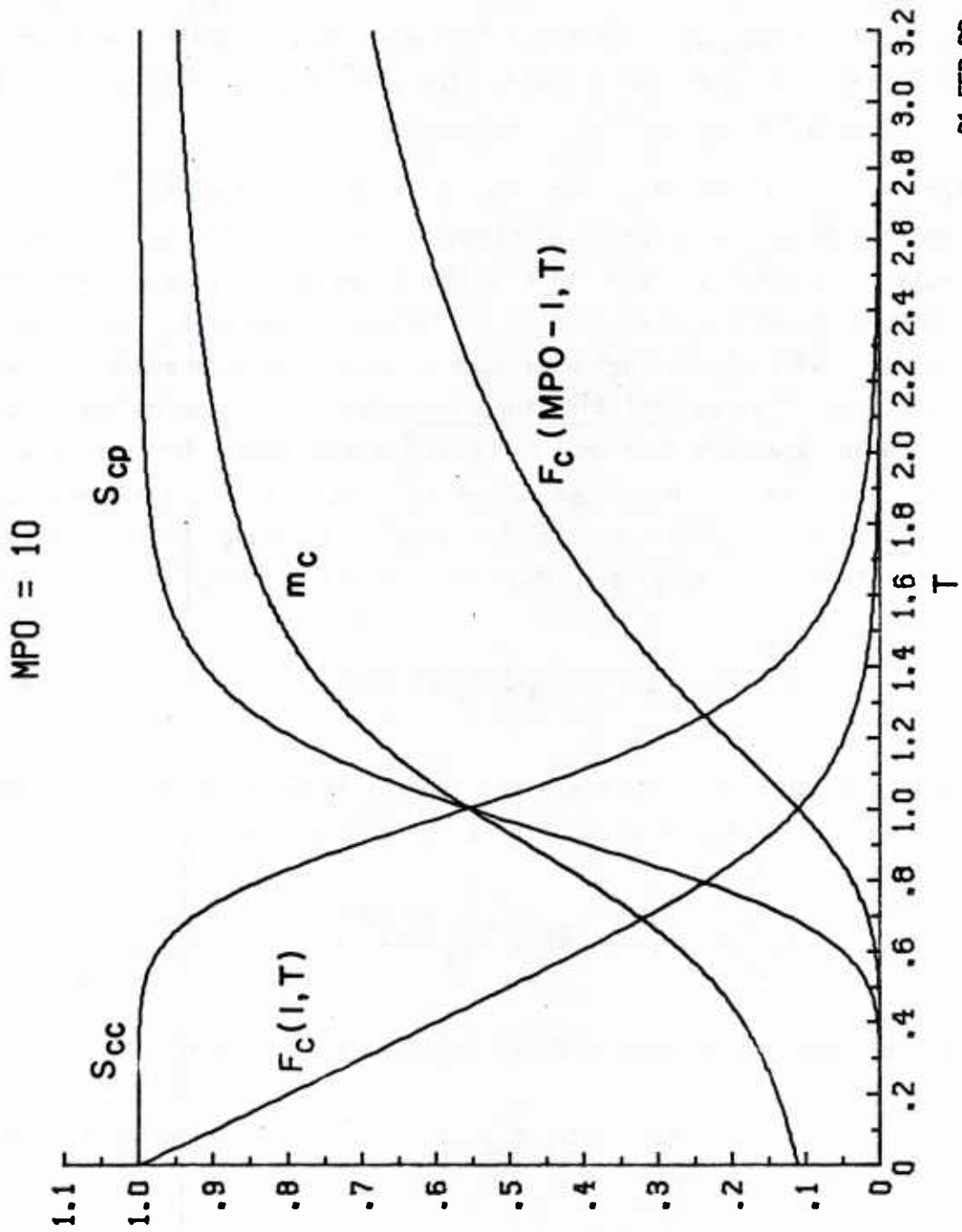
$$T = (1/2)n_c(0)Kt/[1+(1/2)n_c(0)Kt] \quad (\text{A.33})$$

Upon substitution of Equation A.26 into the definition of A.19, we find

$$S_{CC} = m_c f_c(1, T) \quad (\text{A.34a})$$

$$S_{CP} = (m_{p0} - m_c) f_c(m_{p0} - 1, T) \quad (\text{A.34b})$$

The effectiveness S_{CC} which describes cloud-cloud collisions which do not create precipitation and S_{CP} which describes cloud-cloud collisions which create a precipitation drop are shown in Figure A2 as a function of the evolution parameter T . It can be seen that at $T=0$, we have $S_{CP}=0$ since no droplets which are concentrated at $f_c(1,0)=1$ can reach the spectrum dividing



21-FEB-83

Figure A.2 Properties of the cloud distribution function as a function of the evolution parameter T .

size in a single collision. Correspondingly at $T=0$, we have $S_{CC}=1$ since all droplets which exist at $f_C(1,0)=1$ will remain as cloud droplets after their first collision. At $T=1$, we have a flat distribution with $f_C(m,1)=1/(m_{p0}-1)$ and with $S_{CC}=S_{CP}=1/2-1/(m_{p0}-1)$. For $T > 1$, the distribution shifts with most cloud droplets near the spectrum dividing size where $f_C(m_{p0}-1) \approx 1$. In this state we have $S_{CC} \approx 0$ and $S_{CP} \approx 1$.

Description of the evolution of the distribution function is thus essential for the proper description of cloud evolution and the precipitation production rate. As our collision rate closure, we shall assume that the cloud distribution function to be used in the determination of $S_{\alpha\beta}$ is a power law form consistent with the Smoluchowski form of Equations A.31 and A.32. We regard the function T as an evolution function which describes the evolution of the cloud droplet spectrum from one which is peaked about the elementary spectrum size, $v=v_0$, $m=1$, $T=0$ to one which is flat with all sizes equally represented: $f_C(m) \rightarrow 1/(m_{p0}-1)$. We fix the value of T through Equation A.27. For the form Equation A.31, $m_C(T)$ from Equation A.5a is given by

$$m_C(T) = \frac{1}{1-T} [1-(m_{p0}-1)f_C(1) T^{m_{p0}-1}] \quad (A.35)$$

Thus, the evolution function T is determined implicitly by Equations A.27 and A.35. The dispersion for the form Equation A.31 is given by

$$\sigma_C^2(T) = \frac{m_C T - (m_{p0} - m_C) [1 - m_C (1-T)]}{m_C^2 (1-T)} \quad (A.36)$$

Under these closure hypotheses the collisional rates become

$$N_{CC} = n_C^2 K_{CC} S_{CC}(T) \quad (A.37a)$$

$$N_{CP} = n_C^2 K_{CC} S_{CP}(T) \quad (A.37b)$$

$$M_{CP} = n_C q_C K_{CC} S_{CP}(T) \quad (A.37c)$$

$$N_{pc} = n_p n_c K_{pc} \quad (\text{A.37d})$$

$$M_{pc} = n_p q_c K_{pc} \quad (\text{A.37e})$$

$$N_{pp} = \frac{1}{2} n_p^2 K_{pp} \quad (\text{A.37f})$$

Because of the strongly diminished collision efficiency $e^{(s)}$ for particles of significantly disparate size, we neglect the contributions of shear collisions to K_{pc} . Because of the large differential sedimentation rate of large drops, we similarly neglect shear contributions to K_{pp} .

The effectiveness with variable collision kernel is assumed to be approximately the same as the effectiveness with a constant collision kernel. This closure assumption places some burden upon an appropriate choice for the average kernels K_{cc} , K_{pc} , K_{pp} . We select as "average" kernels the forms

$$K_{cc} = k^{(s)}(m_c^+, m_c^-) + k^{(ds)}(m_c^+, m_c^-) \quad , \quad (\text{A.38a})$$

$$K_{pc} = k^{(ds)}(m_p, m_c) \quad , \quad (\text{A.38b})$$

$$K_{pp} = k^{(ds)}(m_p^+, m_p^-) \quad , \quad (\text{A.38c})$$

where the sizes are specified as

$$m_c^\pm = m_c(1 \pm \sigma_c/2) \quad , \quad (\text{A.39a})$$

$$m_p^\pm = m_p(1 \pm \sigma_p/2) \quad . \quad (\text{A.39b})$$

The precipitation dispersion σ_p is not a critical parameter of the model since it principally controls the rate N_{pp} . The rate N_{pp} is not a critical rate since the precipitation flux divergence $\partial(\overline{V}_p \overline{q}_p)/\partial x_i$ will dominate over N_{pp} for precipitation drops in excess of 50 μm in clouds of the order of several km or less in depth. We assume σ_p is given in terms of the precipitation flux by a parameterization (Marshall and Palmer, 1948); it may be as satisfactory to take it as a fixed cloud type parameter. We assume that the precipitation distribution function shapes are not important for the rates N_{pc} , N_{pp} and it is permissible to set $S_{pc}=1$, $S_{pp}=1/2$.

Since the power law form Equation A.31 is always monotone decreasing with size it does not allow bi-modality within cloud. It should be noted, however, that the collisional process which induces bi-modality into the spectrum (other than specially chosen initial conditions) is the rapid increase of the collision kernel (both in collision cross-section and efficiency) with an increase in size of the larger collision partner. There is thus a consistency between the cut-off of the monotone decrease of the cloud spectrum at $m=m_{p0}$ and the large collision kernel associated with drops for $m>m_{p0}$. Hence the total droplet spectrum allows for bi-modality with the second mode (when it occurs) always occurring in the precipitation part of the spectrum (Figure A1).

Our microphysical theory is thus closed. The moisture variables in a cloudy, precipitating atmosphere are described by the moisture, cloud and precipitation variables q , q_p , n_c , n_p . These variables are governed by the conservation laws Equations A.12 through A.15. The rates appearing in these conservation laws are given by Equations A.37. The evolution function T is central to these collisional and liquid-vapor rates and is determined by m_c from Equations A.31 and A.35. The model coefficient of the closure is the elementary number density n_0 .

TURBULENT ENSEMBLE AVERAGE EQUATIONS

Mean Equations

The turbulent ensemble averages of the cloud and precipitation equations, Equations A.12 through A.15, are

$$\overline{Dq}/Dt + \partial(\overline{u_i'q'} + \overline{V_{pi}q_p} + \overline{V_{pi}'q_p'})/\partial x_i = 0 \quad , \quad (\text{A.40})$$

$$\overline{Dn_c}/Dt + \partial(\overline{u_i'n_c'})/\partial x_i = -\overline{N_{cc}} = \overline{N_{cp}} - \overline{N_{pc}} + \overline{N_{cv}} \quad , \quad (\text{A.41})$$

$$\overline{Dq_p}/Dt + \partial(\overline{u_i'q_p'} + \overline{V_{pi}q_p} + \overline{V_{pi}'q_p'})/\partial x_i = \overline{M_{cp}} + \overline{M_{pc}} - \overline{M_{pv}} \quad , \quad (\text{A.42})$$

$$\overline{Dn_p}/Dt + \partial(\overline{u_i'n_p'} + \overline{V_{pi}n_p} + \overline{V_{pi}'n_p'})/\partial x_i = \overline{N_{cp}} - \overline{N_{pp}} \quad . \quad (\text{A.43})$$

Since $V_{pi} = V_i(m_p)$ and m_p is a function of q_p and n_p through Equation A.25, the fluctuation V_{pi}' may be represented as

$$V_{pi}' = a_i q_p' - b_i n_p' \quad , \quad (\text{A.44})$$

where

$$a_i \equiv \frac{\partial V_{pi}}{\partial m_p} \frac{\partial m_p}{\partial q_p} \quad , \quad b_i \equiv \frac{\partial V_{pi}}{\partial m_p} \frac{\partial m_p}{\partial n_p} \quad . \quad (\text{A.45})$$

The correlations involving V_{pi}' then reduce to correlations involving the fundamental set of variables q , q_p , n_i , n_p and the turbulent precipitation fluxes of mixing ratio and number may be expressed as

$$\overline{V_{pi}'q_p'} = a_i \overline{q_p'^2} - b_i \overline{q_p'n_p'} \quad , \quad (\text{A.46a})$$

$$\overline{V_{pi}'n_p'} = a_i \overline{q_p'n_p'} - b_i \overline{n_p'^2} \quad . \quad (\text{A.46b})$$

For $V_{pi} \sim m_p^{\alpha/3}$, it follows from Equations A.46a and A.46b that

$$\overline{V_{pi} q_p'} = \alpha/3 \left(\overline{q_p'^2} / \overline{q_p}^2 - \overline{q_p' n_p'} / \overline{q_p} \overline{n_p} \right) \overline{V_{pi}} \overline{q_p} \quad , \quad (\text{A.47a})$$

$$\overline{V_{pi} n_p'} = \alpha/3 \left(\overline{q_p' n_p'} / \overline{q_p} \overline{n_p} - \overline{q_p'^2} / \overline{q_p}^2 \right) \overline{V_{pi}} \overline{n_p} \quad . \quad (\text{A.47b})$$

We shall term the flux $\overline{V_{pi} q_p + V_{pi} q_p'}$ the precipitation flux and the flux $\overline{u_i q_p'}$ the turbulent precipitable water flux. We see that net flux consists of both turbulent and precipitation contributions. The term $\overline{u_i q_p'}$ represents the turbulent transport of precipitation drops by turbulent updrafts and down drafts; it can significantly diminish or enhance the pure precipitation flux $\overline{V_{pi} q_p + V_{pi} q_p'}$.

The new non-collisional correlations introduced which directly involve cloud and precipitation are the turbulent precipitable water flux $\overline{u_i q_p'}$, the turbulent cloud number flux $\overline{u_i n_c'}$, and the turbulent precipitation number flux $\overline{u_i n_p'}$. The collisional correlations required are $\overline{M_{cc}}$, $\overline{N_{cv}}$, $\overline{N_{pc}}$, $\overline{M_{cp}}$, $\overline{M_{pc}}$, and $\overline{N_{pp}}$. The condensation-evaporation correlations required are $\overline{N_{cv}}$ and $\overline{M_{pv}}$.

The ensemble averages of the derived moisture variables follow from Equations A.10 and A.11 as:

$$\overline{q_c} = \overline{r} (\overline{q_\lambda} - \overline{q_p}) + \overline{r' q_\lambda'} - \overline{r' q_p'} \quad , \quad (\text{A.48a})$$

$$\overline{q_v} = \overline{r} \overline{q_s} + (1-\overline{r})(\overline{q} - \overline{q_p}) - \overline{r' q_\lambda'} - \overline{r' q_p'} \quad , \quad (\text{A.48b})$$

$$\overline{q_\lambda} = \overline{q} - \overline{q_s} \quad . \quad (\text{A.48c})$$

We see that there are second-order correlation contributions to the mean cloud and vapor mixing ratios.

First Order Rate Approximation

On the basis of the slow time scales of the collisional rate terms in Eqs. A.13 through A.15, we propose a first order rate approximation in which we retain the mean collision rates \overline{N}_{CC} , \overline{N}_{CP} , \overline{N}_{PC} , \overline{M}_{CP} , \overline{M}_{PC} , \overline{N}_{PP} and the liquid-vapor rate \overline{M}_{PV} (which must also appear in the virtual potential temperature equation), but we neglect their fluctuation contributions to the second-order correlation equations for $\overline{u_i'q_p'}$, $\overline{u_i'n_c'}$, $\overline{u_i'n_p'}$, etc.

In this approximation, the instantaneous rates given by Equations A.37 become

$$\overline{N}_{CC} = (\overline{n_c^2 + n_c'^2}) \overline{K}_{CC} S_{CC}(\overline{T}) , \quad (\text{A.49a})$$

$$\overline{N}_{CP} = (\overline{n_c^2 + n_c'^2}) \overline{K}_{CC} S_{CP}(\overline{T}) , \quad (\text{A.49b})$$

$$\overline{M}_{CP} = (\overline{n_c q_c + n_c' q_c'}) \overline{K}_{CC} S_{CP}(\overline{T}) , \quad (\text{A.49c})$$

$$\overline{N}_{PC} = (\overline{n_p n_c + n_p' n_c'}) \overline{K}_{PC} , \quad (\text{A.49d})$$

$$\overline{M}_{PC} = (\overline{n_p q_c + n_p' q_c'}) \overline{K}_{PC} , \quad (\text{A.49e})$$

$$\overline{N}_{PP} = \frac{1}{2} (\overline{n_p^2 + n_p'^2}) \overline{K}_{PP} . \quad (\text{A.49f})$$

In the above decomposition we have assumed the droplet loading is never large enough to affect the eddy dynamics and thus the collision kernels are de-correlated from the droplet concentrations. We have also interpreted \overline{S}_{CC} as $S_{CC}(\overline{T})$, etc. The ensemble average of the collision kernels given by Equations A.22 through A.25 require the ensemble average fluid shear \overline{G} and the ensemble average net acceleration $\left| \overline{g_i + Du_i/Dt} \right|$. For simplicity, but without

essential restriction, we shall neglect the contribution of mean fluid shear $\partial \bar{u}_i / \partial x_j$ and mean acceleration $D\bar{u}_i / Dt$. Following Saffman and Turner (1955), we approximate the ensemble average acceleration as

$$\overline{g_i + Du_i^j / Dt} = \sqrt{g^2 + a^2} \quad (\text{A.50})$$

where \bar{a} is the rms acceleration

$$\bar{a}^2 = \left(\overline{\frac{Du_i^j}{Dt}} \right)^2 \quad (\text{A.51})$$

Before we can evaluate the quantities \bar{a} and \bar{G} as well as all correlations involving droplet variables n_c , q_p , n_p we must first consider the structure of atmospheric turbulence and its influence on the motion of liquid drops. Atmospheric turbulence consists of the motion of eddy structures ranging from the largest energy containing scale Λ to the microscale λ_0 where molecular dissipation comes into play. Correspondingly, the large scale eddies have a characteristic time scale $\tau_\Lambda = \Lambda / \hat{q}$ where \hat{q} is the rms turbulence velocity. The turbulence dissipation rate $\epsilon = 1/4 \hat{q}^3 / \Lambda$ is preserved through this turbulent cascade. The smallest eddies of scale $\lambda_0 = (\nu^3 / \epsilon)^{1/4}$ possess a characteristic microtime $\tau_{\lambda_0} = (\nu / \epsilon)^{1/2}$, a characteristic shear $G_{\lambda_0} = \tau_{\lambda_0}^{-1} \sim \epsilon^{1/2}$ and a characteristic acceleration $a_{\lambda_0} = \lambda_0 / \tau_{\lambda_0}^2 \sim \epsilon^{3/4}$. The magnitudes of these quantities for the range of turbulence dissipation rates encountered in the atmosphere are presented in Table A5.

TABLE A5. TURBULENCE LENGTH, TIME, ACCELERATION, AND SHEAR SCALES
IN THE ATMOSPHERE FOR DISSIPATION SCALE EDDIES

ϵ	λ_0	τ_{λ_0}	a_{λ_0}/g	G_{λ_0}
(m^2/sec^3)	(μm)	(ms)	-	(s^{-1})
0.001	1510	130	0.009	7.7
0.01	846	42	0.05	23.8
0.10	476	13	0.28	76.9
1.0	268	4.2	1.58	238
10.0	151	1.3	8.9	769

Since the dissipation rate is preserved through the cascade, the fluctuation time of an eddy of scale λ is $\tau_\lambda = \tau_{\lambda_0} (\lambda/\lambda_0)^{2/3}$. The characteristic shear in an eddy of scale λ is $G_\lambda = G_{\lambda_0} (\lambda/\lambda_0)^{-2/3}$ and the acceleration in an eddy of scale λ is $a_\lambda = a_{\lambda_0} (\lambda/\lambda_0)^{-1/3}$.

For those conditions where $\tau_r/\tau_\lambda \gg 1$ the droplet motion de-correlates completely from the turbulence of the air and there is no influence of turbulence on the collision kernels appearing in Equations A.22 and A.23. The ensemble mean shear \bar{G} and acceleration \bar{a} experienced by the drops in the absence of mean shear and acceleration tends to zero. At the opposite extreme for $\tau_r/\tau_\lambda \ll 1$ the droplets are completely correlated with the full turbulent cascade. The corresponding ensemble mean shear \bar{G} which such droplets will experience is given by

$$\bar{G} = \sqrt{2/15} G_{\lambda_0} . \quad (A.52)$$

(Taylor, 1935). The rms acceleration which the droplet will experience is

$$\bar{a} = \sqrt{1.3} a_{\lambda_0} . \quad (A.53)$$

(Batchelor, 1950).

Let us now examine the droplet relaxation time τ_r relative to the eddy fluctuation time τ_λ . From Table A3 it can be seen that over a considerable range of importance the droplet relaxation time τ_r is much greater than the microscale time τ_{λ_0} and the motion of such droplets will not be correlated with the motion of dissipation scale eddies. On the other hand, the macrotime τ_Λ is rarely less than 10 seconds under atmospheric conditions (except deep in the surface layer) so that the droplet motion is correlated (even for 1000 μm drops) with a large part of the turbulent cascade.

When $\tau_{\lambda_0} < \tau_r < \tau_\Lambda$ we postulate that the smallest eddy scale λ whose motion the droplet will follow is determined by the condition $\tau_\lambda \approx \tau_r$ and thus this scale is given by

$$\lambda = \lambda_0 (\tau_r / \tau_{\lambda_0})^{3/2} \quad (\text{A.54})$$

correspondingly the maximum shear G_λ and maximum acceleration a_λ which such drops can experience is

$$G_\lambda = G_{\lambda_0} (\tau_r / \tau_{\lambda_0})^{-1} \quad , \quad (\text{A.55})$$

$$a_\lambda = a_{\lambda_0} (\tau_r / \tau_{\lambda_0})^{-1/2} \quad . \quad (\text{A.56})$$

We now formulate the general ensemble average shear and accelerations as

$$\bar{G}(m) = c(s) \tau_{\lambda_0}^{-1} \text{Min} \left(\begin{array}{c} \tau_{\lambda_0} / \tau_r(m) \\ 1 \end{array} \right) \quad , \quad (\text{A.57})$$

$$\bar{a}(m) = c(ds) a_{\lambda_0} \text{Min} \left(\begin{array}{c} \tau_{\lambda_0}^{1/2} / \tau_r^{1/2}(m) \\ 1 \end{array} \right) \quad . \quad (\text{A.58})$$

where we indicate the explicit dependence upon droplet size and $c(s)$ and $c(ds)$ are model constants. For droplets which are embedded in an isotropic cascade we may take $c(s) = \sqrt{2/15}$, $c(ds) = \sqrt{1.3}$.

It can be seen that for $\tau_r(m) \gtrsim \tau_{\lambda_0}$, the ensemble mean shear $\bar{G}(m)$ becomes independent of ϵ ; the ensemble mean acceleration, however, continues to increase with ϵ as $\bar{a}(m) \sim a_{\lambda_0} \tau_{\lambda_0}^{1/2} \sim \epsilon^{1/2}$ whereas $\bar{a}(m) \sim a_{\lambda_0} \sim \epsilon^{3/4}$ for $\tau_r(m) \lesssim \tau_{\lambda_0}$.

The ensemble average kernels are thus given by Equations A.38 and Equations A.22 through A.24 with G given by $\bar{G}(m^+)$ and Du_i/Dt by $\bar{a}(m^+)$ where m^+ is the size of the larger collision partner and $\bar{G}(m)$, $\bar{a}(m)$ are given by Equations A.57 and A.58.

The relative importance of turbulent shearing collisions compared to gravitational sedimentation collisions in evolving the elementary spectrum depends upon the magnitudes of the turbulence dissipation level ϵ and the droplet spectrum dispersion σ_c . In Figure A3 we exhibit the ratio of the turbulent shear kernel $K_{CC}^{(s)}$ to differential gravitational sedimentation kernel $K_{CC}^{(ds)}$. In Figure A4 we show the ratio of the total collisional kernel $K_{CC}^{(s)} + K_{CC}^{(ds)}$ with all turbulence effects included to the turbulence-free differential sedimentation rate $K_{CC}^{(ds)}$. It can be seen in Figure A3 that for cloud droplets dispersed over the range of 6 to 20 μm radius, turbulence induced shearing collisions play an important role in cloud evolution for dissipation rates in excess of $0.01 \text{ m}^2/\text{s}^3$. For wider dispersions, differential sedimentation will be more dominant; for narrower distributions turbulence shearing dominates the collisional process. For strong turbulence as might exist in cumulus corresponding to $\epsilon \sim 1\text{-}10 \text{ m}^2/\text{s}^3$, turbulence induced shearing collisions may be the principal collisional broadening and spectral evaluation mechanism. In Figure A4 it can be seen that when both turbulent shearing and acceleration effects are included in the full collision kernel, turbulence effects dominate the collision kernel for $\epsilon \gtrsim 0.05 \text{ m}^2/\text{sec}^3$.

Turbulence Equations

In the first order rate approximation, we neglect the contributions of the collisional and liquid vapor rates to the higher-order turbulence correlations. The turbulence equations for the cloud and precipitation variables $\overline{u_i n'_c}$, $\overline{u_i n'_p}$, $\overline{u_i q'_p}$ and their other appropriate second-order correlations are those of second-order closure theory for passive scalars. (Lewellen, 1978; Oliver, Lewellen and Williamson, 1978). Since drops up to

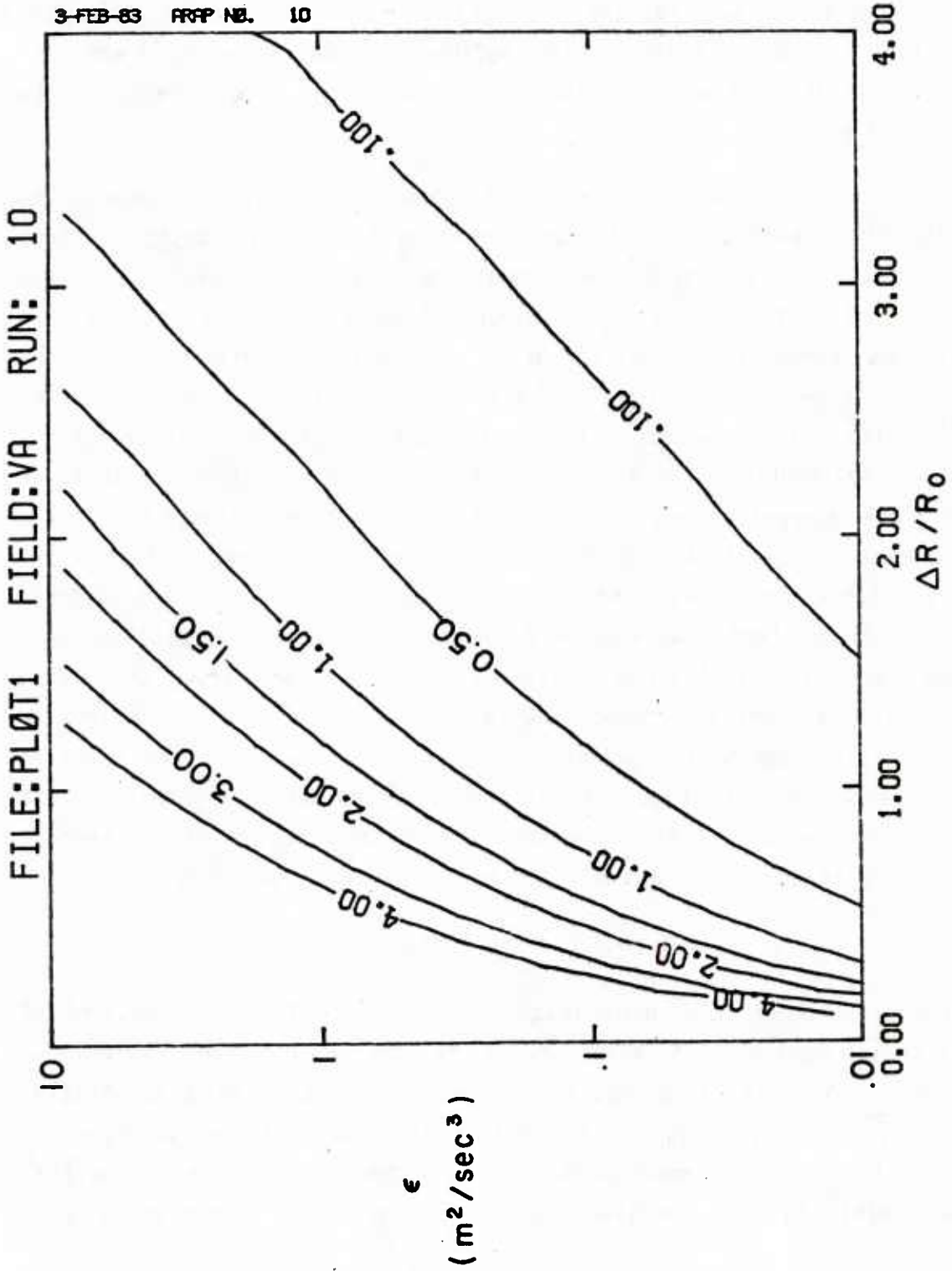


Figure A.3 Isoplots of the ratio of the turbulent shear collision kernel $K(S)$ to the differential sedimentation kernel $K(ds)$ (in which the turbulence induced acceleration a is suppressed) as a function of turbulence dissipation rate ϵ and the difference in collisional partner radii $\Delta R/R_0$. The elementary drop radius R_0 is $6 \mu m$.

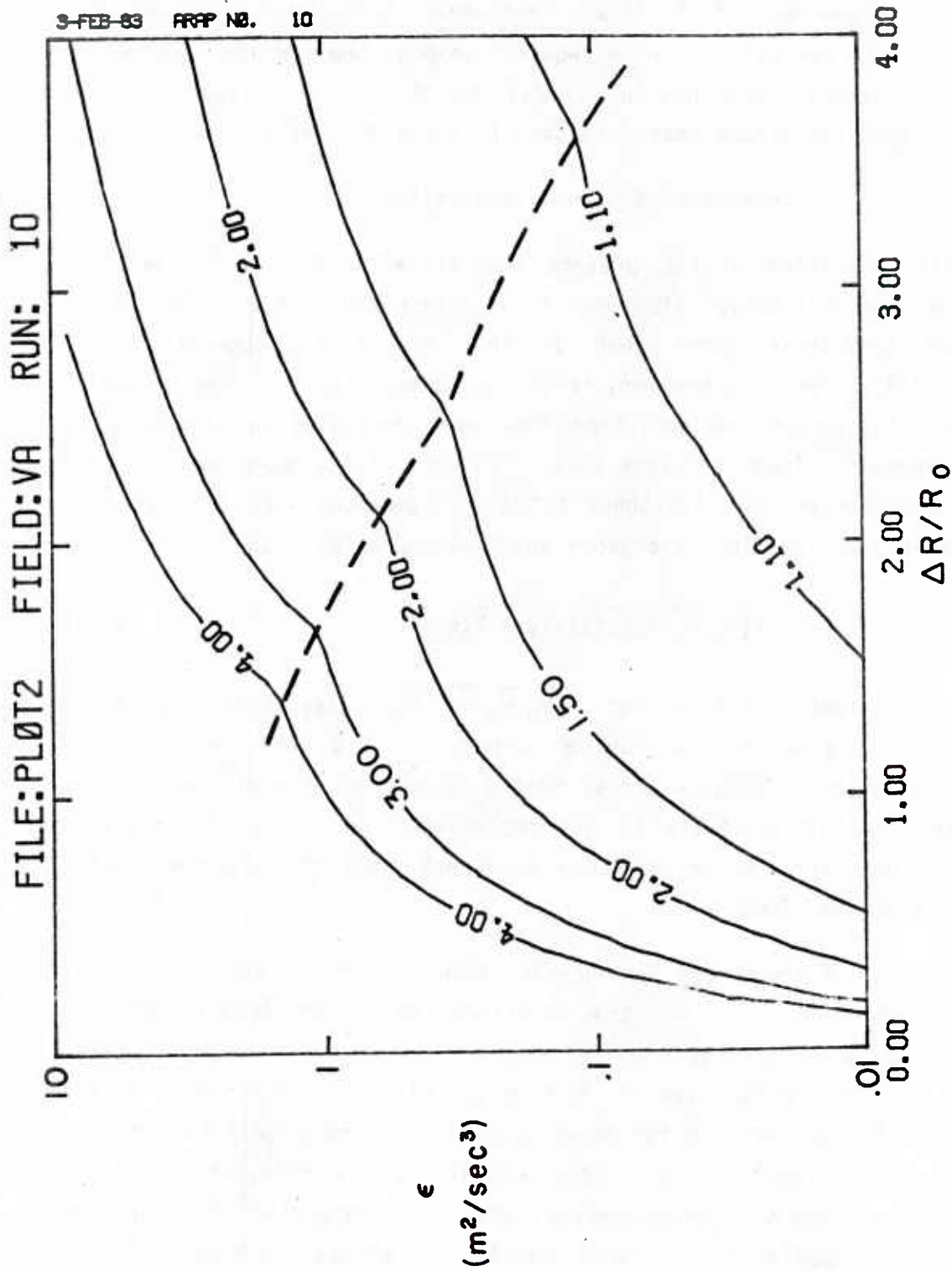


Figure A4. Isopleths of the ratio of total collision kernel, $K(s) + K(ds)$ with all turbulence effects included to the gravitational sedimentation kernel, $K(do)$ (in which \bar{a} is suppressed) as a function of turbulence dissipation rate ϵ and the difference in collisional partner radii $\Delta R/R_0$. The elementary cloud drop radius R_0 is $6 \mu\text{m}$. At high turbulence levels and for larger drop sizes, the turbulent droplet effects are no longer correlated with the full cascade.

1000 μm are still correlated with the large eddies, the turbulence equation for the cloud and precipitation will not require any de-correlation of the droplet motion in the bulk of the flow. Appropriate turbulence equations with droplet de-correlation will only be required deep in the surface layer where the time of turbulence approaches the relaxation time of the largest drops. Such surface layer forms have been developed by Lewellen (1977).

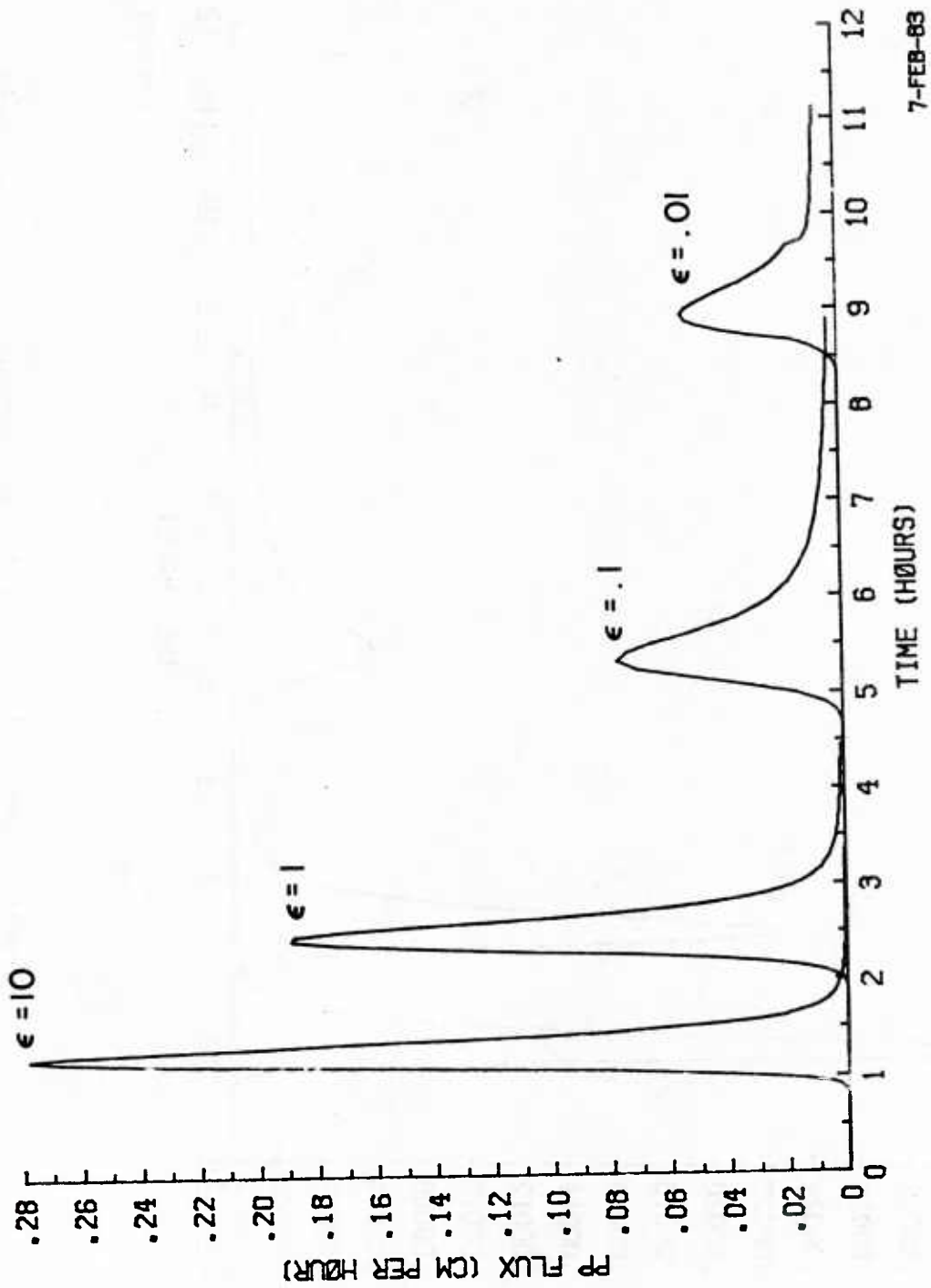
Homogeneous Cloud Illustration

The full properties of the present theoretical model for cloud and precipitation can only be revealed when it is integrated with a fully-coupled inhomogeneous turbulence model such as that of Oliver, Lewellen, and Williamson (1978). We can, however, reveal certain of its features including the general behavior of the evolution time and precipitation intensity in simple homogeneous cloud illustrations. In this first homogeneous cloud illustration, we neglect all transport terms in Equations A.40 through A.43 except the precipitation flux divergence which we approximate as

$$\partial(\overline{V_{pi}q_p} + \overline{V_{pi}'q_p'}) / \partial x_i = \overline{V_p q_p} / \ell_c \quad (\text{A.59})$$

with a similar representation for $\partial(\overline{V_{pi}n_p} + \overline{V_{pi}'n_p'}) / \partial x_i$ where ℓ_c is a characteristic cloud depth. We further assume that at time $t=0$ the total liquid water existing is cloud water so that $\overline{q_p}(0)=0$. We also assume that the liquid water existing initially is not replenished by further decreases in saturation mixing ratio or by moisture transport into the cloud as water precipitates from the cloud.

The evolution of the cloud and precipitation variables for a range of turbulence dissipation rates for the conditions of marine cloud in Table A6 are shown in Figures A5 through A7. The most basic and general trend in these illustrations is in the decrease of the time to reach a maximum precipitation water level as well as the time for onset of a significant precipitation flux as the turbulence levels rise. This result is a manifestation of the increased rates N_{cc} and N_{cp} (which control the auto-conversion of cloud) as the turbulence dissipation level rises. At the very highest turbulence levels $\epsilon \sim 1-10 \text{ m}^2/\text{s}^3$ the cloud droplets are progressively de-correlated with the smallest scale eddies in the cascade and the turbulent shearing mechanism



7-FEB-63

Figure A.5 Precipitation Flux for homogeneous cloud illustration for various turbulence dissipation rates.

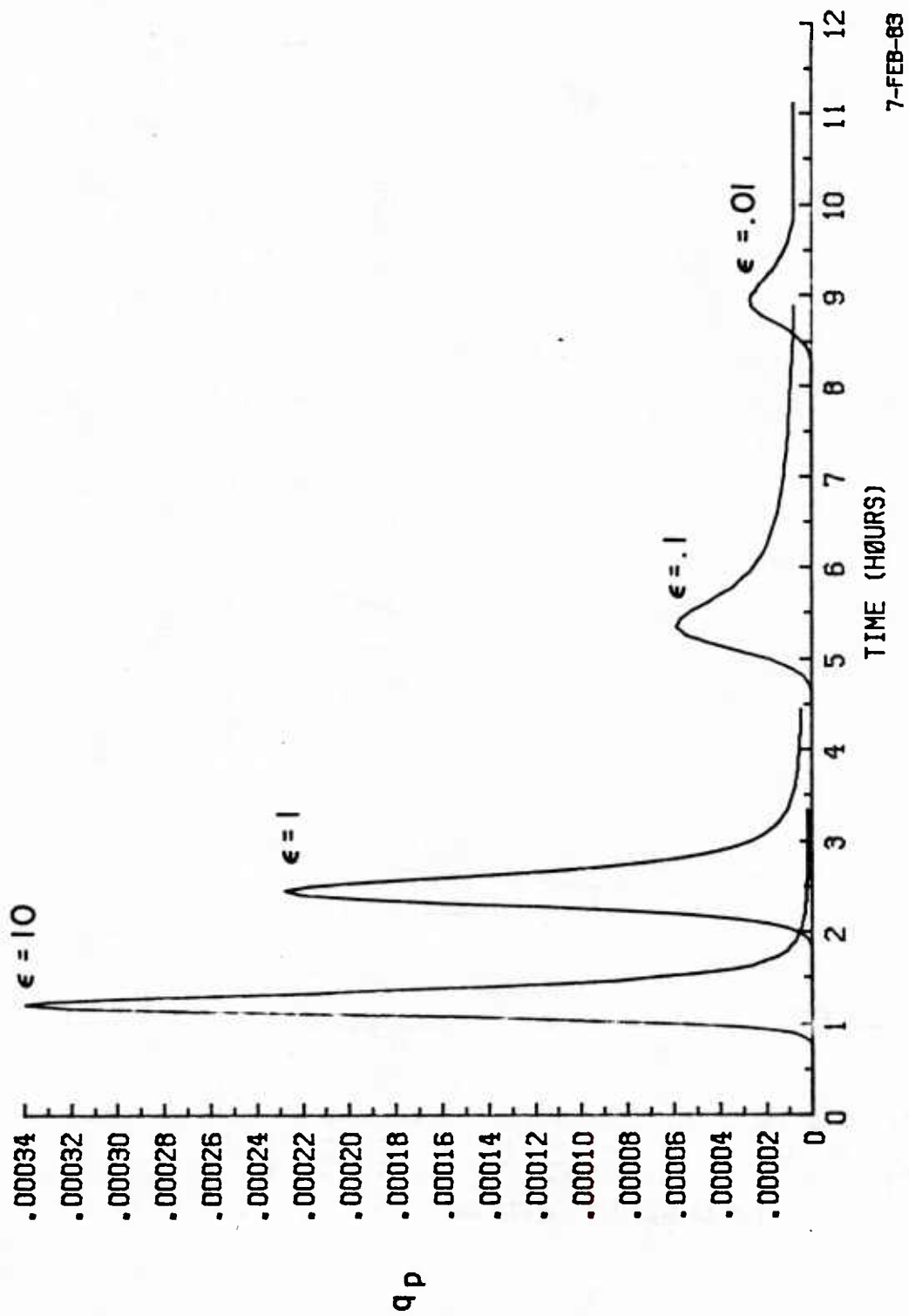
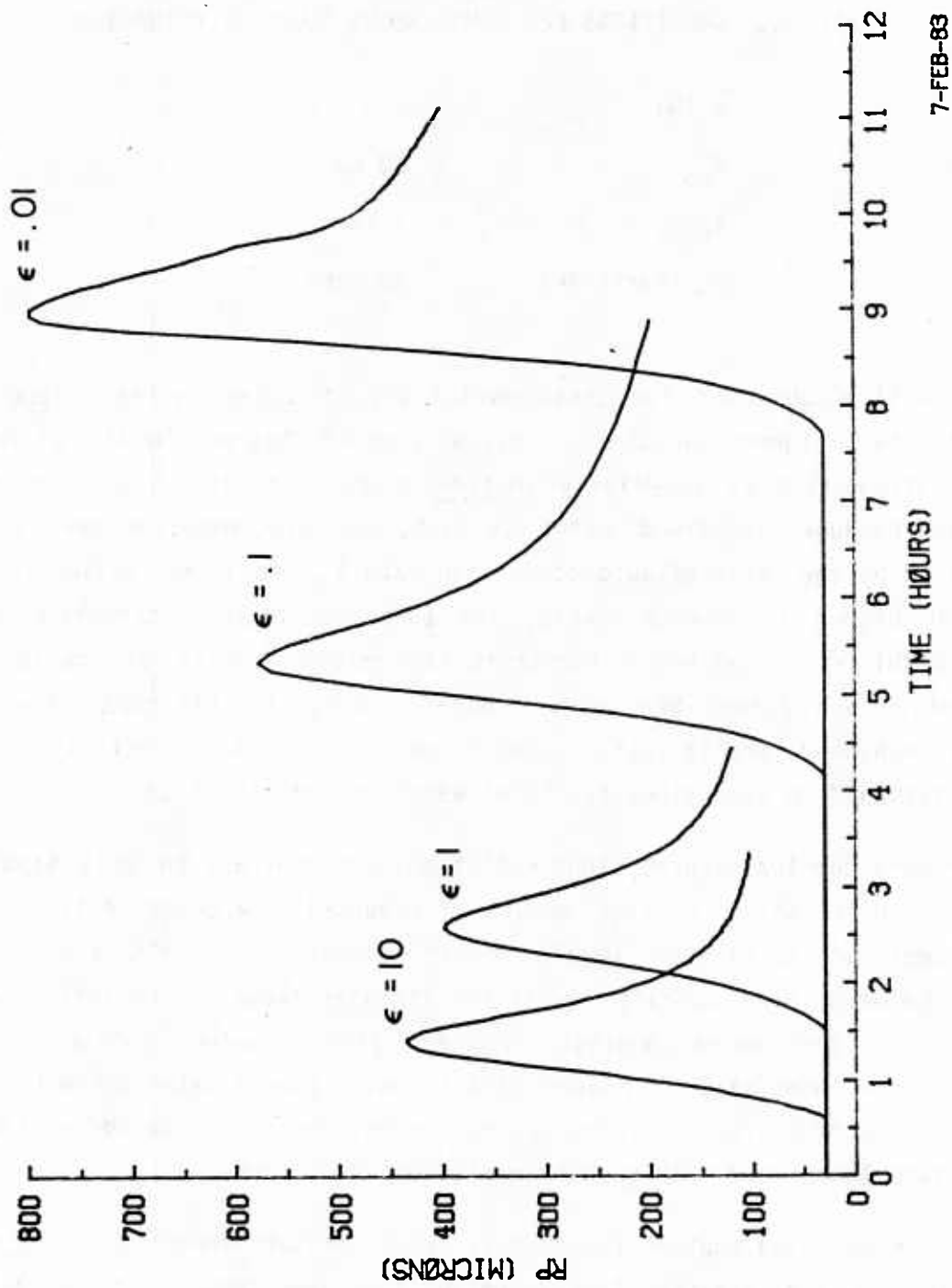


Figure A.6 Precipitation mixing ratio for homogeneous cloud illustration for various turbulence dissipation rates.



7-FEB-63

Figure A.7 Precipitation drop radii for homogeneous cloud illustration for various turbulence dissipation rates.

becomes limited; the turbulent acceleration \bar{a} continues to grow, however, as $\epsilon^{1/3}$.

TABLE A6. CONDITIONS FOR HOMOGENEOUS CLOUD ILLUSTRATION

$\bar{q}_l(0)$	1.0 g/kg
R_{po}	30 μm
z_c	1 km
n_0 (maritime)	200/cm ³

It will be observed for these evolutions at fixed initial cloud water content that higher turbulence levels promote higher levels of maximum precipitation flux at relatively smaller average precipitation drop sizes. This is because at fixed water content, the precipitation drop size is controlled by the ratio of auto-conversion rate N_{cp} to cloud collection rate N_{pc} . At higher turbulence levels, the turbulent shear contribution to N_{cp} enhances this ratio and hence increases the number density of precipitation drops which are formed before the cloud is completely collected. The result of the enhanced precipitation number density is a relatively smaller precipitation drop size since the total water content is fixed.

In more complex natural cloud evolutions (in contrast to this simplified illustration in which a fixed amount of cloud water appears instantaneously independent of turbulence level) higher turbulence levels are strongly correlated with high updraft levels (or stronger cloud top radiative cooling in stratus) and correspondingly higher liquid water content. Since precipitation drop size increases directly with liquid water content, larger precipitation drop size predicted by the present model will be correlated with higher turbulence levels in such natural cloud evolutions.

It may be noted that at the highest levels of turbulence ($\epsilon \sim 1-10 \text{ m}^2/\text{s}^3$) a significant precipitation flux is established over several tens of minutes. Such turbulence levels may be characteristic of the dynamics within strong cumulus cells and it is of interest to examine the evolutions predicted here

with those of a popular precipitation model (Kessler, 1969) which is parameterized for strong cumulus convection and contains no mechanistic description of the role of turbulence. The results of the same case presented in Figures A5 through A7 predicted by the Kessler model are shown in Figure A8. The time scales and general evolution seem comparable to the present model for turbulence levels $\epsilon \geq 1\text{m}^2/\text{sec}^3$, save for the smaller precipitation sizes predicted. It should be noted, however, that the present model has no empirical parameters restricting it to such cumulus clouds. Thus, the high turbulence levels of the present model generate precipitation of high number density and moderate size ($R_p \approx 450 \mu\text{m}$). Thus, while the Kessler model by virtue of its parameterization is incapable of describing the stratus case in absence of updraft, we believe the present model when integrated with fluid dynamic mean motion including an updraft, would predict rain drop sizes consistent with the Kessler model and the Marshall-Palmer parameterization which is the key part of its model structure.

Concluding Remarks

Atmospheric turbulence can play a significant role in the evolution and development of cloud and precipitation. Both collisional and non-collisional turbulent processes can be operative; in the present work we have developed the turbulent collisional effects in detail, incorporated them in a simplified microphysical closure model, and carried out the appropriate turbulent ensemble averages with attention to the droplet correlations with the turbulent eddy cascade. Further study is required to define the conditions under which non-collisional turbulence mechanisms are important.

The operational model for cloud and precipitation which has been developed exhibits results in terms of time scales and magnitudes of precipitation sizes and fluxes which are consistent with those naturally occurring in the atmosphere. The turbulence levels which effect these results are typical of naturally occurring turbulence levels in the atmosphere.

The present model provides an extension of Kessler's parameterization by providing a direct dependence on turbulence level of his parameter for autoconversion from cloud water to rain water. This generalization is accomplished at the expense of carrying two more variables; the turbulence

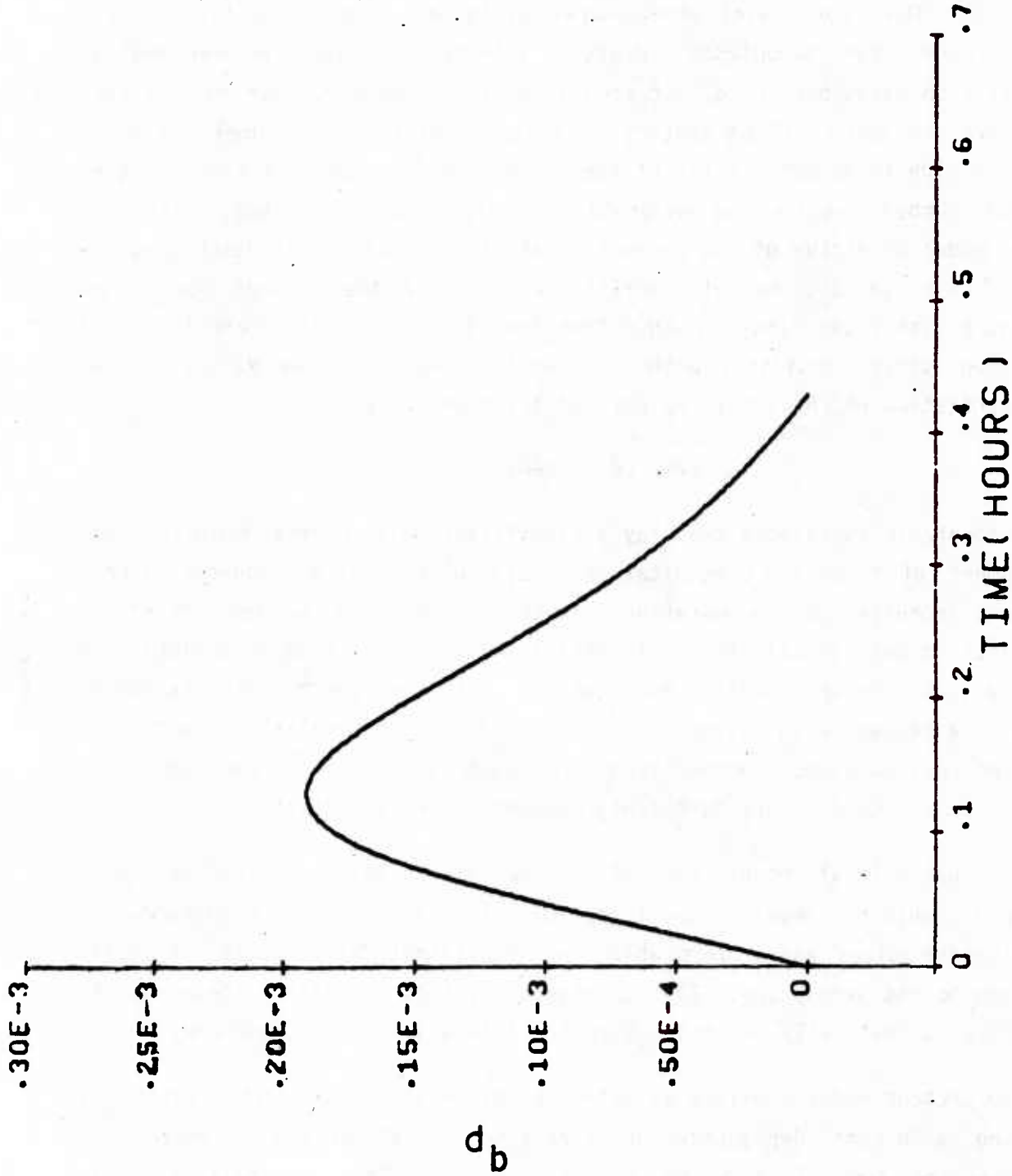


Figure A.8 Evolution of the precipitation water mixing ratio for the homogeneous cloud evolution conditions of Figures (A.5)-(A.7) as predicted by the Kessler model. There is no dependence upon turbulence in the Kessler Model.

dissipation rate and the cloud drop number density. Even if the turbulence dissipation rate is not directly carried in a numerical cloud model, it can be approximately related to whatever dynamical variables are provided to control entrainment. Variations in the cloud drop number density from its environmental input value provide the measure of dispersion in the cloud droplet spectrum which is essential in describing the evolution from cloud to precipitation.

REFERENCES

- Baker, M.B., R.G. Corbin and J. Latham, 1980: "The influence of entrainment on the evolution of cloud droplet spectra: I. A model of inhomogeneous mixing," *Quart. J. Roy. Meteor. Soc.*, 106, 581-598.
- Bartlett, J.T. and P.R. Jonas, 1973: "On the Dispersion of the sizes of droplets growing by condensation in turbulent clouds," *Quart. J. Roy. Meteor. Soc.*, 98, pp. 150-164.
- Batchelor, G.K., 1950: *Quart. J. Roy. Meteor. Soc.*, 76, 133.
- Berry, E.X., 1967: "Cloud Droplet Growth by Collection," *J. Atmos. Sci.*, 24, 688-701.
- Gunn, R., and G.D. Kinzer, 1949: "The terminal velocity of fall for water drops in stagnant air," *J. Meteor.*, 6, 452-461.
- Jeou-Jong, J., 1966: "Statistical Theory of Precipitation Process," *Tellus*, XVIII 4, 722-729.
- Jonas, P.R., and B.J. Mason, 1982: "Entrainment and the droplet spectrum in cumulus clouds," *Quart. J. Roy. Meteor. Soc.*, 108, 857-869.
- Kessler, E., 1969: "On the Distribution and Continuity of Water Substance in Atmospheric Circulations," *Met. Monograph*, 10, No. 32, American Meteorological Society, Boston, 84 pp.
- Levin, L. and Yu. S. Sedunov, 1966: "The Theoretical Model of the Drop Spectrum Formation Process in Clouds," *PAGEOPH* 69, 320-335.
- Lewellen, W.S., D.A. Oliver, M.E. Teske, H. Segur, and O. Cote (1977): "1977 Status Report on Low-Level, Atmospheric Turbulence Model for Marine Environments," A.R.A.P. Report No. 320.
- Lewellen, W.S., D.A. Oliver, M.E. Teske, H. Segur, and O. Cote, 1977: "1977 Status Report on Low-Level, Atmospheric Turbulence Model for Marine Environments," A.R.A.P. Report No. 320.

- Marshall, J.S., and W. McK. Palmer, 1948: "The distribution of raindrops with size," *J. Meteor.*, 5, 165-166.
- Mason, B.J., 1971: *The Physics of Clouds*, Clarendon Press, Oxford, 671 pp.
- Mason, B.J., and P.R. Jonas, 1974: "The evolution of droplet spectra and large droplets by condensation in cumulus clouds," *Quart. J. Roy. Meteor. Soc.*, 100, 23-38.
- Oliver, D.A., W.S. Lewellen and G.G. Williamson, 1978: "The Interaction Between Turbulent and Radiative Transport in the Development of Fog and Low-Level Stratus," *J. Atmos. Sci.*, 35, 301-316.
- Orville, H.D., and Jeng-Ming Chen, 1982: "Effects of Cloud Seeding, Latent Heat of Fusion, and Condensate Loading on Cloud Dynamics and Precipitation Evolution: A Numerical Study," *J. Atmos. Sci.*, 39, 2807-2827.
- Saffman, P.G. and J.S. Turner, 1956: "On the Collision of Drops in Turbulent Clouds," *J. Fluid Mech.*, 1, 16-30.
- Sedunov, Yu. S., 1974: *Physics of Drop Formation in the Atmosphere*, John Wiley & Sons, New York, NY.
- Smoluchowski, M., 1917: *J. Phys. Chem.*, 92, 129.
- Swift, D.L., and D.K. Friedlander, 1964: "The Coagulation of Hydrosols by Brownian Motion and Laminar Shear Flow," *J. Colloid Sci.*, 19, 621-647.
- Taylor, G.I., 1935: *Proc. Roy. Soc. A.*, 151, 429.
- Twomey, S., 1966: "Computations of Rain Formation by Coalescence," *J. Atmos. Sci.*, 23, 404-441.
- Warshaw, M., 1967: "Cloud droplet Coalescence: Statistical Foundations and a One-dimensional Sedimentation Model," *J. Atmos. Sci.*, 24, 278-286.
- Wilhelmson, R.B., and J.B. Klemp, 1981: "A three-dimensional numerical simulation of splitting severe storms on 3 April 1964," *J. Atmos. Sci.*, 38, 1581-1600.

APPENDIX B

INCORPORATION OF AN ANISOTROPIC LENGTH SCALE INTO SECOND-ORDER CLOSURE MODELING OF THE REYNOLDS STRESS EQUATION

by R. I. Sykes, C. Cerasoli*
W. S. Lewellen and C. Swanson*

INTRODUCTION

A critical feature of any second-order closure model is how the macroscopic nature of a given turbulent flow field is incorporated into the model. A second-order closure model attempts to provide a unique relationship between the means, variances and covariances of the primary variables independent of specific boundary conditions. Since turbulence is a property of the macroscopic flow field rather than a local, single point property of the fluid, it is natural to expect that some information from the two point averages will be required to uniquely define the relationships between the first and second-order moments at a single point. In current models this macroscale information is supplied either by a length scale equation, or equivalently an equation governing the dissipation of turbulent kinetic energy. All other macroscales entering the problem are then assumed to be directly proportional to this single macroscale. This assumption is not universally valid, particularly in the presence of a wall and/or stratification.

Lewellen and Sandri (1980) made an attempt to introduce a simple two scale approach in order to permit the horizontal velocity variance to follow completely different scaling than that obeyed by the vertical velocity variance in the atmospheric surface layer under unstable, convective conditions. The resulting two scale model permitted the horizontal velocity variance to scale with the mixed layer height, consistent with available data, rather than follow the Monin-Obukhov scaling which governs the vertical velocity variance. The present report describes how this same result can be

*The contributions of C. Cerasoli and C. Swanson to this work were supported by other Navy contracts.

obtained in a more natural way which provides a firmer foundation for extending the model to more general flows. By considering the turbulent energy to be composed of two populations of eddies, one large and one small, the two length scales appear naturally. The only empirical information needed to complete the model is an algebraic relationship governing the partition of the Reynolds stress between the large and the small scales.

A MODEL FOR THE WALL-EFFECT

Our conceptual model of the turbulent flow near a wall without shear is motivated by the turbulence spectra measured near walls. The spectra of Thomas and Hancock (1977), Willis and Deardorff (1974), and Kaimal (1978) all show the same general features, namely that the wavelength of the peak in the normal velocity component spectrum decreases linearly to zero at the wall, while that of the tangential components remains roughly constant. Kaimal's spectra are shown in Figure B1. This is interpreted straightforwardly as large eddies being forced to flow tangential to the wall, so that their normal velocity component vanishes, and only small local eddies contain any significant normal energy.

Previous second-order closure models only contain one length (or time) scale, and this always goes linearly to zero at the wall. Thus we expect such models to be able to predict normal component correlations reasonably well, but not the horizontal ones. Our remedy for this problem is to consider the flow near the wall to be comprised of two populations of eddies. The first is the small scale population which is the one currently described by second-order closure models. This population has a length scale proportional to the distance from the wall, and is fully three-dimensional, i.e., all components of the Reynolds stress tensor have the same order of magnitude. The second population are the large eddies with a length scale determined by the flow scales away from the wall. These eddies are two-dimensional at the wall since their normal energy component vanishes. We therefore write our modeled Reynolds stress equations as follows:

$$\frac{D}{Dt} \overline{u_i u_j} = - \overline{u_i u_k} \frac{\partial u_j}{\partial x_k} - \overline{u_j u_k} \frac{\partial u_i}{\partial x_k} + g_j \overline{u_i \theta} + g_i \overline{u_j \theta}$$

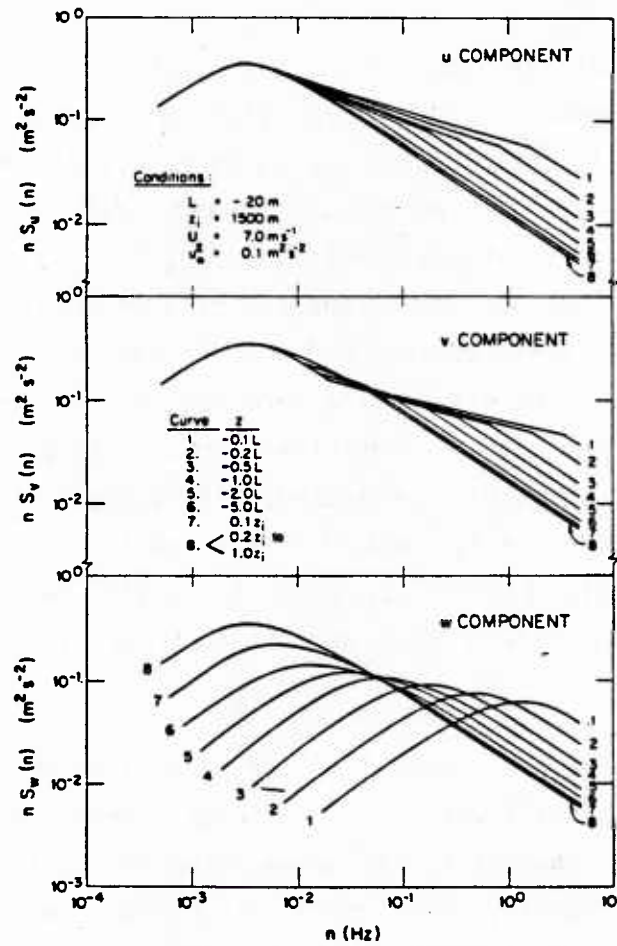


Figure B1.

Normalized velocity spectra as a function of height for the atmospheric boundary layer under thermally unstable conditions (Kaimal, 1978). The spectral peaks for the horizontal velocities, u and v , remain constant, while the spectra peak for w moves to small lengths as the ground is approached.

$$\begin{aligned}
& - \frac{q_L}{\Lambda_H} \left(\overline{u_i u_j^L} - \frac{q_L^2}{2} (\delta_{ij} - n_i n_j) \right) - \frac{q_S}{\Lambda_V} \left(\overline{u_i u_j^S} - \frac{q_S^2}{3} \delta_{ij} \right) \\
& + v_c \frac{\partial}{\partial x_\ell} \left[\left(q_S \Lambda_V \delta_{\ell m} + q_L \Lambda_H (\delta_{\ell m} - n_\ell n_m) \right) \frac{\partial}{\partial x_m} \overline{u_i u_j} \right] - \frac{2}{3} b \frac{q_S^3}{\Lambda_V} \delta_{ij}
\end{aligned} \tag{B.1}$$

where $\overline{u_i u_j}$ is the total Reynolds stress, and $\overline{u_i u_j^L}$, $\overline{u_i u_j^S}$ represent the large and small contributions, respectively; also $q_L^2 = \overline{u_i u_j^L}$, and $q_S^2 = \overline{u_i u_j^S}$. Λ_V is the normal or vertical (anticipating the convective application) length scale, and Λ_H is the tangential or horizontal length scale. $\overline{u_i \theta}$ is the turbulent heat flux, g_i is the gravitational vector, and $n_i = (0, 0, 1)$ is the unit vector normal to the wall. Thus our model consists of a three-dimensional "return to isotropy" term for the small eddies, and a corresponding two-dimensional term for the large eddies. The dissipation term depends only on the small eddies, since the large eddies must cascade their energy through the small scale eddies before it is ultimately dissipated. The diffusion term contains small eddies diffusing isotropically, whilst large eddies only diffuse in the tangential plane. Note that if $\overline{u_i u_j^L} = 0$, i.e., all the energy is in small scales, then we recover the single scale equations of Lewellen (1977) with $b=1/8$, $v_c=0.3$.

At this stage we have not specified the partition of $\overline{u_i u_j}$ between large and small scales; we shall make this partition algebraically by reference to the measured spectra. The horizontal energy spectra from the experiment of Thomas and Hancock (1977), show that after the energy peak at a scale determined by the free stream turbulence, the spectrum falls off smoothly into an inertial range with no irregularity at the smaller scales where the vertical energy peaks. This spectral shape is very similar in Kaimal's atmospheric measurements--provided the spectra are taken outside the surface shear layer, i.e., $z/L \gtrsim 5$, where z is the height above the ground and L is the Monin-Obukhov length. The existence of an inertial range prompts the use of a simple scaling law to estimate the small scale horizontal energy, viz.

$$\overline{u_i u_j^s} = \left(\frac{\Lambda_V}{\Lambda_H} \right)^{2/3} \overline{u_i u_j}, \quad i \neq 3, j \neq 3$$

Thus, the horizontal energy at wavelengths of order Λ_V are simply scaled down from the large wavelength total by the ratio of length scales to the two-thirds power. To complete the model, we have

$$\overline{u_i u_j^s} = \overline{u_i u_j}, \quad i=3 \text{ or } j=3$$

and

$$\overline{u_i u_j^L} = \overline{u_i u_j} - \overline{u_i u_j^s}.$$

Thus all the energy in correlations involving the vertical component is contained in small scales, and the large eddy energy is the remainder; hence there is no large eddy energy in vertical components.

To complete the model specification, we write the heat flux equations as

$$\frac{D}{Dt} \overline{u_i \theta} = - \overline{u_i u_j} \frac{\partial T}{\partial x_j} + \frac{g_i}{T} \overline{\theta^2} - A \frac{q_s}{\Lambda_V} \overline{u_i \theta} \quad (\text{B.2})$$

and temperature variance:

$$\frac{D}{Dt} \overline{\theta^2} = - 2 \overline{u_j \theta} \frac{\partial T}{\partial x_j} - 2bs \frac{q_s}{\Lambda_V} \overline{\theta^2} \quad (\text{B.3})$$

These are the standard equations from Lewellen (1977), and we use the same coefficients, i.e., $A=0.75$, $s=1.8$, which is tantamount to assuming that the temperature fluctuations are all in the small scale part of the spectrum. This is justified because the production terms in these equations only involve the vertical velocity component which is only present at small scale.

Finally, length scales are specified by the same scale equation as Lewellen (1977) for the vertical scale, but using small scale energies appropriately, i.e.

$$\begin{aligned} \frac{D\Lambda_V}{Dt} = & 0.35 \frac{\Lambda_V}{q_s^2} \frac{\partial u_i u_j}{\partial x_j} + 0.6bq_s + 0.8 \frac{g_i}{T} \frac{\Lambda_V}{u_i \theta} \frac{\Lambda_V}{q_s} \\ & + 0.3 \frac{\partial}{\partial x_j} \left(q_s \Lambda_V \frac{\partial \Lambda_V}{\partial x_j} \right) - \frac{3}{8q_s} \left[\frac{\partial}{\partial x_j} (q_s \Lambda_V) \right]^2 \end{aligned} \quad (\text{B.4})$$

and $\Lambda_H = \max \Lambda_V$ where the maximum is taken over the domain.

Thus, in essence we accept that the original model described by Lewellen (1977) does a creditable job of predicting the small scale part of the spectrum near the wall, and we therefore maintain the small scale dynamics. However, we include a two-dimensional large scale component which is dominant near the wall, and use an inertial range scaling law to obtain the partition between the two energies. Note that although this conceptual model was arrived at through consideration of the turbulence close to the wall, the model reverts naturally to the single scale model as one moves out to the middle of the flow because $\Lambda_V \approx \Lambda_H$ in the central region, and therefore $\overline{u_i u_j}^L \approx 0$.

MODEL RESULTS FOR SHEAR-FREE FLOWS

Convection between Flat Plates at Fixed Temperature

The first experimental flow we compare with is thermal convection between horizontal flat plates held at fixed temperatures. The data for comparison are from Deardorff and Willis (1967), and we use their highest Raleigh number data of 10^7 , since we include no low Reynolds number terms in our model equations. Equations B.1 through B.4 were solved numerically with an imposed heat flux at the lower boundary, $z=0$, and plane of symmetry conditions at $z=D/2$ where D is the distance between the horizontal plates. At the lower boundary we set

$$\frac{\partial}{\partial z} \overline{u^2} = \frac{\partial}{\partial z} \overline{v^2} = \frac{\partial}{\partial z} \overline{\theta^2} = 0$$

and $\overline{w^2} = 0, \overline{w\theta} = H_0$.

Figure B2 shows the r.m.s. turbulence components from the model scaled by w_* where

$$w_*^3 = \frac{g}{T} H_0 D.$$

The experimental values are plotted also as continuous lines with error bars indicating the general level of scatter in the data. Note that the experimental values had to be rescaled for this plot, and it was necessary to use a definite value for the heat flux to achieve this. The value used was the Globe and Dropkin (1959) empirical function value since Deardorff and Willis regard their direct measurements of turbulent heat flux as less reliable; the difference between the values is somewhat less than 10%. There is good agreement between the predicted and measured values for both vertical and horizontal components. There is a slight increase in horizontal energy near the wall in the experiment, and the magnitude of this increase is underpredicted but the model does maintain the horizontal energy right up to the wall and does actually show a 10% increase from the value in the middle of the flow. Below $z=0.075D$, the measured energy falls off toward zero, which is an indication of the viscous boundary layer effect. The vertical energy level is also well predicted, with some over prediction for small z , which again is probably a viscous effect.

Figure B3 shows r.m.s. temperature fluctuations scale by $\theta_* = H_0/w_*$, and again the predicted values are very accurate except in the region close to the surface where molecular diffusion becomes significant.

Convection from a Heated Plate with an Overlying Stable Layer

In this flow, a constant heat flux H_0 is applied at the base of an infinite layer of stably stratified fluid, and a convective mixed layer grows in depth with time. The model was run until a self similar solution was obtained, and the results were plotted in dimensionless form with z_i as the length scale, and $w_*^3 = gH_0z_i/\bar{T}$ as velocity scale. Here z_i is the depth of the mixed layer, measured to the point with maximum temperature variance at the top of the layer. The experimental values are from Willis and Deardorff (1974).

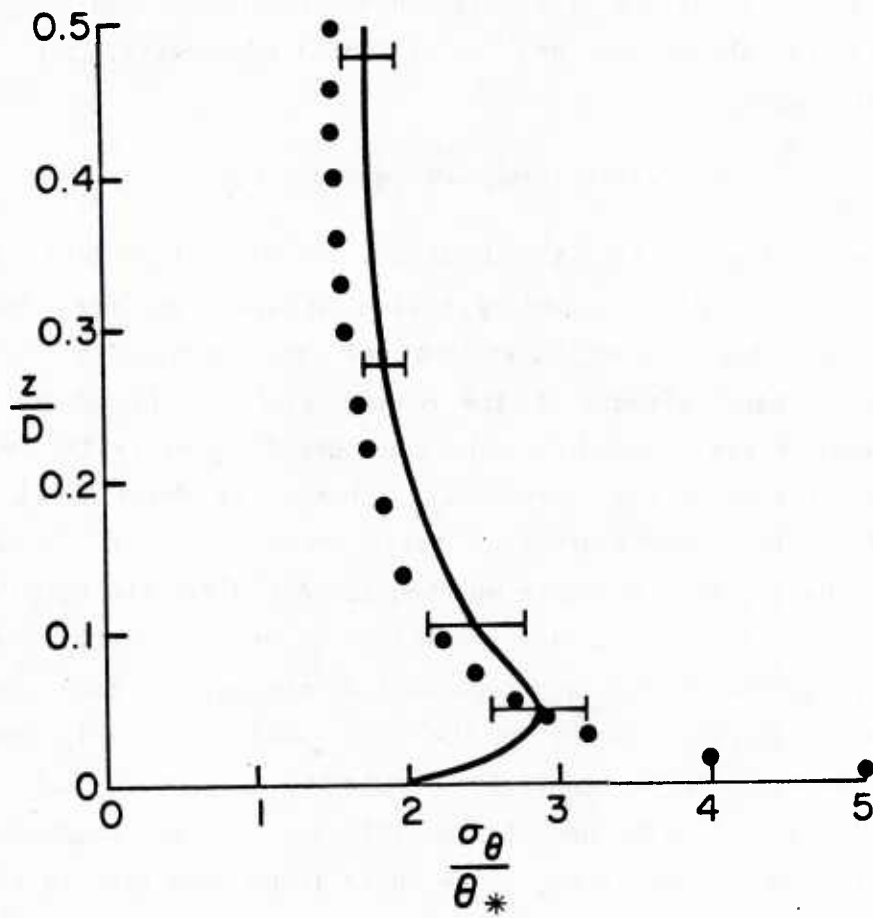


Figure B3. R.m.s. temperature fluctuations for convection between flat plates. Solid line represents the laboratory data, and the model predictions are plotted as dots. Error bars indicate the scatter in the data.

Figure B4 shows velocity variances, and excellent agreement between measured and predicted profiles. It is of interest to note that in this case the horizontal variance is slightly over predicted at the surface. Figure B5 shows the temperature variance which is very closely predicted in the lower 80% of the mixed layer, but the large maximum at the inversion is not predicted. This is a failure of the second-order closure model to predict the entrainment fluxes, which Zeman and Lumley (1976) have noted, but is not the subject of this paper.

Shear-free Turbulent Boundary Layer

In this experiment by Thomas and Hancock (1977), a turbulent free stream is made to pass a plane boundary moving at the same mean speed. This experiment is a rather inconclusive test of the model for two reasons. Firstly, the primary effect of the moving wall is the generation of an impulsive pressure field which brings the normal velocity to rest at the boundary, and distorts the turbulence spectra as described by Hunt and Graham (1978). Our second-order closure model cannot predict this instantaneous change, and therefore we need to initialize the calculation with a field that satisfies the boundary conditions. The experimental section was not very long, so the results are dependent on the initial conditions and the latter were not measured. Secondly, the experiment is clearly non-ideal in the sense that the two tangential components, streamwise and transverse, behave quite differently with downstream distance; the two components must be identical in the ideal experiment, since there is no mean flow in the frame of the moving wall. Furthermore, we found the experimenter's suggestion that streamwise pressure gradients were responsible for the differences to be unsubstantiated, since these were of much too small a magnitude to effect any significant changes when included in the calculation.

We initialized the model with the theoretical profiles of Hunt and Graham, and then integrated forward approximately six turbulence time scales, Λ/q , where Λ and q refer to free stream values. This integration distance was estimated from the measurements of turbulent energy and length scales at the downstream portion of $x/M=25$. In this comparison we have used the relation $L_u=1.5\Lambda$ to relate the integral length scale of the measurements to the model length scale. This relation was obtained by Sandri (1977) for isotropic

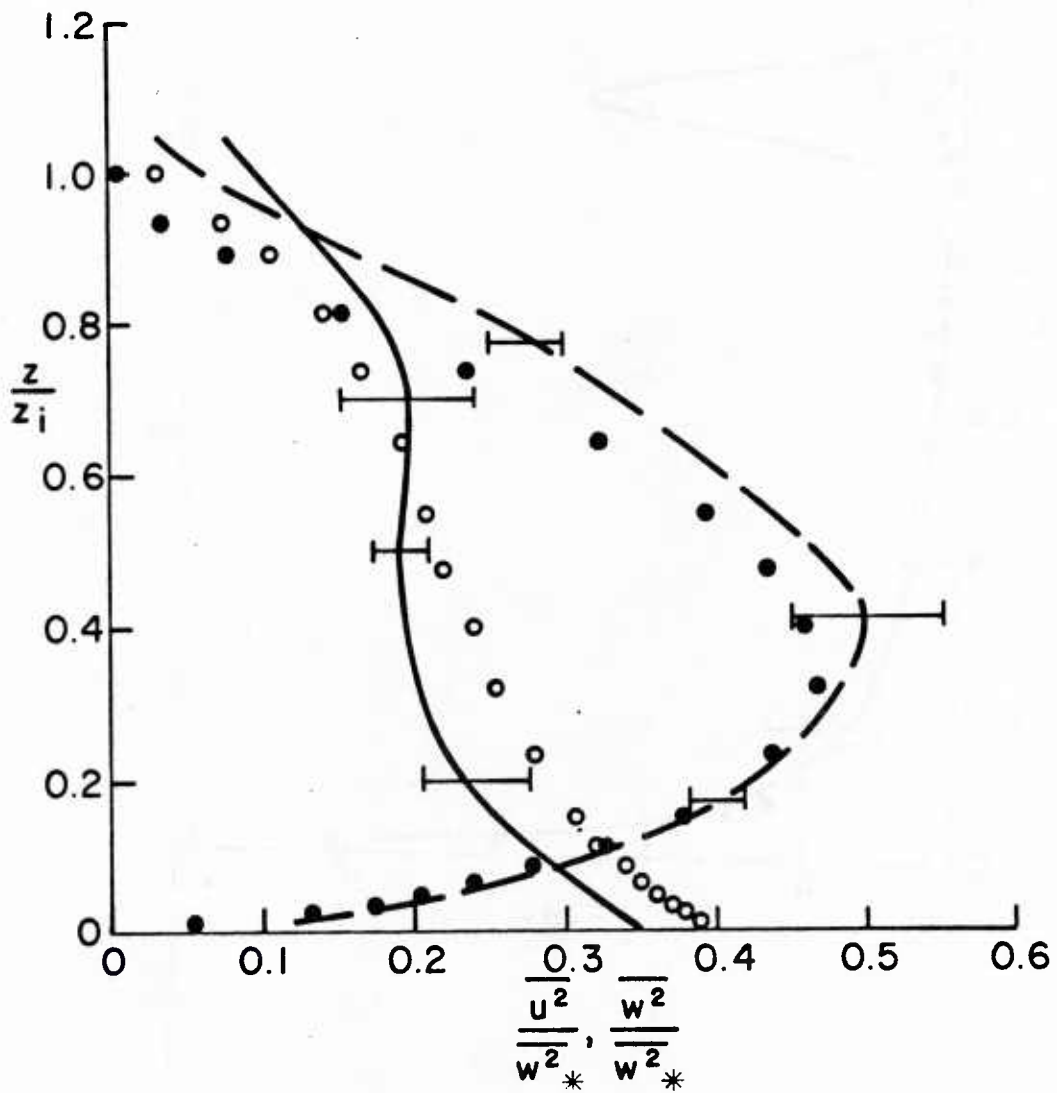


Figure B4. Turbulent velocity variances for inversion-capped convective layer. Symbols are as in Figure B1, and the laboratory data is from Willis and Deardorff (1976).

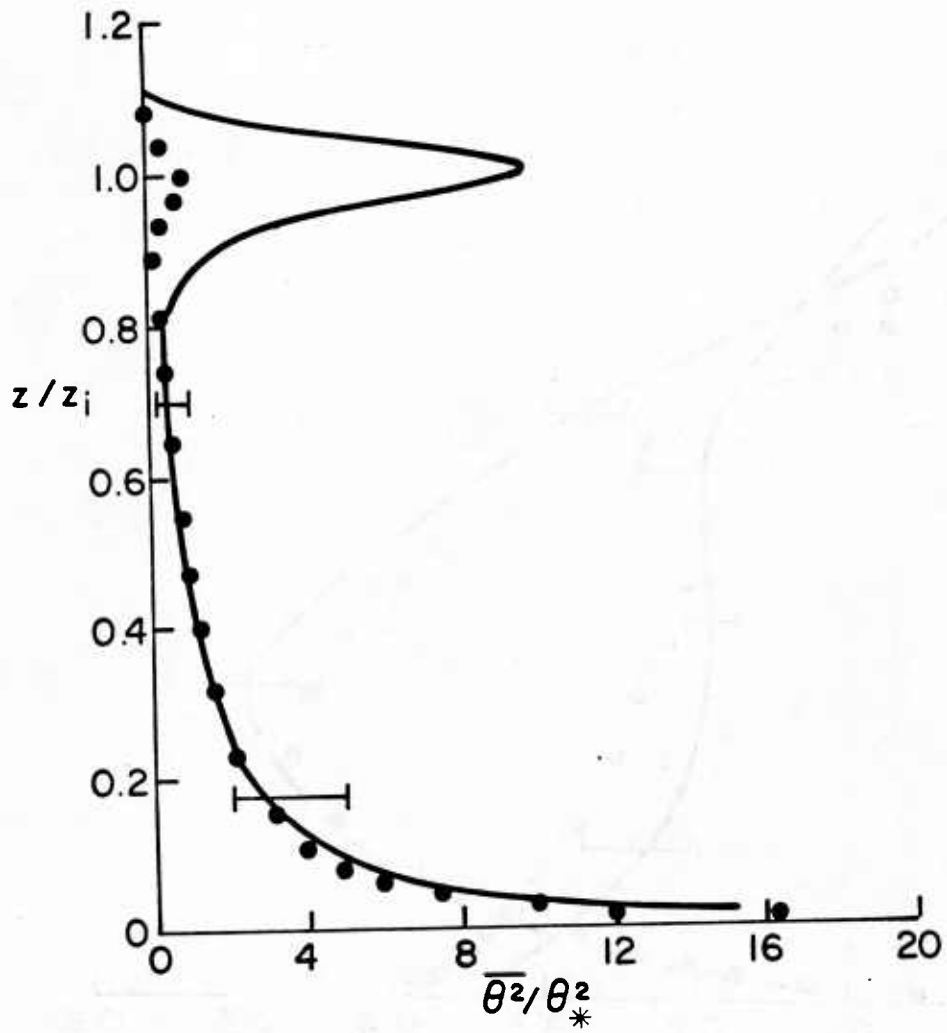


Figure B5. Temperature variances for inversion-capped convective layer. Symbols as in Figure B2.

turbulence and is valid as we use it only for the free stream values.

Figure B6 shows measured and predicted profiles of the normal energy, $\overline{w^2}$, and the transverse energy, $\overline{v^2}$. Velocities are scaled by the free stream turbulent velocities, and the normal coordinate is scaled by the free stream integral length scale. We note that in the experiment, $\overline{u^2}$ shows a strong peak at the wall which increases with downstream distance. Hunt and Graham suggest this could be some disturbance close to the wall diffusing outward, and our predictions undoubtedly show much better agreement with the transverse component, since $\overline{u^2} = \overline{v^2}$ in the model. The main features of the prediction are that the initial peak of 1.5 at the wall in $\overline{v^2}$ is rapidly reduced, and has fallen to 1.03 at $x/M=25$. The asymptotic model value is 0.95 far downstream. The prediction of $\overline{v^2}$ is in close agreement with the measurements, which show a virtually constant value. However, the model prediction of the development of $\overline{w^2}$ is that the initial profile diffuses outward, while the measurements show an unchanging profile. Thus at $x/M=25$, we have the correct shape for the profile, but the scaling length appears to be too big by almost a factor of 2. In view of the non-ideal nature of the experiment in terms of the behavior of $\overline{u^2}$, it seems unwise to speculate on the discrepancies in the comparisons. All we can really conclude is that the model does predict the observed qualitative results.

THE EFFECT OF WALL-LAYER SHEAR

In the atmospheric boundary layer, we generally have both thermal convection and mean shear present at the same time. The relative importance of these two effects in the main part of the boundary layer is measured by the ratio L/z_i , where

$$L = \frac{u_*^3 \overline{T}}{\kappa g H_0}, \text{ the Monin-Obukhov length,}$$

and z_i is the inversion height; u_* is the surface friction velocity, H_0 the surface heat flux, and κ is von Karman's constant, taken to be 0.39 here.

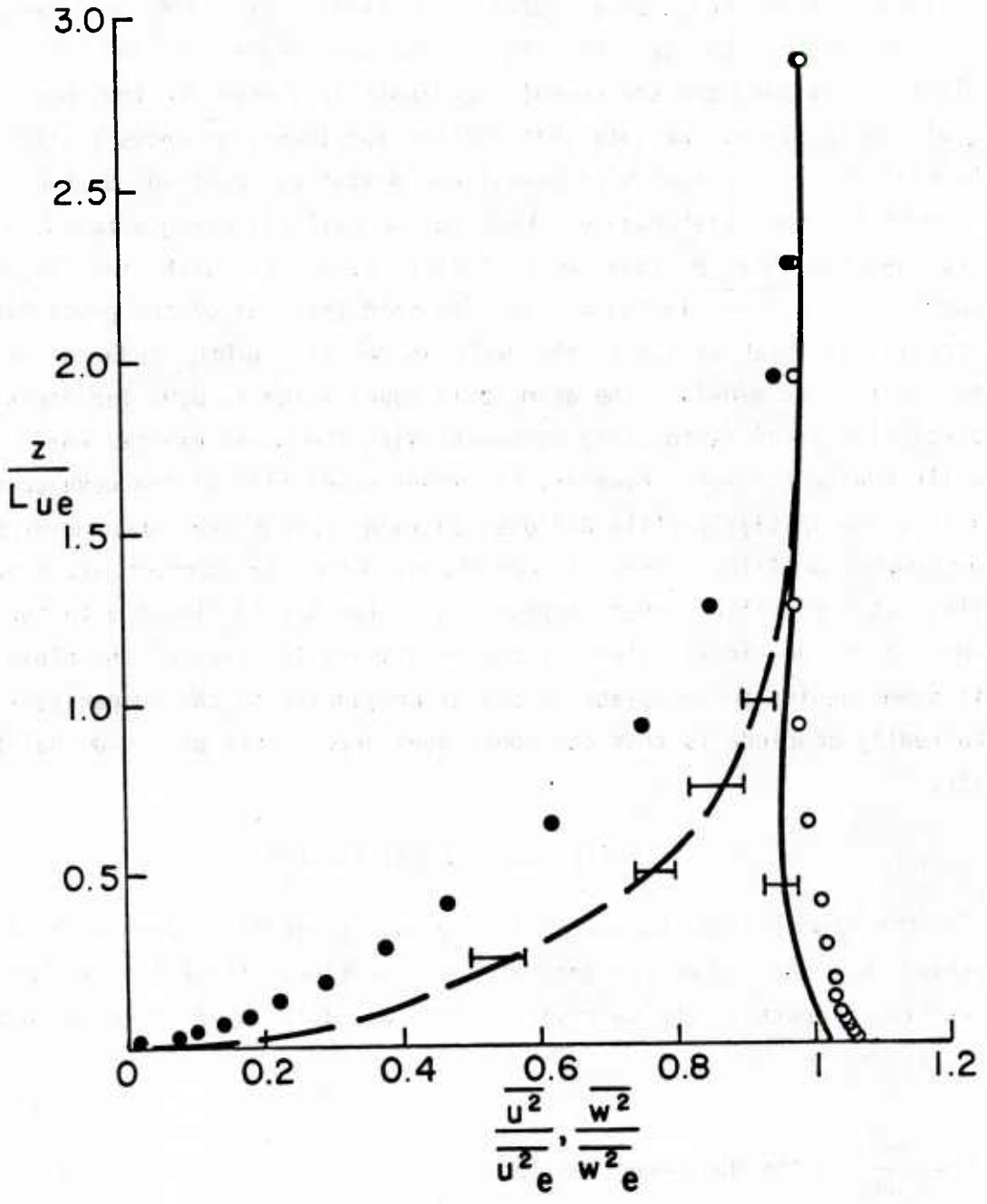


Figure B6. Turbulent velocity variances for the shear-free wall layer compared with the data of Thomas and Hancock (1977). Symbols as in Figure B1.

When $z < 0(L)$, shear effects become important and our simple model of the partition between large and small eddies is then no longer appropriate. In this region, the shear production term in the turbulence energy equation is directly producing significant small scale horizontal energy, and our inertial range scaling law will fail. This can be seen in the spectra of Kaimal (1978), which show a bulge at higher wave numbers in the horizontal spectra where $z < 0(L)$. We therefore require a more sophisticated energy partition. We have tried to keep the partition as simple as possible, since our principal goal in this paper is the development of a model for large eddies near a wall. We shall describe an extension of the algebraic partition which allows the computation of shear flows, and although we base the model on a crude physical model of the energy spectrum, it should be regarded mainly as a simple device to extend the range of applicability of the model to cover practical calculations of the atmospheric boundary layer.

The alternative to an algebraic partition would be to carry two sets of equations for large and small scales separately, in the manner introduced by Hanjalic et al. (1979). Ultimately this may well be the best way to proceed, but the interaction terms between the two scales require a good deal of modeling effort, because Hanjalic et al.'s assumption of isotropy in the small scales is inappropriate here. We therefore prefer to keep the model as simple as possible at this stage, and at least determine what conditions a more general model needs to satisfy.

Our assumption will be that the energy in the small scales arises both from the cascade from larger scales and also from direct production in the small scale part of the spectrum. The small scale production in the case of the atmospheric boundary layer is

$$P_s = -2 \overline{u_i u_j} \frac{\partial u_i}{\partial x_j},$$

i.e. the shear production term, since this is generating small scale energy in the horizontal components near the wall. Since this becomes increasingly dominant near the wall where the time scales are very short, we have

$$2b \frac{q_S^3}{\Lambda_V} \rightarrow P_S \quad \text{as } \frac{z}{L} \rightarrow 0,$$

i.e. the production balances dissipation. In fact, these terms are so singular in the logarithmic layer, that it is necessary to allow this exact balance very close to the wall. Thus

$$\overline{u_S^2} + \overline{v_S^2} = \left(\frac{P_S \Lambda_V}{2b} \right)^{2/3} - \overline{w^2} \quad \text{as } \frac{z}{L} \rightarrow 0$$

Therefore, if

$$f_S = \frac{\overline{u_S^2} + \overline{v_S^2}}{\overline{u^2} + \overline{v^2}},$$

then

$$f_S = \frac{(P_S \Lambda_V / 2b)^{2/3} - \overline{w^2}}{q^2 - \overline{w^2}} \quad \text{as } \frac{z}{L} \rightarrow 0 \quad (\text{B.5})$$

Before combining this result with the energy cascade result, a further complication of the shear production is that it does not necessarily generate $\overline{u_S^2}$ and $\overline{v_S^2}$ equally. A simple equilibrium argument shows that

$$\frac{\overline{u_S^2}}{\overline{u_S^2} + \overline{v_S^2}} = \frac{1 + P_{su}/P_S}{3}$$

where P_{su} is the shear production term in the $\overline{u^2}$ equation. Thus, defining

$$\alpha = \frac{1 + P_{su}/P_S}{3},$$

and

$$f_{so} = \frac{(P_S \Lambda_V / 2b)^{2/3} - \overline{w^2}}{q^2 - \overline{w^2}},$$

our final model for the small scale horizontal components is

$$\overline{u_s^2} = \alpha f_{s0} (\overline{u^2 + v^2}) + \left(\frac{\Lambda_V}{\Lambda_H} \right)^{2/3} \overline{u^2}, f_{s0} > 0 \quad (\text{B.6})$$

$$\overline{v_s^2} = (1-\alpha) f_{s0} (\overline{u^2 + v^2}) + \left(\frac{\Lambda_V}{\Lambda_H} \right)^{2/3} \overline{v^2}, f_{s0} > 0 \quad (\text{B.7})$$

Otherwise

$$\frac{\overline{u_s^2}}{\overline{u^2}} = \frac{\overline{v_s^2}}{\overline{v^2}} = \left(\frac{\Lambda_V}{\Lambda_H} \right)^{2/3} \quad (\text{B.8})$$

Thus we have a simple algebraic partition which satisfies the requirements of allowing an exact small scale balance very close to the wall, and going back to our original inertial large scaling when there is negligible small scale production.

RESULTS FOR THE ATMOSPHERIC SURFACE LAYER

The main point of our large eddy model is that the energy in the horizontal components near the surface is "passive", in the sense that it does not affect the vertical correlations. This is indeed the case, and all the similarity variables in the surface layer are within a few percent of the results of Lewellen and Teske (1974) and are therefore not presented again here. However, the horizontal components now show a larger energy depending on the value of the horizontal scale, Λ_H . In the following comparisons $\Lambda_H = 0.235z_i$; this result is obtained from the scale Equation B.4.

Figure B7 shows a typical surface layer profile for the three energy components with $z_i/L=50$. The velocities are scaled by the surface friction velocity, u_* . The features to note are that $\overline{w^2}$ is 1.4 at the wall, in accord with the neutral log layer value, and then increases asymptotically like $z^{2/3}$ for large z . On the other hand, the horizontal components are larger, and remain relatively constant right down to the wall. There are variations of a

few percent close to the wall, and this is due to the precise nature of our small scale energy partition function. The atmospheric measurements show the horizontal energy remaining constant within the scatter of the data which is about 10%. We might note that several simpler versions of the partition function (i.e., not satisfying all the requirements of Section 4) all gave unreasonable profiles in the sense of energy doubling at the wall or decreasing by 50%.

A comparison of the r.m.s. horizontal energy,

$$\sigma_h = \sqrt{\frac{\overline{u^2} + \overline{v^2}}{2}},$$

against the observed values is shown in Figure B8. We have plotted the value of σ_h from the model at $z/L=3$, i.e., outside the region of the surface variation. The model predictions lie well within the scatter of the observations at moderate z_i/L ; there are only two data points at high values, and the model over predicts these by about 10%.

Finally, we note that with the formulation of small scale energy given by Eqs. B.5-B.7, all the energy is contained in the small scales for neutral flows, e.g., boundary layer or channel flows, and also in the stable atmospheric surface layer. Hence, for these flows the predictions are unchanged from the earlier single scale model.

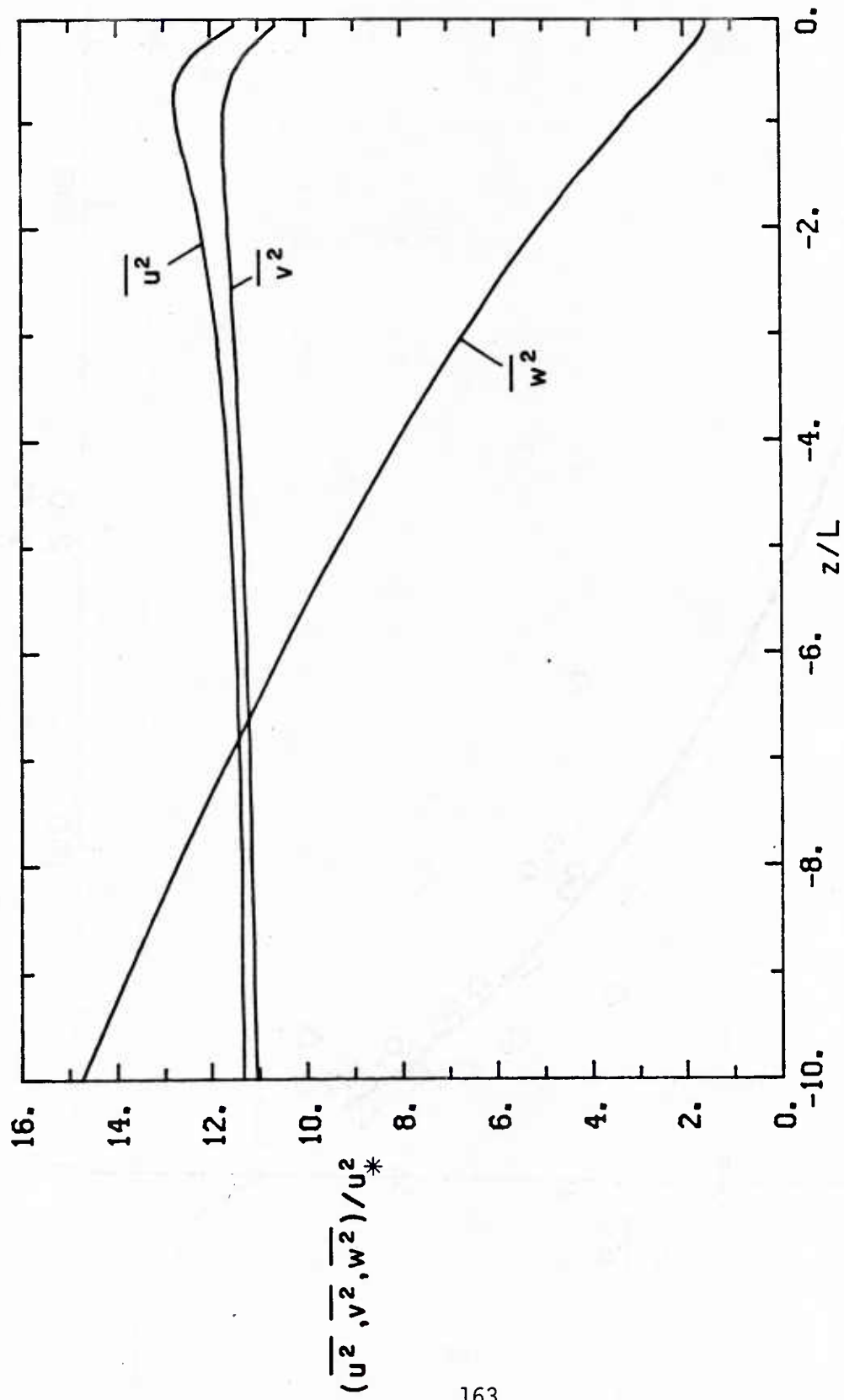


Figure B7. Predicted turbulent velocity variances in the atmospheric surface layer for $z_i/L=50$.

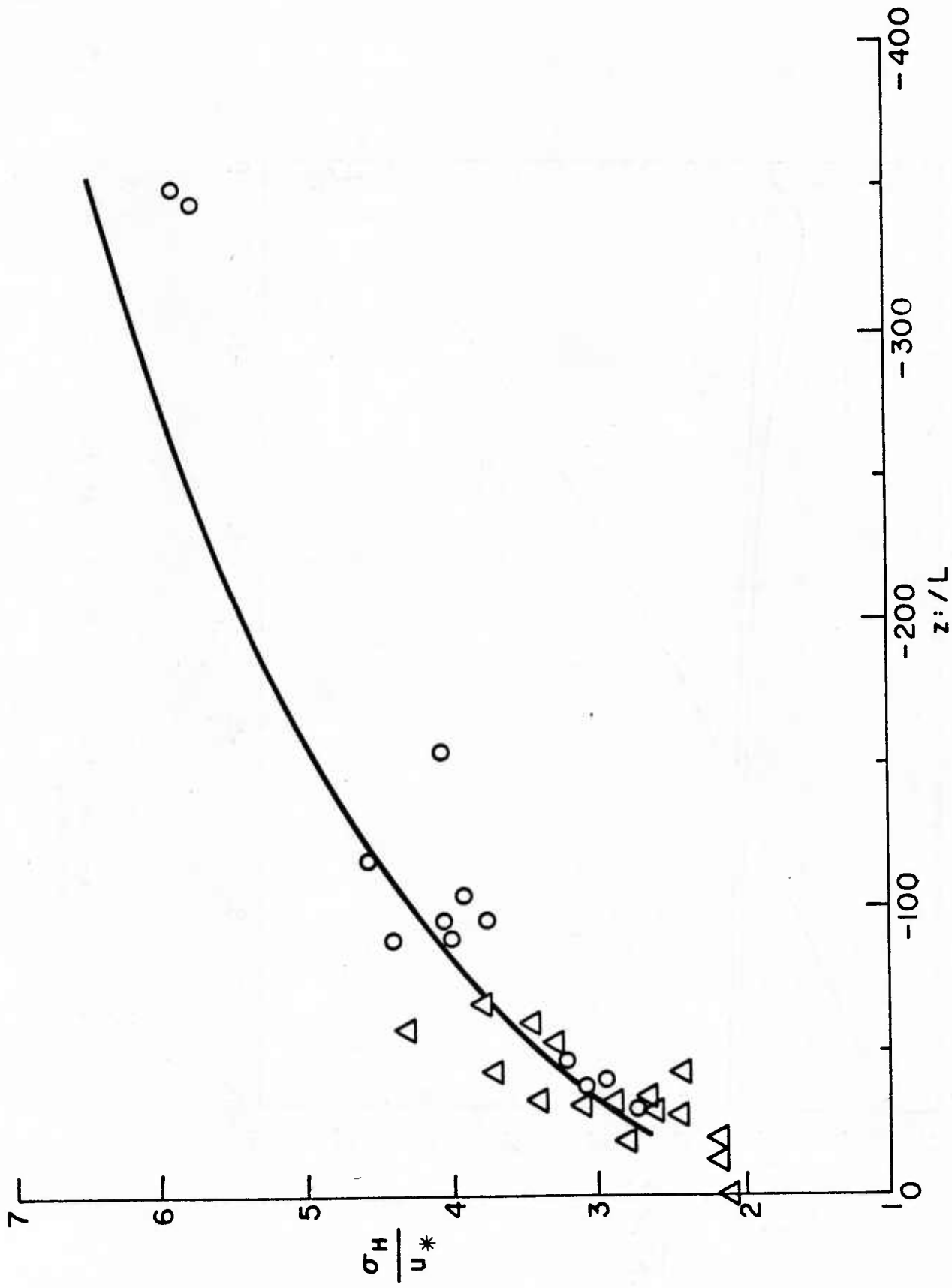


Figure B8. Comparison between r.m.s. horizontal turbulence energy predictions and observations as a function of z/L . The model prediction is shown as a solid line. The data are from Panofsky et al. (1977).

CONCLUSION

A second-order closure model which accounts for the effects of a rigid wall on large scale turbulent eddies has been presented. The basis of the model is a partitioning of the turbulent kinetic energy between small scale three-dimensional eddies and large scale eddies which only have tangential energy components near the wall. The relative partitioning of the tangential energy has been made using the inertial range spectral distribution. The model performs well for a number of flows in which the energy is principally in large scale eddies.

A somewhat over-simplified description of the model would be that we retain the original single scale equations for the small scale component, and then scale up tangential components using the ratio of the two length scales. This view has some utility in that it is correct except for the turbulent diffusion terms in the Reynolds stresses; it also has some basis in observation, since the spectra of tangential velocity components do show an apparently undisturbed inertial range fall off from the energy containing length scales. However, the diffusion terms are not always negligible in the flows we have considered, so that there is some effective coupling between the two scales; in fact the diffusion is the dominant mechanism in the surface layer profiles of horizontal energy in Section 4. Furthermore, the dynamical basis of this model is very useful in developing corresponding two scale equations for passive scalars in the atmosphere, where the small scale is no longer the controlling scale in the equations; the work on scalar diffusion will be presented in a subsequent paper.

The main conclusion from this study is that several aspects of wall turbulence can be accurately described using the very simple conceptual notion of passive horizontal energy, so that the active turbulence is calculated with the usual closure model, but the active part of the turbulence is derived from the total using a simple hypothesis for the spectral shape.

REFERENCES

- Deardorff, J.W. and Willis, G.E. (1967), "Investigation of turbulent thermal convection between horizontal plates," *J. Fluid Mech.*, 28, 675-704.
- Globe, S. and Dropkin, D. (1959), "Natural convection heat transfer in liquids confined by two horizontal plates heated from below," *Heat Trans. & Fluid Mech. Inst.*, pp. 156-176, Berkeley, University of California.
- Hanjalic, K., Launder, B.E., and Schiestel, R. (1979), "Multiple-time-scale concepts in turbulent transport modeling," Second Symposium on Turbulent Shear Flows, Imperial College, London, England.
- Hunt, J.C.R. and Graham, J.M.R. (1978), "Free-stream turbulence near plane boundaries," *J. Fluid Mech.*, 84, 209-235.
- Kaimal, J.C. (1978), "Horizontal velocity spectra in an unstable surface layer," *J. Atmos. Sci.*, 35, 18-24.
- Lewellen, W.S. (1977), "Use of Invariant Modeling," Handbook of Turbulence, Vol. 1, Ed. Frost, W. and Moulden, T.H., Plenum Publishing Corp.
- Lewellen, W.S. and Sandri, G. (1980), "Incorporation of an Anisotropic Scale into Second-order Closure Modeling of the Reynolds-stress equations," Appendix A, Report No. 420, Aeronautical Research Associates of Princeton, Inc., Princeton, NJ.
- Lewellen, W.S. and Teske, M.E. (1974), "Prediction of the Monin-Obukhov similarity functions from an invariant model of turbulence," *J. Atmos. Sci.*, 30, 1340-1365.
- Panofsky, H.A., Tennekes, H., Lenschow, D.H., and Wyngaard, J.C. (1977), "The characteristics of turbulent velocity components in the surface layer," *Boundary-Layer Met.*, 11, 355-361.
- Sandri, G. (1977), "A new approach to the development of scale equations for turbulent flows," Report No. 302, Aeronautical Research Associates of Princeton, Inc., Princeton, NJ.
- Thomas, N.H. and Hancock, P.E. (1977), "'Grid' turbulence near a moving wall," *J. Fluid Mech.* 82, 481-496.
- Willis, G.E. and Deardorff, J.W. (1974), "A laboratory model of the unstable planetary boundary layer," *J. Atmos. Sci.*, 31, 1297-1307.
- Zeman, O. and Lumley, J.L. (1976), "Modeling buoyancy driven mixed layers," *J. Atmos. Sci.*, 33, 1974-1988.

DISTRIBUTION

SPECIAL ASST. TO THE ASST.
SECRETARY OF THE NAVY (R&D)
ROOM 4E741, THE PENTAGON
WASHINGTON, DC 20350

CHIEF OF NAVAL RESEARCH (2)
LIBRARY SERVICES, CODE 734
RM 633, BALLSTON TOWER #1
800 QUINCY ST.
ARLINGTON, VA 22217

OFFICE OF NAVAL RESEARCH
CODE 422AT
ARLINGTON, VA 22217

OFFICE OF NAVAL RESEARCH
CODE 420
ARLINGTON, VA 22217

CHIEF OF NAVAL OPERATIONS
(OP-952)
U.S. NAVAL OBSERVATORY
WASHINGTON, DC 20390

CHIEF OF NAVAL OPERATIONS
NAVY DEPT. OP-986G
WASHINGTON, DC 20350

CHIEF OF NAVAL OPERATIONS
U.S. NAVAL OBSERVATORY
DR. R. W. JAMES, OP-952D1
34TH & MASS. AVE., NW
WASHINGTON, DC 20390

CHIEF OF NAVAL MATERIAL
NAVY DEPT. MAT-0724
WASHINGTON, DC 22332

NAVAL DEPUTY TO THE
ADMINISTRATOR, NOAA
ROOM 200, PAGE BLDG. #1
3300 WHITEHAVEN ST. NW
WASHINGTON, DC 20235

OFFICE OF NAVAL RESEARCH
EAST/CENTRAL REGIONAL OFFICE
BLDG. 114, SECT. D
459 SUMMER ST.
BOSTON, MA 02210

OFFICE OF NAVAL RESEARCH
SCRIPPS INSTITUTION OF
OCEANOGRAPHY
LA JOLLA, CA 92037

COMMANDING OFFICER
NORDA, CODE 335
NSTL STATION
BAY ST. LOUIS, MS 39529

COMNAVOCEANCOM
NSTL STATION
BAY ST. LOUIS, MS 39529

COMMANDING OFFICER
FLENUMOCEANCEN
MONTEREY, CA 93940

SUPERINTENDENT
LIBRARY REPORTS
U.S. NAVAL ACADEMY
ANNAPOLIS, MD 21402

COMMANDER (2)
NAVAIRSYSCOM
ATTN: LIBRARY (AIR-00D4)
WASHINGTON, DC 20361

COMMANDER
NAVAIRSYSCOM (AIR-330)
WASHINGTON, DC 20361

COMMANDER
NAVAIRSYSCOM
MET. SYS. DIV. (AIR-553)
WASHINGTON, DC 20360

COMMANDER
NAVAL SEA SYSTEMS COMMAND
ATTN: LCDR S. GRIGSBY
PMS-405/PM-22
WASHINGTON, DC 20362

COMMANDER
NAVOCEANSYSCEN
ATTN: CODE 4473
SAN DIEGO, CA 92152

COMMANDER
NAVOCEANSYSCEN
DR. J. RICHTER, CODE 532
SAN DIEGO, CA 92152

COMMANDER
NAVSURFWEACEN, CODE R42
DR. B. KATZ, WHITE OAKS LAB
SILVER SPRING, MD 20910

DIRECTOR
NAVSURFWEACEN, WHITE OAKS
NAVY SCIENCE ASSIST. PROGRAM
SILVER SPRING, MD 20910

COMMANDER
PACMISTESTCEN
GEOPHYSICS OFFICER
PT. MUGU, CA 93042

NAVAL POSTGRADUATE SCHOOL
METEOROLOGY DEPT.
MONTEREY, CA 93940

NAVAL POSTGRADUATE SCHOOL
OCEANOGRAPHY DEPT.
MONTEREY, CA 93940

NAVAL POSTGRADUATE SCHOOL
PHYSICS & CHEMISTRY DEPT.
MONTEREY, CA 93940

LIBRARY
NAVAL POSTGRADUATE SCHOOL
MONTEREY, CA 93940

USAFETAC/TS
SCOTT AFB, IL 62225

AFGL/LY
HANSCOM AFB, MA 01731

AFOSR/NC
BOLLING AFB
WASHINGTON, DC 20312

COMMANDER & DIRECTOR
ATTN: DELAS-D
U.S. ARMY ATMOS. SCI. LAB
WHITE SAND MISSILE RANGE
WHITE SANDS, NM 88002

COMMANDING OFFICER
U.S. ARMY RESEARCH OFFICE
ATTN: GEOPHYSICS DIV.
P.O. BOX 12211
RESEARCH TRIANGLE PARK, NC
27709

DIRECTOR (12)
DEFENSE TECH. INFORMATION
CENTER, CAMERON STATION
ALEXANDRIA, VA 22314

DIRECTOR
OFFICE OF ENV. & LIFE SCI.
OFFICE OF THE UNDERSEC OF
DEFENSE FOR RSCH & ENG, E&LS
RM 3D129, THE PENTAGON
WASHINGTON, DC 20505

DR. W. D. NEFF
WAVE PROPAGATION LABORATORY
BOULDER, CO 80303

DR ROGER PIELKE
DEPT OF ATMOS. SCIENCES
COLORADO STATE UNIVERSITY
FT. COLLINS, CO 80523

DR. JOOST BUSINGER
DEPT. OF ATMOS. SCIENCES
UNIV. OF WASHINGTON
SEATTLE, WA 98195

DR. RAY NOONKESTER
NAVAL OCEAN SYSTEMS CENTER
SAN DIEGO, CA 92152

DR. S. A. PIACSEK
NORDA, CODE 322
NSTL STATION
BAY ST. LOUIS, MS 39529

MR. WILLIAM ROGERS
CALSPAN CORP.
BUFFALO, NY 14225

DR. JEROME WEINSTOCK
NOAA
AERONOMY LABORATORY
BOULDER, CO 80303

DR. JAMES DEARDORFF
DEPT. OF ATMOS. SCIENCES
OREGON STATE UNIV.
CORVALLIS, OR 97331

DR. R. A. ANTONIA
MECHANICAL ENGINEERING DEPT.
UNIV. OF NEWCASTLE
N.S.W. 2308 AUSTRALIA

DR. J. C. ANDRE
DIRECTION DE LA METEOROLOGIE
EERM/GMD
92100 BOULOGNE, FRANCE

DR. EARL E. GOSSARD
WAVE PROPAGATION LAB, R45X6
ENVIRONMENTAL RESEARCH LABS
BOULDER, CO 80303

DR. TETSUJI YAMADA
LOS ALAMOS NATIONAL LAB
P.O. BOX 1663, MS 466
LOS ALAMOS, NM 87545

DR. MARVIN WESELY
ARGONNE NATIONAL LAB
ARGONNE, IL 60439

DR. JOHN LUMLEY
SIBLEY SCHOOL OF MECHANICAL &
AEROSPACE ENGINEERING
CORNELL UNIVERSITY
ITHACA, NY 14853

DR. F. T. M. NIEUWSTADT
ROYAL NETHERLANDS
METEOROLOGICAL INSTITUTE
DE BILT, THE NETHERLANDS

DR. W. R. COTTON
DEPT. OF ATMOS. SCIENCES
COLORADO STATE UNIVERSITY
FT. COLLINS, CO 80523

DR. JOHN WYNGAARD
NCAR
P.O. BOX 3000
BOULDER, CO 80307

DR. ROBERT BORNSTEIN
DEPT. OF METEOROLOGY
SAN JOSE STATE UNIVERSITY
SAN JOSE, CA 95192

DR. BRIAN LAUNDER
MECHANICAL ENGINEERING DEPT.
UNIVERSITY OF MANCHESTER
P.O. BOX 88
MANCHESTER M60 1QD ENGLAND

DR. W. C. REYNOLDS
MECHANICAL ENGINEERING DEPT.
STANFORD UNIVERSITY
STANFORD, CA 94305

DR. GILLES SOMMERIA
LABORATOIRE DE METEOROLOGIE
DYNAMIQUE
E.N.S. 24 RUE LHOMOND
75005 PARIS, FRANCE

DR. PH. BOUGEALT
DIRECTION DE LA METEOROLOGIE
EERM/GMD
92100 BOULOGNE, FRANCE

DR. JOEL FERZIGER
MECHANICAL ENGINEERING DEPT.
STANFORD UNIVERSITY
STANFORD, CA 94305

DIRECTOR
NATIONAL METEORO. CENTER
NWS, NOAA
WWB W32, RM 204
WASHINGTON, DC 20233

ACQUISITIONS SECT. IRDB-D823
LIBRARY & INFO. SERV., NOAA
6009 EXECUTIVE BLVD.
ROCKVILLE, MD 20852

DIRECTOR
OFFICE OF PROGRAMS RX3
NOAA RESEARCH LAB
BOULDER, CO 80302

DIRECTOR
GEOPHYS. FLUID DYNAMICS LAB
NOAA, PRINCETON UNIVERSITY
P.O. BOX 308
PRINCETON, NJ 08540

DIRECTOR
TECHNIQUES DEVELOPMENT LAB
GRAMAX BLDG.
8060 13TH ST.
SILVER SPRING, MD 20910

DIRECTOR
NATIONAL WEATHER SERVICE
GRAMAX BLDG.
8060 13TH ST.
SILVER SPRING, MD 20910

HEAD, ATMOS. SCIENCES DIV.
NATIONAL SCIENCE FOUNDATION
1800 G STREET, NW
WASHINGTON, DC 20550

LABORATORY FOR ATMOS. SCI.
NASA GODDARD SPACE FLIGHT CEN.
GREENBELT, MD 20771

CHAIRMAN
INSTITUTE OF ATMOS. PHYSICS
UNIV. OF ARIZONA
TUCSON, AZ 85721

ATMOSPHERIC SCIENCES DEPT.
UCLA
405 HILGARD AVE.
LOS ANGELES, CA 90024

CHAIRMAN, METEOROLOGY DEPT.
UNIVERSITY OF OKLAHOMA
NORMAN, OK 73069

CHAIRMAN, METEOROLOGY DEPT.
CALIFORNIA STATE UNIVERSITY
SAN JOSE, CA 95192

NATIONAL CENTER FOR ATMOS.
RSCH., LIBRARY ACQUISITIONS
P.O. BOX 3000
BOULDER, CO 80302

CHAIRMAN, METEOROLOGY DEPT.
METEORO. & SPACE SCI. BLDG.
1225 W. DAYTON ST.
MADISON, WI 53706

UNIVERSITY OF WASHINGTON
ATMOSPHERIC SCIENCES DEPT.
SEATTLE, WA 98195

COLORADO STATE UNIVERSITY
ATMOSPHERIC SCIENCES DEPT.
FORT COLLINS, CO 80523

CHAIRMAN, METEOROLOGY DEPT.
PENNSYLVANIA STATE UNIV.
503 DEIKE BLDG.
UNIVERSITY PARK, PA 16802

FLORIDA STATE UNIVERSITY
ENVIRONMENTAL SCIENCES DEPT.
TALLAHASSEE, FL 32306

GEOPHYS. SCIENCES COLLECTION
THE UNIVERSITY OF CHICAGO
JOSEPH REGENSTEIN LIBRARY
1100 E. 57TH STREET
CHICAGO, IL 60637

DIRECTOR
COASTAL STUDIES INSTITUTE
LOUISIANA STATE UNIVERSITY
ATTN: O. HUH
BATON ROUGE, LA 70803

ATMOSPHERIC SCIENCES DEPT.
OREGON STATE UNIVERSITY
CORVALLIS, OR 97331

UNIVERSITY OF MARYLAND
METEOROLOGY DEPT.
COLLEGE PARK, MD 20742

CHAIRMAN
ATMOS. SCIENCES DEPT.
UNIVERSITY OF VIRGINIA
CHARLOTTESVILLE, VA 22903

CHAIRMAN
METEOROLOGY DEPT.
MASSACHUSETTS INSTITUTE OF
TECHNOLOGY
CAMBRIDGE, MA 02139

ATMOSPHERIC SCI. RSCH. CENTER
NEW YORK STATE UNIV.
1400 WASHINGTON AVE.
ALBANY, NY 12222

ARVIN/CALSPAN ADVANCED TECH.
CENTER
ATMOS. SCI./ENV. SCI. DEPT.
P.O. BOX 400
BUFFALO, NY 14225

METEOROLOGICAL OFFICE LIBRARY
LONDON ROAD
BRACKNELL, BERKSHIRE
RG 12 1SZ, ENGLAND

EUROPEAN CENTRE FOR MEDIUM
RANGE WEATHER FORECASTS
SHINFIELD PARK, READING
BERKSHIRE RG29AX, ENGLAND

DUDLEY KNOX LIBRARY - RESEARCH REPORTS



5 6853 0107766 7

U207735